TRUSSES WITH REDUCED THERMAL EXPANSION:

THEIR DESIGN, AND MASS AND STIFFNESS PENALTIES.

Submitted by Nunzio Maria Andrea Palumbo to the University of Exeter

as a thesis for the degree of

Doctor of Philosophy in Engineering

In March 2013

I certify that all material in this thesis which is not my own work has been identified and that no material has previously been submitted and approved for the award of a degree by this or any other University.

Nunzio Maria Andrea Palumbo

Signature: ……..

Abstract.

This thesis focused on the mechanisms involved in negative thermal expansion of 2D/3D lattice structures. The effects of varying the constituent materials and geometry were explored. The lattices had geometries similar to those found in light-weight structures in many transport applications, including aerospace and spacecraft. One specific case was to determine how to reduce the coefficient of thermal expansivity (CTE) of such structures to near zero, by using two constituent materials with contrasting CTEs, without incurring penalties in terms of other elastic and failure properties, mass and manufacturability. The lattice geometries able to exhibit altered CTE were explored, and penalties in terms of other elastic properties were quantified. The results were scale-independent and so were generic to all such lattices. Analytical prediction and generic relationships between the geometries of the lattices and their performance were proposed. Experimental validation of the model predictions was undertaken using physical samples.

The thermomechanical properties were simulated by commercial finite element method (FEM) codes (Ansys 11, Ansys, Inc.). Ansys parametric design language was adopted to generate large sets of solutions to be evaluated against chosen criteria. Results show small or, in some cases, no penalties to be paid in terms of stiffness and mass for implementing dual-material lattices with near-zero CTE. Such lattices may compete favourably with high-cost and high-density materials (e.g. Invar) and the manufacture of dual-material lattices can be by standard processes or alternative new process such as Additive Layer Manufacturing (ALM).

An example of truss core sandwich application for aerospace application was modelled by FEM. Applications as cores in sandwich panels might be the first route by which the ALM manufacturing process is required to develop dual-material capability.

Title Page.

Abstract.

Table of Contents.

List of Figures.

List of Tables.

Nomenclature.

Acknowledgements.

Contents

NOMENCLATURE

$(AG)_{eq}$	Equivalent shear rigidity
$(EI)_{eq}$	Equivalent flexural rigidity
$\overrightarrow{ABj}$	Shear loading plane in structures formed from pyramids
$F_{\overrightarrow{ABj}}$	Load acting in $\overrightarrow{AB}$ direction
$G_{\overrightarrow{ABj}}$	Shear modulus in $\overrightarrow{ABj}$ direction
$\delta_{\overrightarrow{AB}}$	Total deflection in $\overrightarrow{AB}$ direction
$[K_{xy}]$	Global stiffness matrix
$[K_{xy}]^{(e)}$	Global stiffness matrix of the e^{th} element
$[K_{x'y'}]^{(e)}$	Elementary stiffness matrix of the e^{th} element
$[T]^{(e)}$	Transformation matrix of the e^{th} element
$[T]^{(e)T}$	Transpose of transformation matrix of the e^{th} element
$[V_{Tx'y'}]^{(e)T}$	Transpose of a vector of the equivalent applied forces in the local system of the e^{th} element
$[V_{x'y'}]^{(e)}$	Vector of the forces and moment at the i node of the e^{th} element in the local system
$\{F_{xy}\}$	Vector of the applied forces and moment in the global system
$\{V_{xy}\}^{(e)}$	Vector of the applied forces and moment in the global system of the e^{th} element
$\{\delta_{xy}\}$	Vector of the linear and rotational displacements
$\{\delta_{x'y'}\}^{(e)}$	Vector of the linear and rotational displacements in local axes of the e^{th} element

1	Number of the structures' phases, high thermal expansivity beam in dual-material structures
2	Number of the structures' phases, low thermal expansivity beam in dual-material structures
2D	Two-dimensional structure
3D	Three-dimensional structure
a	Length low thermal expansivity beams in two-dimensional unit cell
A	Cross-sectional area of the considered face of the RVE
$A_1^{(p1)}$	Cross-sectional area of the p_1^{th} beam member associated with $\delta_{1a}^{(p1)}$, high thermal expansivity beam in dual-material structures
$A_2^{(p2)}$	Cross-sectional area of the p_2^{th} beam member associated with $\delta_{2a}^{(p2)}$, low thermal expansivity beam in dual-material structures
A_e	Cross-sectional area of the e^{th} element
A_i	Apparent cross-sectional of the RVE normal to the loading axis i
Al	Aluminium alloy
ALM	Additive layer manufacturing
b	Length high thermal expansivity beams in two-dimensional unit cell or base length of three-dimensional unit cell
c	Truss core thickness in a sandwich panel
CCF	Carbon fibre composites
CTE	Coefficient thermal expansivity
d	Spacing of the mid-planes of the face sheet in a sandwich panel
DM	Dual-material

DMLS	Direct Metal Laser Sintering
E	Young's modulus constituent material or vibrational energy
E_a	Young's modulus low thermal expansivity beam members
E_b	Young's modulus high thermal expansivity beam members
E_e	Young's modulus of the e^{th} beam member constituent material
E_{eff}	Effective Young's modulus
E_f	Young's modulus of fibres in composites
E^f_{11}	Young's modulus of the face sheets in the 1-direction, corresponding to the Young's modulus in x direction of the TMC face sheets, E_s
E_i	Young's modulus in i direction
E_m	Young's modulus of matrix in composites
E_{max}	Maximum Young's modulus in y direction
E_s	Young's modulus low thermal expansivity constituent material
e^{th}	Number of the beam member
F	Force
f	f is the volume fraction of fibre in composites
FE	Finite Element
FEM	Finite element method
F_i	Total force in i direction
$F_{x'i}^{(e)}$	Axial force at node i of the e^{th} beam member
G^c_{13}	Shear modulus of the pyramidal core 13-direction, corresponding to the shear modulus in xy direction of the core, G_{xy}
G_{eff}	Effective shear modulus

G_{ij}	Shear modulus in *ij* direction
G_{max}	Maximum shear modulus in *xy* direction
h	Height of unit cell
h/b	Aspect ratio three-dimensional unit cell
h/l	Aspect ratio two-dimensional unit cell
h_{2i}	Height of the triangles and/or pyramids located in *i* direction of the unit cell formed from phase 2, low thermal expansivity phase in dual-material structures
h_{2j}	Height of the triangles and/or pyramids located in *j* direction of the unit cell formed from phase 2, low thermal expansivity phase in dual-material structures
h_{2x}	Height of the triangles and/or pyramids located in *x* direction of the unit cell formed from phase 2, low thermal expansivity phase in dual-material structures
h_{2y}	Height of the triangles and/or pyramids located in *y* direction of the unit cell formed from phase 2, low thermal expansivity phase in dual-material structures
I	Second moment of area
I_e	Second moment of area e^{th} beam member
ijk	Global axes
Inv	Invar
$j_1^{(p1)}$	Term equal to 1, 2 or 4 indicating full, half or quarter cross-sectional area of set of p_2^{th} phase 1 beam members according to the number of shared

	neighbouring cells
$j_2^{(p2)}$	Term equal to 1, 2 or 4 indicating full, half or quarter cross-sectional area of set of p_2^{th} phase 2 beam members according to the number of shared neighbouring cells
K	Structural stiffness
K^{-1}	Reciprocal of Kelvin temperature
K_i	Structural stiffness in i direction
l	Length base of two-dimensional unit cell
$l^{(e)}$	Length of the e^{th} element
$L_{1i}^{(p1)}$	Length of set of p_1^{th} phase one beam members lying in line with the i axis, high thermal expansivity beam in dual-material structures
L_{1x}	Length of phase 1 beam members lying in line with the x axis, high thermal expansivity beam in dual-material structures
L_{1y}	Length of phase 1 beam members lying in line with the y axis, high thermal expansivity beam in dual-material structures
$L_{2i}^{(p2)}$	Length of set of p_2^{th} phase 2 beam members lying inclined to the i axis, high thermal expansivity beam in dual-material structures
$L_{2j}^{(p2)}$	Length of set of p_2^{th} phase 2 beam members lying inclined to the j axis, low thermal expansivity beam in dual-material structures
l_e	Length of the e^{th} element
l_f	Final lengths
L_i	Length of RVE in i direction
l_o	Initial lengths

L_p	Span between the outer supports in a sandwich panel
$M_i^{(e)}$	Moment at node *i* of the e^{th} beam member
$m_i^{(e)}$	Moment at node *i* of the e^{th} element
MMC	Metal matrix composite
MN	Monolithic
n_1	Total number of phase 1 beam elements, high thermal expansivity beam in dual-material structures
n_2	Total number of phase 2 beam elements, low thermal expansivity beam in dual-material structures
N_i	Number of possible structures for each 'type [N]' case
N_i	Value required by the equilibrium and compatibility of unit cells under the axial loading in *i* direction
N_{ij}	Value required by the equilibrium and compatibility of unit cell under the shear loading in *ij* direction
NTE	Negative thermal expansivity
N_x	Value required by the equilibrium and compatibility of unit cells under the shear loading in *x* direction
N_{xy}	Value required by the equilibrium and compatibility of unit cells under the shear loading in *xy* direction
N_y	Value required by the equilibrium and compatibility of unit cells under the shear loading in *y* direction
p_1^{th}	Number of the phase 1 beam elements, high thermal expansivity beam in dual-material structures

$p_{2^{th}}$	Number of the phase 2 beam elements, low thermal expansivity beam in dual-material structures
PTE	Positive thermal expansivity
quasi-RUM	Quasi-rigid unit modes
r	Radius beam member
RUM	Rigid unit modes
RVE	Representative Volume Element
SCS-6	Silicon Carbide fibre
SiC	Silicon carbide
t	Thickness beam members
T	Temperature
t_e	Thickness of the beam member in y' direction
Ti	Titanium alloy
Ti-6Al-4V	Titanium alloy
TMC	Titanium matrix composite
t_{ti}	Thickness of titanium face sheet in sandwich panel
t_{TMC}	Thickness of titanium matrix composite face sheet in sandwich panel
u_y	Uniform displacement in y direction
V	Volume unit cell
v_{f1}	Volume fraction phase 1, high thermal expansivity phase in dual-material structure
v_{f2}	Volume fraction phase 2, low thermal expansivity phase in dual-material structure

$V_{xi}^{(e)}$	Force components in x direction global axes at node i of the e^{th} element
$V_{x'i}^{(e)}$	Force components in x' direction local axes at node i of the e^{th} element
$V_{yi}^{(e)}$	Force components in y direction global axes of the e^{th} element
$V_{y'i}^{(e)}$	Force components in y' direction local axes at node i of the e^{th} element
x_1	Displacement at node 1
x_2	Displacement at node 2
$x'y'$	Local axes
xyz	Global axes
ZTE	Near-zero thermal expansivity
α	Coefficient thermal expansivity constituent material
α_a	Coefficient thermal expansivity low thermal expansivity beam members
α_b	Coefficient thermal expansivity high thermal expansivity beam members
α_e	Coefficient thermal expansivity of the e^{th} beam member constituent material
α_{eff}	Effective coefficient thermal expansivity
α_i	Coefficient thermal expansivity i direction
α_l	Linear coefficient thermal expansivity
α_s	Coefficient thermal expansivity in low thermal expansivity constituent material
α_v	Volume coefficient of thermal expansivity
γ	Shear strain
δ	Displacement or deflection sandwich panel
δ_{1a}	Axial deflection of phase 1 in-line beam members, high thermal expansivity beam in dual-material structures

$\delta_{1a}^{(p1)}$	Axial deflection of set of p_1^{th} phase in-line beam members, high thermal expansivity beam in dual-material structures
δ_{2a}	Axial deflection of phase 2 inclined beam members, low thermal expansivity beam in dual-material structures
$\delta_{2a}^{(p2)}$	Axial deflection of set of p_2^{th} phase 2 inclined beam members, low thermal expansivity beam in dual-material structures
δ_i	Displacement of the normal face of the RVE
ΔT	Variation of temperature
$\delta_{xi}^{(e)}$	Displacement components in x direction global axes at node i of the e^{th} element
$\delta_{x'i}^{(e)}$	Displacement components in x' direction local axes at node i of the e^{th} element
$\delta_{yi}^{(e)}$	Displacement components in y direction global axes at node i of the e^{th} element
$\delta_{y'i}^{(e)}$	Displacement components in y' direction local axes at node i of the e^{th} element
ε	Strain
ε_i	Axial strain in i direction
θ	Angle measurement
$\theta_i^{(e)}$	Rotational degree of freedom at node i
ν	Poisson's ratio constituent material
ν_{ij}	Poisson's ratio in ij direction
ρ	Density of the cellular structure or density constituent material
ρ^*	Relative density of the truss material
ρ_s	Density of the solid

τ	Shear stress acting on the RVE parallel to $\overrightarrow{AB}$
ω_i	Internal angles of the unit cells
σ_i	Stress acting on the RVE parallel to *i* axis
σ_Y	Yield stress

Acknowledgements.

I would like to thank Professor Ken E. Evans and Professor Chris W. Smith for their supervision and support during the years of my PhD project. I would also like to thank Professor Fabrizio Scarpa for his guidance and support.

I gratefully acknowledge financial support from Great Western Research (GWR) and EADS UK Ltd. I also gratefully acknowledge the technical support of Mr Jonathan Meyer (EADS Innovation Works Ltd, UK).

Finally, thanks also to Dr Wayne Miller for the several discussions on the subject of my thesis and his useful support.

1 INTRODUCTION AND LITERATURE REVIEW

1.1 Introduction and thesis outline

The main target of this PhD work was to design lattice structures (or truss structures) with specific thermomechanical properties notably near-zero Coefficient of Thermal Expansivity (CTE). More particularly, the aim was to design structures with tailored thermal distortion for applications where thermal management is an important requirement. This study tries to extend the understanding of such types of structure and of the mechanism that drives reduced or negative thermal expansivity. In particular, structural performance combined with a reduced and/or near-zero thermal expansivity was quantified and the possible penalties, in terms of additional mass or reduced stiffness, calculated. Lattices in both monolithic and dual-material form were studied and compared. Although some structures can present geometrical complexity, all the designs proposed can be manufactured by traditional manufacturing process or by innovative processes such as Additive Layer Manufacturing (ALM). Several applications can be targeted for these structures, ranging from aerospace to transport applications, and sporting goods. An application-specific case study is presented.

The present thesis has been organised in eight chapters as follows.

The first chapter contains a detailed literature review with a comprehensive overview of all the previous work in all the relevant areas approached (thermal expansivity, lattice structures, etc.). The second and third chapters explore 2D and 3D designs in both monolithic and dual-material configuration, exploring the thermal mechanical behaviour

both analytically and numerically, in order to quantify the structural performance combined with reduced thermal distortion and to set simple design roles for such structures. The fourth chapter develops an alternative numerical tool to generate 2D/3D lattices under specific constraints in terms of nodal connectivity and number of beams, creating ranges of thermomechanical behaviours for several examples proposed. The fifth chapter presents an experimental validation of the thermal behaviour of the monolithic and dual-material structures proposed in Chapters 2 and 3. The sixth chapter present non-linear FEM models of an application proposed during the PhD project period by the sponsor, EADS Innovation Works Ltd (UK), to enhance ALM manufacturing process. Chapters 7 and 8 present the overall discussion and, conclusion and future work.

1.2 Thermal Expansion

Engineering materials usually expand in response to heating and contract in response to cooling, the rate of which is the Coefficient of Thermal Expansion (CTE). However, there are a growing number of materials, synthetic and naturally occurring, that contract upon heating and thus exhibit a Negative Coefficient of Thermal Expansion (NTE). The coefficient of thermal expansion, α, is a measure of a material change in dimensions as a result of temperature change. This can be a change in length or a volume change. The linear coefficient α_l is defined as (Lennard-Jones, 1924):

$$\frac{l_f - l_0}{l_0}\frac{1}{(\Delta T)} = \alpha_l \qquad \textbf{1.1}$$

where l_0 and l_f are the initial and final lengths respectively, ΔT is the variation of temperature and the coefficient α_l is the linear coefficient of thermal expansion. It represents a material property and it is representative of the extent to which a material expands upon heating. The unit of α_l is a reciprocal of temperature (e.g. K^{-1}). As can be seen in Equation 1.1 $\frac{l_f - l_0}{l_0}$ is, by definition, a strain.

Similarly, it is possible to define a volumetric coefficient α as (Lennard-Jones, 1924):

$$\frac{\Delta V}{V_0}\frac{1}{(\Delta T)} = \alpha_v \qquad \textbf{1.2}$$

where V_o is the initial volume, ΔV is the change of volume and the coefficient α_v is the volume coefficient of thermal expansion. For an isotropic material in which the thermal

expansion is isotropic, the value of the volume coefficient of thermal expansion is (Lennard-Jones, 1924):

$$\alpha_v = 3\alpha_l \qquad \textbf{1.3}$$

because α^2 and higher terms tend to be negligible.

In the anisotropic case

$$\alpha_v = \alpha_i + \alpha_j + \alpha_k \qquad \textbf{1.4}$$

where *i*, *j* and *k* represent orthogonal directions.

From an atomic perspective, the effect of temperature change can be understood by consideration of the potential energy versus interatomic distance curve, see Figure 1.1.

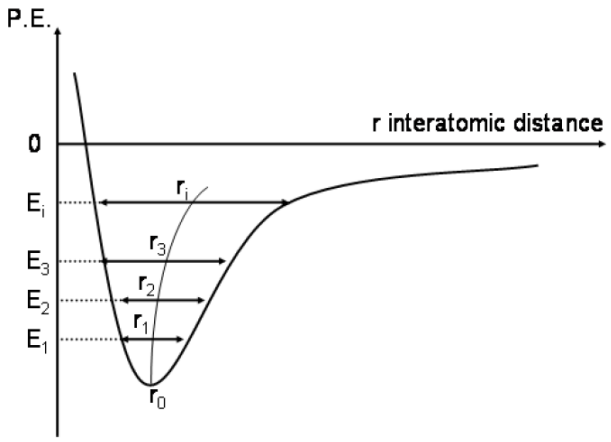

Figure 1.1. Potential energy versus interatomic distance asymmetric curve (Lennard-Jones, 1924).

The minimum of the curve, r_0, represents the equilibrium interatomic spacing at 0 *K*. With increasing temperature, the vibrational energy, *E*, also increases, with a correspondingly larger amplitude of the interatomic distance. The harmonic approximation predicts that there is no thermal expansion of the lattice; that is the average interatomic

spacing does not increase with increasing atomic displacement (temperature) for a harmonic oscillator. In practice, real materials are characterised by non-parabolic dependences of potential energy on displacement and they exhibit clear signs of anharmonic behaviour. It is this asymmetry in the potential energy curve which actually causes the thermal expansion behaviour, i.e. an increase in the mean distance between the atoms. A symmetric energy potential curve would cause no net change in interatomic separation, i.e. zero thermal expansion.

If materials contract upon heating, they have a Negative Coefficient of Thermal Expansion (NTE). In recent years, these materials have been studied experimentally and theoretically.

1.3 Negative Thermal Expansion

1.3.1 Mechanisms

Negative Thermal Expansion (NTE), reviewed by Barrera et al. (2005), arises when the underlying thermal expansion of chemical bonds is overruled by other mechanisms, driving a contraction in a linear dimension or overall volume. This behaviour has been studied experimentally and theoretically for some time (Baughman and Galvão, 1995; Evans, 1999; Sleight, 1995, 1998b; Tao and Sleight, 2003a).

Although various categories of material show NTE, most attention has been focused on the mechanisms involved in negative thermal expansion of metal oxide structures (Evans, 1999; Evans et al., 1998; Sleight, 1995, 1998b) and, to an extent, siliceous zeolites. Oxide structures can be used as an example to demonstrate a common structural

mechanism for negative thermal expansivity. This mechanism implicates relative movement (translation and rotation) within the molecular structure of a compound, more so than the actual change of length of individual bonds within the structure itself, see Figure 1.2, which does happen but is dominated by larger deformations. The structure shifts to a lower volume arrangement as heat energy is increased in the system. The bond lengths change as expected due to anharmonic atom vibration, see Figure 1.1, but the effect is smaller than that of the structural reorganisation. Possible mechanisms that drive this reorganisation are explained below.

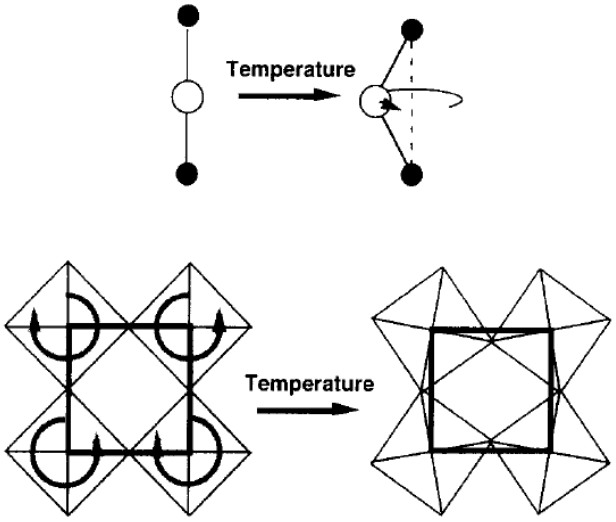

Figure 1.2. A schematic representation of how the relative movement within the molecular structure of a compound can give rise to NTE (Evans et al., 1998).

One mechanism for intrinsic negative thermal expansion, pertaining to the ferroelectric oxides, has been identified by Sleight (1998b). In the low temperature range, this mechanism is based on increasing symmetry of polyhedra with increasing temperature. The average metal-oxygen (M-O) distances in polyhedra decreases as the polyhedra become more regular. This causes contraction in one direction capable of giving a small overall volume cell contraction and can be attributed to a decrease of distortion of MO_6 and

AO_{12} polyhedra due to the minimisation of anion–anion repulsions when the polyhedra become more regular. Sleight shows that negative thermal expansion exists in $BaTiO_3$ and $PbTiO_3$, and other AMO_3 (A=Alkali metal; M=Metal) oxides at low temperatures (just below their tetragonal-to-cubic phase transitions). Normal positive thermal expansion is observed for both $BaTiO_3$ and $PbTiO_3$ above the tetragonal-to-cubic phase transition.

A second mechanism of negative thermal expansion is a result of the normal positive thermal expansion of certain M-O bonds (Sleight, 1995, 1998a, 1998b). Some hexagonal structures, like cordierite ($Mg_2Al_2Si_5O_{18}$), *β*-eucryptite ($LiAlSiO_4$) and NZP ($NaZrP_3O_{14}$) show this mechanism (Sleight, 1998b). The Si-O, P-O, Al-O and Zr-O bonds are stronger than Mg-O, Li-O and Na-O bonds. The result is that these structures show an anisotropic thermal expansion due to the negligible thermal expansion of the strong bonds compared with the significant thermal expansion of the weak bonds. This means that thermal expansion in *a* and *b* directions always occurs in the opposite sense to *c* direction, Figure 1.3. For example, if CTE in *a* and *b* directions is positive then CTE in *c* direction would be negative. The net effect of this mechanism is a very low volume expansion. Sleight proposed a model for these materials, taking into account constant Si-O, P-O, Al-O and Zr-O bonds. The thermal expansion of the Mg-O, Li-O and Na-O bonds is known and therefore their impact on the global behaviour can be calculated. The O-O distance of a shared edge or shared face in linked octahedral and tetrahedral is invariant. This feature results in the positive thermal expansion occurring along *a* and *b* directions of the crystal in cordierite and *β*-eucryptite, and along *c* direction of NZP. As the sheet of edge-shared polyhedral in cordierite and *β*-eucryptite expands along *a* and *b* directions, it is pulled together along the *c* direction. On heating of NZP, chains of face-shared octahedral expand along weak Na-O bonds in the *c* direction. At the same time, twisting P-O bonds of

constant length pull these chains together, and this therefore results in a thermal contraction along *a* and *b* directions. These types of mechanism rationalise negative thermal expansion in one or two directions but they do not lead to a negative volume expansion based on unit cell changes.

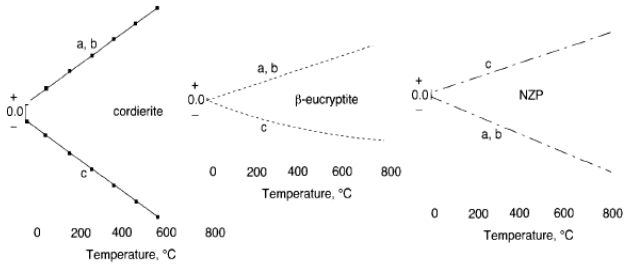

Figure 1.3. Thermal expansion of three anisotropic materials (Sleight, 1995).

The model described above is not able to explain, for instance the small negative expansion seen for some members of *β*-eucryptite and the NZP family (Sleight, 1995, 1998a, 1998b). Sleight models a third mechanism for negative thermal expansion based on interstitial cation migration within a network, changing sites as a function of temperature. For instance, in *β*-eucryptite, the Li^+ cations are located mainly in tetrahedral sites. Sleight's study has explained that movement of just a few per cent of the Li^+ cations to the octahedral sites can cause the observed negative volume thermal expansion. This study also suggests that thermal expansion properties of some members of the NZP family depend critically on the varying positions of the interstitial cations with temperature.

A fourth mechanism for negative thermal expansion is based on the transverse thermal motion of oxygen in an M-O-M linkage (Sleight, 1995, 1998a, 1998b). If the M-O bonds are sufficiently strong, they will show the usual positive thermal expansion. The primary vibration of oxygen will be perpendicular to a line joining the two metal atoms when increasing the temperature. If the average M-O-M angle is 180º (the situation is more

complicated if this average is not close to 180º) this increased oxygen vibration will pull the metal atoms together, which can then shrink the entire lattice in some structures, Figure 1.4. In general, these transverse modes have lower energy than longitudinal modes, and result in NTE only at very low temperatures in a number of materials (for instance SiO_2 below room temperature) (Evans, 1999; Sleight, 1998a, 1998b).

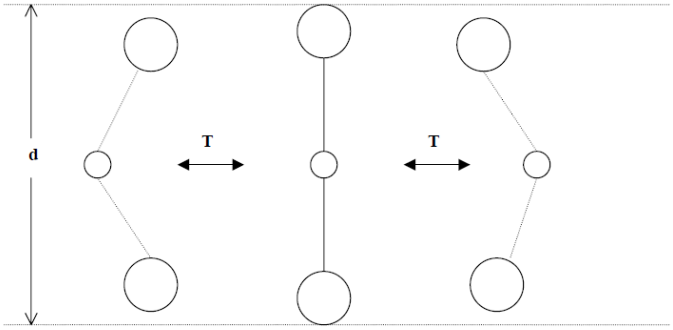

Figure 1.4. Apparent decrease of interatomic distances due to the thermal vibration of 2-coordinated oxygen atoms (Tao and Sleight, 2003a).

The above vibrational theory has been extended to materials with framework structures consisting of more or less rigid groups of several atoms (usually tetrahedra or octahedra) (Evans, 1999). Some of these structures permit low frequency vibrations (transverse thermal motion, as seen above) involving rotations of the 'rigid units', giving rise to marked negative expansion. In other structures, apparently geometrically similar, such vibrations do not occur. Because the neighbouring rigid units are connected to each other only through a shared atom or a linking bond, it is possible for their mean orientations to change with temperature. An example of this mechanism is found in the low-temperature form of quartz, α, causing the expansion to be positive. In the high-temperature form, β, the mechanism is forbidden, and the expansion becomes negative (Evans, 1999). These mechanisms suggest that thermal expansivity varies because resistance to transverse motion of bonds depends upon the details of the surrounding network as well as the nature of the

M-O-M bridge itself. A valuable model has been developed to describe the occurrence of these thermal expansion behaviours in framework structures (Evans, 1999; Giddy et al., 1993; Heine et al., 1999; Tao and Sleight, 2003a, 2003b) based on rigid polyhedra (SiO_4, WO_4, ZrO_6, etc.) linked by shared oxygen atoms at the corners. Large amplitude transverse vibrations of the oxygen atoms can occur only through coupled vibrations of the tetrahedra and octahedra forming the structure. Such vibrations are called rigid unit modes or RUMs. They involve no changes in intra-unit bond distances and angles, and thus have large amplitudes and low frequencies. The concept is illustrated by the 2D lattice shown in Figure 1.5a, where rigid MO_4 squares are hinged to their neighbours by shared oxygen atoms. Figure 1.5b shows possible RUMs, in which neighbouring squares rotate in opposite directions. It is possible to note that the rotational motion in this 2D structure, showing the rotation of the units by an angle θ, reduces the size of the square unit cell (NTE), Figure 1.5b.

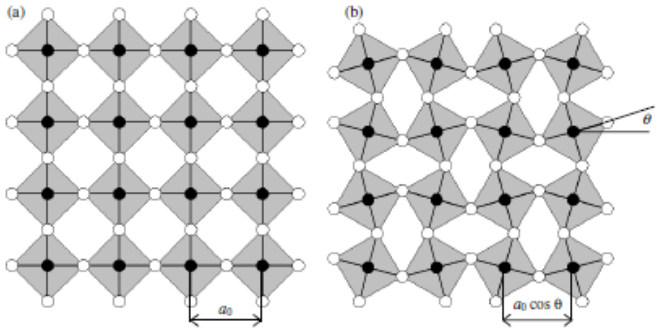

Figure 1.5 (a and b). Rotational motion in a 2D lattice: a) ideal structure before rotation, b) after rotation (Barrera et al., 2005).

Another mechanism, discussed by Evans (1999), which can also give rise to NTE, is magnetostrictive phenomena in the region of a magnetic phase. For materials with significant magnetoelastic coupling, the normal vibrational mode that drives positive thermal expansion can be compensated by a large contraction, driven by a change in

magnetic structure. This is the case for alloys such as 'Invar' $Fe_{0.65}Ni_{0.35}$, and transition metals such as Cr and α-Mn over a restricted temperature range.

The main underlying mechanisms, both microstructural and molecular, discussed above, although not yet completely understood and sometimes concentrating on a specific instance of CTE (negative or positive), can be exploited in a manner allowing their generalised and practical use in the development of tailored thermal expansion of artificial or synthetic materials or structures.

1.3.2 Cubic and isotropic materials

Cubic and isotropic materials showing isotropic thermal expansion have been reviewed by Barrera et al. (2005).

ALKALI HALIDES

The alkali halides are the family of ionic compounds with simple chemical formulae X^+Y^- or XY, where X is an alkali metal and Y is a halogen. One of the most well-known of these is sodium chloride (NaCl). The internal crystalline structure, at room temperature, is centred cubic; usually face-centred cubic. Experimentally, negative thermal expansion due to vibrational mechanisms has been found in materials with open structures, where coordination numbers are small such as RbBr (rubidium bromide) and RbI (rubidium iodide). In these compounds, the thermal expansion becomes negative below about 8 *K* (Barron et al., 1980).

TETRAHEDRALLY COORDINATED STRUCTURES

Tetrahedrally coordinated structures, such as the series of semiconductors with the diamond, zinc blend or wurzite structure (e.g. zinc iron sulphide mineral), may show NTE.

For instance, the volume coefficient of thermal expansion of CuCl (cuprous chloride) reaches a minimum of around - 8×10^{-6} K^{-1} and does not become positive until 100 *K*. Conversely, in diamond itself, the covalent bonding is very strong and the expansion remains positive at all temperatures. At high temperatures, none of the tetrahedrally coordinated structures have negative thermal expansion, although for many of them the CTE is small, as reviewed by Barrera et al. (2005).

CUBIC ZrW_2O_8 AND SIMILAR CRYSTALS

Cubic zirconium tungstate (ZrW_2O_8) is known to give rise to a large isotropic negative expansion in a wide temperature range (Ernst et al., 1998; Evans, 1999; Pryde et al., 1996). The negative volume coefficient of thermal expansion is from low temperatures to about 1050 *K*. The crystal has a cubic structure. WO_4 tetrahedra and ZrO_6 octahedra are linked such that each ZrO_6 unit shares its corners with six different WO_4 units, while each WO_4 unit shares only three of its corners with each ZrO_6 unit; the remaining oxygen in each WO_4 tetrahedron is formally singly coordinated, Figure 1.6. The existence of terminal oxygen enhances flexibility. Theoretical analyses (Pryde et al., 1998; Pryde et al., 1996) reveal families of RUMs and quasi-RUMs of high and low frequencies. This result is confirmed by experimental analyses such as elastic and inelastic neutron scattering (Ernst et al., 1998; Mittal et al., 2001), heat capacity (Ramirez and Kowach, 1998) and other measurements. The mechanism for negative thermal expansion has been further investigated by means of quasi-harmonic lattice dynamics (Mittal and Chaplot, 1999), high pressure Raman spectroscopy and X-ray absorption (Cao et al., 2002).

The thermal expansivity of ZrW_2O_8 has been determined between 2 *K* and 520 *K* by high resolution powder diffractometry (David et al., 1999). Mary et al. (1996) extended

measurements of thermal expansion from room temperature up to 1050 *K*. Results are shown to be consistent with previous measurement. The coefficient of thermal expansion is negative down to at least 15 *K*. Above 50 *K*, the volume coefficient of thermal expansion is $\alpha_v \approx$ - 27 × 10^{-6} K^{-1}, up to about 350 *K*. Above 450 *K*, the expansion is still negative but smaller in magnitude ($\alpha_v \approx$ -13 × 10^{-6} K^{-1}), presumably because the disordered structure reduces the number of RUMs and quasi-RUMs. This behaviour continues up to 1050 *K*.

The thermal expansivity of cubic HfW_2O_8 is essentially identical (Mary et al., 1996). Negative expansion has also been found in crystals of similar structure with composition $ZrMo_2O_8$ (Allen and Evans, 2003), $Zr_{1-x}Hf_xW_2O_8$ and $ZrW_{2-x}Mo_xO_8$ (Evans, 1999), and $Zr_{1-x}M_xW_2O_{8-y}$ (M=Sc, In, Y) (Nakajima et al., 2003).

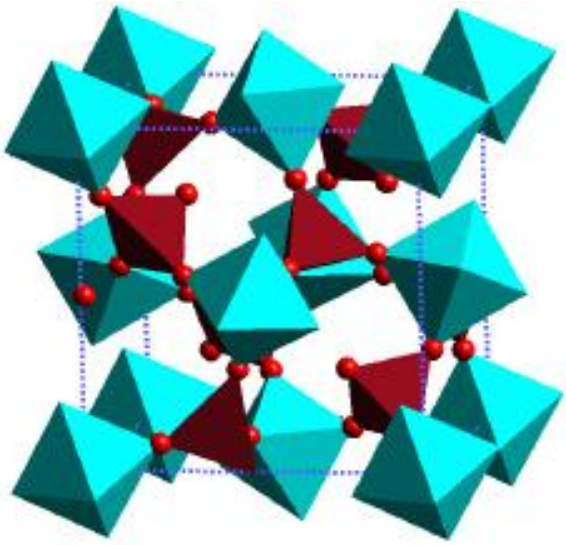

Figure 1.6. The room temperature structure of ZrW_2O_8. ZrO_6 octahedra (light blue) and WO_4 tetrahedra (dark red) are shown. The spheres are oxygen atoms (Barrera et al., 2005).

CUBIC AM_2O_7

This is a family of compounds in which A=Th, Zr, Hf, Sn, and M=P, V. The structure is usually cubic and it is closely related to that of ZrW_2O_8. Each pair of tetrahedra

in the zirconium tungstate structure is replaced by a M_2O_7 unit, in which the two MO_4 tetrahedra are linked by a common oxygen. The higher coordination number than that present in the ZrW_2O_8 has been found to allow quasi-RUMs but not RUMs (Pryde et al., 1996). The structure of the AM_2O_7 compounds (e.g. ZrV_2O_7) is less flexible because of the presence of pairs of linked tetrahedral units. This more complex structure involves 3D rotation of polyhedral units and small amplitude transverse vibrations of M-O-M bridges (Evans, 1999). At higher temperatures, most oxygen angles open up, causing a reduction in volume (NTE) due to both the translation and rotation of the repeating tetrahedra units. Obviously the behaviour changes greatly within the AM_2O_7 family. The mechanism that drives NTE in ZrV_2O_7 is similar to that described before. There is a strong positive coefficient of thermal expansion up to 375 *K* and a strong negative coefficient of thermal expansion ($- 7.1 \times 10^{-6}\ K^{-1}$) at around 400-500 *K*, presumably due to the quasi-RUMs (Evans, 1999). NTE continues to about 1073 K, where decomposition occurs (Khosrovani et al., 1997; Korthuis et al., 1995).

For ZrP_2O_7, the coefficient of thermal expansion is very low and positive ($\alpha_v \approx + 5.4 \times 10^{-6}\ K^{-1}$) above 600-700 *K* (Evans, 1999; Korthuis et al., 1995). For some of the solid solutions (e.g. $ZrV_{2-x}P_xO_7$), there is a very low and positive thermal expansion at room temperature and a negative expansion at higher temperature (Evans, 1999; Korthuis et al., 1995).

Results in the HfV_2O_7 - HfP_2O_7 systems are essentially identical to those in the ZrV_2O_7 - ZrP_2O_7 systems (Korthuis et al., 1995).

SILICA AND ZEOLITES

Cristobalite is a high temperature polymorph of quartz, meaning that it is composed of the same chemistry (SiO_2), but has a different structure. The structure is cubic and it consists of SiO_4 tetrahedra in which every oxygen atom is shared with a neighbouring tetrahedron. The coefficient of thermal expansion of α-cristobalite, a high-density phase of cristobalite, is positive, while that of β-cristobalite, a low-density phase, is negative (Yamahara et al., 2001). This behaviour has been successfully simulated in molecular dynamics studies. It has been shown that for cristobalite the thermal expansion is correlated to the average Si-O-Si angle. These variations with increasing temperature bring about the normal thermal expansion for α-cristobalite and negative thermal expansion for β-cristobalite. For β-cristobalite, the anomaly, negative thermal expansion, is attributed to the great freedom of transverse oxygen vibration.

Zeolites are microporous crystalline solids with well-defined structures. Generally, they contain silicon, aluminium and oxygen in their framework and cations, water and/or other molecules within their pores. Many zeolites occur naturally as minerals, while others are synthetic. A defining feature of zeolites is that their frameworks are made up of 4-connected networks of atoms. One way of thinking about this is in terms of tetrahedra, with a silicon atom in the centre and oxygen atoms at the corners. These tetrahedra can then link together by their corners to form a rich variety of structures. The framework structure may contain linked cages, Figure 1.7, cavities or channels.

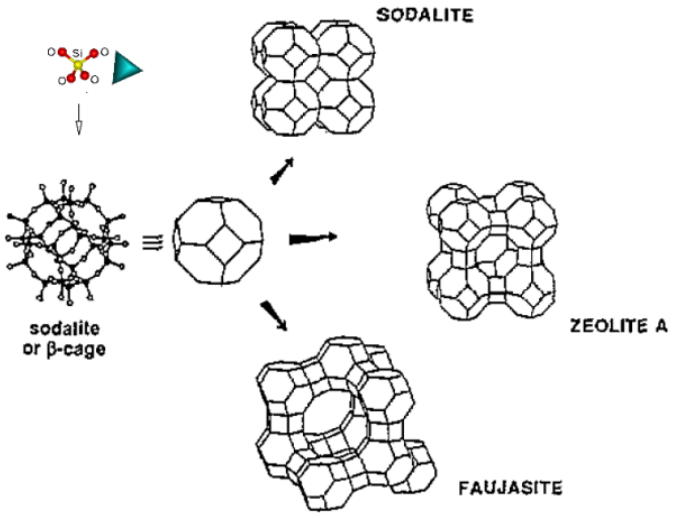

Figure 1.7. Cage; the sodalite or β-cage, linked to create the structure of sodalite, zeolite A and faujasite (zeolite X/Y) (Couves et al., 1993).

Couves et al. (1993) have reported an application of a lattice dynamical method to predict the lattice parameters contraction with temperature for three cubic materials. Two were pure silica, siliceous sodalite and siliceous faujasite, and one was Na^{+}-zeolite X. The simulations predicted positive expansion for siliceous sodalite and for the siliceous faujasite and a significant contraction in the lattice parameter for the Na^{+}-zeolite X, with temperature. These predictions were subsequently confirmed by powder diffraction measurements. A strong isotropic negative thermal expansion ($\alpha_v \approx -4.2 \times 10^{-6}\ K^{-1}$) has been found over the whole range between 50 *K* and 500 *K* for siliceous faujasite (Attfield and Sleight, 1998).

For non-cubic zeolites, see Section 1.3.3.

GLASSES AND GLASS CERAMICS

Barron et al. (1980) reviewed glasses and glass ceramic materials. Experiments have shown that in some temperature (below 150 *K*) regimes pure vitreous silica (lower density

than crystalline form) exhibits negative thermal expansion. For some other tetrahedrally bonded glasses, the thermal expansion is still negative at low temperatures whereas for non-tetrahedrally bonded glasses (including polymeric ones) it has been found to be positive (except below about 1 *K*). Values for α/T of around - 0.5 × 10^{-9} K^{-2} for various silica glasses and - 3.5 × 10^{-9} K^{-2} for polymeric PMMA glass have been found.

Glass ceramics are important technical materials that are formed in the glassy state and then partially crystallised to give high mechanical strength with zero porosity. Generally, the thermal expansion depends crucially on composition; the addition of $LiAlO_2$ to silica leads to strong negative thermal expansion (see also Section 1.3.3).

1.3.3 Anisotropic materials

Anisotropic materials (non-cubic structures), reviewed by Barrera et al. (2005), can show negative coefficients of thermal expansion, like cubic materials. Even when the volume coefficient of thermal expansion is positive, one or two of the three principal linear coefficients of thermal expansion may be negative. The underlying mechanisms driving negative expansion in these materials are similar to those seen in cubic materials.

WURZITE STRUCTURE AND HEXAGONAL ICE

These structures are hexagonal with a tetrahedral coordination similar to that of the cubic zinc-blend structures and, like the cubic structures, can show negative expansion over wide ranges below room temperature, sometimes with considerable anisotropy. For instance, zinc oxide shows a negative coefficient of thermal expansion below 100 *K* (Yates et al., 1971); the linear coefficient of thermal expansion parallel to the *c* direction of the crystal is $\alpha_{//} \approx$ - 0.7 × 10^{-6} K^{-1} at about 90 *K* and stays negative up to 130 *K* whilst

perpendicular to the *c* direction of the crystal $\alpha_{\perp} \approx -0.2 \times 10^{-6}\ K^{-1}$ at about 90 *K* and stays negative up to about 100 *K*.

LAYERED STRUCTURES

An ideal layered structure is an assembly of large macromolecules held together mainly by Van de Waals forces in one direction (e.g. *c* direction for axial crystals) and covalent linking in the other two directions (e.g. *a* and *b* for axial crystals), reviewed by Barrera et al. (2005). Covalent linking within a layer is so strong that the layer can be considered almost rigid in *a* and *b* directions thus, it is difficult to deform the layers in these directions. The hexagonal crystal graphite is a simple example (Bailey and Yates, 1970). The coefficient of expansion perpendicular to the axis, $\alpha_{\perp}$, is negative over a wide range below room temperature ($\alpha_{\perp} \approx -1.5 \times 10^{-6}\ K^{-1}$ at about 273 *K*) (Riley, 1945), while the expansion parallel to the axis, $\alpha_{/\!/}$, is positive.

Arsenic is another elemental crystal for which $\alpha_{\perp}$ is negative below room temperature. At room temperature, the linear coefficient of thermal expansion is $\alpha_{\perp} \approx 0 - 1.5 \times 10^{-6}\ K^{-1}$ (White, 1972). Zinc and cadmium (Barron et al., 1980) are yet further examples.

There are more complex structures (and bonding) in which it becomes more difficult to predict or explain the thermal expansion, for instance magnesium chloride ($MgCl_2$) shows a highly unusual thermal behaviour (Soriano et al., 2001); the expansion is highly anisotropic, being small and negative at low temperature for dilations perpendicular to the main crystal axis (*c* direction) and larger and always positive for dilations parallel to the main crystal axis. At about 60 *K*, there is a crossover above which the expansion is considerably larger and more positive along the *a* and *b* directions, than along the *c*

direction, contradicting the 'general rule' that anisotropic crystals expand more along the 'softer' axes and less in the 'harder' directions, with graphite being the classic example of such a layered crystal.

CHAIN STRUCTURES

Crystalline polymers have a chain structure, and are elastically stiff only along their main direction. For linear chains, thermal expansion is positive in the plane normal in relation to the chain direction, while thermal expansion along the chain direction is often negative, and typically, an order of magnitude less than that normal to the chain (Barron et al., 1988). The mechanism that drives negative anisotropic thermal expansion is similar but inverse to that shown in layered structures: the thermal expansion along the chain direction is thus small and negative (obviously until the temperature is high enough to excite vibrations in the strong bonds).

Tellurium provides an example of negative linear coefficient of thermal expansion along the chain direction, $\alpha_{//}$ (Hortal and Leadbett, 1972). Thermal expansion measurements carried out by Hortal show coefficient of thermal expansion parallel to the chain direction negative ($\alpha_{//} \approx - 0.12 - 2.10 \times 10^{-6} K^{-1}$) and coefficient of thermal expansion perpendicular to the chain direction positive ($\alpha_{\perp} \approx 0.15 - 29.2 \times 10^{-6} K^{-1}$) over the temperature range 4 *K* to 200 *K*.

Some polymers, like polyethylene, at low temperatures show a negative thermal expansion along the chains' direction and positive thermal expansion in directions perpendicular to the polymer chains. Orthorhombic polyethylene shows this behaviour (Bruno et al., 1998).

OXIDES

Paratellurite (TeO_2) has a tetragonal rutile structure. At room temperature, the linear coefficients of thermal expansion $\alpha_{//}$ (parallel to the crystal axis) and $\alpha_{\perp}$ (perpendicular to the crystal axis) are both positive. The linear coefficient of thermal expansion ($\alpha_{\perp}$) and the volume coefficient of thermal expansion (α_v) become negative below 10 *K* and 7 *K*, respectively (White et al., 1990). Hexagonal $CuScO_2$ has a delafossite structure. Each Sc atom is octahedrally coordinated to six atoms. Li (Li et al., 2002) shows negative volume thermal expansion between adjoining oxygen layers where $\alpha_v \approx -4 \times 10^{-6} K^{-1}$ below 300 *K*. Orthorhombic melanothallite (Cu_2OCl_2) has negative thermal expansion above room temperature in the *b* direction of the crystal $\alpha_b \approx -26.7 \times 10^{-6} K^{-1}$; positive coefficient of thermal expansion is seen in *a* direction of the crystal (Krivovichev et al., 2002). This behaviour has been explained by a 'hinge mechanism' (variation of the angle between chains of Cu_2OCl_2).

ANISOTROPIC OXIDES WITH FRAMEWORK STRUCTURES

There are some oxides with a framework structure that have lower than cubic symmetry. These types of structure give anisotropic expansion. The RUM and quasi-RUM mechanisms drive the negative thermal expansion as with cubic framework structure but in this case, the expansion is anisotropic. These structures are usually built of AO_4 tetrahedra and BO_6, with the corners linked by two coordinated oxygen atoms. $ZnSiO_4$ shows the linear coefficient of thermal expansion $\alpha_{//}$ (parallel to the crystal axis) to be negative below 150 *K* and $\alpha_{\perp}$ (perpendicular to the crystal axis) is negative below room temperature (White and Roberts, 1988). Zn_2GeO_4 has been studied recently, showing an average coefficient of thermal expansion of $\alpha_{ave} \approx -3.4 \times 10^{-6} K^{-1}$ below room temperature and $\alpha_{ave} \approx 3.9 \times 10^{-6}$

K^{-1} above, indicating that it could be a useful low-expansion material at room temperature (Stevens et al., 2004).

QUARTZ AND SIMILAR CRYSTAL

The open structure of quartz is composed of SiO_4 tetrahedra linked by shared oxygen atoms at each corner. Negative thermal expansion is found above 846 *K*. The linear coefficients of thermal expansion $\alpha_{//}$ (parallel to the crystal axis) and $\alpha_{\perp}$ (perpendicular to the crystal axis) decrease as *T* increases, and they soon become small and negative. This is probably due to the rotation of the tetrahedra about their mean symmetric orientation. This behaviour is in accordance with molecular dynamics simulations (Kihara, 2001).

There are compounds (MPO_4) with structures similar to that of quartz, in which silicon is replaced by Al, Fe or Ga and by P. $FePO_4$ shows thermal expansion similar to quartz (Mittal et al., 2002).

ZEOLITES AND $AlPO_4$s

Several studies confirm a strong negative expansion in many non-cubic zeolites and $AlPO_4$s (Lightfoot et al., 2001). Papers show the thermal behaviour of $AlPO_4$-17 (Tao and Sleight, 2003a, 2003b) and hydrated HZSM-5 orthorhombic zeolite (Marinkovic et al., 2004). $AlPO_4$-17 exhibits an average linear coefficient of thermal expansion of -11.7×10^{-6} K^{-1} between 18 *K* and 300; HZSM-5 orthorhombic zeolite exhibits an overall average linear coefficient of thermal expansion of -9×10^{-6} K^{-1} between 313.15 *K* and 653.15 *K*.

ORTHOROMBIC ZrW_2O_8

Cubic ZrW_2O_8 transforms to an orthorhombic phase at pressures over 0.2 GPa (Jorgensen et al., 1999). This structure is less open and the average W and O coordination

numbers are increased. Below about 150 *K*, the expansion is almost isotropic, with the volume coefficient of thermal expansion $\alpha_{ave} \approx -5 \times 10^{-6}\ K^{-1}$. Expansion is small at room temperature and above 350 *K* is highly anisotropic, with the linear coefficients of thermal expansion in the crystal directions $(\alpha_a, \alpha_b, \alpha_c) \approx (11.5, 4.5, -10.5) \times 10^{-6}\ K^{-1}$.

$Sc_2(W_4)_3$ AND SIMILAR CRYSTALS

Orthorhombic scandium tungstate is a framework structure containing WO_4 tetrahedra and ScO_6 octahedra joined at the corners; all oxygen atoms are shared. The thermal expansion is anisotropic, with the linear coefficients of thermal expansion in the crystal directions α_a and α_c negative and α_b positive; the volume coefficient of thermal expansion $\alpha_v \approx -6.5 \times 10^{-6}\ K^{-1}$ between 50 *K* and 450 *K*, and negative thermal expansion continues up to at least 1073 *K* (Evans et al., 1998). The same general mechanisms operate as in ZrW_2O_8 and ZrW_2O_7.

There are many other $A_2M_3O_{12}$ compounds that have the same crystal structure but have positive expansion below the phase transition temperature (e.g. 178 *K* for $Sc_2(MO_4)_3$) (Evans and Mary, 2000). In $Lu_2(WO_4)_3$ (Forster et al., 1998) and $Y_2(WO_4)_3$ (Forster and Sleight, 1999) α_a, α_b and α_c are all negative, and the magnitude of the negative α_v for $Lu_2(WO_4)_3$ is three times that of $Sc(WO_4)_3$ but in this case, their hygroscopicity limits the possible applications.

LITHIUM ALUMINA SILICATES

β-spodumene ($LiAlSi_2O_6$), β-eucryptite ($LiAlSiO_4$) and many derivative solids show ultra-low or negative expansion, reviewed by Barrera et al. (2005). In β-eucryptite the linear coefficient of thermal expansion in one crystal direction (α_c) is negative above 20 *K* ($\alpha_c \approx -20 \times 10^{-6}\ K^{-1}$ at 300 *K*) and in the other directions, the expansion is positive (thus α_v

is close to zero over a wide temperature range). Cer-Vit (a registered trade mark of the Owens-Illinois Glass Company) and Zerodur (made by Schott AG) are two existing materials for which experimental measurements show near-zero thermal expansion. These very low expansion materials are commercially developed and exploited in the fabrication of large optical components (because they maintain their shape in a wide range of temperature and operative conditions) and also of ceramics, for tableware. These materials also play an important role in calibrating the thermal expansion in applications that require thermal stability.

NZP AND RELATED COMPOUNDS; OTHER PHOSPHATES

The NASICON (Sodium Super-Ionic Conductor) or NZP family (based on the $NaZr_2(PO_4)_3$ structure) has been studied for several engineering applications, see topic review by Barrera et al. (2005). In order to obtain a wide range of expansion behaviour (from negative to zero, and positive expansion) it is possible to replace Na by diverse elements such as Cs, Cu, H and Li. $NbTi(PO_4)_3$ shows negative thermal expansion, $Ca_{0.25}Sr_{0.25}Zr_2(PO_4)_3$ zero expansion, and $Ca_{0.25}Na_{0.5}Zr2(PO_4)_3$ positive thermal expansion (Woodcock and Lightfoot, 1999). The NZP structure itself contains corner-sharing ZrO_6 octahedra, each of which is connected to six PO_4 tetrahedra, whilst each PO_4 tetrahedron is linked to four ZrO_6 octahedra. The mechanism that drives anisotropic thermal expansion in this open structure (α_c is generally positive and α_a negative) is, once again, the coupled rotation of the oxygen-sharing polyhedral building blocks. Composites of NZP (with negative α_v), and YIG (with positive α_v), yttrium iron garnet ($Y_3Fe_5O_{12}$), have been prepared and exploited as ferromagnetic zero-expansion ceramics for radar-invisible space mirrors which would not distort with varying exposure to the sun (Roy and Agrawal, 1997).

Many other phosphates have negative expansion in at least one direction. Tetragonal $NbOPO_4$ has positive linear coefficients of thermal expansion parallel and perpendicular to the crystal axis up to about 473 *K*, above which $\alpha_{\perp}$ is small and negative (Amos et al., 1998).

METAL-ORGANIC FRAMEWORK STRUCTURES

These structures are framework structures formed by metal ions. Small negative expansion below room temperature ($\alpha_c \approx -1.5 \times 10^{-6}\ K^{-1}$) has been reported (Hohn et al., 2002) for the tetragonal $Sr(C_2(COO)_2)$.

POLYCRYSTALS AND COMPOSITES; MICROCRACKING

It is possible to form materials with negative thermal expansion by exploiting either the different thermal expansion coefficient of crystallites present in polycrystals or the thermal expansion coefficient of different components of composites. Landert (2004) shows that materials can be formed with negative thermal expansion in at least one direction, although the expansion of each component is positive in the overall range of temperatures.

The possible microcrack mechanism in polycrystals, due to local stresses generated by the mismatch of orientations and of the coefficients of thermal expansion of crystallites, may alter the expansion of these materials. The cracks opening and closing by temperature change may lead the material to show negative expansion (even if the crystallites have positive expansion) or enhance negative expansion, as reviewed by Barrera et al. (2005).

1.4 Engineering of Negative Thermal Expansion Structures

Materials may experience a wide range of operating temperatures, thus considerable practical interest has been developed in thermal expansion of materials, for instance where materials of differing CTEs abut. It is therefore interesting to investigate the range of thermal expansion coefficients attainable in materials (e.g. cellular solids or composites) and to develop procedures to design such materials to exploit extreme or unusual thermal expansion behaviour (positive thermal expansion, zero thermal expansion and negative thermal expansion), also addressing performance and the limitations, in terms of other mechanical properties combined with altered CTE.

1.4.1 Cellular solids

Materials with significant porosity (with 20% or less of their interior volume occupied by solids) are generally called cellular solids (Evans et al., 2001). Defined as being 'made up of an interconnected network of solid struts or plates which form the edges and faces of cells', they show unique properties unachievable by their solid counterparts (Gibson and Ashby, 1999a) such as high strength accompanied by a relatively low mass, good energy absorption characteristics and high compression strength. Often, they also provide good thermal and acoustic insulation properties. They are found in many natural and man-made structures. Cancellous or trabecular bone, wood, cork and the honeycomb structure of beehives are common natural cellular materials. Man-made cellular solids may be found in a variety of structures such as sandwich panels, cushioning foams, compact heat exchangers, heat resistant ceramic tiles of space shuttles and artificial implants, as reviewed by Kumar and McDowell (2004).

Although known and used for a long time (essentially as cores of light-weight sandwich panel structures to increase specific flexural stiffness of some structures and not as primary load-bearing members), cellular solids are gaining attention due to their huge potential in diverse engineering applications in aerospace, automotive, naval and biomedical industries. In addition, rapid progress in manufacturing (e.g. rapid additive manufacturing techniques) promises new applications.

Cellular networks may have stochastic (e.g. foams) or periodic (e.g. honeycombs) topologies, based on the distribution of the solid phase (Evans et al., 2001), Figure 1.8.

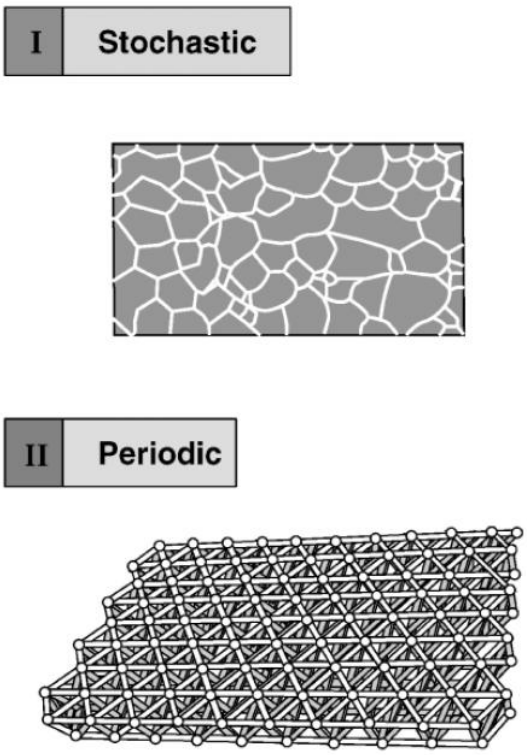

Figure 1.8. Schematic illustration of the two predominant topologies exhibited by cellular materials (Evans et al., 2001).

Generally, foams have stochastic microstructures (Gibson and Ashby, 1999a). The pores can be contiguous, in which case the foam is known as open-cell foam, Figure 1.9a, or the pores are separated by walls, creating closed-cell foam, Figure 1.9b.

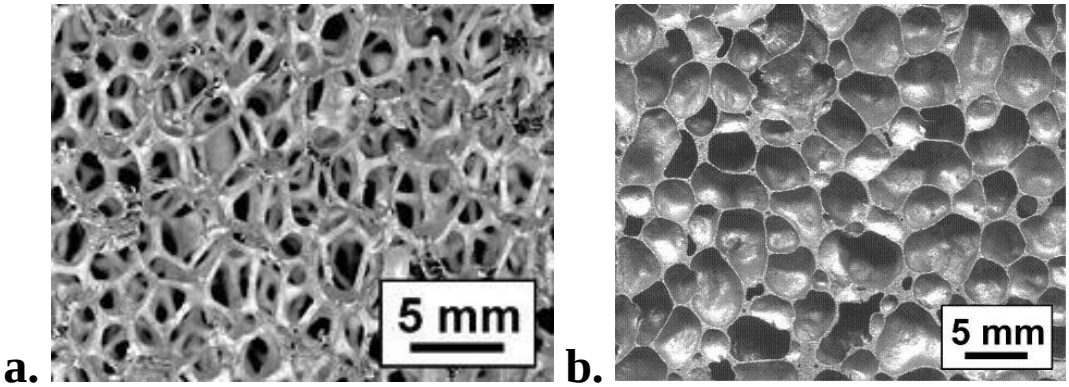

Figure 1.9 (a and b). Open-cell and closed-cell foam topologies (Tan, 2008).

Recently, cellular solids with periodic architectures have raised enormous interest in engineering applications. Although more expensive than random cellular solids, the advantage of these materials over the random cellular solids is that they can be designed to optimise multifunctionality by placing material at locations where mechanical, thermal and other types of performance are maximised.

Cellular solids with periodic architectures are composed of periodic unit cells. They include either honeycomb forms, Figure 1.10a, corrugated (prismatic) forms, Figure 1.10b, (Wadley, 2006), or microtruss assemblies (Evans et al., 2001), referred to as lattice materials, Figure 1.10c.

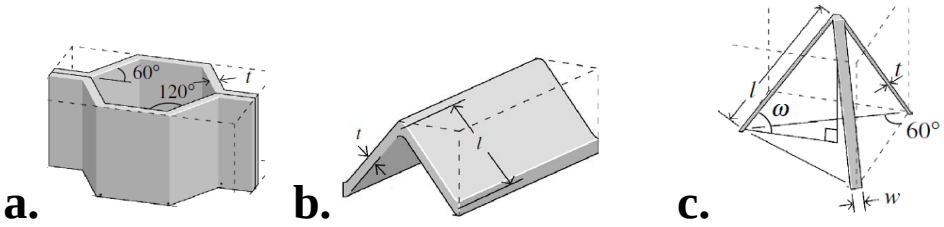

Figure 1.10 (a, b and c). Examples of a) hexagonal honeycomb, b) triangular prismatic and c) tetrahedral truss unit cell topologies used as core structures in sandwich panels (Wadley, 2006).

Wadley (2006) showed that periodic cellular metals with honeycomb and corrugated (prismatic) topology are widely used for the cores of light-weight sandwich panel structures. Honeycombs have closed-cell pores and are well suited for thermal protection whilst also providing efficient load support; corrugated (prismatic) core structures provide less efficient and highly anisotropic load support, but enable cross-flow heat exchange opportunities because their pores are continuous in one direction. More recently, significant interest has emerged in microstructure, with periodic architecture known as lattice truss structures, with open-cell structure consisting of three-dimensional interconnected void spaces (Evans et al., 2001; Wadley, 2006; Wallach and Gibson, 2001; Wicks and Hutchinson, 2004), Figure 1.11. Sandwich plates with truss cores may be optimally designed, allowing minimum weight, subject to any combination of loads (Deshpande and Fleck, 2001; Wicks and Hutchinson, 2001). Moreover, the void spaces may allow fluid to flow through them increasing, for example heat dissipation.

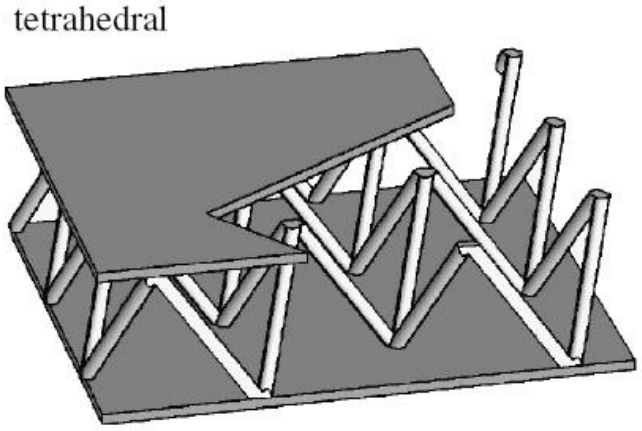

Figure 1.11. Example of lattice truss tetrahedral topology configured as the core of sandwich panel structures (Wadley, 2006).

The trusses can be arranged in several configurations, depending upon the intended application (Evans et al., 2001).

Mechanical properties of cellular solids have been extensively discussed in the seminal book by Gibson and Ashby (1999a). Mechanical properties of the unit cells have been mainly derived from beam theory as a function of the overall relative density of the cellular material, as seen in Gibson and in Hayes (Gibson and Ashby, 1999a; Hayes et al., 2004). Periodic cellular structures have been found to exhibit higher stiffness and peak strength than random cellular structures. The loss of periodicity rapidly activates the bending modes of deformation and this causes a rapid decay in the ability of the structure to deform in a predominantly stretch mode (Alkhader and Vural, 2008; Gibson and Ashby, 1999a; Wadley, 2006). Recently, Hayes et al. (2004) have derived both the elastic and plastic properties of 2D cellular structures of various topologies. For uniform (periodic) cell structures, analytical solutions are obtained by analysing a periodic unit cell, whereas for non-uniform (random) cell structures, computational analyses have been used. A strain-energy-based approach has been used by Kumar and McDowell (2004) to derive elastic

constant for periodic cell structures. Furthermore, recent structural optimisation studies have been carried out to develop an understanding of properties and to identify the influence of the independent parameters of cellular topology on overall mechanical response (Alkhader and Vural, 2008; Wallach and Gibson, 2001; Wicks and Hutchinson, 2001; Zhou et al., 2004).

Recent developments in the manufacturing of cellular solids appear to extend their possible applications. New efficient manufacturing techniques have been devised which permit entire cellular solids to be produced at scales ranging from millimetres to tens of centimetres. Two different types of periodic cellular structures have been successfully manufactured: honeycombs and truss structures. The traditional manufacturing techniques have been reviewed extensively by Wadley (2006) and Williams et al. (2005). Jacobsen et al. (2007) have proposed a Self-Propagating Photopolymer Waveguide technique to create mesoscale truss structures. This technique is capable of significant flexibility and control of the geometry of the resulting cellular structure. Some researchers have looked into using layer-based additive manufacturing processes (ALMs) for the manufacturing of cellular solids with intricate internal geometry (Williams et al., 2005). ALM may be a means of providing the design freedom that is absent from traditional cellular material manufacturing processes.

DUAL-MATERIAL LATTICE STRUCTURES

Many attempts have been made to design periodic cellular solids capable of exploiting thermal management applications. When an anisotropic solid is subject to a change in temperature, all components of the strain tensor can change. Consequently, the Coefficient of Thermal Expansion (CTE) is a second-rank tensor (Nye, 1957). Since the

tensor for the Coefficient of Thermal Expansion (CTE) is second-rank, monolithic honeycombs and foams cannot have CTEs other than their constitutive materials unless other materials are included. Lakes (1996, 2007) has described cellular solids consisting of bilayer ribs, Figure 1.12. It has been shown that certain network structures (cellular solids) containing three phases (two layered solid phases and void space) can generate negative thermal expansion in two dimensions, depending on the relative thermal expansion of each layer. The NTE is the result of rotations and bending of beams within the structures due to thermal expansivity mismatch. These bilayer network NTE mechanisms are apparently not known at the atomic level.

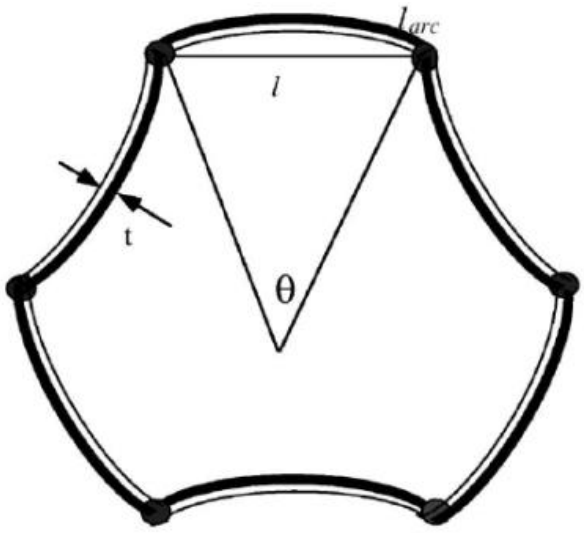

Figure 1.12. Hexagonal lattice cell with curved dual-material ribs (Lakes, 2007).

Given this concept, several investigators have been interested in theoretical and experimental (or both) approaches in dual-material structures (structures comprising repeating unit cells of two materials) that can exhibit large positive, zero or large negative thermal expansion. These dual-material structures utilise the 'principle of internal geometric constraints' to drive NTE (Oruganti et al., 2004). Constraints are set up inside the material

to prevent it from freely expanding outward by accommodating strains internally. Such constraints require either three phase materials (e.g. cellular solids with two materials and void space) as seen in (Aboudi, 2008; Aboudi and Gilat, 2005; Grima et al., 2008; Grima et al., 2007; Jefferson and al., 2009; Lakes, 1996, 2007; Lim, 2005; Miller et al., 2008a; Oruganti et al., 2004; Qi and Halloran, 2004; Sigmund and Torquato, 1996, 1997; Steeves et al., 2007) or two dissimilar materials to form composites (e.g. laminates), as shown in section 1.4.2.

Attempts have been made to make artificial NTE materials via computational design methods; 'artificial' referring to materials that have been designed rather than discovered (e.g. have tailored properties). Sigmund and Torquato (1996, 1997) designed an isotropic NTE artificial material by a three phase numerical topology optimisation method, Figure 1.13. This design is essentially an elaborate arrangement of dual-material beams. The NTE artificial material is composed of periodic base cells. Each periodic base cell is made of two different material phases with positive thermal expansion and a void phase. The two material phases are required to have similar elastic tensors but different thermal strain coefficient tensors (similar stiffness but widely differing thermal expansion). The numerical topology optimisation method finds the distribution of materials that achieves the predefined thermo-elastic properties subject to certain constraints (e.g. the volume fraction of different phases in a periodic base cell) by the topology optimisation method and determines the effective properties of the structure (consisting of these periodic base cells) by the numerical homogenisation method. A first attempt to fabricate such NTE structures by direct metal deposition was proposed by Mazunder et al. (2000).

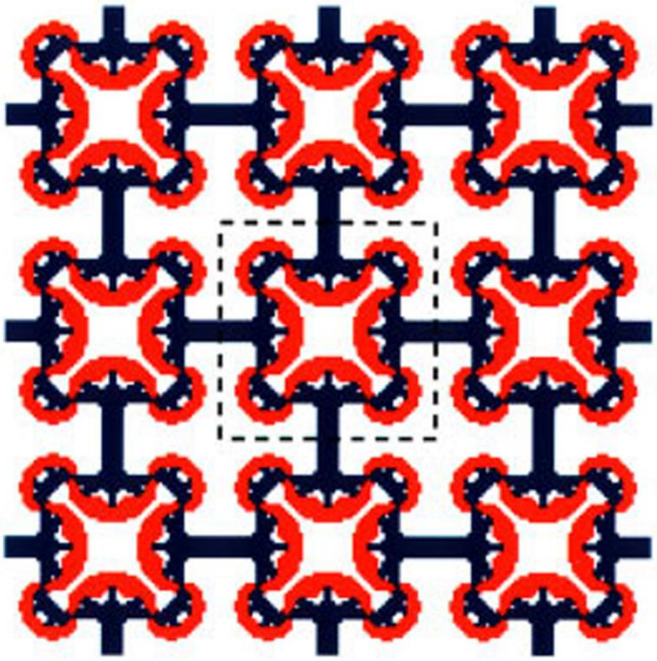

Figure 1.13. Optimal microstructure composed of a hypothetical high expansion phase (red) and low expansion (blue), and a void phase for negative thermal expansion (Sigmund and Torquato, 1996).

Oruganti et al. (2004) demonstrated an NTE Ni-Cr cellular structure designed by the homogenisation method discussed earlier. The bi-metallic structure was fabricated of Ni and Cr by direct metal deposition (DMD). Results obtained show a large reduction in overall CTE. It is seen that along the *x* and *y* directions the specimen contracts, up to about 373.15 *K* and 323.15 *K*, respectively. Beyond these temperatures, it expands continuously. The CTEs along these two directions during the very initial contraction phase are about 3.9 $\times 10^{-6}\ K^{-1}$ (CTEs of nickel and chromium, respectively are $13 \times 10^{-6}\ K^{-1}$ and $6 \times 10^{-6}\ K^{-1}$). This value is close to the designed value of about $4 \times 10^{-6}\ K^{-1}$. Comparable results have been obtained from iron-nickel alloy bi-metallic cellular beams (Qi and Halloran, 2004). The Fe-36%Ni (well-known as invar alloy) and Fe-60%Ni structure was previously designed by the homogenisation method and subsequently microfabricated by coextrusion. The material exhibits a linear negative thermal expansion with a coefficient of thermal

expansion of - 3 × 10^{-6} K^{-1}, close to the value of - 3.2 × 10^{-6} K^{-1} designed by the homogenisation method. More recently, Aboudi (2008) and Aboudi and Gilat (2005) have proposed a computational theory based on a fine homogenisation technique able to model micromechanically periodic multiphase composites. Two particular configurations of lattice blocks have been proposed (Aboudi and Gilat, 2005) consisting of two distinct materials with positive thermal expansion and a void phase, Figure 1.14. Although it should be mentioned that not every lattice block configuration is possible, results show that these lattice blocks provide negative coefficients of thermal expansion. In fact, the micromechanical analysis of the repeating unit cells predicts that the effective coefficients of thermal expansion in two directions are negative and positive in at least one direction.

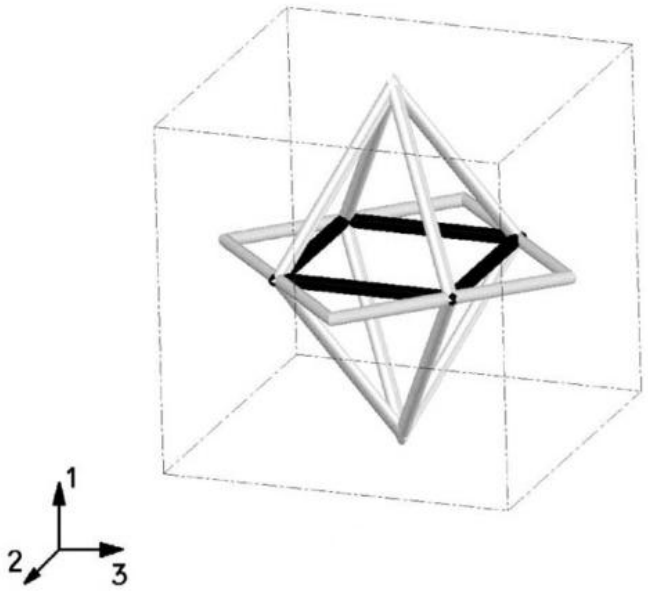

Figure 1.14. Repeating unit cell of one lattice blocks configuration proposed by Aboudi and Gilat (2005).

Some analytical and numerical approaches have also been carried out to design a material that exhibits negative thermal expansion (NTE). Lim (2005) proposes an analytical model in which a cellular microstructure exhibits anisotropic thermal expansion. The cellular microstructure considered is idealised with a representative volume element (RVE)

consisting of thermally inexpansible rod elements and thermally expansible rod elements that drive both positive and negative thermal expansion along principal axes, Figure 1.15.

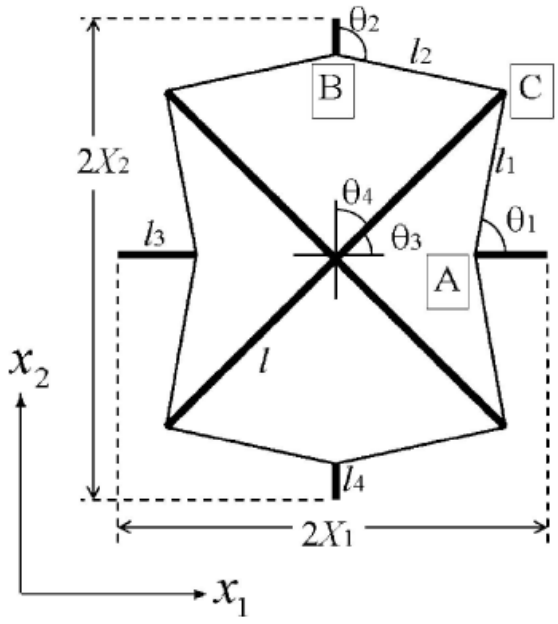

Figure 1.15. Idealised volume element showing anisotropic thermal expansion (Lim, 2005).

More recently, theoretical and analytical models of novel triangular units have been presented. Trusses of different materials connected together through hinges may exhibit positive, zero and even negative thermal expansion (Grima et al., 2007; Grima et al., 2008; Miller et al., 2008a; Palumbo et al., 2011; Steeves et al., 2007). Steeves et al. (2007) introduces a 'structurally robust' triangular unit that achieves low thermal expansivity, combined with high stiffness. The unit cell is fully triangulated and does not rely on rotational resistance at the joints for structural rigidity, Figure 1.16.

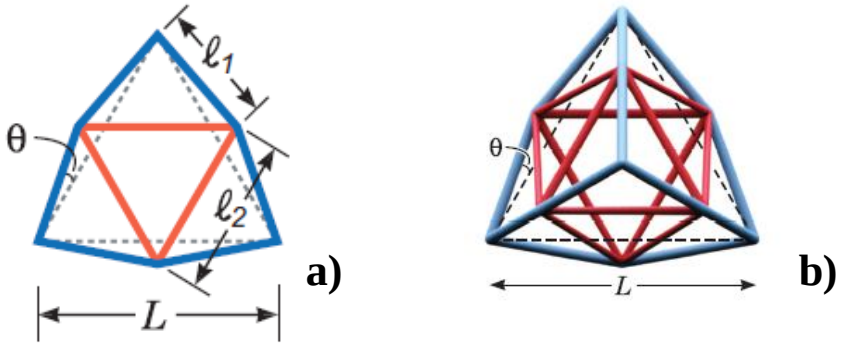

Figure 1.16 (a and b). a) Two-dimensional lattice with a low coefficient of thermal expansion; b) three-dimensional lattice with a low coefficient of thermal expansion (Steeves et al., 2007).

Miller et al. (2008a) develops a systematic and generalised scale-independent procedure to design NTE structures from a positive thermal expansivity triangular unit, Figure 1.17. The triangular base unit consists of corner-hinged beam-like elements, all with positive coefficient of thermal expansivity (one of which has a relatively larger thermal expansivity). This unit may be tessellated into complex two-dimensional or three-dimensional structures. It is possible to tune the thermal expansion of the structure (positive, zero or negative), dependent upon the temperature load, via the triangle geometry and ratio of the element CTEs.

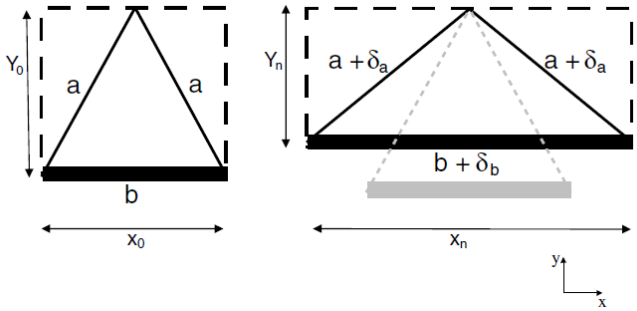

Figure 1.17. Triangle unit cell showing anisotropic negative thermal expansion in one direction (Miller et al., 2008a).

The original concept for dual-material structures exhibiting large positive, zero or large negative thermal expansion by Lakes (1996) has been recently proposed by Jefferson et al. (2009). The bilayer network is shown in Figure 1.18. Closed form analytic expressions for prediction of the thermal expansivity, and consequent internal stressing of the structure, as well as several finite element simulations, which demonstrate the design performance under non-uniform thermal load, are proposed. However, Jefferson's design (as well as the original design by Lakes) has low stiffness because near-zero thermal expansion and isotropic negative expansion designs are achieved by internal bending deformation.

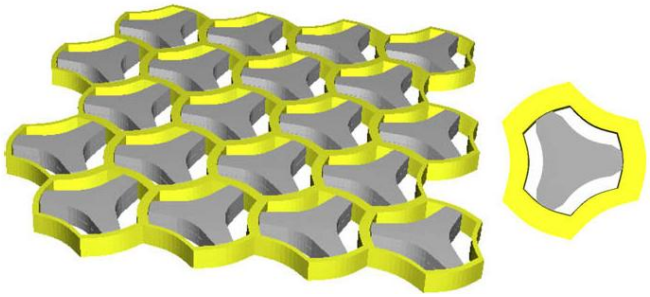

Figure 1.18. Low thermal expansion lattice proposed by Jefferson (2009).

1.4.2 Laminated composites

Laminated composites are high-performance polymer components, consisting of layers or laminae stacked in a predetermined arrangement that act together as a single layer. There is a wide array of literature concerning the properties, manufacturing and applications of laminate composite materials (Gay and Hoa, 2007; Hull and Clyne, 1996). The laminate's thermo-elastic response can be predicted by laminated plate theory, as reported by Halpin et al. (1992). This method of predicting CTE gives an exact algebraic

solution but does not necessarily show evidence of the occurrence of anomalous CTE in $\pm\theta$ angle-ply laminate.

DUAL-MATERIAL LAMINATE

The same principle, as seen behind the controlled thermal expansion of cellular solids (Section 1.4.1), also leads to the negative thermal expansion in composites (e.g. laminates). The combination of two dissimilar materials (with two different coefficients of thermal expansivity) may form composites having positive, near-zero or even negative thermal expansion. Analytical and experimental studies have been made in an attempt to explore the possibility of making laminated fibre composites with tunable CTEs. Ito et al. (1999) demonstrates, by the classical laminated plate theory, that a fibre-reinforced, symmetric, balanced, angle-ply laminate composite may exhibit negative coefficient of thermal expansion in one in-plane principal direction, Figure 1.19. Experimental results obtained for the glass fibre/polypropylene system (fibres and matrix have positive thermal expansion themselves) show an unexpectedly large negative thermal expansion, at $\theta = 30^{o}$ ($- 8 \times 10^{-6}\ K^{-1}$ at about 343.15-353.15 *K*), contradicting the classical theory that predicts near-zero thermal expansion. Ito et al. (2000) suggest that this could be due to the matrix creep effect. Landert et al. (2004) confirm that in-plane negative thermal expansion values can be obtained in a specific direction in a symmetric, balanced, angle-ply glass-fibre/polypropylene system. The physical conditions required for a very large value of negative thermal expansion is: that the tensile modulus of the individual plies, in the direction parallel to the fibres, must be larger than the shear modulus in that direction. An alternative highly cross-linked polyurethane rubber matrix, reinforced with fibres of invar (Fe-36%Ni) has been proposed. It has been shown that this system is more stable, with

increasing temperature, than the polypropylene system. This provides a value of the coefficient of thermal expansion of as large as - $50 \times 10^{-6}\, K^{-1}$, at around 373.15 *K*.

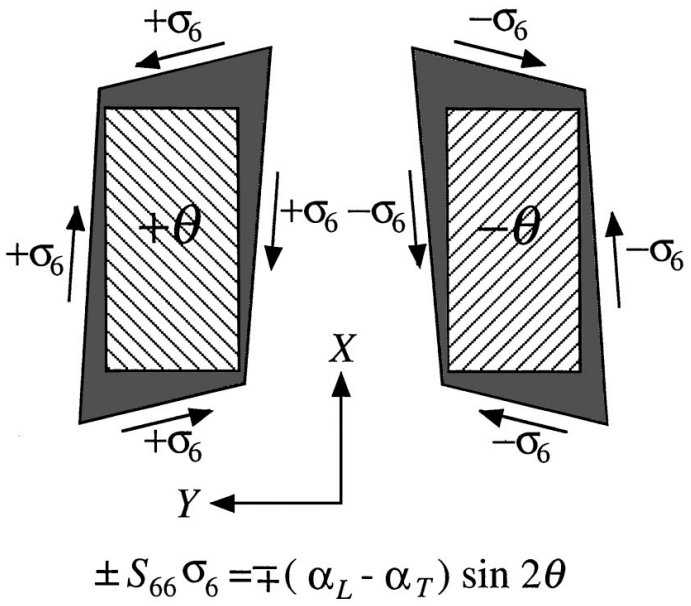

Figure 1.19. Composite laminate showing negative thermal expansion in one direction (Ito et al., 2000).

Another approach to obtain negative thermal expansivity has been proposed by Kelly et al. (2005, 2006). The idea is to make use of a large Poisson's ratio, able to drive a contraction in the lateral direction which accompanies an axial extension. A device, involving a strip of a material of relatively low thermal expansion coefficient with a large Poisson's ratio and a frame of a material of relatively high thermal expansion coefficient, has been proposed to obtain this extreme negative value of expansivity, as predicted, Figure 1.20.

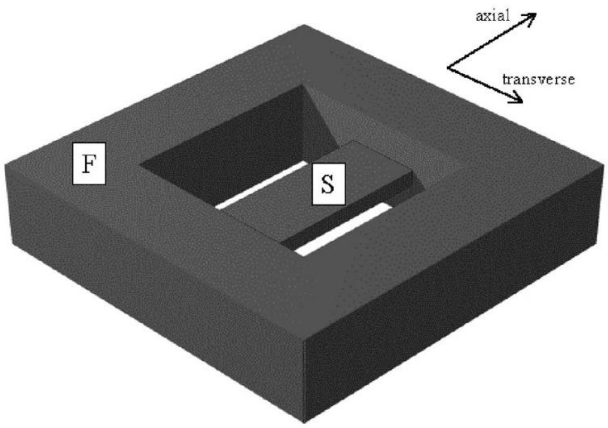

Figure 1.20. Device to control thermal expansion by use of the Poisson's ratio (Kelly et al., 2005).

It has been shown (Sections 1.4.1 and 1.4.2) that the principle behind engineering NTE in cellular materials or laminates is the same. Artificial dual-material structures with differing thermal expansivities may drive NTE behaviour, yet, although the principle is essentially the same, cellular solids permit a larger range of attainable CTEs than composites (e.g. laminates), and also allow both isotropic and anisotropic behaviour. This is due to the empty regions in the structure in which a large amount of displacement is possible.

In general, studies described in Sections 1.4.1 and 1.4.2 may also aim to explore mechanisms and possible approaches to design negative thermal expansion structures of practical interest. None of these studies present unifying underlying principles for the design of NTE structures. Miller et al. (2008a) represents the first reported attempt at designing NTE structures from positive thermal expansivity units by a systematic, rational and generalised scale-independent procedure. Miller's conceptual model, based on a simple unit cell with triangular geometry, is capable of describing adequately the CTE of framework type structures, composites and molecular frameworks, allowing both isotropic and anisotropic behaviour.

1.5 Applications

There are a number of potential applications for materials with zero or negative coefficient of thermal expansion. Thermal expansion behaviour may be exploited in applications that require specific coefficients of thermal expansion such as positive, negative, or zero in the same specific temperature range.

In electronic packaging, thermal management is an important issue (Jin and Mavoori, 1998). Heat sinks are essential for preventing thermal damage to heat-sensitive components such as electronic chips. At present, the common heat sink materials (e.g. aluminium and copper) have a higher coefficient of thermal expansion than silicon. This CTE mismatch may lead to several failure mechanisms, thereby seriously decreasing the reliability and the lifetime of the device. The use of NTE materials (such as silicon) can represent an attractive way to minimise or control the thermal mismatch of an electronic device (Miller et al., 2009).

There is also considerable interest in using negative thermal expansion materials in the pure form, either as films or as ceramic bodies (Sleight, 1998a, 1998b). A known application may be Pyrex® glass and 'oven to table' cookware in which a low expansion ceramic is employed for its resistance to thermal shock (Evans, 1999).

In medicine, another interesting application is to control the thermal expansion of the composites used in teeth fillings (Sleight, 1998a, 1998b). It has been supposed that an important reason of failure between teeth and teeth fillings is due to their thermal expansion mismatch. Groups working on thermal expansion coefficient of dental composites have developed filling composites using low thermal expansivity zirconium tungstate.

Materials showing negative or near-zero coefficient of thermal expansion can be employed in aerospace applications, where materials are subjected to large temperature changes (Oruganti et al., 2004). For instance, the aerospace industry pioneered the use of composites, incorporating fibres with a negative axial CTE in a matrix having a positive CTE to make unibody casings for satellites. These composites can maintain their shape and size across a large temperature range, thereby reducing thermally induced failures.

Multifunctional sandwich structures incorporating very low-density insulation as the core, with the structural stiffness provided by a hot face consisting of a low (or zero) thermal expansion lattice is of interest in hypersonic vehicles flying within the atmosphere to minimise thermal mismatch stresses with the lattice face (Steeves and Evans, 2011).

Zero expansion materials are also of interest to researchers. For example, in high precision optical mirrors, materials with very small coefficients of expansion are useful to enhance high optical precision, where temperature fluctuations degrade the quality of the optics (Evans, 1999; Stevens et al., 2004). Materials with controlled expansion also have an application as packaging for refractive index gratings, leading to more precise control of reflected wavelength (Evans, 1999; Kelly et al., 2005).

Perhaps the most obvious applications for negative thermal expansion behaviour are those involving composite materials, in which the overall expansion coefficient can be tailored to exploit positive, negative or zero thermal expansion. More recently, cellular solids are finding engineering applications in many technological areas, from ultra-light-weight multifunctional structures to automobile and aerospace components, furniture and sporting goods (Zhou et al., 2004). Thermal expansion management in these materials may broaden the possible applications, encompassing higher value.

2 NEAR-ZERO THERMAL EXPANSIVITY 2D LATTICE STRUCTURES: PERFORMANCE IN TERMS OF MASS AND MECHANICAL PROPERTIES.

2.1 Introduction

Lattice structures are a wide category of man-made structures, formed by tessellating a unit cell in either two or three dimensions and which exhibit unique properties, unachievable by their solid counterparts, such as high strength accompanied by a relatively low density; good energy absorption characteristics and high compressive strength (Ashby, 2006; Evans et al., 2001; Gibson and Ashby, 1999a).

Applications of lattice structures are wide-ranging from their current use in sandwich panels (occurring as honeycombs or truss cores), as cushioning foams, compact heat exchangers, heat-resistant ceramic tiles and artificial biological implants, to emerging applications such as in furniture design, automotive and aerospace industries and sporting goods products (Kumar and McDowell, 2004; Zhou et al., 2004). Many applications which make use of lattice structures also suffer considerable problems due to thermally driven distortion and/or stress, for example support structures in spacecraft (Xue and Ding, 2004). Such structures are manufactured by welding or joining straight rods or tubes to make larger structures (Uozumi and Kito, 2007) or by wire bending and brazing for smaller truss core structures (Wadley et al., 2003). The emergence of new manufacturing processes such as additive layer manufacturing (ALM), which may allow much more freedom in the design of their geometry, offer potential for further performance improvement. Geometry is the main determinant factor in performance (Evans et al., 2001; Gibson and Ashby, 1999a;

Miller et al., 2008a; Wadley et al., 2003). Interest in lattice structures in sandwich panels is growing because of their extremely good density-specific performance (Hyun et al., 2003; Queheillalt et al., 2008; Queheillalt and Wadley, 2005; Rathbun et al., 2006; Wallach and Gibson, 2001; Wang et al., 2003).

Lattice structures are widely used in satellites for support of appendages such as antennae and photovoltaic arrays. Antennae are prone to thermal distortion problems due to the cyclic thermal nature of an orbiting craft (Xue et al., 2007; Xue and Ding, 2004). They are required to have high stiffness to weight ratio, low-density and dimensional stability over a large temperature range (Kunze and Bampton, 2001). A satellite antenna usually consists of a large circular reflector and a supporting lattice (or scaffold). The dimensional stability of the antenna depends, in large part, upon the lattice support's distortion, whereby antenna stability is maintained most effectively by decreasing the linear (circumferential) thermal expansion of the lattice (Uozumi and Kito, 2007). Current solutions to thermal management, for instance in communication satellites, usually employ high-performance materials which have inherently low CTE, for example carbon fibre, reinforced, ceramic matrix composites (Krenkel, 2004), SiC/Al composites (Yan et al., 2008), metal matrix composites (Mirache, 2001). These single materials offer solutions that are, of course, limited to a single CTE value and are also often expensive to implement. A solution that uses less limiting exotic materials and is customisable is sought to avoid these problems and minimise cost.

Dual-material lattices have been proposed as an alternate solution for thermal distortion problems, initially by Lakes (1996, 2007) and subsequently others (Aboudi and Gilat, 2005; Grima et al., 2007; Ito et al., 1999; Jefferson et al., 2009; Kelly et al., 2005;

Landert et al., 2004; Lim, 2005; Miller et al., 2008a; Miller et al., 2008b; Qi and Halloran, 2004; Sigmund and Torquato, 1996; Steeves et al., 2007). The core principle in all of these works relies on the basis that a 2D or 3D lattice network structure or composite, containing two solid phases with different constituent CTEs, can be made to exhibit a wide range of thermal expansivity, including large positive, negative or zero CTE values. If a CTE can be ascribed to a structure, then the CTE of these dual-material structures is dependent upon the relative CTE of the constituent materials and the lattice geometry (Miller et al., 2008a). The tailored CTE is the result of rotations and/or distortion of beams within the lattice due to thermal expansivity mismatch between constituent members. Unusual values of CTE, especially negative CTE (NTE), have been the subject of considerable interest in organic and inorganic solid studies of late (Evans, 1999; Miller et al., 2009).

This chapter explores the thermally induced distortion of a 2D lattice, with geometries similar to those found in structures in, for instance satellites, and which are easily realisable via standard manufacturing processes. The intention was to design lattices with reduced CTE without severe penalties, in terms of structural integrity or weight, or ease of manufacture. The mechanism for tailoring the CTE was that of Miller et al. (2008a). The resulting designs would also be independent of scale and thus have wider general application to combat problems of dimensional stability.

2.2 Methodology

Two complementary parametric studies of lattice geometry and constituent materials were undertaken in order to explore i) the maxima, minima and limits of CTE and ii) low CTE in combination with other desirable physical properties and with commonly used materials, all constrained within realistic limitations of standard manufacturing processes. The parametric studies are described in detail below. The design of these dual-material lattices is based upon the triangulated 2D lattice described by Miller et al. (2008a), implemented into a structure similar to those found in communication satellite antennae, e.g. Alphasat I-XL (EADS Astrium, Netherlands), see Figure 2.1 (ESA and Huart, 2010). The lattice structures were formed from beams made from one of two materials, each with different mechanical and thermal properties, specifically, elastic modulus, CTE and density. Predictions of the lattice properties were made via the finite elements (FE) method, described below. A commercial FE code (Ansys 11, Ansys, Inc.) was used. Alternative, more formal optimisation methods of the lattice CTE (such as topological optimisation) may have identified better optima but at the likely cost of ease of manufacture. The goal of the present chapter was to devise lattices exhibiting zero or near-zero CTE, with topologies amenable to standard manufacturing methods, that deform primarily via axial loading of members, rather than flexure, as the lattice members are far stiffer when not subjected to significant bending.

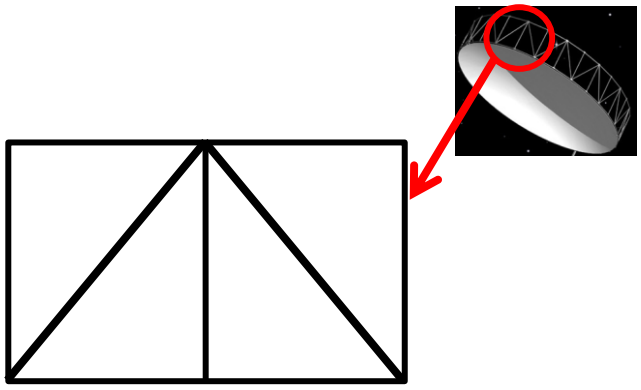

Figure 2.1. Sketch of the Alphasat I-XL satellite (ESA and Huart, 2010), and the form of the lattice truss which supports the antenna reflector dish.

In the parametric studies, two lattice structures were analysed, see Figure 2.2. The first lattice structure (Lattice 1) was a modification of the structure shown in Figure 2.1, the satellite antenna. The constituent material of the two angled beams (labelled *b*) was changed for another, with a higher CTE. The second lattice structure (Lattice 2) was modified from the first by the addition of further angled beams and the exchange of some of the high and low CTE beams. These unit cells could be tessellated into more complex 2D and 3D arrays (Miller et al., 2008a), which are not considered here.

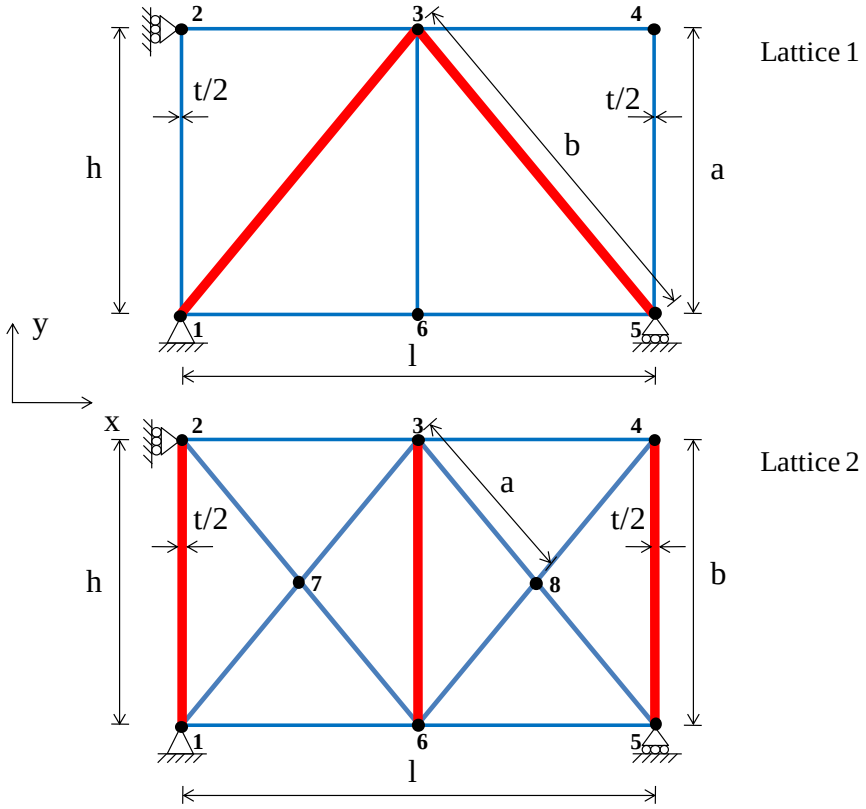

Figure 2.2. The two lattice structures in question. Beams of different constituent materials are shown in bold (red) and thin (blue) lines, bold indicating relatively higher constituent CTE, and thin, relatively lower. The applied boundary conditions are indicated by the roller bearings and fixed points.

The parametric studies allowed identification of the important geometric and material parameters which drive CTE and other properties. They were restricted in scope deliberately in order to constrain solutions to those easily realisable with current manufacturing processes. It is far harder to implement such restrictions via numerical optimisation methods, e.g. Sigmund and Torquato (1997). The lattices were modelled by considering the structure to be part of an infinite periodic array of 2D tessellating unit cells, whose global response could be described by that of the unit cell (Gibson and Ashby, 1999a). Here, we considered a plane array of unit cells repeating in only one axis (the *x* axis in Figure 2.2), reflecting the circumferential antenna support structure, though the results in terms of CTE were applicable to a full 2D array. The lattices were made of beams with a

circular cross-section area. The beam elements can be reasonably considered to be axially loaded long, slender structural beams. Diagrams of the periodic unit cells are shown in Figure 2.2.

The lattice parameters varied in the first parametric study were:

i) the relative lengths of the beams b/a (ranging from 1.05 to 2 for Lattice 1; and ranging from 0.1 to 1.95 for Lattice 2),

ii) the ratio of the constituent materials' elastic moduli, E_b/E_a (ranging from 0.1 to 100),

iii) the ratio of the constituent materials' CTEs, α_b/α_a (ranging from 1 to 10).

The output parameters of the models were CTE in the x and y axes.

The second parametric study was complementary to the previous one. It examined some specific cases, using widely available materials (see Table 2.1). The constraint on the geometry of the lattice (point i above) was retained, but the properties of the constituent materials were driven by those of the materials reported in Table 2.1. For the second parametric study, output parameters were axial CTEs, structural stiffnesses, and masses.

Following the evaluation of CTEs, structural stiffness and mass were evaluated for lattice unit cells with aspect ratio, h/l, kept constant for all the case studies and set equal to that which provided the lowest CTE in the x axis (according to the second parametric study). The beam diameter/thickness (t in Figure 2.2) was allowed to vary so as to retain constant mass (to compare relative stiffnesses) or so as to retain constant stiffness (to compare relative masses). Benchmarks used for comparison were monolithic lattices (single constituent materials), formed from aluminium alloy [Al], alpha/beta titanium alloy

[Ti], Invar 36® (Carpenter Technology Corporation, USA) [Invar], or carbon fibre composite [CCF].

It should be noted that commonly, foams, honeycombs or lattices when used as a 'material' (such as in a sandwich core) are often ascribed an effective elastic modulus. In this case, since all structures herein were of similar external dimensions, the effective modulus of any such lattice is linearly related to its structural stiffness.

Material	E *(GPa)*	ρ *(g/cm^3)*	α *(× 10^{-6} K^{-1})*
Al	73	2.77	23.30
Ti	114	4.54	9.26
Invar	148	8.05	4.36
CCF	120	1.60	0.10
Al 6082	73.2	2.77	24.0
Grade 2 Ti	114	4.54	9.1

Table 2.1. The material properties of the materials considered in the case studies and in the experimental validation.

The forces and displacements of the lattice structures were determined using commercial finite element code (Ansys 11, Ansys, Inc.). For each beam member within the unit cell, three-dimensional elastic beam elements (specifically 'beam3' in Ansys) were used, since they had both axial and flexural deformation capability. The finite element code follows a matrix theory for bar systems (*Theory Reference* for Ansys). Lattices were considered as two-dimensional rigid-jointed frameworks. Figure 2.3 shows the load and displacement components of a lattice beam. Local axes are distinguished by a′.

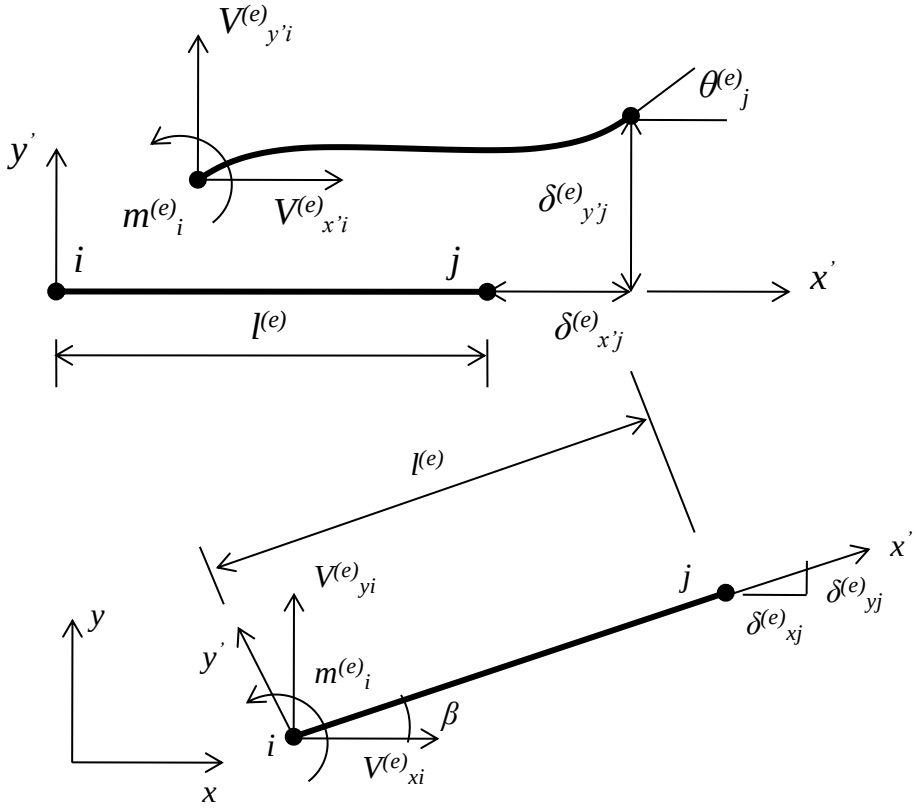

Figure 2.3. Load and displacement components of a general beam element in lattice structures considered. $V^{(e)}_{x'i}$, $V^{(e)}_{y'i}$ and $\delta^{(e)}_{x'i}$, $\delta^{(e)}_{y'i}$ are the force and displacement components in the local $x'y'$ axes at node *i*; $V^{(e)}_{xi}$, $V^{(e)}_{yi}$ and $\delta^{(e)}_{xi}$, $\delta^{(e)}_{yi}$ are the force and displacement in the global *xy* axes at node *i*; $m_i^{(e)}$ and $\theta_i^{(e)}$ are the moment and rotation at node *i*.

The global stiffness matrix that satisfies the transformation between local and global coordinates of the e^{th} element of the structures may be defined as:

$$\left[K_{xy}\right]^{(e)} = [T]^{(e)T}\left[K_{x'y'}\right]^{(e)}[T]^{(e)} \qquad \textbf{2.1}$$

where $[T]^{(e)}$ is the transformation matrix and $\left[K_{x'y'}\right]^{(e)}$ is the elementary stiffness matrix of the e^{th} beam.

For the structural elements considered in Figure 2.3:

$$\left[K_{x'y'}\right]^{(e)} = \begin{bmatrix} \frac{E_eA_e}{l_e} & 0 & 0 & \frac{-E_eA_e}{l_e} & 0 & 0 \\ 0 & \frac{12E_eI_e}{l_e^3} & \frac{6E_eI_e}{l_e^2} & 0 & \frac{-12E_eI_e}{l_e^3} & \frac{6E_eI_e}{l_e^2} \\ 0 & \frac{6E_eI_e}{l_e^2} & \frac{4E_eI_e}{l_e} & 0 & \frac{-6E_eI_e}{l_e^2} & \frac{2E_eI_e}{l_e} \\ \frac{-E_eA_e}{l_e} & 0 & 0 & \frac{E_eA_e}{l_e} & 0 & 0 \\ 0 & \frac{-12E_eI_e}{l_e^3} & \frac{-6E_eI_e}{l_e^2} & 0 & \frac{12E_eI_e}{l_e^3} & \frac{-6E_eI_e}{l_e^2} \\ 0 & \frac{6E_eI_e}{l_e^2} & \frac{2E_eI_e}{l_e} & 0 & \frac{-6E_eI_e}{l_e^2} & \frac{4E_eI_e}{l_e} \end{bmatrix}$$

2.2

where E_e is the Young's modulus of the isotropic base constituent material, l_e is the length of the e^{th} beam element having cross-sectional area A_e, and second moment of area I_e.

Since the elements are rigidly connected at the nodes, the displacements (both linear and rotational) of a particular node are the same for every element connected to it. Also, the condition for equilibrium of the structure may be expressed as:

$$\{F_{xy}\} = \sum \{V_{xy}\}^{(e)} = \sum \left[K_{xy}\right]^{(e)} \{\delta_{xy}\}^{(e)} = \left[K_{xy}\right]\{\delta_{xy}\}$$

2.3

where $\left[K_{xy}\right]$ is the global stiffness matrix of the overall lattice, and the vectors $\{F_{xy}\}$ and $\{\delta_{xy}\}$ contain the applied forces and moments in the global system, and the corresponding linear and rotational displacements.

The boundary conditions applied were periodic, i.e. the vertical edges of the unit cell were forced to remain in the *y* axis (vertical), reflecting the linear tessellating nature of the cell in this application. Displacements of the unit cell in the *x* and *y* directions are not

constrained (boundary conditions are periodic). The lengths of beams *a*, and *b* were allowed to vary independently (as described in point i) of the first and second parametric studies). The beams shown as thick lines in Figure 2.2 were formed from a material of relatively high CTE, and beams shown as thin lines were formed from a material of relatively lower CTE (Miller et al., 2008a).

The CTE values for the lattices were calculated by solving Eq. (2.3) and converting the resultant maximal displacements $\{\delta_{xy}\}$ in *x* and *y* axes into axial strains and thus into CTE since the temperature change was unitary. The change in temperature (temperature load) is considered as a vector of equivalent applied force defined as:

$$\{V_{T\,x'y'}\}^{(e)T} = \{-\alpha_e E_e A_e \Delta T \quad 0 \quad 0 \quad \alpha_e E_e A_e \Delta T \quad 0 \quad 0\}^{(e)T} \qquad \textbf{2.4}$$

where ΔT is the variation of temperature.

Structural stiffnesses K_x and K_y were calculated by applying a unit concentrated mechanical load iteratively in the *x* and *y* axes of the lattices and solving Eq. (2.3). The components in the *x* and *y* axes of the vector of applied force, $\{V_{xy}\}^T$, at the node in question, were divided by the resulting displacement at that node, giving the values of the stiffness in *x* and *y* axes, respectively. Treating each member of the unit cell as linear springs, the appropriate force displacement relationship is:

$$F = K(x_2 - x_1) \qquad \textbf{2.5}$$

with x_1 and x_2 being the displacements of the node in question. The masses of the lattices were calculated from beam dimensions and known densities.

2.2.1 Comparison FE solution vs. Truss Analysis

A comparison of the FE model with truss analysis method was undertaken by comparing Lattice 1 solutions using Al/Ti pairings at a value of the relative lengths, *b/a*, equal to 1.4.

The method of analysis used could be also adopted in statically indeterminate structures (Lattice 2 for instance). However, for simplicity and for brevity, truss analysis method was not applied to Lattice 2.

2.3 Results

2.3.1 CTE, First Parametric Study

For Lattice 1, the value of α_x was the same as the CTEs of the constituent materials, and the effect of varying the relative lengths (b/a) and mechanical properties (E_b/E_a and α_b/α_a) of the constituent materials was negligible, see Figure 2.4a and Figure 2.4b. The value of α_y was outside the range of constituent CTE values, and the effect of varying the relative lengths (b/a) and mechanical properties (α_b/α_a) of the constituent materials was to produce a large positive value of CTE, see Figure 2.4a and Figure 2.4b. It is in line with the behaviour of other proposed structures, where CTE was able to fall outside the range of constituent CTE values, for example (Lakes, 1996, 2007; Miller et al., 2008a), however, it was not possible to obtain a near-zero or negative value of CTE for Lattice 1 without the use of at least one inherently NTE constituent material.

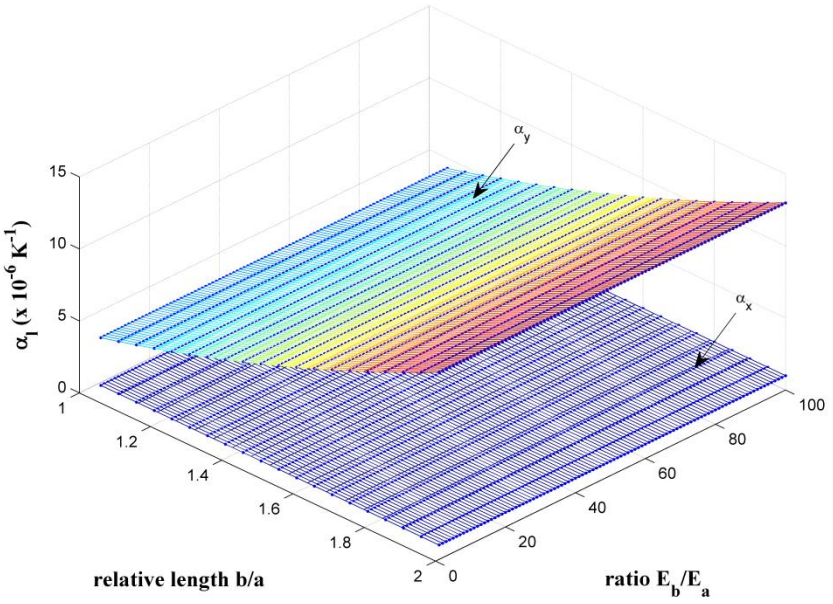

a)

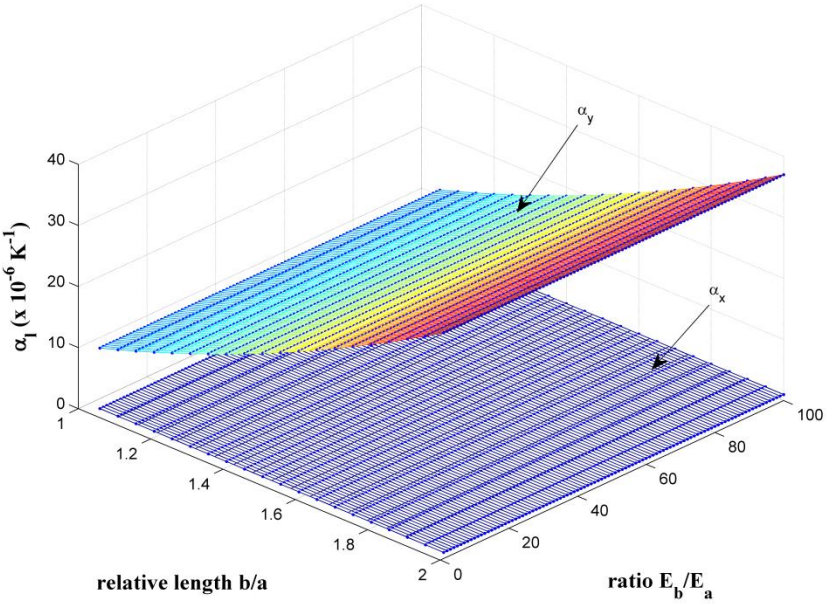

b)

Figure 2.4 (a and b). Graphs of the sensitivity of α_x and α_y to b/a and E_b/E_a in Lattice 1. Two cases are shown; Figure 2.4a with α_b/α_a = 4, and Figure 2.4b with α_b/α_a = 10.

For Lattice 2, the value of α_y was bounded by the CTEs of the constituent materials. Two of the important results for Lattice 2 are shown in Figure 2.5a and Figure 2.5b,

respectively, where α_b/α_a have been chosen to demonstrate near-zero CTE (α_b/α_a = 4, Figure 2.5a) and large negative CTE (α_b/α_a = 10, Figure 2.5a). Note that lattices with values of *b/a* approaching two will be very anisotropic and are likely to suffer severely reduced buckling loads since they have long thin beams. It is possible to obtain near-zero and even negative CTE in the *x* axis, but never simultaneously in the *y* axis without an inherently NTE constituent material. From Figure 2.5b, it seems as if larger values of *b*/*a* would yield α_y tending to zero, though this is not possible since for this structure, the geometric limit for *b*/*a* is approximately 2 (at *b*/*a* the two beams become coincident). The limit for α_x = 0 is approximately $\alpha_b/\alpha_a < 4$ and this is regardless of geometry, as is shown in Figure 2.5a, in which the minimum of the curve is near to but larger than zero. It is clear that Lattice 2 is capable of exhibiting zero or negative CTE and is unbounded by the constituent materials' CTE with appropriate choice of geometry and materials. It is always highly sensitive to the relative lengths *b/a* of the unit cell, that is the CTE is minimal if *b*/*a* is between 1.40 and 1.65, see Figure 2.5a. The 'critical ratio' of α_b/α_a (that which minimises α_x) is 4 for a near-zero CTE when $b/a \approx 1.65$. For larger values of α_b/α_a ratios, for instance 10, NTE is possible with *b/a* = 1.65, see Figure 2.5. In general, attainment of zero CTE or NTE is largely dependent upon the relative expansivities of the beams, α_b and α_a, and upon the relative lengths, *b* and *a*. Furthermore, beyond $E_b/E_a \geq 10$ the CTE of the structure is largely insensitive to the ratio of the constituent moduli, whereas below this value, it has a significant influence, see Figure 2.5a and Figure 2.5b.

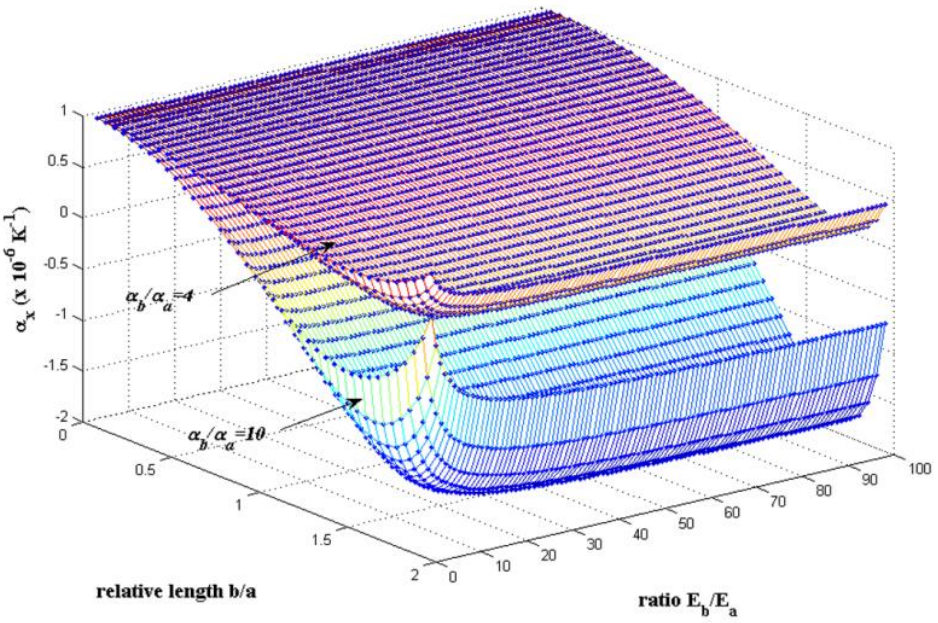

a)

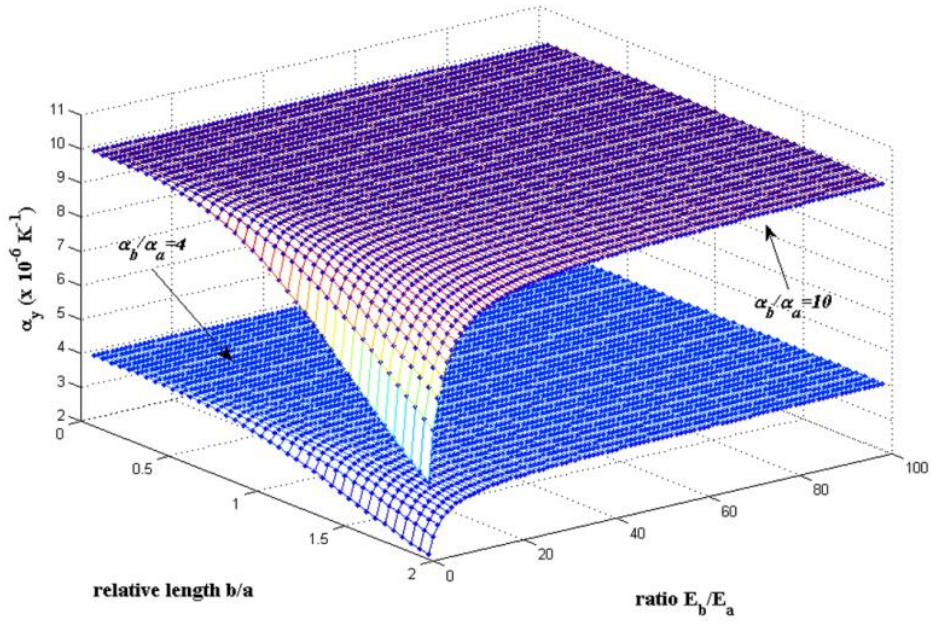

b)

Figure 2.5 (a and b). Graphs of the sensitivity of α_x and α_y to b/a and E_b/E_a in Lattice 2. Two cases are shown; Figure 2.5a α_x with α_b/α_a = 4 and α_b/α_a = 10, and Figure 2.5b α_y with α_b/α_a = 4 and α_b/α_a = 10.

2.3.2 CTE, Second Parametric Study

Results for the second complementary parametric study, using pairings of widely used materials, are shown in Figure 2.6a, Figure 2.6b, Figure 2.7a and Figure 2.7b, including Al/Ti, Al/Invar, Al/CCF, Ti/Invar and Ti/CCF, (properties given in Table 1). These material pairings exhibited much smaller CTE α_x in the form of Lattice 2 than in the form of Lattice 1, as expected (CTE α_x in the form of Lattice 1 is always the same as the CTEs of the constituent materials). Note that these pairs of materials all have $E_b/E_a \leq 1$ and only the pairings of Al/CCF and Ti/CCF have $\alpha_b/\alpha_a > 10$. Pairings of materials with high E_b/E_a ratios and high α_b/α_a are unusual since high CTE is usually found in conjunction with low values of E. For these case studies, CTE is minimised if b/a is approximately 1.45.

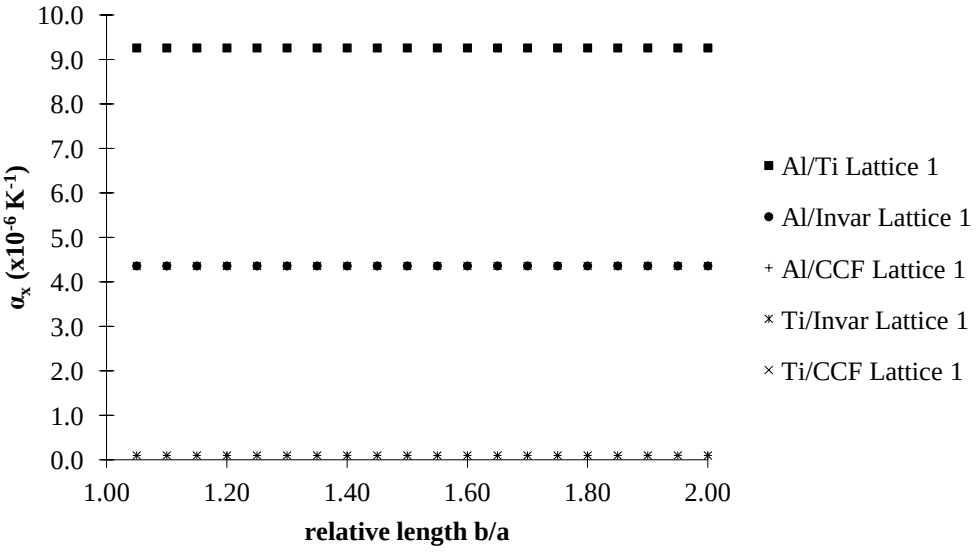

a)

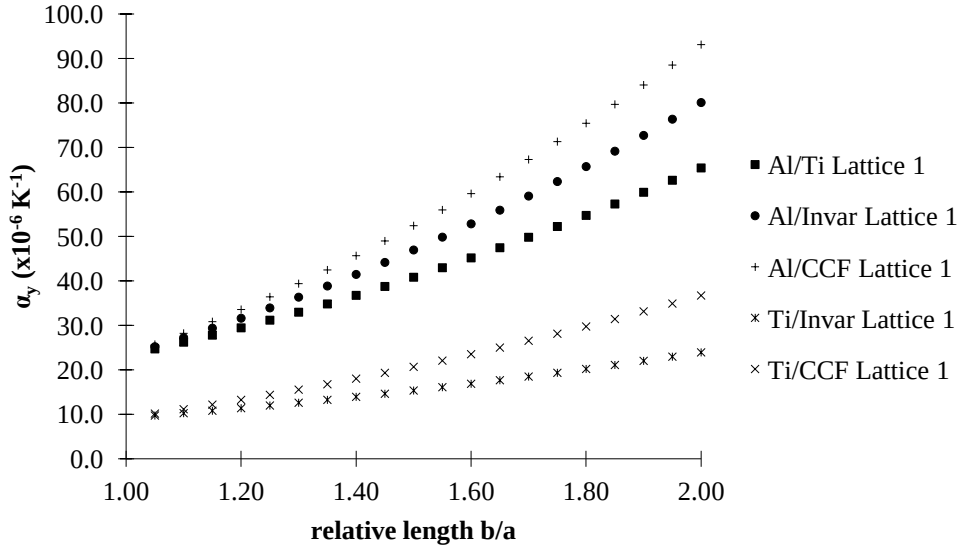

b)

Figure 2.6 (a and b). a) The value of α_x in Lattice 1 with variation of the relative lengths *b*/*a*; b) The value of α_y in Lattice 1 with the variation of the relative lengths *b*/*a*.

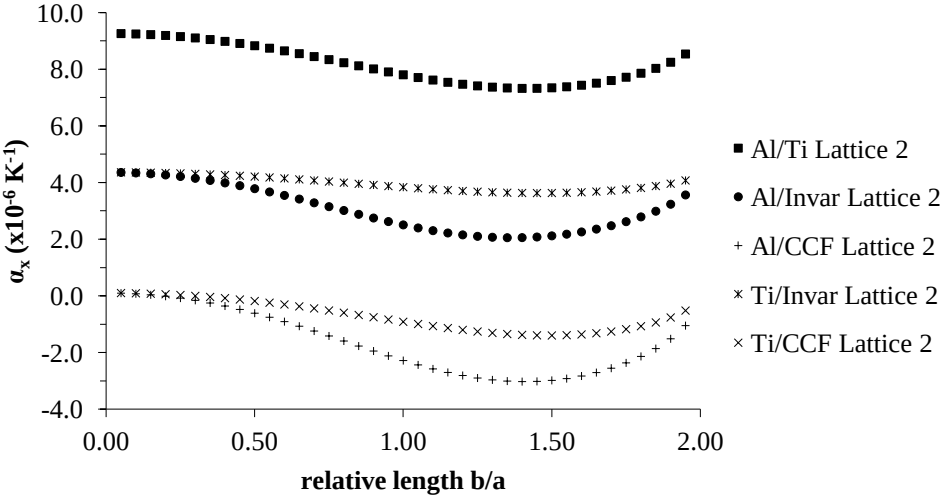

a)

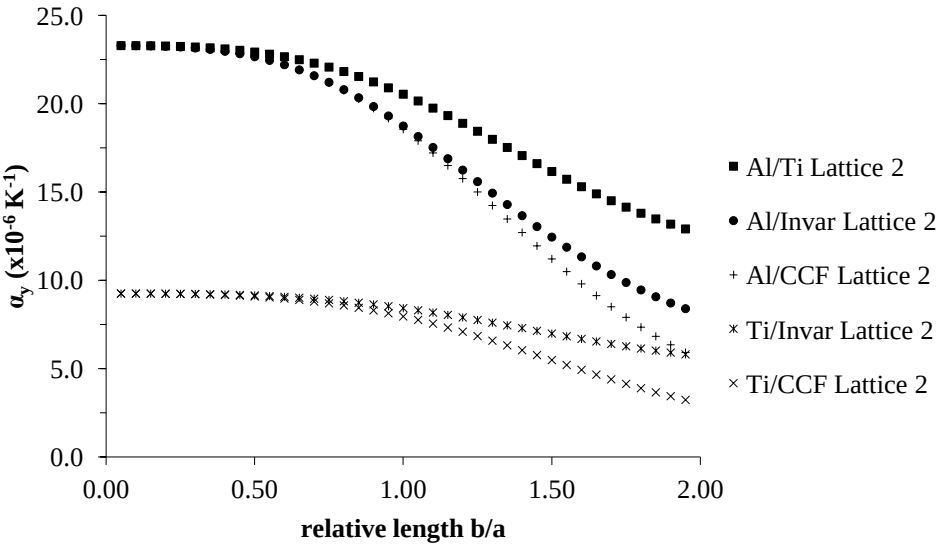

b)

Figure 2.7 (a and b). a) The value of α_x in Lattice 2 with variation of the relative lengths b/a; b) The value of α_y in Lattice 2 with the variation of the relative lengths b/a.

A more complete listing of minimised CTE α_x and CTE α_y results for Al, Ti, Invar and CCF material pairings in the form of Lattice 2 is given in Table 2.2. For these results and for all further case studies, a value of b/a = 1.45 was used because this is the local minimum for $E_b/E_a \leq 1$, as seen above. The CTEs of monolithic Ti and Invar structures were used as benchmarks. Compared to the titanium benchmark, all case study pairings had lower CTE, whereas compared to monolithic Invar, only some pairings had lower CTE. The lowest CTE values were for Al/CCF and Ti/CCF, where $\alpha_x = -3 \times 10^{-6}\ K^{-1}$ and $\alpha_x = -1.4 \times 10^{-6}\ K^{-1}$, and the highest were for Al and Ti material pairing where $\alpha_y = 16.2 \times 10^{-6}\ K^{-1}$. It is possible, using common materials, to reduce the CTE in the x direction to lower than both constituent materials' CTE values, and CTE in the y direction to lower than just the larger constituent material's CTE.

	Ti	Invar	Al/Ti	Al/Invar	Al/CCF	Ti/Invar	Ti/CCF
CTEα_x ($\times 10^{-6} K^{-1}$)	9.3	4.4	7.3	2.1	- 3.0	3.6	- 1.4
CTEα_y ($\times 10^{-6} K^{-1}$)	9.3	4.4	16.2	12.5	11.2	7.0	5.5
vs Ti % α_x	-	47.0	79.2	22.8	- 32.2	39.10	- 15.10
vs Ti % α_y	-	47.0	174.6	134.5	121.2	75.5	53.3
vs Invar % α_x	212.3	-	168.3	48.5	- 68.4	83.2	- 32.1
vs Invar % α_y	212.3	-	370.8	285.6	257.3	160.4	126.0

Table 2.2. CTEs of benchmark materials and case study pairings (Lattice 2), absolute values and relative to benchmarks.

2.3.3 Stiffness and mass in second parametric study

Comparisons were made between lattice structures, specifically Lattice 1 and 2 in monolithic form and Lattice 2 in dual-material form, in terms of their structural stiffness on an equal mass basis, and their mass on an equal stiffness basis. That is, monolithic and dual-material lattices were configured to have similar stiffnesses or similar masses, and their masses or stiffness compared. These comparisons highlight any penalty incurred due to the reduction of CTE by using dual-materials. All comparisons between Lattice 1 and 2, and versus the monolithic benchmarks, are shown in Table 2.3. In all these comparisons, the value of b/a was set to 1.50, i.e. the aspect ratio of the unit cell h/l was 0.6.

It is clear that compared to monolithic carbon fibre composite, none of the dual-material lattices is as stiff on an equal mass basis. The best performing dual-material lattices, i.e. that which retains the highest structural stiffness in conjunction with the lowest CTE in the *x* axis at a given mass, were the Ti/CCF lattice and Al/CCF lattices. They were stiffer in all axes versus all other monolithic structures, except carbon fibre. In general, when comparing a dual-material lattice to a monolithic lattice formed from either of the

constituent materials, stiffnesses are bounded by those of the constituent materials whilst CTE is reduced markedly.

The masses of the dual-material Lattice 2 structures are shown in Table 4, compared to the masses of the benchmark monolithic lattices in both forms (Lattice 1 and Lattice 2), on an equal stiffness basis (K_x). Material pairings involving Invar performed less well, being usually denser than monolithic benchmarks. Pairings not involving Invar were usually comparable to monolithic benchmarks, and pairings involving carbon fibre composite were generally much less dense. Notably, it is possible to retain stiffness and significantly reduce both CTE and mass using Al/CCF pairings (130% reduction in CTE vs. monolithic titanium in Lattice 1 or 2, 45-60% reduction in mass vs. monolithic titanium in Lattice 1 or 2) and Ti/CCF pairings (115% reduction in CTE vs. monolithic titanium in Lattice 1 or 2, 45-50% reduction in mass vs. monolithic titanium in Lattice 1 or 2). Similarly to stiffness, mass is bounded by those of the constituent materials whilst CTE is reduced markedly.

It is thus possible to markedly reduce CTE and improve either or both mass and stiffness to suit a specific requirement. It seems that dual-material lattices suffer no or little penalty, in terms of stiffness or mass compared to similar monolithic lattices, in exchange for sometimes large reductions in CTE.

Benchmark lattice	Lattice Type				
Monolithic Al, Lattice 1	Lattice 2				
	Al/Ti	Al/Invar	Al/CCF	Ti/Invar	Ti/CCF
K*x* (%)	86.4	65.9	209.1	66.1	188.6
K*y* (%)	63.1	43.9	149.8	51.9	156.4
Mass (%)	115.7	151.4	47.8	155.1	55.3
Monolithic Ti, Lattice 1	Lattice 2				
	Al/Ti	Al/Invar	Al/CCF	Ti/Invar	Ti/CCF
K*x* (%)	90.6	58.9	219.7	67.7	190.1
K*y* (%)	63.1	43.9	149.8	51.9	156.4
Mass (%)	109.9	144.1	45.4	147.5	52.5
Monolithic Invar, Lattice 1	Lattice 2				
	Al/Ti	Al/ Invar	Al/CCF	Ti/ Invar	Ti/CCF
K*x* (%)	124.0	94.6	299.8	91.7	259.4
K*y* (%)	90.6	63.0	214.5	72.1	224.2
Mass (%)	80.5	105.5	33.8	107.9	38.5
Monolithic CCF, Lattice 1	Lattice 2				
	Al/Ti	Al/ Invar	Al/CCF	Ti/ Invar	Ti/CCF
K*x* (%)	30.1	25.4	73.7	22.7	58.2
K*y* (%)	22.1	16.8	52.8	17.8	55.1
Mass (%)	328.7	430.3	135.7	440.5	157.0
Monolithic Ti, Lattice 2	Lattice 2				
	Al/Ti	Al/ Invar	Al/CCF	Ti/ Invar	Ti/CCF
K*x* (%)	105.4	80.5	255.0	78.7	220.6
K*y* (%)	86.8	60.4	205.7	69.7	215.0
Mass (%)	94.9	124.2	39.2	127.1	45.3

Table 2.3. Comparison of benchmark monolithic Lattices vs. dual-material Lattice 2. Stiffness in *x* and *y* axes is compared on an equal mass basis; mass is compared on an equal stiffness basis.

2.3.4 Comparison FE solution vs. Truss Analysis

The CTE values for pin-jointed lattice truss shown in Figure 2.2, Lattice 1, were calculated by truss analysis, assuming that the cross-sectional area of all members is equal to *A* and the relative lengths, *b/a*, equal to 1.4.

The magnitude and direction of the vertical deflection at joint 3 was determined and then converted into strain and thus into CTE, α_y, since the temperature change was unitary. Similarly, the horizontal deflection at joint 4 was determined and then converted into strain and thus into CTE, α_x.

The vertical deflection at joint 3, due to temperature change, was calculated by applying a unit load only in a vertical direction (opposite direction to the positive *y* direction in Figure 2.2) at joint 3 and determining the magnitude and sense of unknown member forces (i.e. the *u* forces).

The vertical deflection $\delta_{v,3} = \sum \Delta L_T \times u$ where $\Delta L_T = \alpha L \Delta T$ is the variation of length of each member due to temperature change and *u* member forces.

The vertical deflection $\delta_{v,3}$ and the corresponding CTE, α_y, were calculated and shown in tabular form, see Table 2.4.

Lattice Type						
Lattice 1						
Members	Length (*L*) *(mm)*	Cross-section (*A*) *(mm^2)*	Modulus (*E*) *(MPa)*	*u* forces	ΔL_T *(× 10^{-6} mm)*	$\Delta L_T \times u$ *(× 10^{-6} mm)*
1-2	0.714286	0.007853982	114000	0	6.61	0
1-6	0.699854	0.007853982	114000	0.49	6.48	3.1755
1-3	1	0.007853982	73200	- 0.7	23.3	- 16.310
2-3	0.699854	0.007853982	114000	0	6.48	0
3-6	0.714286	0.007853982	114000	0	6.61	0
5-6	0.699854	0.007853982	114000	0.49	6.48	3.1755
3-4	0.699854	0.007853982	114000	0	6.48	0
3-5	1	0.007853982	73200	- 0.7	23.3	- 16.31
4-5	0.714286	0.007853982	114000	0	6.61	0
					∑	- 26.269

Table 2.4. Tabular form of the calculated vertical deflection $\delta_{v,3}$.

The vertical deflection $\delta_{v,3}$ was equal to - 26.269 × 10^{-6} *mm*. The *-ve* sign indicates that the deflection is in the opposite direction to the applied unit load. The vertical deflection was converted into strain (by dividing for the 3-6 member length) and thus into CTE, α_y, since the temperature change was unitary. The coefficient of thermal expansivity in *y* direction was equal to $\alpha_y \approx +\ 36.776 \times 10^{-6}\ K^{-1}$. This value is comparable to the numerical model (FE).

The horizontal deflection at joint 4, due to temperature change, was calculated by applying a unit load only in a horizontal direction (the same direction as the positive *x* direction in Figure 2.2) at joint 4 and determining the magnitude and sense of unknown member forces (i.e. the *u* forces).

The horizontal deflection $\delta_{h,4}$ and the corresponding CTE, α_x, were calculated and shown in tabular form, see Table 2.5.

Lattice Type						
Lattice 1						
Members	Length (*L*) *(mm)*	Cross-section (*A*) *(mm^2)*	Modulus (*E*) *(MPa)*	*u* forces	ΔL_T *(× 10^{-6} mm)*	$\Delta L_T \times u$ *(× 10^{-6} mm)*
1-2	0.714286	0.007853982	114000	0	6.61	0
1-6	0.699854	0.007853982	114000	0	6.48	0
1-3	1	0.007853982	73200	0	23.3	0
2-3	0.699854	0.007853982	114000	1	6.48	6.48
3-6	0.714286	0.007853982	114000	0	6.61	0
5-6	0.699854	0.007853982	114000	0	6.48	0
3-4	0.699854	0.007853982	114000	1	6.48	6.48
3-5	1	0.007853982	73200	0	23.3	0
4-5	0.714286	0.007853982	114000	0	6.61	0
					∑	12.961

Table 2.5. Tabular form of the calculated horizontal deflection $\delta_{h,4}$.

The horizontal deflection $\delta_{h,4}$ was equal to + 12.961 × $10^{-6}mm$. The *+ve* sign indicates that the deflection is in the same direction as the applied unit load. The vertical deflection was converted into strain (by dividing for the length of the lattice in *x* direction, *l*, see Figure 2.2) and thus into CTE, α_x, since the temperature change was unitary. The coefficient of thermal expansivity in *x* direction was equal to $\alpha_x \approx + 9.26 \times 10^{-6}\ K^{-1}$. This value is comparable to the numerical model (FE).

2.4 Discussion

Of the two lattice structures explored, Lattice 1, inspired directly by an existing spacecraft structure Figure 2.1, had limited scope for reduction of CTE. The second, with two additional beams (Figure 2.2), Lattice 2, had much better scope for reduction of CTE and retention of good mechanical properties such as stiffness. Whilst Lattice 2 was not optimal in terms purely of reduced CTE, since other structures exist with far more extreme CTEs (Jefferson et al., 2009; Lakes, 1996, 2007; Miller et al., 2008a; Steeves et al., 2007), these extreme CTE structures tend to suffer large penalties in terms of other properties, especially if mass is considered. It may be the case that such extreme structures might not be adopted widely in practice, since a requirement for a specific CTE will rarely come without requirements for other mechanical properties. The Lattice 2 structure presented here seems likely to offer a very good compromise between reduced CTE, high stiffness, low mass and general structural integrity. Some other postulated 2D and 3D structures offer extreme CTEs but are likely to have very much lower stiffnesses, due to their not being fully triangulated (Lakes, 1996, 2007; Sigmund and Torquato, 1996), as Jefferson et al. (2009) indicates, or they are corner sharing and thus compliant off axis or in shear (Aboudi

and Gilat, 2005). There are some other postulated structures which seem to be able to retain high stiffness as well as reduced CTE (Steeves et al., 2007).

The conditions in the Lattice 2 structure required for this good compromise, and indeed likely to be generic across all such lattice-type structures, is that a triangulated dual-material structure is present but that its shrinkage under heating is resisted by stiffeners. The CTE reduction is primarily driven by the geometry of the lattice and the mismatch in the constituent's CTE and elastic moduli. The critical conditions for near-zero CTE are: that the high expansivity beam is 40-60% longer than the lower expansivity beam; there is at least a fourfold difference between the CTEs of the constituent materials; and there is at least a fivefold difference in elastic moduli between constituent materials, see Figure 2.5a. Pairings of materials such as carbon fibre and titanium, carbon fibre and aluminium, as well as aluminium and titanium are very suitable for the manufacture of these structures, see Table 2.3.

There is little or in some cases no penalty to be paid in terms of stiffness and mass for implementing such dual-material lattices, except in comparison to high stiffness and low mass monolithic carbon fibre composites. However, carbon fibre composite has two drawbacks: i) its CTE is fixed within a small range of values near to but above zero (the range is dependent on the stack sequence and volume fraction), and this may be undesirable where a match to another component's CTE or exactly zero CTE is required; and ii) it is many times more expensive than metal alloys.

The lattice structures examined here may reduce CTE by means of swapping overall distortion for internal stress as the slenderness ratio of the rigid-jointed members tends to zero. Given wide fluctuations in temperatures, these stresses will of course eventually cause

failure, most notably, fatigue failure in aluminium. The absolute value of temperature will most likely affect carbon fibre composite which has a degradation temperature, typically of 493.15 *K*.

Lattice 1 is statically determinate. Adding members to this structure, Lattice 2, has led to static indeterminacy, and hence a state of self-stress. Therefore, dual-material Lattice 1 has no stress associated with the thermal strain (when the slenderness ratio of the rigid-jointed members tends to infinite), dual-material Lattice 2 develops stress when the structure is heated uniformly. The different determinacy of Lattice 1 and Lattice 2 well explains the effect of varying the mechanical properties (E_b/E_a) of the constituent materials on the value of α_x and α_y for Lattice 2, compared to the negligible effect on Lattice 1, Figure 2.4 and Figure 2.5.

Given the anisotropic nature of the geometry of these lattice structures, it is not possible to arrange for isotropic CTE within a single lattice cell. However, it is possible, by tessellating alternately orthogonally aligned cells, to ensure isotropic near-zero CTE, as was shown in Miller et al. (2008a). By doing so, the global axial values of CTE would be bound by the constituent cells' CTE values (α_x and α_y), and therefore not bound by the constituent materials' CTEs.

The manufacture of such lattice structures would seem to present no special problems beyond those already widely known, of joining dissimilar materials together. From the point of view of the calculations herein, the particular method of joining is not very important, so joining beams via pins would be as effective as welding or adhering.

The designs herein are scale-independent and so are as valid for large spacecraft structures as for truss cores. The designs presented here are 2D but obviously similar

mechanisms could be extended to 3D, with little impact upon choice of manufacturing methods.

The two-dimensional rigid-jointed lattices proposed herein were found to compare well with similar pin-jointed structures (specifically Lattice 1). For consistency, slenderness ratio was kept the same for both rigid-jointed and pin-jointed structured lattices. Comparison was conducted using truss analysis.

2.5 Conclusion

It has been shown that lattice structures formed from materials with large and positive CTEs can exhibit markedly reduced CTE in at least one axis. Geometric and material property criteria have been given for the reduction of CTE, in such lattices, to zero or negative values. The approach effectively swaps external distortion for internal stress (as the slenderness ratio of the members tends to zero or as the structures tend to static indeterminacy, in the case of Lattice 2, for instance). Performance against other criteria such as stiffness, and mass was not significantly affected by the use of dual-material lattices, though there could be limiting temperature changes before failure. Manufacturing of such lattice structures seemed to require nothing new in terms of large-scale structures and to be possible, via emerging manufacturing technologies, for smaller scale structures. This approach could potentially alleviate the need for the use of exotic and expensive materials.

3 HIGH PERFORMANCE 3D TRUSSES: LIMITS OF THERMAL DISTORTION AND ELASTIC PROPERTIES.

3.1 Introduction

Three-dimensional lattice-type trusses are widely used in structural roles because of their excellent low-density and high mechanical performance (Ashby, 2006; Wallach and Gibson, 2001). A good deal of work is ongoing in the mechanics and computational engineering communities on optimisation of trusses for specific applications (Deshpande and Fleck, 2001; Deshpande et al., 2001; Evans et al., 2001; Sonmez, 2011; Wadley, 2006; Wicks and Hutchinson, 2001). Recently, truss lattices have been proposed for use in applications where thermal distortion is a problem and the truss can bring about a reduced thermally driven distortion because the truss is formed from two or more materials with contrasting thermal expansivities (Aboudi and Gilat, 2005; Grima et al., 2007; Lakes, 1996, 2007; Miller et al., 2008a; Palumbo et al., 2011; Steeves et al., 2007). Several other researchers have investigated controlled thermal distortion of other types of cellular solids and composites (Jefferson et al., 2009; Kelly et al., 2005; Sigmund and Torquato, 1997). It is accepted that there is a penalty for reduced thermal distortion in such truss lattices, in terms of reduction of performance in other functionalities such as stiffness (Palumbo et al., 2011). The key issue addressed in this chapter is the extent of this penalty and the geometrical factors which drive it.

There are several potential applications where thermal distortion is a problem, for instance space and aerospace (Jefferson et al., 2009; Steeves and Evans, 2011) where truss lattices are very widely used (Aboudi and Gilat, 2005; Miller et al., 2008a; Queheillalt et

al., 2008; Wadley, 2006; Wallach and Gibson, 2001). There are many published geometries for such truss lattices, which have been proposed, and in some cases optimised, for specific applications. However, there is not yet a generalised framework for prediction of the thermal distortion or mechanical properties of these truss lattices. In other words, there are no generic guidelines for designers of truss lattices with reduced thermal distortion.

Analytical and empirical relationships have been developed in the last decade to describe the mechanical behaviour of individual lattices, mostly assuming axial deformation of members (Deshpande et al., 2001; Evans et al., 2001; Wallach and Gibson, 2001; Wicks and Hutchinson, 2001). Predicted moduli from these approaches are functions of the relative density with an empirical constant related to the truss architecture, loading orientation and node design. Of note is that these equations are valid only for nearly isotropic lattices, and therefore strongly anisotropic truss lattices cannot be adequately described. In fact, many structures such as pyramids are not nearly isotropic (Hyun et al., 2003). Deshpande and Fleck, and Wicks and Hutchinson gave a generalised relationship for the elastic constants of pyramidal and tetrahedral core truss lattices, also based on axial deformation of members (Deshpande and Fleck, 2001; Wicks and Hutchinson, 2001) but which does not require isotropy. Other approaches such as finite elements make no such assumptions but are much less generalised.

This chapter sets out the relative performance, in terms of thermal distortion combined with stiffness, of seven truss lattice designs which are either already in use or are proposed in the literature, in monolithic and dual-material forms. Some of these truss lattices were originally developed for high stiffness only and others for stiffness combined with reduced thermal expansivity. The seven designs were chosen because they were

typical of many such truss lattices and because they lend themselves to fabrication from dual materials. There are some other postulated structures which seem to be able to retain high stiffness as well as reduced CTE (Steeves et al., 2007), however, these models were not considered because they do not lend themselves to be tessellated by simple translation in the *x* and *z* axes. This could form part of future research work. All designs were considered on an equal volume fraction (or apparent density) basis. A generalised framework for prediction of performance is suggested.

3.2 Methodology

3.2.1 Numerical Modelling

The elastic constants and the thermal distortion of the seven truss lattices, chosen because they were typical of many such truss lattices and because they lend themselves to fabrication from dual materials, were calculated using the finite element (FE) method, allowing the internal angles and lengths of the unit cell of the lattice to vary in a parametric study. All lattices were considered in both monolithic and dual-material forms, noting that in monolithic form the apparent CTE α, of any monolithic lattice is the same as that of the constituent material. To aid comparison, the volume fraction of the solid component (i.e. the truss members) was kept constant across all cases, specifically 0.6% of the total unit cell volume.

The repeating unit cell for the truss lattices are shown in Table 3.1. Note that the *x*, *y* and *z* axes for all structures are similar to that shown in Figure 3.1 for the representative volume element (RVE).

Wallach (Wallach and Gibson, 2001)	2001	(Wallach)	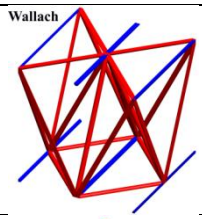
Aboudi (Aboudi and Gilat, 2005)	2005	(Aboudi I)	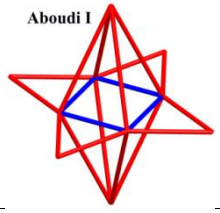
Aboudi (Aboudi and Gilat, 2005)	2005	(Aboudi II)	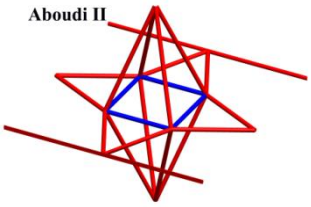
Wadley (Wadley, 2006)	2006	Double pyramidal (SqBasedPyr)	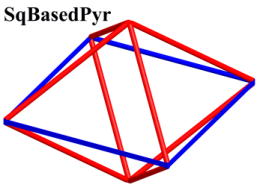
Miller (Miller et al., 2008a)	2008	Double tetrahedral (TrBasedPyr)	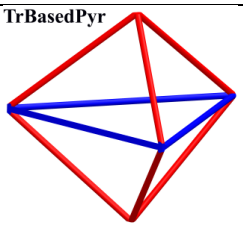
Miller (Miller et al., 2008a)	2008	(3Dstar)	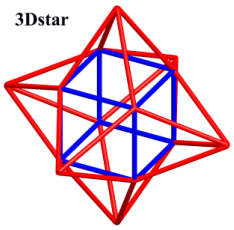
Queheillalt (Queheillalt et al., 2008)	2008	Square based pyramid (Pyr)	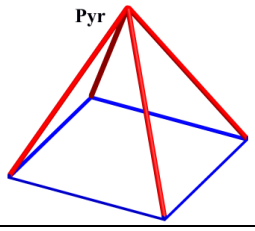

Table 3.1. The unit cells studied. Beams of different constituent materials are shown in clear colour (red) and darker colour (blue), clear colour indicating relatively low thermal expansivity and dark colour, higher.

A commercial FE code (Ansys 11, Ansys, Inc.) was used to simulate the properties of both the dual-material truss lattices and their monolithic counterparts. For each unit cell, see Table 3.1, periodic boundary conditions were applied so that the cell behaved as if in an infinite three-dimensional array, following Wallach and Gibson (2001); in effect, a representative volume element (RVE) approach, see Figure 3.1. The unit cells have square bases of length *b* and height of length *h*. Note that, tessellation in an infinite three-dimensional array of some of these 3D trusses would require reflection rather than translation (Pyr and Wallach, for instance, see Table 3.1). These structures tessellate by translation in the *x* and *z* axes but not in the *y* axis. It is facile to derive correct unit cells for these structures (simply by reflecting the structure shown across the *xz* plane) which would tessellate by translation in the *y* axis. In such cases, the properties would be similar to those we present here except that the aspect ratio of the unit cell would be doubled. Employing the parametric design language within the FE software, the three-dimensional unit cells were generated, meshed and solved for 20 iterations of each unit cell, in both monolithic and dual-material forms, and involving three axial and three shear deformations and one temperature field simulation. In total, 1,960 simulations were run. For each beam member within the unit cell, three-dimensional elastic beam elements (specifically 'beam4' in Ansys) were used, which had axial and flexure deformation capability.

In the dual-material configurations, some beams were formed from relatively high thermal expansivity materials and some from lower thermal expansivity materials. The decision over constituent material in individual beams was made in order to manifest the largest change in thermal expansivity in at least one dimension, according to the results set out in Miller et al. (2008a). Beam elements located in the unit cell faces and edges were shared between two or four other unit cells, as appropriate. For such beam members, the

cross-sectional area A and the second moment of area I were reduced to a half or quarter, according to the number of shared neighbouring cells (two for faces and four for edges). In the case of the dual-material trusses, each member beam was formed from one of two constituent materials, specifically titanium and aluminium, which have different inherent physical, mechanical and thermal expansivity properties, as shown in Table 3.2.

The apparent elastic moduli and apparent thermal expansivity were analysed as a function of the aspect ratio of the unit cell, h/b (see Figure 3.1). This ratio captures the details of the internal angles and of the members' lengths of the unit cells. In order to permit a consistent and fair comparison between monolithic and dual material configurations, and between different truss lattice geometries, the volume fraction of the high, v_{f1}, and low expansivity beam members, v_{f2}, i.e. 0.3% each, were kept constant in all models. The resultant overall relative density ρ^* (sum of v_{f1} and v_{f2}) for all the structures in this study was 0.006, which is typical for this kind of truss structure. The range of aspect ratios h/b considered ranged from 0.1 to 2.0.

Nine independent elastic constants (E_i, G_{ij}, v_{ij}) were calculated for each unit cell, as required for a complete description of a material with orthotropic symmetry (Hearmon, 1978; Wallach and Gibson, 2001). Different boundary conditions were applied for axial and shear loading modes. In the axial cases, symmetry constraints were applied so that the cells' faces remained planar and parallel. For axial deformation, a small normal axial displacement was applied to nodes on one face. The contralateral face was constrained not to displace axially. The axially parallel faces were constrained to remain planar and parallel by defining coupled node sets subject to the linear constraint equation, as defined in Ansys, which enforces the displacement of each node in the axial direction to be similar. The total

force F_i was calculated by summing the axial forces in the nodes on the normal displaced face. The Young's moduli E_i were calculated from:

$$F_i = \frac{AE_i}{L_i}\delta_i \quad \textbf{3.1}$$

with δ_i being the displacements on the normal face, L_i is the length of the unit cell in i direction and A is the cross-sectional area of the RVE. For clarity in results, E_i were normalised to the Young's modulus of the low thermal expansivity solid strut material and the relative density of the truss structure.

The Poisson's ratios, ν_{ij}, were calculated as:

$$\nu_{ij} = -\frac{\varepsilon_i}{\varepsilon_j} \quad \textbf{3.2}$$

where j is the loading direction, and ε is the axial strain in i and j directions.

For shear displacements, the boundary conditions and displacements were applied by imposing a simple shearing deformation. To effect simple shear, nodes on one face were displaced in the axis of the face, whilst nodes on the contralateral face were fixed. The faces perpendicular to the displacement were free to deform. In special cases (for instance, the 3Dstar) pairs of nodes at equal heights on these opposing faces were constrained to displace identically in the direction normal to the applied shear displacement, i.e. they were coupled (Wallach and Gibson, 2001). The shear moduli G_{ij} were calculated from:

$$F_i = \frac{AG_{ij}}{L_j}\delta_i \quad \textbf{3.3}$$

with δ_i being the displacements on a face in i direction, L_j is the length of the RVE in j direction and A is the cross-sectional area of the considered face of the RVE. The G_{ij} were normalised to the Young's modulus of the low thermal expansivity solid strut material and the relative density of the truss structure.

The apparent thermal expansivity values (CTEs) for the lattices were calculated by applying a unitary thermal load and converting the resultant displacements in the global x, y, and z axes into axial strains, and thus into CTE since the temperature change was unitary. The CTEs were normalised to the thermal expansivity of the low thermal expansivity solid strut material members.

In order to have a simple figure of merit for elastic and CTE performance for swift comparison between geometries, volume averaged elastic constants were calculated as generalised means according to the method of Ji (2004), specifically the geometric mean for the elastic moduli (E_x, E_y, E_z, etc) and arithmetic mean for the CTEs (α_x, α_y and α_z). Since both positive and negative CTEs' values were expected from the structures proposed, the arithmetic mean was used for CTE. All property data are shown as a function of the aspect ratio of the unit cell. Full data sets, i.e. all 9 elastic constants and 3 CTEs, are also given for a subset of the samples which were typical of the range of behaviours.

3.2.2 Validation

A validation of the FE models was undertaken by comparing their predictions against well-established models of monolithic truss lattices by Wallach and Gibson (2001).

Material	*E* *(GPa)*	*v*	*ρ* *(g/cm^3)*	*α* *(× 10^{-6} K^{-1})*
Al	73	0.33	2.77	23.30
Ti	114	0.322	4.54	9.26

Table 3.2. Mechanical properties of the materials considered in the case studies.

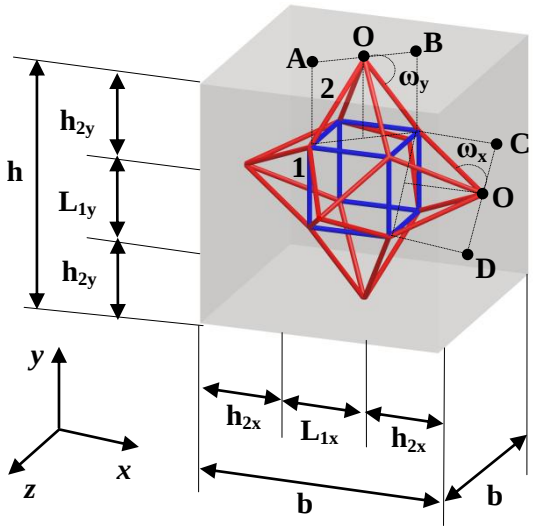

Figure 3.1. RVE: Representative Volume Element.

3.2.3 Analytical Modelling

Analytical expressions were derived for the CTEs, axial and shear moduli for some of the truss lattices. The unit cells are all formed from triangles and/or pyramids, with more or less complexity. The expressions for CTE were developed from a geometrical basis, in a manner similar to that of Miller et al. (2008a), which was possible because only axial deformation in the beam members was considered, i.e. flexural deformation was ignored. Such trusses are known to be stretch dominated (Deshpande and Fleck, 2001; Wallach and Gibson, 2001), that is axial deformation dominates over flexural deformation. The expressions for CTE for all the structures are shown below in Table 3.3, where high thermal expansivity members are represented by subscript 1 and low thermal expansivity members by subscript 2:

Wallach:		
(1.1) $\alpha_x = \alpha_2$ (upper limit) $\alpha_x = 2\alpha_2 - \alpha_1$ (lower limit)	**(1.2)** $\alpha_y = \frac{b^2}{8h^2}\left[\left(\frac{8h^2}{b^2}+1\right)\alpha_2 - \alpha_1\right]$ (lower bound)	**(1.3)** $\alpha_z = \alpha_1$
Aboudi I:		
(2.1) $\alpha_x = \frac{1}{6}[5\alpha_2 + \alpha_1]$	**(2.2)** $\alpha_y = \frac{2b^2}{9h^2}\left[\left(\frac{9h^2}{2b^2}+1\right)\alpha_2 - \alpha_1\right]$	**(2.3)** $\alpha_z = \frac{1}{6}[5\alpha_2 + \alpha_1]$
Aboudi II:		
(3.1) $\alpha_x = \frac{1}{12}[11\alpha_2 + \alpha_1]$ (lower bound)	**(3.2)** $\alpha_y = \frac{2b^2}{9h^2}\left[\left(\frac{9h^2}{2b^2}+1\right)\alpha_2 - \alpha_1\right]$	**(3.2)** $\alpha_z = \frac{1}{6}[5\alpha_2 + \alpha_1]$
SqBasedPyr:		
(4.1) $\alpha_x = \alpha_1$	**(4.2)** $\alpha_y = \frac{2b^2}{h^2}\left[\left(\frac{h^2}{2b^2}+1\right)\alpha_2 - \alpha_1\right]$	**(4.3)** $\alpha_z = \alpha_1$
TrBasedPyr:		
(5.1) $\alpha_x = \alpha_1$	**(5.2)** $\alpha_y = \frac{3b^2}{2h^2}\left[\left(\frac{2h^2}{3b^2}+1\right)\alpha_2 - \alpha_1\right]$	**(5.3)** $\alpha_z = \alpha_1$
3Dstar		
(6.1) $\alpha_x = \frac{1}{6}\left[\left(\frac{h^2}{b^2}+5\right)\alpha_2 + \left(1-\frac{h^2}{b^2}\right)\alpha_1\right]$	**(6.2)** $\alpha_y = \frac{1}{3}\left[\left(\frac{b^2}{h^2}+2\right)\alpha_2 + \left(1-\frac{b^2}{h^2}\right)\alpha_1\right]$	**(6.3)** $\alpha_z = \frac{1}{6}\left[\left(\frac{h^2}{b^2}+5\right)\alpha_2 + \left(1-\frac{h^2}{b^2}\right)\alpha_1\right]$
Pyr		
(7.1) $\alpha_z = \alpha_1$	**(7.2)** $\alpha_y = \frac{b^2}{2h^2}\left[\left(\frac{2h^2}{b^2}+1\right)\alpha_2 - \alpha_1\right]$	**(7.3)** $\alpha_z = \alpha_1$

Table 3.3. Thermal expansivity relations of the seven unit cells shown in Table 3.1.

Analytical expressions for the CTEs of the 3Dstar structure are fully described in the following, as an example. The RVE for the 3Dstar structure is shown in detail in Figure 3.1. In a similar manner, equations were derived for all the structures proposed here.

The thermal expansivity in *x* direction, α_x^{3Dstar} (corresponding to the Equation (6.1) in Table 3.3), is a function of the high thermal expansivity members, represented by subscript 1, and low thermal expansivity members, represented by subscript 2. Specifically, it is a function of high thermal expansivity members, thermal expansivity of the pyramids located in that direction, and geometry of the 3Dstar structure, see Figure 3.1.

Using the equation of the thermal expansivity of the triangle, fully described in Miller et al. (2008a), and substituting the appropriate parameters' values, the equation of the thermal expansivity for the pyramids located in *x* direction, α_x^{Pyr}, can be written as:

$$\alpha_x^{Pyr} = \frac{4\left(L_{2x}^{(p_2)}\right)^2 \alpha_2 - \left(\overline{CD}\right)^2 \alpha_1}{4\left(L_{2x}^{(p_2)}\right)^2 - \left(\overline{CD}\right)^2}$$

3.4

where $L_{2x}^{(p_2)}$ is the length of the inclined p_2^{th} low thermal expansivity beam in *x* direction, as in Figure 3.2, and $\overline{CD}$ is the length of the segment, as reported in Figure 3.1.

Using Pythagoras' theorem and trigonometry, it is possible to calculate terms $L_{2x}^{(p_2)}$ and $\overline{CD}$ as follows:

$$\overline{CD} = 2\left[\left(\frac{L_{1z}^{(p_1)}}{2}\right)^2 + \left(\frac{L_{1y}^{(p_1)}}{2}\right)^2\right]^{\frac{1}{2}}$$

3.5

where $L_{1z}^{(p1)} = L_{1x} = \frac{b}{3}$ is the length of the in-line with the axis p_1^{th} high thermal expansivity beam in *z* direction, and where $L_{1y}^{(p_1)} = L_{1y} = \frac{h}{3}$ is the length of the in-line with the axis p_1^{th} high thermal expansivity beam in *y* direction,

and

$$L_{2x}^{(p_2)} = \left[\left(\frac{\overline{CD}}{2}\right)^2 + (h_{2x})^2\right]^{\frac{1}{2}}$$

3.6

where $h_{2x} = \frac{b}{3}$ is the height of the pyramids located in *x* direction.

The change in length in *x* direction for the 3Dstar structure, Δx, can be defined as:

$$\Delta x = \alpha_x^{3Dstar} L_x \Delta T$$

3.7

and

$$\Delta x = \alpha_x^{Pyr} h_{2x} \Delta T + \alpha_1 \frac{L_{1x}^{(p_1)}}{2} \Delta T$$

3.8

where $L_{1x}^{(p_1)} = L_{1x} = \frac{b}{3}$ is the length of the in-line with the axis high thermal expansivity beam in *x* direction, and $L_x = h_{2x} + \frac{L_{1x}^{(p_1)}}{2}$ represents the initial length considered and ΔT the temperature change.

Substituting 3.7 into 3.8, and rearranging, the thermal expansivity in *x*-direction, α_x^{3Dstar}, can be defined as:

$$\alpha_x^{3Dstar} = \frac{\alpha_x^{Pyr} h_{2x} + \alpha_1 \frac{L_{1x}^{(p_1)}}{2}}{h_{2x} + \frac{L_{1x}^{(p_1)}}{2}}$$

3.9

Substituting 3.4-3.6 into 3.9, and substituting all the appropriate parameters' values, the thermal expansivity in *x*-direction, α_x^{3Dstar}, is:

$$\alpha_x^{3Dstar} = \frac{1}{6}\left[\left(\frac{h^2}{b^2}+5\right)\alpha_2 + \left(1-\frac{h^2}{b^2}\right)\alpha_1\right]$$

3.10

In a similar way, can be derived the thermal expansivity in *y* direction, α_y^{3Dstar} (corresponding to the Equation (6.2) in Table 3.3), for the 3Dstar structure. Thermal expansivity in *z* direction, α_z^{3Dstar} (corresponding to the Equation (6.3) in Table 3.3), is equal to α_x^{3Dstar} because of symmetry.

By employing beam mechanics for a stretch-dominated pyramid and following a similar method to that of Deshpande and Fleck (2001), relations were formulated for the two axial stiffnesses (there is symmetry in most of the unit cells which requires that $E_x=E_z$) and one shear stiffness G_{xy} (there is symmetry in most of the unit cells which requires that $G_{xy}=G_{zy}$), often key properties for sandwich panel cores. The shear modulus G_{xz} was not developed since either i) the structure is bending dominated in that plane (e.g. the Pyr geometry), therefore much more compliant and so unlikely to be deployed to resist shear in that orientation, or ii) symmetry requires that $G_{xz}=G_{xy}=G_{zy}$ when $h/b = 1$ (e.g. the 3DStar geometry). The relations for the elastic constants for all the structures can be derived individually.

For all the structures proposed, the moduli values can be calculated as the result of the contribution of axial deflection of in-line members δ_{1a} (always high thermal expansivity members in these structures) and inclined members δ_{2a} (always the low thermal expansivity members in these structures) in the direction of the loading mode considered, see Figure 3.1 and Figure 3.2 to 3.5. For some of the seven structures proposed, it is possible to simplify the obtained equations due to the absence of either in-line or inclined members for specific loading directions.

Young's moduli.

The axial Young's moduli, E_i, were calculated by the method illustrated in Figure 3.2. A stress, σ_i, acting on the RVE parallel to the *i* axis, acts on the set of p_1^{th} high thermal expansivity beams lying in line with the axis, of length $\frac{L_{1i}^{(p_1)}}{2}$, and the set of p_2^{th} low thermal expansivity beams, inclined to the axis, of length $L_{2i}^{(p_2)}$, to deform axially. A detail from an example structure is shown in Figure 3.2, from the RVE in Figure 3.1. Membership of p_1^{th} and p_2^{th} may be zero for some structures. By enforcing equilibrium and compatibility and using standard beam theory, it is then possible to calculate deflections for all beam members, and hence, by summation for the entire structure. Using the applied load and the resulting deflection, strains and stresses can be calculated, and therefore the Young's moduli.

An axial load of $F_i \cos(0°)$ acts on the upright p_1^{th} member and hence, from standard beam theory, the axial deflection is:

$$\delta_{1a}^{(p_1)} = \frac{F_i \left(\frac{L_{1i}^{(p_1)}}{2} \right)}{E_1 A_1^{(p_1)}} \qquad \textbf{3.11}$$

where E_1 is the Young's modulus of the p_1^{th} high thermal expansivity solid strut material and A_1 is the associated cross-sectional area of that beam member.

Similarly, an axial load of $\frac{F_i}{\sin(\omega_i)}$ acts on the inclined p_2^{th} member and hence, from standard beam theory, the axial deflection is:

$$\delta_{2a}^{(p_2)} = \frac{F_i L_{2i}^{(p_2)}}{E_2 A_2^{(p_2)} \sin(\omega_i)}$$

3.12

where E_2 is the Young's modulus of the p_2^{th} low thermal expansivity solid strut material and A_2 is the associated cross-sectional area.

The total deflection in i direction is then:

$$\delta_i = \delta_{1a}^{(p_1)} + \frac{\delta_{2a}^{(p_2)}}{\sin(\omega_i)} = \frac{F_i\left(\frac{L_{1i}^{(p_1)}}{2}\right)}{E_1 A_1^{(p_1)}} + \frac{F_i L_{2i}^{(p_2)}}{E_2 A_2^{(p_2)} \sin^2(\omega_i)}$$

3.13

and the corresponding axial strain:

$$\varepsilon_i = \frac{\delta_i}{\frac{L_{1i}^{(p_1)}}{2} + h_{2i}}$$

3.14

where h_{2i} is the height of the triangles and/or pyramids located in i direction of the unit cell formed from relatively low thermal expansivity materials.

The Young's modulus parallel to i is:

$$E_i = \frac{\sigma_i}{\varepsilon_i} = \frac{(N_i)\left[\left(\frac{L_{1i}^{(p_1)}}{2}\right) + h_{2i}\right]}{\frac{\left(\frac{L_{1i}^{(p_1)}}{2}\right)}{E_1 A_1^{(p_1)}} + \frac{L_{2i}^{(p_2)}}{E_2 A_2^{(p_2)} \sin^2(\omega_i)}} \frac{1}{A_i}$$

3.15

where N_i is a value required by the equilibrium and compatibility of unit cells under the axial loading in i direction. N_i is equal to 4 if a square based pyramid is located in i

direction of the unit cell. Note, the area A_i is the apparent area of the RVE normal to the loading axis.

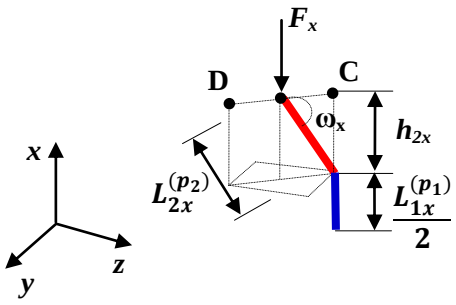

Figure 3.2. Beams and loads giving linear elastic stiffness in *i*=*x* direction of the unit cells by stretching mode.

In order to retain constant volume fraction of the high, v_{f1}, and low expansivity beam members, v_{f2}, across all geometries, the cross-sectional area of the beam members was calculated as follows:

$$A_1^{(p_1)} = \left[\frac{v_{f1}V}{\left(\sum_{p_1=1}^{n_1}\frac{L_1^{(p_1)}}{j_1^{(p_1)}}\right)}\right]\frac{1}{j_1^{(p_1)}} \qquad \textbf{3.16}$$

and

$$A_2^{(p_2)} = \left[\frac{v_{f2}V}{\left(\sum_{p_2=1}^{n_2}\frac{L_2^{(p_2)}}{j_2^{(p_2)}}\right)}\right]\frac{1}{j_2^{(p_2)}} \qquad \textbf{3.17}$$

where $A_1^{(p_1)}$ is the cross-sectional area of the p_1^{th} beam member (high thermal expansivity beam in dual-material structures), $A_2^{(p_2)}$ is the cross-sectional area of the p_2^{th} beam member (low thermal expansivity beam in dual-material structures), $V = hb^2$ is the volume of the RVE in Figure 3.1 and $j_1^{(p_1)}$and $j_2^{(p_2)}$ are terms equal to 1, 2 or 4 indicating full, half or quarter cross-sectional area, according to the number of shared neighbouring cells and n_1 and n_2 the total number of high and low thermal expansivity beam members in the unit cells.

Shear loading.

Symmetry present in the pyramid structures produces transverse isotropy, i.e. the transverse shear modulus of the structure is independent of orientation for any plane lying in the *i*, *j* or *k* axis parallel to the height of the triangles and/or pyramids located in that direction of the unit cell (Nye, 1957). Thus, for ease of calculation, these shear moduli were obtained considering the shear loading in ($\overrightarrow{AB}j$) plane in the structure formed from pyramid, see Figure 3.3. A finite element model was run, confirming the validity of the assumption.

By considering the deformation of only the inclined members, the transverse shear moduli, G_{ij}, were calculated by the method illustrated in Figure 3.3. A shear stress, τ, acting on the RVE, parallel to $\overrightarrow{AB}$ causes the p_2^{th} low thermal expansivity beams, acting in *j* direction, those of length $L_{2j}^{(p_2)}$, to deform axially. The load carried by the p_1^{th} (in-line) members is much smaller than the p_2^{th} members because of the boundary condition applied. Since the structure is under compatibility, the deformation of the structure is governed by

deformation of the p_2^{th} members. One set is shown in Figure 3.3 for unit cells formed from pyramids in *j* direction (all the structures proposed).

An axial load of $\frac{F_{\overline{AB}}}{\cos(\omega_j)}$ acts on the inclined p_2^{th} member and hence, from standard beam theory, the axial deflection is:

$$\delta_{2a}^{(p_2)} = \frac{F_{\overrightarrow{AB}} L_{2j}^{(p_2)}}{E_2 A_2^{(p_2)} \cos(\omega_j)}$$

3.18

The total deflection in $\overrightarrow{AB}$ direction is then:

$$\delta_{\overrightarrow{AB}} = \frac{\delta_{2a}^{(p_2)}}{\cos(\omega_j)} = \frac{F_{\overrightarrow{AB}} L_{2j}^{(p_2)}}{E_2 A_2^{(p_2)} \cos^2(\omega_j)}$$

3.19

and the corresponding shear strain is:

$$\gamma = \frac{\delta_{\overrightarrow{AB}}}{h_{2j}}$$

3.20

where h_{2j} is the height of the triangles and/or pyramids located in *j* direction of the unit cell formed from relatively low thermal expansivity materials.

The shear modulus in *i*-*j* plane is:

$$G_{ij} = G_{\overrightarrow{AB}j} = \frac{\tau}{\gamma} = \frac{(N_{ij})[h_{2j}]}{\frac{L_{2j}^{(p_2)}}{E_2 A_2^{(p_2)} \cos^2(\omega_j)}} \frac{1}{A_j}$$

3.21

where N_{ij} is a value required by the equilibrium and compatibility of unit cells under the shear loading in *i*-*j* plane. N_{ij} is equal to 2 if a square based pyramid is located in *j* direction of the unit cell. Note, the area A_i is the apparent area of the RVE normal to the j axis.

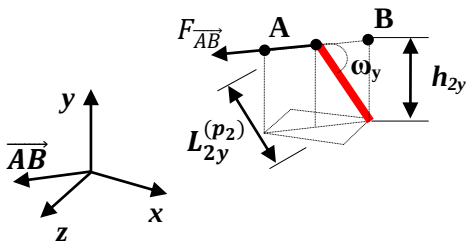

Figure 3.3. Beams and loads giving linear elastic shear in *(i-j)* = *(x-y)* plane of the unit cells by stretching mode.

These equations, Equations 3.11 to 3.21, can easily be applied to all the structures proposed herein. Approximations and assumptions in these expressions will increase the error as the complexity of the structures increases and especially as they differentiate from simple pyramidal or triangulated structures (i.e. Wallach structure). If desired, a simple correction could be made to allow for some extra complexity, for example by enforcing compatibility in the Aboudi II structure in the *x* axis between the additional in-line beams and the inclined beams.

As a relatively simple example, the equations for the Pyr structure are fully described in the following. The RVE for the Pyr structure is shown in detail in Figure 3.4. All the terms in Equations 3.15-3.21 are evaluated and substituted as functions of the base length, *b*, and height, *h*, of the unit cell, see Table 3.1, Figure 3.1 and Figure 3.4. In a similar manner, equations can be described for all the structures proposed here or indeed elsewhere.

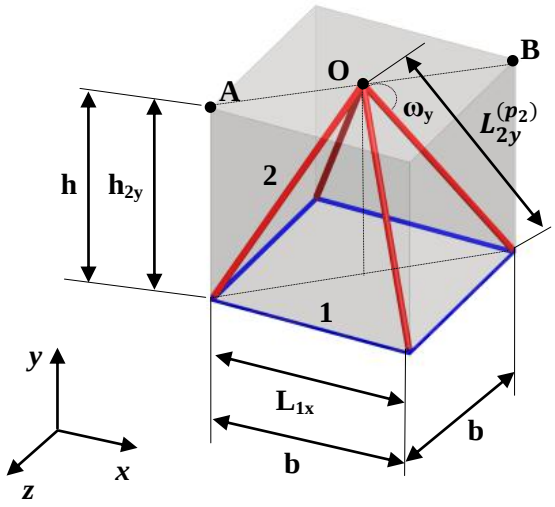

Figure 3.4. Pyr structure: RVE.

By substitution of Equations 3.16 and 3.17 in Equation 3.15, the Young's modulus in the *x* axis can be rewritten as:

$$E_x = \frac{\left((N_x)\left[\left(\frac{L_{1x}^{(p_1)}}{2}\right)+h_{2x}\right]\right)}{\left(\frac{\left(\frac{L_{1x}^{(p_1)}}{2}\right)}{E_1\left\{\left[\frac{v_{f1}V}{\left(\sum_{p_1=1}^{n_1}\frac{L_1^{(p_1)}}{j_1^{(p_1)}}\right)}\right]\frac{1}{j_1^{(p_1)}}\right\}}+\frac{L_{2x}^{(p_2)}}{E_2\left\{\left[\frac{v_{f2}V}{\left(\sum_{p_2=1}^{n_2}\frac{L_2^{(p_2)}}{j_2^{(p_2)}}\right)}\right]\frac{1}{j_2^{(p_2)}}\right\}\sin^2(\omega_x)}\right)}\frac{1}{(bh)}=\frac{E_1 v_{f1}}{2}$$

3.22

where, considering that no low expansivity beam members have any component in this axis, they can be assumed not to contribute to stiffness, hence, all terms with subscript 2 can be neglected. The appropriate substituted parameters' values were as $N_x = 2$ (due to compatibility and equilibrium); $L_{1x}^{(p_1)} = b$, $\sum_{p_1=1}^{n_1}\frac{L_1^{(p_1)}}{j_1^{(p_1)}} = b$ and $j_{1x}^{(p_1)} = 4$ as required by the

geometry of the unit cell and its tessellation (quarter cross-sectional area corresponding to $j_{1x}^{(p_1)} = 4$). In a similar manner, the modulus in *z* direction can be derived because of symmetry.

By substitution of Equations 3.16 and 3.17 in Equation 3.15, the Young's modulus in the *y* axis can be rewritten as:

$$E_y = \frac{\left((N_y)\left[\left(\frac{L_{1y}^{(p_1)}}{2}\right) + h_{2y}\right]\right)}{\left(\frac{\left(\frac{L_{1y}^{(p_1)}}{2}\right)}{E_1\left\{\left[\frac{v_{f1}V}{\left(\sum_{p_1=1}^{n_1}\frac{L_1^{(p_1)}}{j_1^{(p_1)}}\right)}\right]\frac{1}{j_1^{(p_1)}}\right\}} + \frac{L_{2y}^{(p_2)}}{E_2\left\{\left[\frac{v_{f2}V}{\left(\sum_{p_2=1}^{n_2}\frac{L_2^{(p_2)}}{j_2^{(p_2)}}\right)}\right]\frac{1}{j_2^{(p_2)}}\right\}\sin^2(\omega_y)}\right)}\frac{1}{b^2} =$$

$$= E_2 v_{f2} sin^4\left(\arcsin\left(\frac{h}{\left(\frac{b^2}{2} + h^2\right)^{\frac{1}{2}}}\right)\right)$$

3.23

where, considering that no high expansivity beam members have any component in this axis, they can be assumed not to contribute to stiffness, hence, all terms with subscript 1 can be neglected. The appropriate substituted parameters' values were as $N_y = 4$ (due to compatibility and equilibrium); $h_{2y} = h$, $L_{2y}^{(p_2)} = \frac{h}{sin^2(\omega_y)}$, $\omega_y = \arcsin\left(\frac{h}{\left(\frac{b^2}{2}+h^2\right)^{\frac{1}{2}}}\right)$,

$\left(\sum_{p_2=1}^{n_2} \frac{L_2^{(p_2)}}{j_2^{(p_2)}}\right) = \left(4\frac{h}{sin^2(\omega_y)}\right)$ and $j_2^{(p_2)} = 1$ as required by the geometry of the unit cell and its tessellation (full cross-sectional area corresponding to $j_2^{(p_2)} = 1$).

By substitution of Equations 3.16 and 3.17 in Equation 3.21, the shear modulus in the *y* axis can be rewritten as:

$$G_{xy} = \frac{(N_{xy})[h_{2y}]}{\left(\frac{L_{2y}^{(p_2)}}{E_2\left\{\left[\frac{v_{f2}V}{\left(\sum_{p_2=1}^{n_2}\frac{L_2^{(p_2)}}{j_2^{(p_2)}}\right)}\right]\frac{1}{j_2^{(p_2)}}\right\}\cos^2(\omega_y)}\right)}\frac{1}{b^2}$$

$$= \frac{E_2 v_{f2}}{8} sin^2\left(2\arcsin\left(\frac{h}{\left(\frac{b^2}{2}+h^2\right)^{\frac{1}{2}}}\right)\right)$$

3.24

The appropriate substituted parameters' values were as $N_{xy} = 2$ (due to compatibility and equilibrium); $h_{2y} = h$, $L_{2y}^{(p_2)} = \frac{h}{sin^2(\omega_y)}$, $\omega_y = \arcsin\left(\frac{h}{\left(\frac{b^2}{2}+h^2\right)^{\frac{1}{2}}}\right)$, $\left(\sum_{p_2=1}^{n_2} \frac{L_2^{(p_2)}}{j_2^{(p_2)}}\right) = \left(4\frac{h}{sin^2(\omega_y)}\right)$ and $j_2^{(p_2)} = 1$ as required by the geometry of the unit cell and its tessellation (full cross-sectional area corresponding to $j_2^{(p_2)} = 1$).

3.3 Results

3.3.1 Numerical modelling

Thermal Expansivity.

Some general trends are illustrated here using data from only three unit cells (which were typical) for the sake of clarity. It is clear from the data shown in Figure 3.5a, 3.6b and 3.6c, that the internal architecture of the unit cells exerts in a very effective way to manipulate the trusses' thermal expansivity. Figure 3.5a, 3.5b and 3.5c show normalised CTE data for only three of the seven structures analysed herein for the sake of clarity. Generally, negative and near-zero CTEs in the *y* axis were found across the whole range of aspect ratios for all the structures proposed.

Elastic Properties

The aspect ratio of the unit cell has a marked effect upon the axial stiffness in the *y* axis, E_y, but less so in the other axes, see Figure 3.6a, 3.6b and 3.6c. The axial stiffness in the *y* axis was the same for monolithic and dual-material structures. For all structures, the internal angle ω_y is a function of the aspect ratio of the cell, h/b, but ω_x and ω_z remain unchanged as the aspect ratio changes (with 3Dstar the only exception). There is a notable difference in magnitude between axial stiffnesses in different structures in the *x* and *z* axes, and between some monolithic and dual-material configurations, see Figure 3.6a and 3.6c.

Generally, the shear modulus in *x*-*y* direction was the same for monolithic and dual-material structures, see Figure 3.7a, with the Pyr structure usually exhibiting somewhat larger moduli values than the Wallach and 3Dstar cells. Note that G_{zy} is similar to G_{xy} because of symmetry. The shear stiffness also has a marked sensitivity to the cell aspect

ratio. There is a pronounced maximum in the shear stiffness for all structures as the aspect ratio $h/b \rightarrow 0.7$ for structures with single pyramid architectures (e.g. Pyr), and $h/b \rightarrow 1.4$ for structures with double pyramid architectures (e.g. 3Dstar).

Poisson's ratio is also sensitive to the aspect ratio of the unit cell, more so in some geometries than others, see Figure 3.8a, 3.8b and 3.8c. Some geometries exhibited negative values of Poisson's ratio at low values of aspect ratio, a sometimes desirable property (Evans, 1991; Lakes, 1987). In several cases, the value of Poisson's ratio exceeds the upper bound for isotropy, i.e. 0.5, so such structures must be anisotropic.

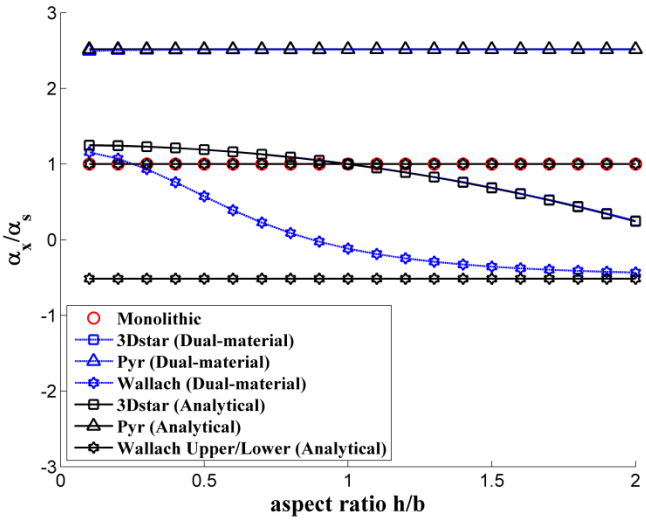

a)

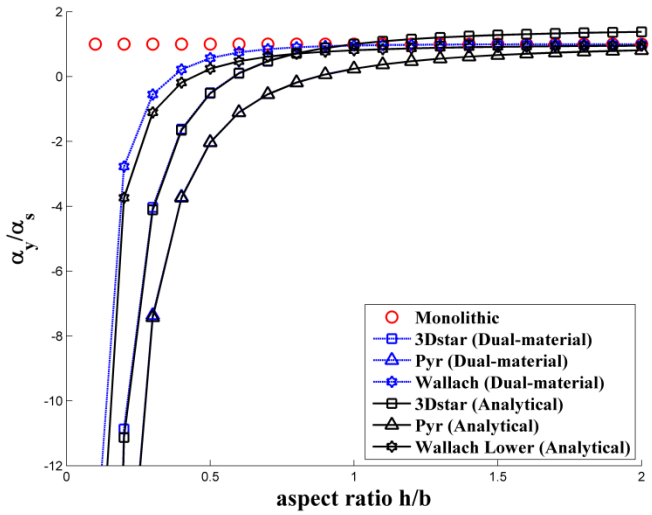

b)

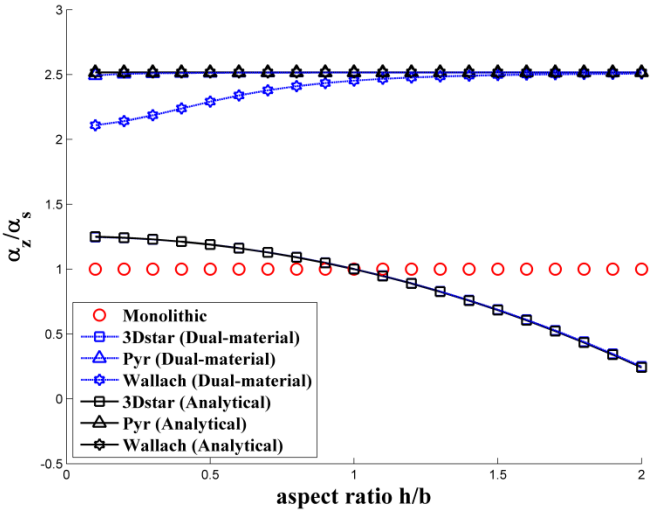

c)

Figure 3.5 (a, b and c). The predicted CTEs, in the *x*, *y* and *z* axes respectively, of 3Dstar, Pyr and Wallach, monolithic and dual-material form, normalised by the thermal expansivity of the low thermal expansivity material. Outputs from Table 3.3 for dual-material structures are reported.

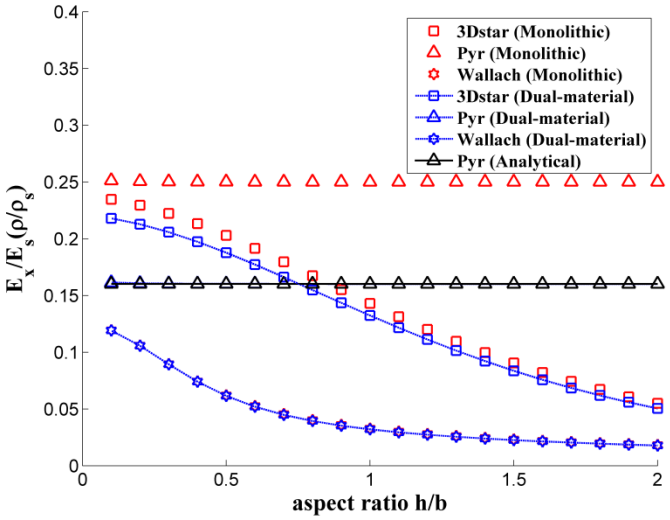
3Dstar (Monolithic)
Pyr (Monolithic)
Wallach (Monolithic)
3Dstar (Dual-material)
Pyr (Dual-material)
Wallach (Dual-material)
Pyr (Analytical)
$E_x/E_s(\rho/\rho_s)$
aspect ratio h/b
0
0.05
0.1
0.15
0.2
0.25
0.3
0.35
0.4
0.5
1
1.5
2

a)

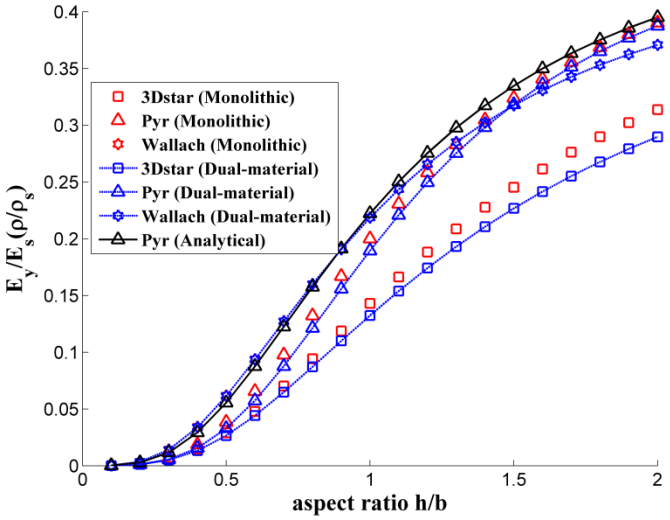
3Dstar (Monolithic)
Pyr (Monolithic)
Wallach (Monolithic)
3Dstar (Dual-material)
Pyr (Dual-material)
Wallach (Dual-material)
Pyr (Analytical)
$E_y/E_s(\rho/\rho_s)$
aspect ratio h/b
0
0.05
0.1
0.15
0.2
0.25
0.3
0.35
0.4
0.5
1
1.5
2

b)

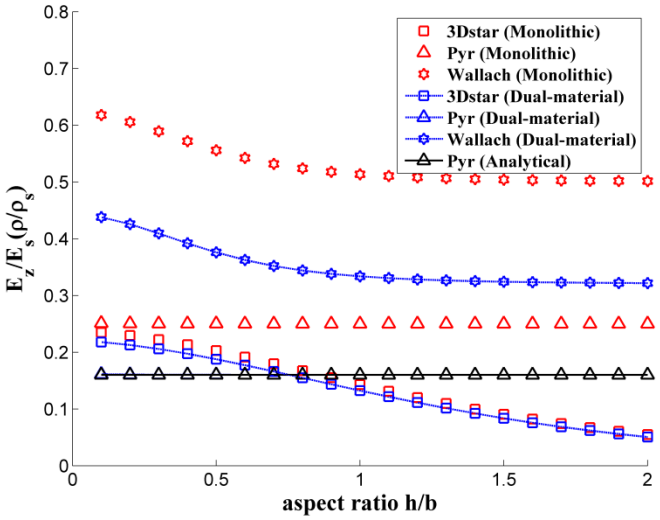

c)

Figure 3.6 (a, b and c). The predicted elastic moduli of 3Dstar, Pyr and Wallach, monolithic and dual-material form, normalised by the Young's modulus of the low thermal expansivity solid strut material and the relative density of the truss material. a) Young's modulus *x*-direction, b) Young's modulus *y*-direction and c) Young's modulus *z*-direction. Outputs from Equations 3.22-3.23 for dual-material Pyr are reported.

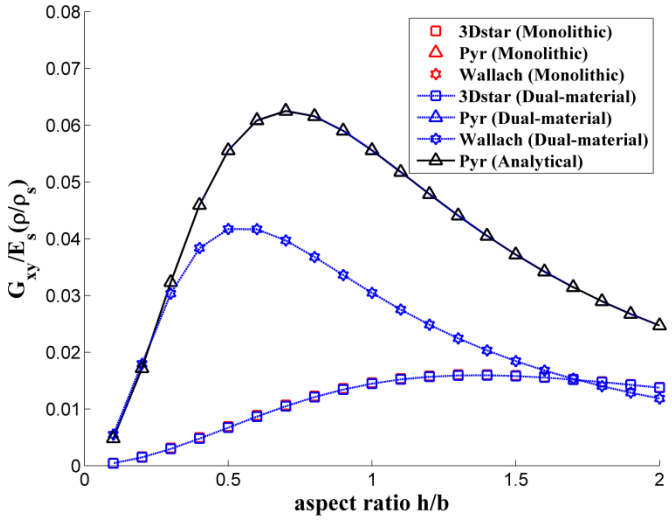

a)

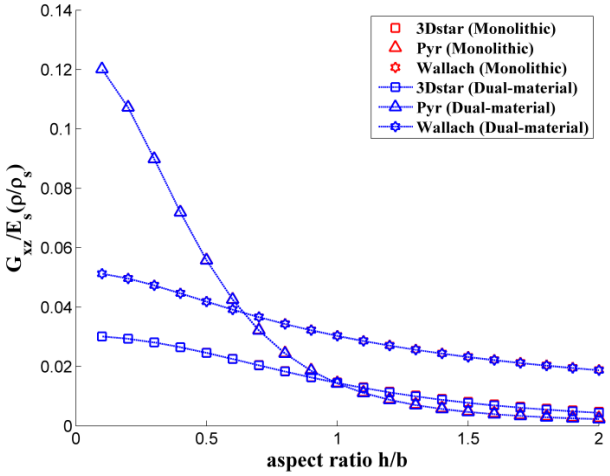

b)

Figure 3.7 (a and b). The predicted shear moduli of 3Dstar, Pyr and Wallach, monolithic and dual-material form, normalised by the Young's modulus of the low thermal expansivity material and the relative density of the truss material. a) *x-y* and *x-z* shear, and b) *z-y* shear. Output from Equation 3.24 for dual-material Pyr is reported.

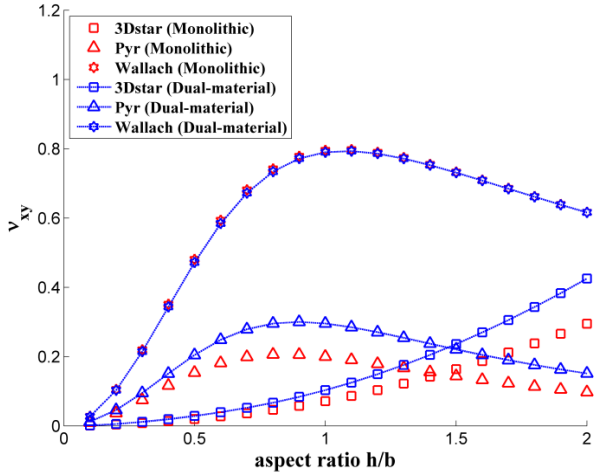
3Dstar (Monolithic)
Pyr (Monolithic)
Wallach (Monolithic)
3Dstar (Dual-material)
Pyr (Dual-material)
Wallach (Dual-material)
ν_{xy}
aspect ratio h/b

a)

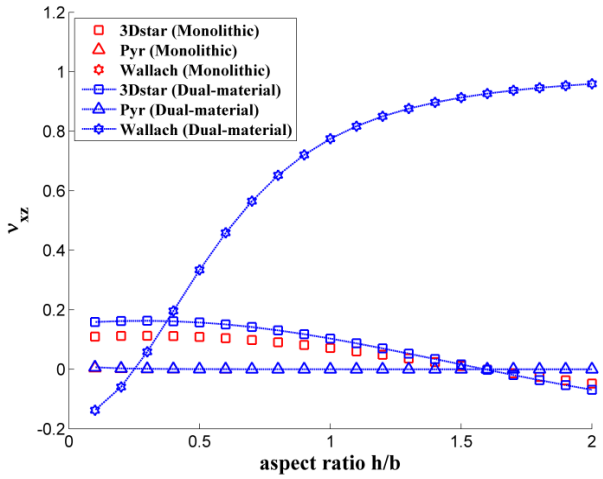
3Dstar (Monolithic)
Pyr (Monolithic)
Wallach (Monolithic)
3Dstar (Dual-material)
Pyr (Dual-material)
Wallach (Dual-material)
ν_{xz}
aspect ratio h/b

b)

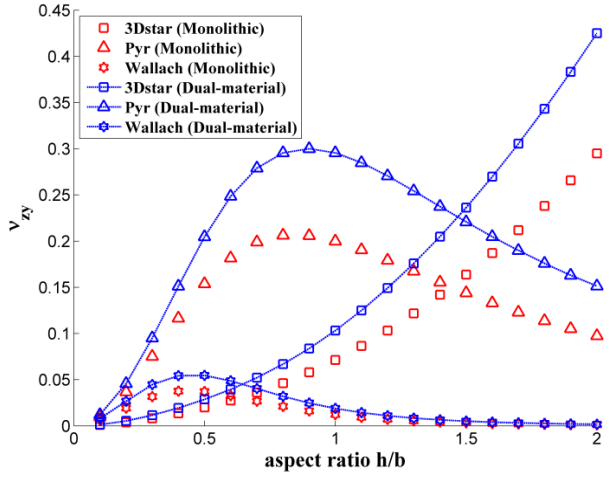

c)

Figure 3.8 (a, b and c). The predicted Poisson's ratio of 3Dstar, Pyr and Wallach, monolithic and dual-material form a) ν_{xy}, b) ν_{xz} and c) ν_{zy}.

The simplified figures of merit for CTE and elastic properties, i.e. effective isotropic volume averaged constants normalised to relative density, are shown in Figure 3.9 and Figure 3.10. The normalised effective moduli and the normalised effective thermal expansivity, α_{eff} of the seven truss structures is shown in Figure 3.9a, 3.10a and 3.10b as a function of the aspect of the unit cells, *h/b*. In general, the monolithic versions are stiffer than the dual-material configurations, and the square based pyramid (Pyr) performs well over most aspect ratios (Figure 3.9b and 3.9c). Highest stiffnesses are obtained with aspect ratios of higher than 1, and with aspect ratios of either 0.7 or 1.4 for single or double pyramidal structures.

The monolithic structures exhibit a range of axial and shear stiffnesses though of course do not vary in CTE, Figure 3.10a and 3.10b. The absolute values of these stiffnesses are marginally higher than for the dual-material configurations. There is a clear fall-off in effective stiffness for the dual-material configurations as the effective CTE decreases.

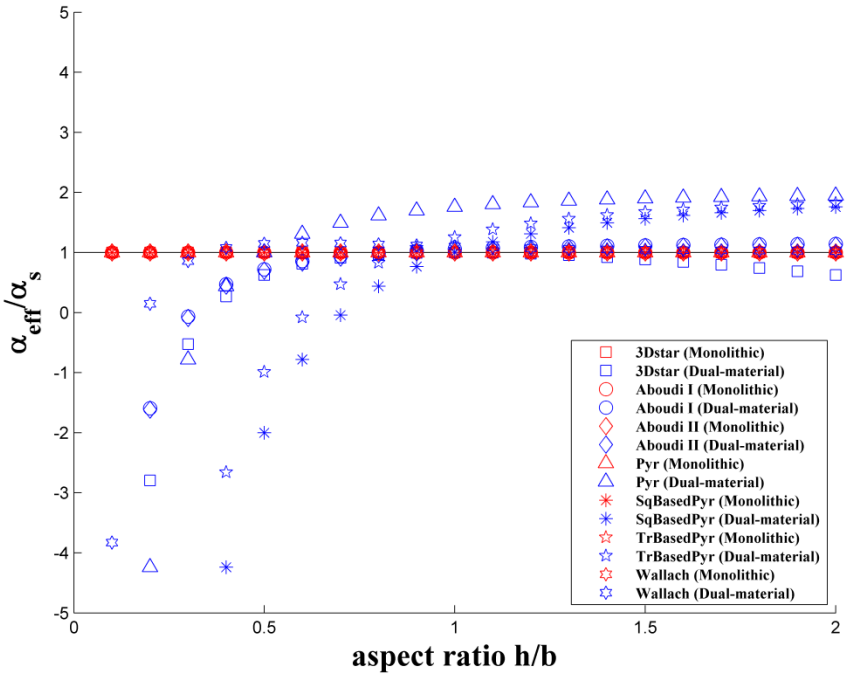
α_{eff}/α_s
aspect ratio h/b
3Dstar (Monolithic)
3Dstar (Dual-material)
Aboudi I (Monolithic)
Aboudi I (Dual-material)
Aboudi II (Monolithic)
Aboudi II (Dual-material)
Pyr (Monolithic)
Pyr (Dual-material)
SqBasedPyr (Monolithic)
SqBasedPyr (Dual-material)
TrBasedPyr (Monolithic)
TrBasedPyr (Dual-material)
Wallach (Monolithic)
Wallach (Dual-material)

a)

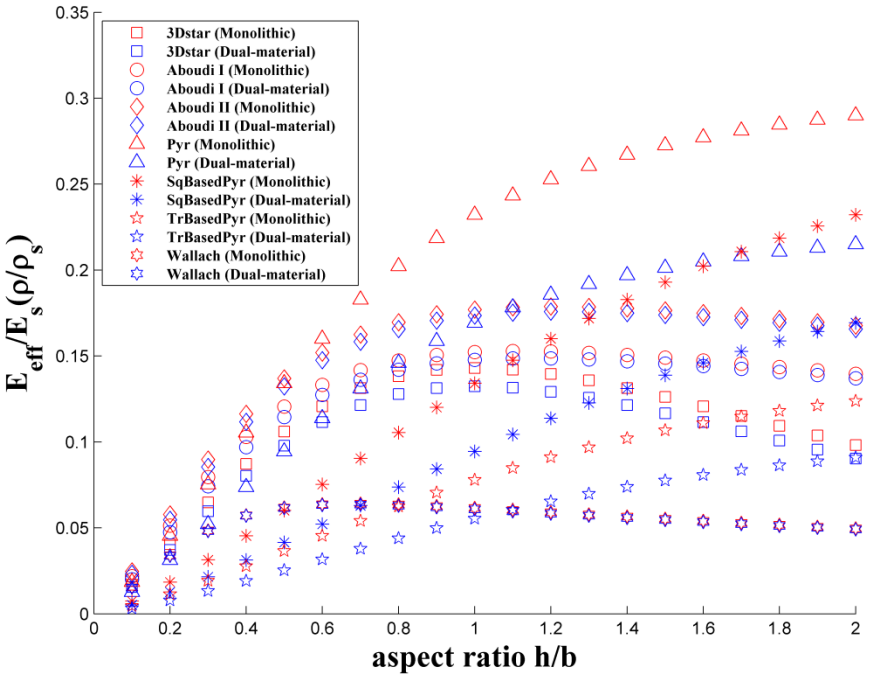
$E_{eff}/E_s(\rho/\rho_s)$
aspect ratio h/b
3Dstar (Monolithic)
3Dstar (Dual-material)
Aboudi I (Monolithic)
Aboudi I (Dual-material)
Aboudi II (Monolithic)
Aboudi II (Dual-material)
Pyr (Monolithic)
Pyr (Dual-material)
SqBasedPyr (Monolithic)
SqBasedPyr (Dual-material)
TrBasedPyr (Monolithic)
TrBasedPyr (Dual-material)
Wallach (Monolithic)
Wallach (Dual-material)

b)

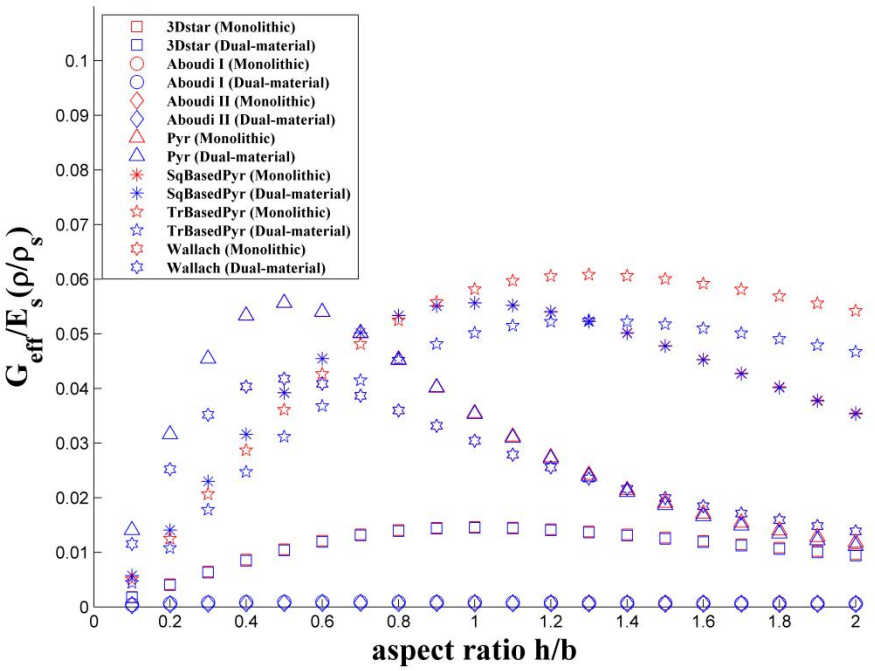

c)

Figure 3.9 (a, b and c). Effective properties using generalised mean; a) Effective CTEs vs. *h/b*; b) Effective Young's modulus vs. *h/b*; c) Effective Shear modulus vs. *h/b*.

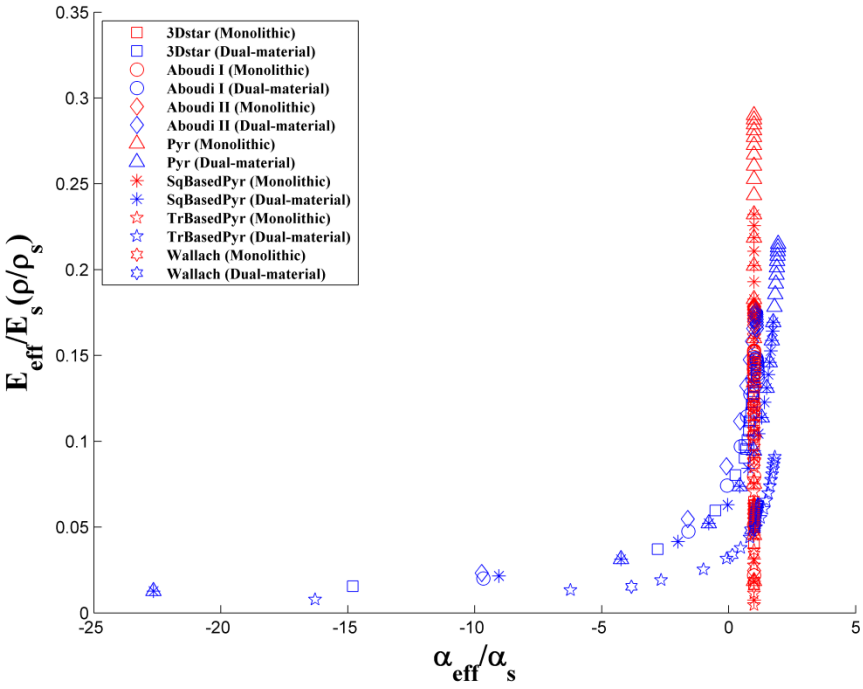

a)

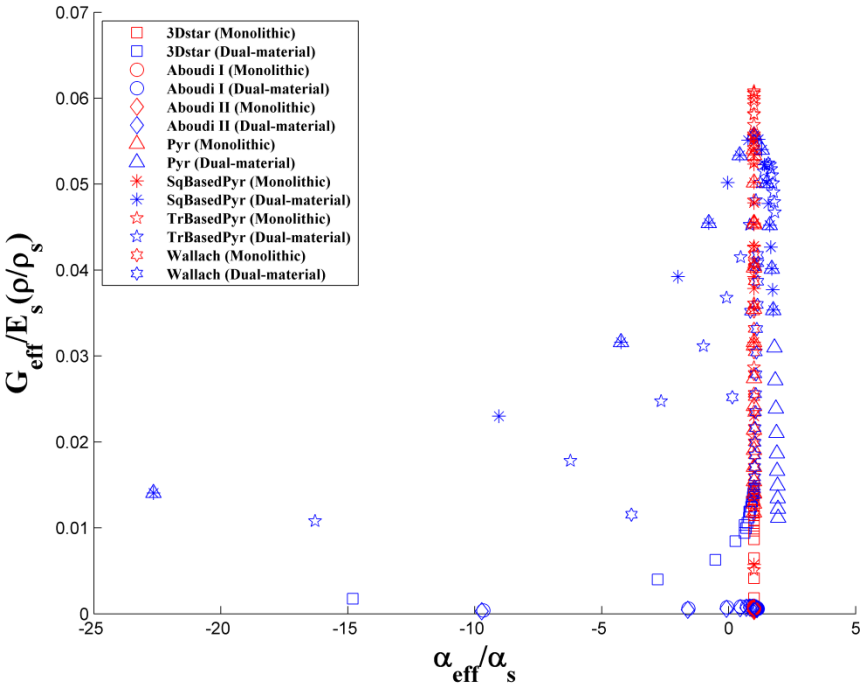

b)

Figure 3.10 (a and b). Effective properties using generalised mean; a) Effective Young's modulus vs. α_{eff}; b) Effective Shear modulus vs. α_{eff}.

3.3.2 Validation

Wallach and Gibson (2001) studied the elastic properties of one particular monolithic 3D truss, making analytical, FE models and experimental measurements, as a function of the aspect ratio of the unit cell. Their unit cell is studied, and their modelling and experimental results are compared with the current predictions for the same monolithic structure over a range of unit cell aspect ratios. Results for the same structure in dual-material form are also shown (aluminium and titanium beams), see Figure 3.11 to 3.14. The data for the monolithic configuration completely overlap Wallach and Gibson's results, supporting the FE models herein.

Negative CTEs are present in some dual-material unit cells, specifically those with aspect ratios, *h/b*, between 0.2 and 0.7, see Figure 3.11. The maximal negative value is at *h/b* = 0.7, which corresponds to a 60% reduction in CTE vs. the monolithic configuration at the same relative density. Corresponding increases in CTEs in orthogonal axes, of between 80-100% vs. the monolithic version, are seen in Figure 3.11. Figure 3.12 shows the predicted axial elastic moduli (E_x, E_y and E_z) plotted as a function of the aspect ratio, *h/b*, of the unit cell. There is no stiffness penalty for the dual-material configurations in *x* and *y* axes vs. the monolithic versions, though there is in the *z* axis. There is a penalty between 25% and 30% in terms of elastic moduli in *z* direction, as reported in Figure 3.12. In summary, there is at least one axis in all of these unit cells in which there is a reduction in CTE but no reduction in stiffness, though penalties are incurred in the other axes in the form of reduced stiffness or increased CTE. Figure 3.13 and Figure 3.14 show that there is no penalty for a reduction in CTE, in terms of shear stiffness and Poisson's ratio in any loading direction.

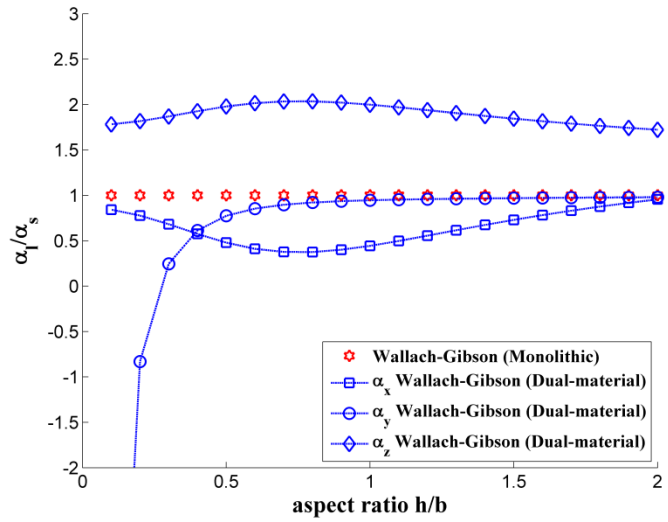

Figure 3.11. The predicted thermal expansivity of Wallach-Gibson planar truss material, monolithic and dual-material form, normalised by the thermal expansivity of the low thermal expansivity material.

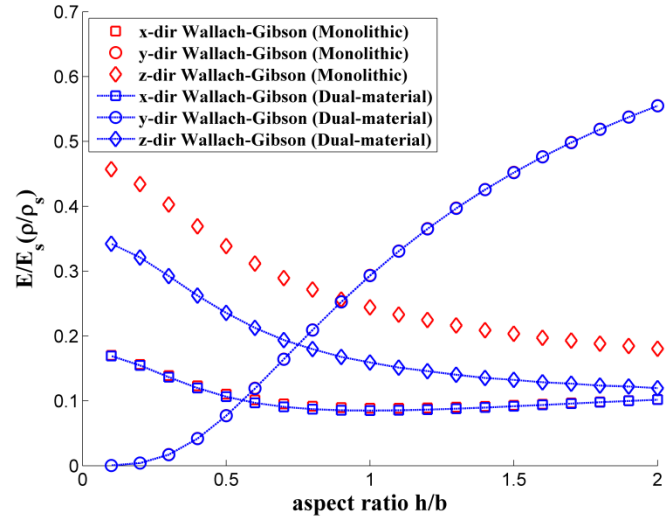

Figure 3.12. The predicted axial elastic moduli of Wallach-Gibson planar truss material, monolithic and dual-material form, normalised by the Young's modulus of the low thermal expansivity solid strut material and the relative density of the truss material.

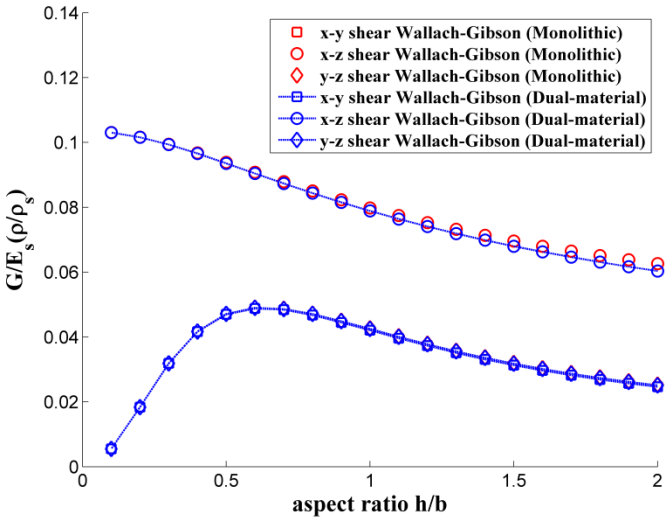

Figure 3.13. The predicted shear moduli of Wallach-Gibson planar truss material, monolithic and dual-material form, normalised by the Young's modulus of the low thermal expansivity solid strut material and the relative density of the truss material.

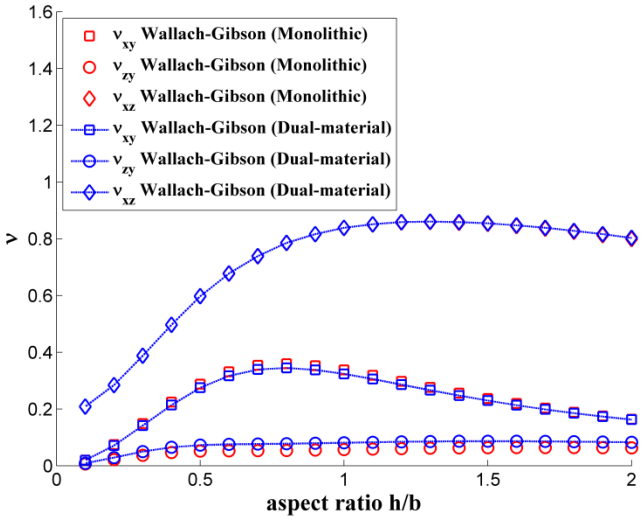

Figure 3.14. The predicted Poisson's ratios of Wallach-Gibson planar truss material, monolithic and dual-material form.

3.3.3 Analytical modelling

The results of the analytical modelling are given as the solid black lines in Figure 3.5 to 3.9. In all cases, there was very good agreement between the analytical and numerical models.

3.4 Discussion

The models were validated well vs. published experimental and theoretical data, see Figure 3.11 to Figure 3.14.

The explicit relations developed for CTE in these structures appear to be accurate, and indicate that CTE in such dual-material trusses is driven by the internal geometry of the unit cell (captured here as the unit cell's aspect ratio, h/b). In those axes where only one material is acting, CTE remains similar to that of that constituent material. For dual-material structures such as those explored here or in other studies (Miller et al., 2008a; Palumbo et al., 2011; Steeves et al., 2007), the differences between their CTEs, at, say, a specified value of aspect ratio, arise because internal angles are dissimilar and because of differing numbers of high and low expansivity beams with components acting along axes of interest. For example, at an aspect ratio of 0.5, the Pyr and Wallach structures have very different CTEs in the y axis, being - 2 and + 0.57, see Figure 3.5b and 3.9a. This is reflected by the relevant equations in Table 3.3, where, most significantly, one of the b^2/h^2 terms is 4 times larger for the Pyr structure, Equations (1.2) and (7.2). This difference arises because the internal architecture of the Pyr structure allows for a smaller ω_y angle at an apparent density. It can be concluded that for a given apparent density, CTE is reduced maximally by a structure with small ω_i angles. The same behaviour, but in different magnitude, can be seen for the effective volume averaged CTEs, see Figure 3.9a. The volume averaged CTE in this sense is a figure of merit, describing the performance of the structure.

The axial stiffness of the dual-material structures is dominated by the contribution of axial deflection of upright members δ_{1a} (high thermal expansivity members) and inclined members δ_{2a} (low thermal expansivity members) in the direction of the considered loading

mode, Equation 3.15. Those structures which have no secondary material with a component in an axis, i.e. low thermal expansivity members do not contribute to the stiffness of the structure in that axis, tend to have their stiffness remain constant as aspect ratio varies, see Figure 3.6a, 3.6c and 3.9a and Equations 3.15 and 3.22. Those with a secondary material component, i.e. low thermal expansivity members, in which they do contribute to the stiffness of the structure, see a change in axial stiffness as aspect ratio changes, see Figure 3.6b, 3.9b and Equations 3.15 and 3.23.

The reduced stiffness between some structures in dual-material and monolithic forms is because of the presence of an inherently lower stiffness (and higher expansivity) material. The differences in stiffness seen among the monolithic structures and among the dual-material structures arise because of some of their different number of beam members. Structures with more beam members have smaller absolute beam thicknesses than those with fewer beam members for the same apparent density and ω_i angles, see Equations 3.16 and 3.17, where the terms are $\left(\sum_{p_1=1}^{n_1} \frac{L_1^{(p_1)}}{j_1^{(p_1)}}\right) \approx n_1 L_1^{(p_1)}$ and $\left(\sum_{p_2=1}^{n_2} \frac{L_2^{(p_2)}}{j_2^{(p_2)}}\right) \approx n_2 L_2^{(p_2)}$ with n_1 and n_2, respectively, the total numbers of high thermal expansivity and low thermal expansivity beam members. That is, $A_1^{(p_1)}$ and $A_2^{(p_2)}$ terms in Equations 3.11-3.24 are generally smaller for structures with larger numbers of beams. It can be concluded that structures with fewer beams will be axially stiffer than those with more beams for a given apparent density and ω_i angles, see Table 3.1 and Figure 3.1, Figure 3.6 and Figure 3.9b and 3.10a. For most of these structures, the stiffness in the *y* axis is similar between monolithic and dual-material configurations because only the low expansivity beams have components acting in this axis, with some exceptions, e.g. 3Dstar, which has components of low and high expansivity beams in all axes, see Table 3.1 and Figure 3.1.

Shear stiffness is largely unaffected by the dual-material configuration, in both *x*-*y* and *x*-*z* planes. The structures are fully triangulated and symmetrical and thus the stretching mode is predominant, as confirmed by Ashby (2006) and Deshpande and Fleck (2001). In these planes for the configurations in Table 3.1, the high thermal expansivity beams generally carry only a relatively small axial load when the structure is loaded in shear, as compared to the low thermal expansivity beams which carry larger axial loads, Figure 3.7a, 3.9c and 3.10b. As can be seen in Equation 3.21, the shear stiffness is a sine squared function of the angle ω_i, and so shear stiffnesses for specific planes exhibit peaks at aspect ratios of either 0.7 or 1.4, see Figure 3.7a. Similar patterns, if less marked, are seen in the effective isotropic shear modulus, see Figure 3.9c.

Shear in the *x*-*z* plane follows all the considerations reported for shear in the *x*-*y* plane because all the structures are pyramidal or triangulated in general in the *x* and *z* directions. Equation 3.21 can easily be rearranged for the shear in the *x*-*z* plane by removing the dependency upon the unit cell height, *h*, see Table 3.1, and Figure 3.1 and 3.7. The behaviour of the Pyr and PyrBased structures in the *x*-*z* plane in terms of shear is bending dominated in both the monolithic and dual-material configurations because the base of the pyramid is non-triangulated, see Figure 3.7b and 3.9c, hence, the much lower shear stiffness in the *x*-*z* plane for the Pyr and PyrBased structures. General equations are not reported for these cases. Triangulation of the pyramid base can be accomplished by introducing a diagonal member across the base.

For the sake of completeness, Poisson's ratio is shown in Figure 3.8a, 3.8b and 3.8c. The results are consistent with the axial strains calculated by FE models. It is worth

mentioning that the Wallach structure in an infinite three-dimensional array can show negative Poisson's ratio values for relatively low values of the aspect ratio, *h/b*.

Figure 3.9 and 3.10 demonstrate the strong dependence between the elastic properties, the thermal expansivity, and the aspect ratios of the unit cells for the seven structures herein. The relations between elastic moduli and the thermal distortion show how, generally, higher moduli are associated with monolithic configurations, but that these structures are constrained to have CTEs similar to the constituent material, see Figure 3.10a and 10b. The dual-material configurations can also exhibit high stiffnesses, if lower in absolute terms than the monolithic, but with the advantage of CTEs not bound to those of either constituent material. Such structures do suffer large penalties in stiffness if their CTE is reduced substantially from either constituent material. Of the structures examined, the SqBasedPyr truss offered the best combination of near-zero CTE and high stiffness, with a normalised effective CTE equal to $\alpha_{eff} \approx 0$ and the normalised effective moduli equal to $E_{eff} \approx 0.06$ and $G_{eff} \approx 0.055$ for an aspect ratio of $h/b = 0.7$.

Periodic structures in the form of lattices and/or truss-like structures exhibiting reduced or near-zero CTE have been proposed, in-line with past literature (Grima et al., 2007; Lakes, 1996, 2007; Miller et al., 2008a; Palumbo et al., 2011; Sigmund and Torquato, 1996, 1997; Steeves et al., 2009; Steeves and Evans, 2011; Steeves et al., 2007). All of these structures use dual materials to drive reduced or zero thermal expansion behaviour. The current analysis permits the prediction of approximate thermal and mechanical properties of stretch-dominated triangulated structures (Equations 1.1 to 7.3, and 3.11 to 3.24), forming a guideline of sorts for the design of such structures. These equations do not predict properties for bending-dominated structures (Jefferson et al., 2009;

Lakes, 1996, 2007; Sigmund and Torquato, 1997), which are not triangulated and therefore are much less stiff.

3.5 Conclusion.

A parametric study was undertaken on seven published 3D truss geometries, with and without dual-material configurations, exploring how the internal geometry of the truss and the resulting thermal expansivity and elastic properties are related. Approximate explicit relations were developed, describing the properties with respect to the internal geometry of the truss structures, see Equations in Table 3.3 and (1.1) to (7.3), and 3.11 to 3.24, which are shown to be capable of predicting patterns of behaviour between different geometries, see Figure 3.5-3.8. It is shown that all of these structures can exhibit very large changes in CTE in dual-material configuration, Figure 3.5 and 3.9a, 3.10a and 3.10b. Maximal stiffness is achieved by engendering a larger internal angle ω_i and minimising the number of high expansivity beams (which are inherently more compliant than the low expansivity beams), see Figure 3.6 and 3.7, Figure 3.9b and 3.9c. Reduction in CTE always incurs a penalty in terms of axial stiffness (see Figure 3.6, and Figure 3.9b and 3.10a) but not in shear stiffness (see Figure 3.7, and Figure 3.9c and 3.10b), on an equal volume fraction (or apparent density) basis. The extent of this penalty is positively linked to the required reduction in CTE, see Figure 3.10a. Some structures can exhibit negative Poisson's ratios despite not having re-entrant architectures, see Figure 3.8b.

If the performance requirement for a truss is near-zero thermal expansivity and high stiffness, the SqBasedPyr truss offers the best performance over a large range of aspect ratios.

4 COMBINATORIAL DETERMINATION OF 3D STRUCTURES: THERMAL DISTORTION AND ELASTIC PROPERTIES

4.1 Introduction

Following the findings in Chapters 2 and 3, the aim of this chapter is to extend that work and generate truss structures with optimal combinations of properties, and to fill the solution space of possible truss designs, in terms of thermomechanical properties of the geometries proposed, quantifying performance, limitations, and penalties compared to monolithic structures or competing concepts. New designs, showing altered thermal expansivity, and known designs from the literature were explored.

A simple and alternative computational combinatorial approach was proposed to generate truss geometries similar to those used in light-weight aerospace and structural applications. The code was developed in Ansys parametric design language (APDL) which is a language running within the Ansys finite elements code. It was intended that the code would iteratively define and describe all possible 3D structures, within user-defined bounds on geometry and connectivity.

More complex numerical methods have been investigated by previous researchers to enumerate, without repetition, all non-crossing rigid bar-and-joint frameworks by graph theory (Avis et al., 2008) or to find free-form tensegrity structures (Tran and Lee, 2010), for instance. Other approaches to truss optimisation include genetic or evolutionary algorithms. This chapter presents a computational approach to generate truss structures from user-defined nodal connectivity and number of beams. This approach permits the generation of known and alternative truss structures by the use of a combinatorial selection

of nodes. Furthermore, the code also permits parametric simulation of all the possible solutions, in terms of thermomechanical properties for these structures in both monolithic and dual-material configuration.

Since all the structures generated were considered as consisting of two phases in both monolithic and dual-material configuration, all the possible combinations of phases were parametrically explored. To each phase, similar physical properties (monolithic configuration) or different properties (dual-material configuration) were associated. The influence of the aspect ratio of the RVE, which is a function of all internal angles, was also parametrically explored.

Solutions were compared with existing truss geometries, proposed as efficient structures in the literature (Aboudi and Gilat, 2005; Miller et al., 2008a; Queheillalt et al., 2008; Wadley, 2006; Wallach and Gibson, 2001). Several structures were, thus, performance ranked here. The amount of data generated by the numerical approach was further post-processed by commercial software as MATLAB (the MathWorks, Inc.) to provide new designs, combining altered thermal expansivity and maximised mechanical properties. A rigorous and consistent comparison between new topologies generated and those in the literature must be carried out in order to assess whether the new designs ever generate enhanced solutions in relation to those in the literature. This chapter does not provide full comparison between the new topologies and those presented in the past literature. Therefore, this chapter cannot prove that the new topologies have absolute enhanced properties compared to competitors. However, this research presents preliminary comparisons and further investigations could form part of future research work.

4.2 Methodology

4.2.1 Geometries generation code

Ansys parametric design language (ADPL) was employed to generate truss structures in the monolithic and dual-material configurations and to simulate their thermomechanical behaviour, exploring all the possible solutions within user-defined constraints (nodal connectivity and number of beams within a quarter or an eighth of the Repetitive Volume Element, RVE).

The code implemented can be divided into the following main steps:

i. Monolithic and dual-material generation of geometries of dual-phase truss structures;
ii. Finite elements modelling of CTEs and elastic constants.

A generic parent Representative Volume Element (RVE), consisting of 27 seed nodes, was defined, see Figure 4.1. Seven initial geometrical base truss structures were defined within this parent RVE by connecting a number of seed nodes with beam members. These seven truss structures were similar to those proposed in Chapter 3 and found in the literature (Aboudi and Gilat, 2005; Miller et al., 2008a; Queheillalt et al., 2008; Wadley, 2006; Wallach and Gibson, 2001). In order to reproduce the initial geometrical base truss structures (for instance to reproduce the truss structures presented in past studies), in some cases, a few additional seed nodes were required.

These seven initial geometrical base truss structures were then assessed for symmetry. This assessment allows the simplification of the initial geometrical base truss structures, reducing them to a quarter (for instance when the initial base truss structure has

two planes of symmetry) or an eighth (for instance when the structure has three planes of symmetry). This simplification allows the generation of a new list of nodal connectivities (the number of beams connected to a node) and a new list of the total number of beam members, which refer to the quarter or the eighth of the initial geometrical base truss structures. These new defined lists are necessary in order to generate new designs besides the initial geometrical base truss structures. Satisfying these new lists of nodal connectivities and number of beams, the code is always capable of generating the initial geometrical base truss structures and all the other possible new truss structures. For some initial geometrical base truss structures, such as pyramid, there is only the initial geometrical base truss structure. For some others, such as the Wallach initial geometrical base truss structure, there are a number of other possible new truss structures. These new alternative truss structures had a similar number of beams and connectivities as the initial parent trusses.

Without these constraints, i.e. of matching the nodal connectivities and the number of beams, the number of possible truss structures is infinite. For each of these truss structures generated (33 in this study), each beam member was iteratively ascribed the property of being either phase 1 or phase 2 (representing material types). For dual-material configurations, the properties of each phase (elastic and CTE) were different, and for monolithic, they were identical. The value of the phase property was varied iteratively for each member in each of the truss structures for the dual-material configurations. In addition, for each truss structure generated and for each configuration of phases, the aspect ratio of the truss structure was also systematically varied.

The combinatorial process was as follows.

Seven initial geometrical base truss structures were considered, the repeating unit cells for these truss lattices are shown in Table 4.1. The structure-finding process is not restricted to just the seven examples proposed but it can be applied to every 2D/3D initial geometrical base truss structure. Herein, the seven three-dimensional structures were chosen because they were typical of many such truss lattices, as already mentioned in Chapter 3. Note that the *x*, *y* and *z* axes of all the proposed structures are similar to that shown in Figure 4.1 for the RVE.

The set of nodal connectivity, the number of beam members, and the symmetry constraints for each quarter or eighth of the initial geometrical base truss structures was named as 'type [N]', with N, ranging from 1 to 7 (arbitrary identification number associated with each initial geometrical base truss structure). See Table 4.2a and b.

Therefore, a quarter or an eighth of the final truss structures were combinatorially generated from the set of nodal connectivity and number of beam members of the quarter or the eighth of the initial geometrical base truss structures, 'type [N]'. Symmetry constraints of the quarter or the eighth of the initial geometrical base truss structures, 'type [N]', were also considered. The combinatorial generation consisted of generating the members of the structures by selecting two arbitrary non-identical nodes (among seed nodes and extra nodes) and connecting them by beam members. In order to generate a quarter or an eighth of the final truss structure from a particular 'type [N]', 10,000 iterations were performed to select two arbitrary non-identical nodes and to connect them. For each of the 10,000 iterations, nodal connectivity and the maximum number of members were checked to ensure that these imposed constraints, i.e. of matching the nodal connectivities and number of beams, were constantly verified. In order to scan all the possible combinations of nodes for generating one (a quarter or an eight of the initial geometrical base structure) or more

final structures from each 'type [N]', 1,500 iterations were performed, corresponding to the generation of potentially 1,500 different structures. The generated non-identical quarter or eighth of the final truss structures, which satisfied the set of nodal connectivities and number of beams, were retained. A convergence test was performed to ensure that all the possible combinations of nodes were explored and that all the possible quarter or eighth of the final truss structures were generated for each 'type [N]'. The convergence test was performed by constantly increasing the iterations. Iterations totalling 10,000 and 1,500, respectively, represented the asymptotic values.

The intersected beam members in the generated quarter or eighth of the final structure were further divided at their points of intersection by Boolean operations. In some cases, these operations resulted in higher number of members within the structures than that specified for each 'type [N]'. For each of these quarter or eighth of the final structures generated, each beam member within them was iteratively ascribed the property of being either phase 1 or phase 2. For each 'type [N]' structure generated, 500 different combinations of phases were attempted. A convergence test was performed in order to ensure that all the possible combinations of phases were explored. The number of iterations was constantly increased, with 500 iterations representing the asymptotic limit. It should be noted that for some 'type [N]' structures generated, the number of possible combinations of phases was largely less than the 500 attempted (e.g. the quarter of the final truss structure generated from 'type 4' allowed only 6 different combinations instead of 500 attempted). Phase 1 or phase 2 represented two different material types. For dual-material configurations, the properties of each phase (elastic and CTE) were different, and for monolithic, they were identical.

The structures generated at this point represent a quarter or an eighth of the final truss structures generated. The quarter or eighth of the final truss structures were finally tessellated to form the appropriate RVE of the final truss structures, following the symmetry constraints in Table 4.2a.

The next and final step of the code was the simulation of the thermomechanical behaviour of the RVE structure, considered as part of a two-dimensional infinite array. This is described in Section 4.2.2.

Figure 4.2 shows graphically, in a flow chart diagram, the procedure used to generate the final truss structures from nodal connectivity and the number of members, and the symmetry constraints. Also, it explains how to simulate their thermomechanical behaviour, as described in this section.

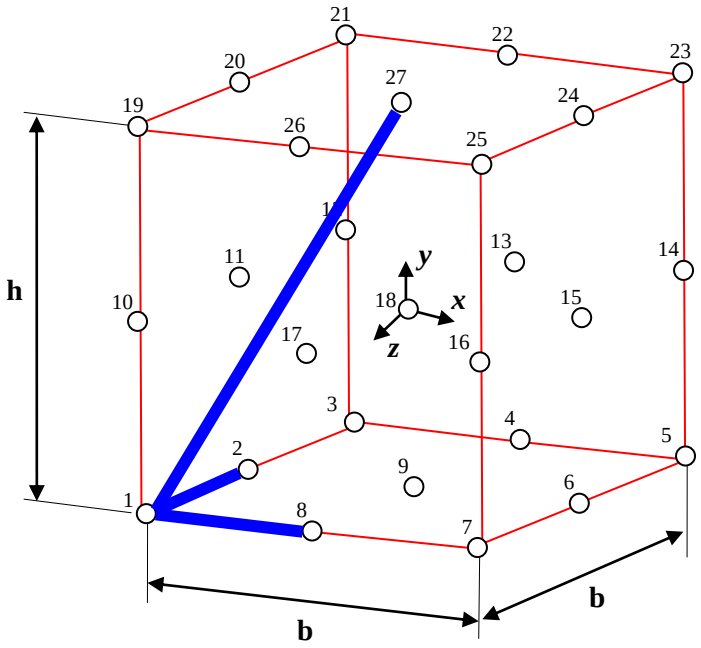

Figure 4.1. RVE and 'seed nodes' locations. Beam members connecting the 'seed nodes' are shown as an example (blue lines). The example reported in figure corresponds to 'type 4'.

	N=1 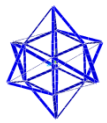		**N=2** 		**N=3** 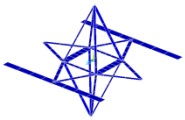		**N=4** 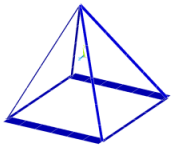
	N=5 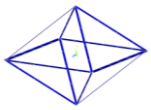		**N=6** 		**N=7** 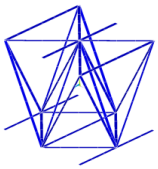		

Table 4.1. Seven initial truss structures, aspect ratio *h/b* = 1. *N* is an arbitrary number associated with each initial geometrical base truss structure to identify it.

type [N]							
N	**1**	**2**	**3**	**4**	**5**	**6**	**7**
sym	x/y/z	x/y/z	x/y/z	x/z	x/y/z	x/y	x/z
number of members	6	5	6	3	3	4	10
seed nodes	**connectivity**	**connectivity**	**connectivity**	**connectivity**	**connectivity**	**connectivity**	**connectivity**
1	-	-	-	3	-	-	1
2	-	-	-	1	-	-	4
3	-	-	-	-	-	-	-
4	-	-	-	-	-	-	-
5	-	-	-	-	-	-	-
6	-	-	-	-	-	-	-
7	-	-	-	-	-	-	-
8	-	-	-	1	-	-	4
9	1	1	1	-	1	2	1
10	-	-	1	-	3	3	-
11	1	1	1	-	1	-	-
12	-	-	-	-	-	-	-
13	-	-	-	-	-	-	-
14	-	-	-	-	-	-	-
15	-	-	-	-	-	-	-
16	-	-	-	-	-	-	-
17	1	1	2	-	1	1	-
18	-	-	-	-	-	-	-
19	-	-	-	-	-	-	4
20	-	-	-	-	-	-	1
21	-	-	-	-	-	-	-
22	-	-	-	-	-	-	-
23	-	-	-	-	-	-	-
24	-	-	-	-	-	-	-
25	-	-	-	-	-	-	-
26	-	-	-	-	-	-	1
27	-	-	-	1	-	-	4

a)

type [N]									
N	**1**			**2**			**3**		
extra seed nodes	**connectivity**			**connectivity**			**connectivity**		
28	-			1			1		
	x	*y*	*z*	*x*	*y*	*z*	*x*	*y*	*z*
	-b/6	*0*	*0*	*-b/6*	*0*	*0*	*-b/6*	*0*	*0*
29	1			5			5		
	x	*y*	*z*	*x*	*y*	*z*	*x*	*y*	*z*
	-b/6	*0*	*+b/6*	*-b/6*	*0*	*+b/6*	*-b/6*	*0*	*+b/6*
30	1			1			1		
	x	*y*	*z*	*x*	*y*	*z*	*x*	*y*	*z*
	-b/6	*-h/6*	*0*	*0*	*0*	*+b/6*	*0*	*0*	*+b/6*
31	6			-			-		
	x	*y*	*z*	*x*	*y*	*z*	*x*	*y*	*z*
	-b/6	*-h/6*	*+b/6*	-	-	-	-	-	-
32	-			-			-		
	x	*y*	*z*	*x*	*y*	*z*	*x*	*y*	*z*
	0	*0*	*+b/6*	-	-	-	-	-	-
33	1			-			-		
	x	*y*	*z*	*x*	*y*	*z*	*x*	*y*	*z*
	0	*-h/6*	*+b/6*	-	-	-	-	-	-
34	-			-			-		
	x	*y*	*z*	*x*	*y*	*z*	*x*	*y*	*z*
	0	*-h/6*	*0*	-	-	-	-	-	-

b)

Table 4.2 (a and b). a) Set of nodal connectivity and number of beam members, and symmetry constraints for each quarter or eighth of the initial geometrical base truss structures within the generic parent Representative Volume Element (RVE); b) Connectivity and coordinates of the additional seed nodes required for 'type 1' , 'type 2' and 'type 3'.

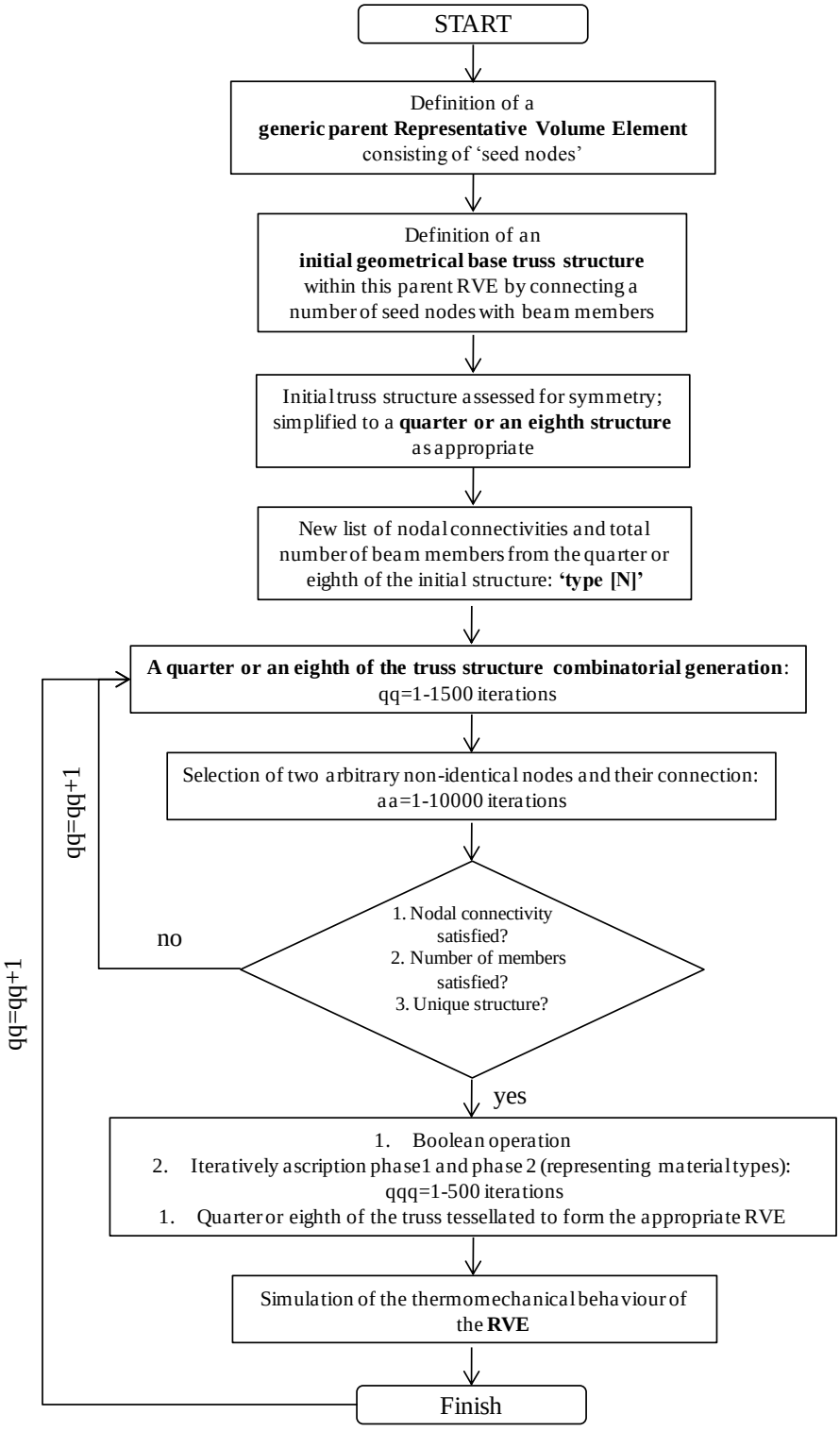

Figure 4.2. Flow chart diagram with the procedure to generate and solve RVE structures.

4.2.2 CTEs and elastic constant modelling

The elastic constants and the thermal distortion of the final truss lattices were calculated using the finite element (FE) method, in a similar way as that presented in Chapter 3. The internal angles and lengths of the unit cell of the lattice were allowed to vary in a parametric study and all lattices were considered in both monolithic and dual-material forms, noting that in monolithic form, the apparent Coefficient of Thermal Expansion, α, (CTE) of any monolithic lattice is similar to that of the constituent material, as mentioned in previous chapters. For each of the quarter or the eighth of the final truss structures, each beam member within them was iteratively ascribed the property of being either phase 1 or phase 2. All the possible arrangements of phases were explored by employing the code presented in Section 4.2.1, for both monolithic and dual-material configurations. Phase arrangements resulted in fully symmetric outcomes in all the generated final truss structures.

To aid comparison, the volume fraction of the solid component (i.e. the truss members) was kept constant across all cases, specifically, 0.6% of the total unit cell volume, as described in Chapter 3. This is an acceptable value for this type of structure.

The repeating unit cell for the initial truss lattices are shown in Table 4.1. Note that the x, y and z axes for all structures are similar to that shown in Figure 4.1 for the representative volume element (RVE).

The code was used to simulate the properties of both the dual-material truss lattices and their monolithic counterparts. For base truss structure, see Table 4.3; periodic boundary conditions were applied so that the cell behaved as if in an infinite three-dimensional array, following Wallach and Gibson (2001); in effect a representative volume element (RVE)

approach, see Figure 4.1. The unit cells have square bases of length, *b* and height of length, *h*. Note that tessellation, in an infinite three-dimensional array of some of these 3D trusses, would require reflection rather than translation ('type 4' and 'type 7' cases for instance, see Table 4.3). These structures tessellate by translation in the *x* and *z* axes but not in the *y* axis, as explained in Section 3.2.1. The three-dimensional unit cells were generated, meshed and solved for 20 iterations of each unit cell, in both monolithic and dual-material forms, and involving 3 axial and 3 shear deformations and 1 temperature field simulation. More than 1,000,000 simulations were run. For each beam member within the unit cell, three-dimensional elastic beam elements (specifically, 'beam4' in Ansys) were used, which had axial and flexure deformation capability.

Consistently with what was described in the previous chapter, Chapter 3, in the dual-material configurations, some beams were formed from relatively high thermal expansivity materials, phase 1, and some from lower thermal expansivity materials, phase 2. All the possible combinations of constituent material in individual beams were made so as to explore all the possible changes in thermal expansivity in all the dimensions, and to allow possible comparison with the results set out in Miller et al. (2008a) and Palumbo et al. (2011). In the monolithic material configurations, beams were also formed from, respectively, phase 1 and phase 2, however, identical physical properties were assigned to the two phases. The ascription of two different phases, phase 1 and phase 2, to each beam member within monolithic base truss structures permitted an iso-volume comparison between the monolithic structures and their dual-material counterparts.

As required by the unit cell approach, beam elements located in the unit cell faces and edges were shared between two or four other unit cells, as appropriate. For such beam

members, the cross-sectional area A and the second moment of area I were reduced to a half or quarter according to the number of shared neighbouring cells (two for faces and four for edges), as reported in Section 3.2.1. In order to retain a constant volume fraction of the phase 1 beam members, v_{f1}, and phase 2 beam members, v_{f2}, across all geometries, the cross-sectional area of the beam members was calculated, according to the Equations 3.16 and 3.17, developed in Chapter 3. A full overview of this approach is found in Chapter 3, Section 3.2.1.

Each beam member of the dual-material trusses was formed from one of two constituent materials, specifically titanium and aluminium, which have different inherent physical, mechanical and thermal expansivity properties, as shown in Table 3.2. These two materials were particularly selected because they do not present variability of the thermal expansivity over a temperature range of 73 K and 473 K. This temperature range is the one considered here, as it is common in applications where thermal stability is required.

The elastic moduli and apparent thermal expansivity were analysed as a function of the aspect ratio of the unit cell, h/b (see Figure 4.1). This ratio captures the details of the internal angles and of the member lengths of the unit cells. In order to permit a consistent and fair comparison between monolithic and dual-material configurations, and between different truss lattice geometries, the volume fraction of phase 1, v_{f1}, and phase 2 beam members, v_{f2}, i.e. 0.3% each, was kept constant in all models. The resultant overall relative density, ρ^* (sum of v_{f1} and v_{f2}) for all the structures in this study, was 0.006, in accordance with what was discussed in Chapter 3. The range of considered aspect ratios, h/b, was from 0.1 to 2.0, with an interval size of 0.1, being a recognised range for practical use (Wallach and Gibson, 2001).

In a similar way to the presentation in Chapter 3, nine independent elastic constants (E_i, G_{ij}, v_{ij}) were calculated for each unit cell, as required for a complete description of a structure (Hearmon, 1978; Wallach and Gibson, 2001). Different boundary conditions were applied for axial and shear loading modes, in a similar way to that presented in Section 3.2.1.

The Young's moduli, E_i, the Poisson's ratios, v_{ij}, and the shear moduli, G_{ij}, were calculated from Equations 3.1, 3.2 and 3.3, respectively. The apparent thermal expansivity values (CTEs) for the lattices were calculated in a similar way to that described in Section 3.2.1.

Data sets, i.e. some of the 9 elastic constants and 3 CTEs, are also given for a subset of the samples, which were typical of the range of behaviours.

To implement these structures as ultra-light sandwich constructions, out-of-plane Young's modulus and the out-of-plane shear modulus are the most important properties (Sypeck, 2005). In order to have a simple figure of merit for elastic and CTE performance for swift comparison between geometries and different concepts, elastic constants (E_y and G_{xy}) and the CTEs (α_y) were shown in comparison with the seminal benchmarks for performance, proposed by Wadley (2006) and Evans et al. (2001). The out-of-plane modulus was compared with the moduli of ideal stretch-dominated structures and of ideal bending-dominated structures, according to the expression:

$$\frac{E_i}{E_s} = \alpha_i \left(\frac{\rho}{\rho_s}\right)^n$$

4.1

with $\alpha_i = 1$ and n equal to 1 for ideal stretch-dominated structures and 2 for ideal bending-dominated structures, and $\frac{\rho}{\rho_s}$ the relative density, as reported in Ashby (2006).

The in-plane shear was compared with the shear modulus of the ideal stretch-dominated structures and of the ideal bending-dominated structures according to the expression:

$$\frac{G_{ij}}{E_s} = \alpha_{ij} \left(\frac{1}{2(1+\nu)}\right)\left(\frac{\rho}{\rho_s}\right)^n$$

4.2

with $\alpha_{ij} = 1$ and n equal to 1 for ideal stretch-dominated structures and 2 for ideal bending-dominated structures, and the Poisson's ration, ν, equal to 3/8, and $\frac{\rho}{\rho_s}$ the relative density, as reported in Ashby (2006).

Performance maps, in logarithmic scale, were presented to highlight all the possible performances obtainable for each 'type [N]' in the dual-material configuration. Monolithic structures were not presented since they showed similar trends of behaviour. CTEs were constrained to the unity and the properties investigated were found to be higher or similar in values, compared to dual-material structures. In particular, the trends between near-zero and/or positive CTEs and out-of-plane Young's modulus and out-of-plane shear modulus results are presented. Since negative values are not possible in logarithmic scale, negative CTEs are not presented. This does not alter the general trends found in the solution.

The ratio between Young's moduli vs. normalised values was also shown as a possible index of the potential high anisotropy of the structures proposed for each 'type [N]' case.

New designs were presented for thermo-responsive sandwich panel applications. Some innovative optimised solutions, showing high Young's and shear moduli, combined with negative thermal expansivity, near-zero and positive thermal expansivity, were extracted from the conducted parametric study. A MATLAB program (the MathWorks, Inc.) was used to post-process all the obtained data.

4.3 Results

4.3.1 Generated geometries

Results obtained by the developed code are presented for seven initial geometrical base truss structures, see Table 4.1, corresponding to seven 'type [N]' cases, as described in Section 4.2.1. From each 'type [N]' presented in Table 4.2a and b, the possible geometrically alternative structures were generated combinatorially. One unique truss structure, $N_i = 1$, was generated by specifying 'type 1', 'type 2', 'type 4', 'type 5' and 'type 6', substantially consisting of the initial geometrical base truss structure. Several geometrically alternative structures were generated from 'type 3' and 'type 7' cases, along with the initial geometrical base truss structure. 'Type 1', 'type 2', 'type 4', 'type 5' and 'type 6' cases do not offer the possibility to generate alternative truss structures because of the particular constraint, i.e. of matching the nodal connectivities and number of beams. Under this particular constraint, just the initial geometrical base truss structures can be generated for these 'type [N]' cases. 'Type 3' and 'type 7' offer the possibility to generate several

alternative truss structures. The particular constraints (nodal connectivity and number of beam members), offer, in these cases, the possibility to generate up to 5 (N_i = 5) and 23 (N_i = 23) geometries, along with the initial geometrical base truss structures, see Table 4.3. A high number of combinatorial iteration (high number of iterations in the code) gave assurance that all the possible alternative base truss structures were generated under the applied constraints.

The geometrical final truss structures generated from 'type 3' and 'type 7' (respectively, structures *a*-*e* and structures *a*-*w*) may differ from each other in terms of the overall number of beam members and/or overall nodal connectivity.

The geometrical final truss structures generated from 'type 7' cases geometrically differed from each other. In some specific cases, the structures were geometrically similar, differing only in spatial orientation, see structures *n* and *u* in Table 4.3, for instance. These results were accepted because different orientation of the unit cell can result in different performance in that specific associated direction.

$N_i = 1$ **type 1**	*a*							
$N_i = 1$ **type 2**	*a*							
$N_i = 5$ **type 3**	*a*	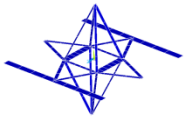	*b*		*c*		*d*	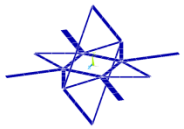
	e							

(cont.)

$N_i = 1$ **type 4**	*a*	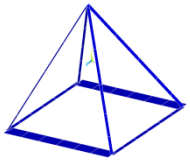						
$N_i = 1$ **type 5**	*a*	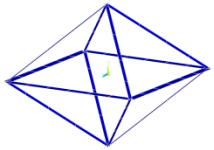						
$N_i = 1$ **type 6**	*a*							
$N_i = 23$ **type 7**	*a*	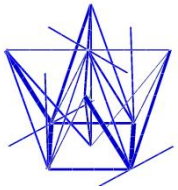	*b*	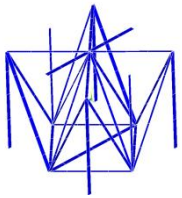	*c*	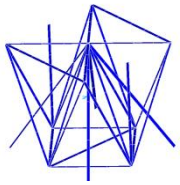	*d*	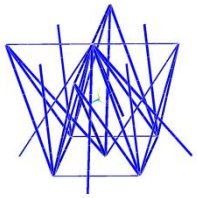

(cont.)

$N_i = 23$								
type 7	*e*	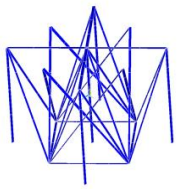	*f*	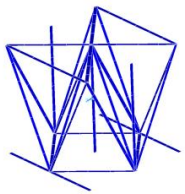	*g*	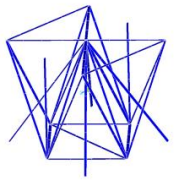	*h*	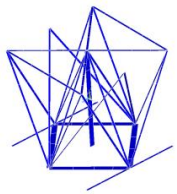
	i	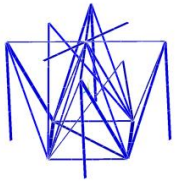	*j*	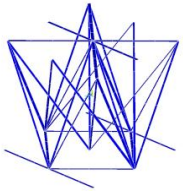	*k*	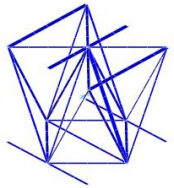	*l*	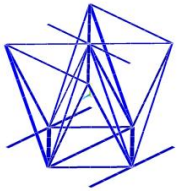
	m	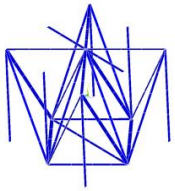	*n*	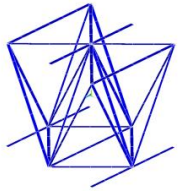	*o*	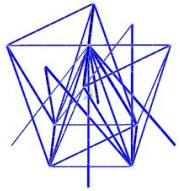	*p*	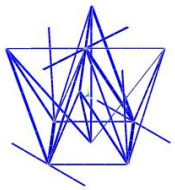
	q	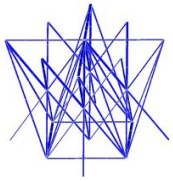	*r*	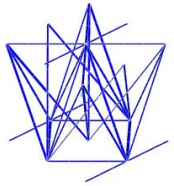	*s*	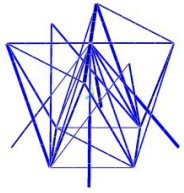	*t*	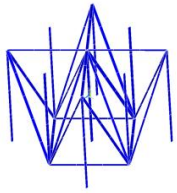
	u	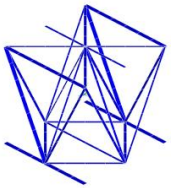	*v*	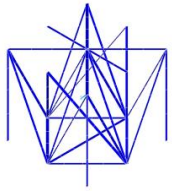	*w*	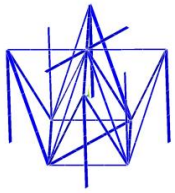		

Table 4.3. Base geometrical truss structures generated by the code. N_i is the number of possible structures for each 'type [N]' case.

4.3.2 Modelling results

There were over 1,000,000 models run so results cannot be easily presented in their entirety. Some expected and unexpected trends are presented here, using data from the seven 'type [N]' cases proposed, in the monolithic and dual-material configuration. The behaviour of only a few of the structures is presented (with typical or alternative behaviours) for the sake of clarity and brevity. As found in Chapter 3, monolithic and dual-material structures may show similar trends, in terms of mechanical properties, however, monolithic structures on an iso-volume basis usually have higher absolute values of the elastic constant, combined with a unique value of the CTE (that of the constituent material). For this reason, most of the results proposed refer to dual-material configurations.

Thermal Expansivity.

Figure 4.3 shows CTEs normalised by the thermal expansivity of the low thermal expansivity constituent material for some of the configurations generated from the seven 'type [N]' cases. For 'type [N]' cases where more than a base geometrical truss structure was possible, that with the largest variation and a typical configuration was displayed. Since the *y* direction is the one that shows a marked reduction in CTE and considering that the out-of-plane properties are key for sandwich constructions, most of the results are for that particular direction. Generally, negative, near-zero and positive CTEs in the *y* axis were found across all the range of aspect ratios for the types [N] proposed. Due to the specific types [N] proposed, and considering that the aspect ratio, *h/b*, produces minimal change in the internal architecture in *x* and *z* directions, the CTEs in *x* and *z* directions were mostly constant and/or bound between the CTEs of the constituent materials, see Figure 4.4 as an example.

Similar trends simulated in *y* direction for all the 'type [N]' cases were shown for some structures of 'type 7' in *x* or *z* direction, Figure 4.5. In these particular structures, the aspect ratio of the unit cell exerts a contribution in terms of CTE, opposite to that attributable to the *y* direction. That is, large positive or large negative CTEs were obtained for high values of the aspect ratio, *h/b*. An analysis of the particular geometries involved in this particular behaviour shows that, for some of the 'type 7' geometrical base truss structures, specifically structures *d*, *e*, *q* and *t*, beam members were disposed to form a pyramidal or triangular structure (more or less complex in *x* and *z* directions). Therefore, a change in the aspect ratio, *h/b*, modifies the internal architecture of the pyramidal or triangular structures in the unit cells, triggering in some cases the mechanism that drives NTE in structures.

Results show a wide range of possible solutions for all the proposed 'type [N]' cases, Figure 4.3, Figure 4.4 and Figure 4.5. In particular, since all the possible arrangements of the phases were explored for each 'type [N]' case, a wide range of behaviours was found in all the investigated RVE directions. The response of all the geometrical base truss structures proposed was found to be approximately symmetric, with respect to a value of unity in the normalised CTE. The number of possible CTE values for each structure was proportional to the number of beams of the quarter or the eight of the structure. Thus, a limited range of possible CTEs was found in 'type 4' and 'type 5' structures, where the number of beams was constrained to three; a wider range of CTEs was found in 'type 7', where the number of beams was ten. For instance, 'type 4' was able to provide just one structure, a pyramid, and 6 different combinations of phases (the quarter model was formed by only 3 beam elements), see Figure 4.3d.

In some cases ratios of thermal expansion of ± 200 were found, 'type 3', 'type 5' and 'type 6', see Figure 4.3c, e and f. Although these solutions appear to be unlikely, they are the result of an extreme aspect ratio, *h/b*, and arrangements of the phases which modify the internal architectures of the pyramidal or triangular structures in the unit cells, triggering in these cases an extreme mechanism that drives extreme positive or negative coefficients of thermal expansivity in the structures. However these results are true very locally and actual non-linear states might be achieved by larger changes in temperature. Buckling and collapse of the structure could be expected for these configurations.

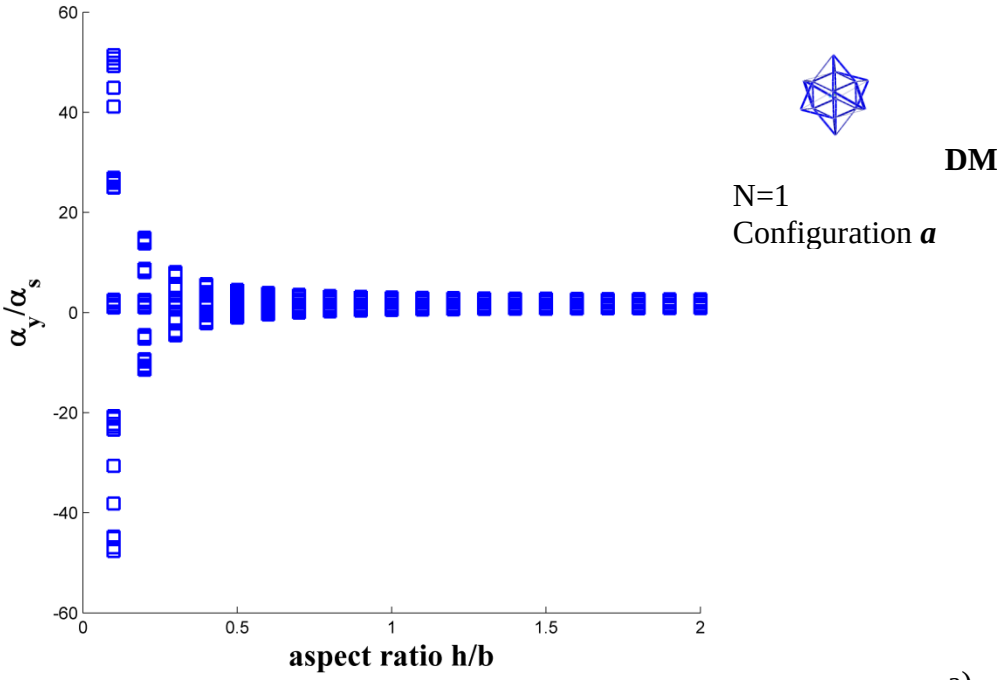

a)

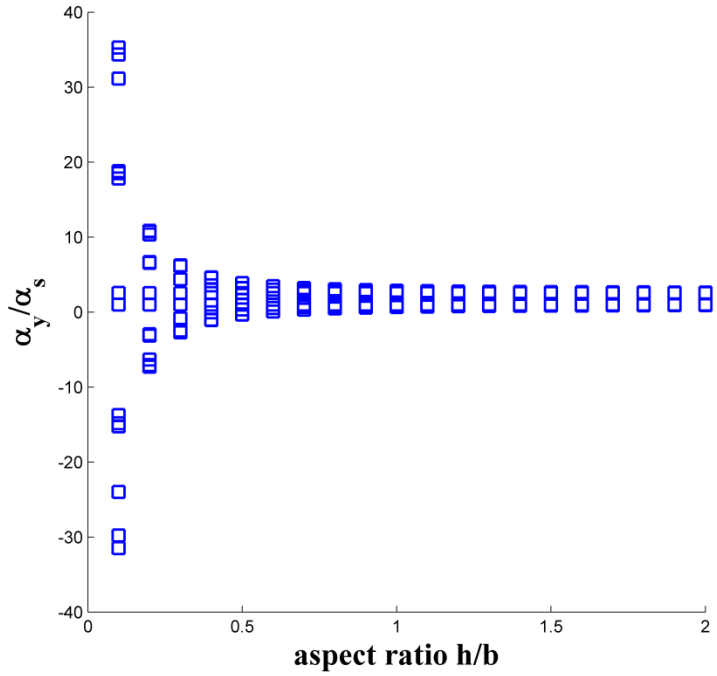

DM

N=2

Configuration ***a***

b)

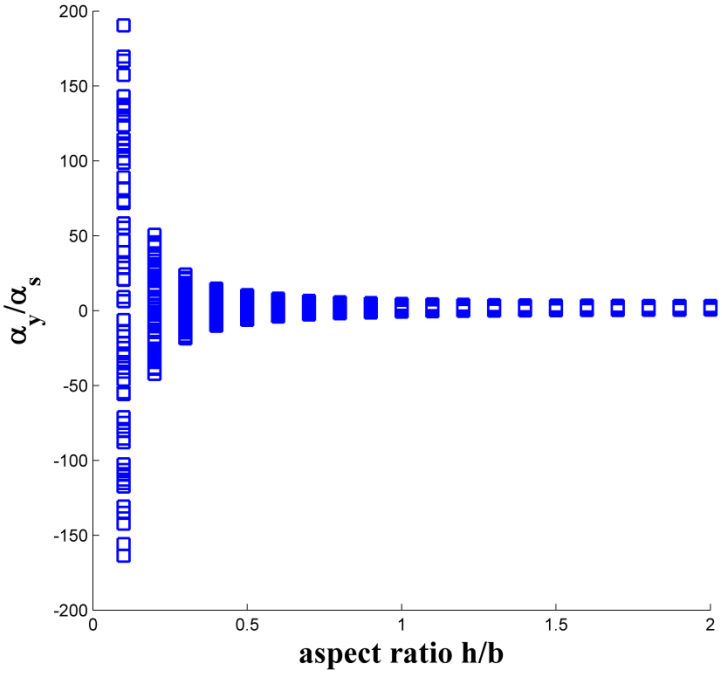

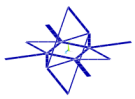

DM

N=3

Configuration ***d***

c)

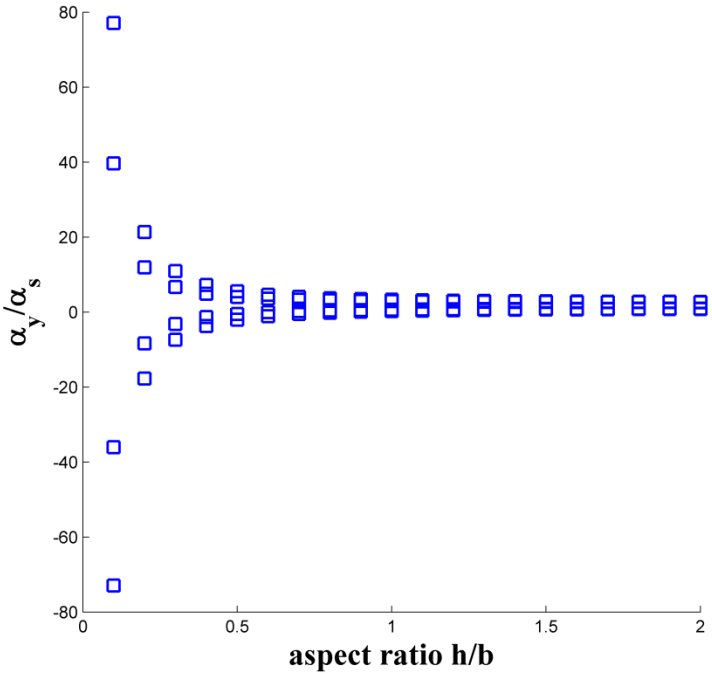

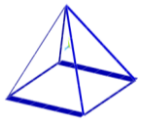

DM

N=4

Configuration ***a***

d)

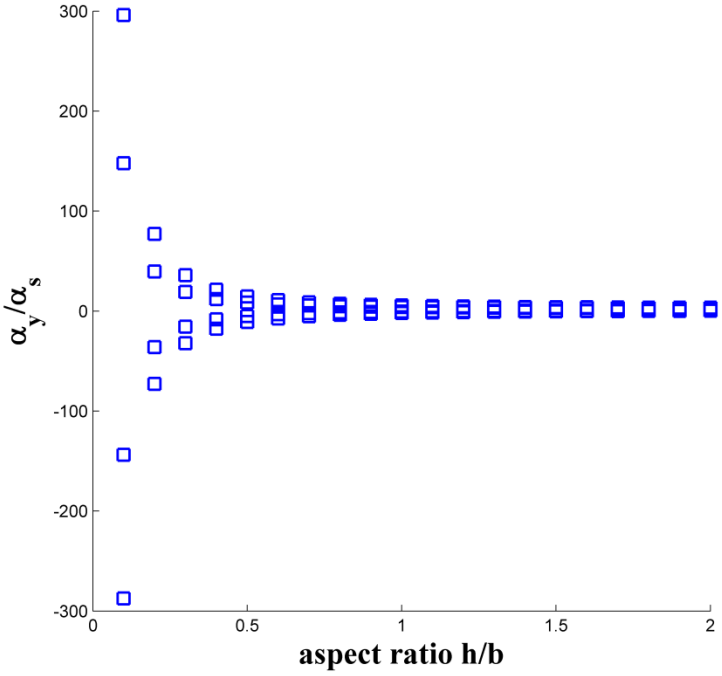

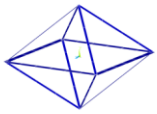

DM

N=5

Configuration ***a***

e)

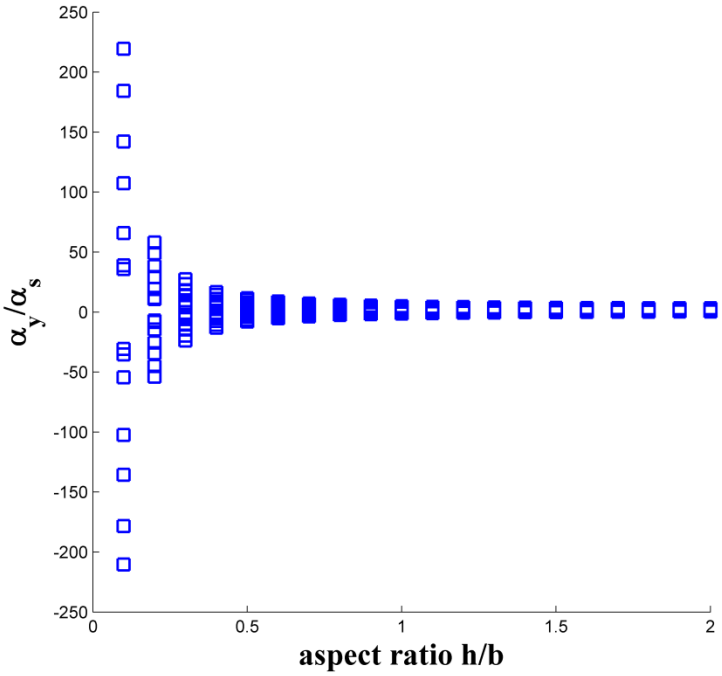

DM

N=6
Configuration ***a***

f)

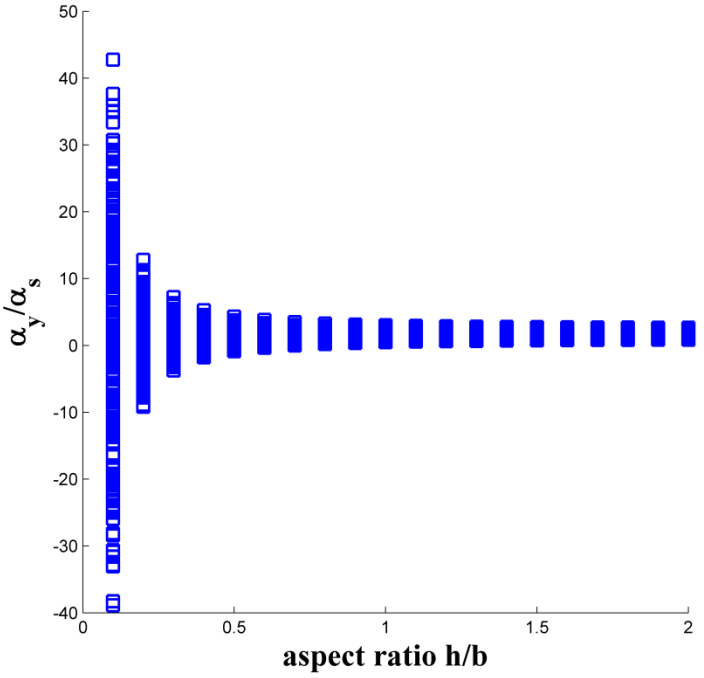

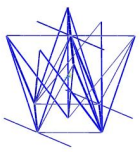

DM

N=7
Configuration ***j***

g)

Figure 4.3 (a-g). The predicted CTEs in the *y* axes of 'type [N]' cases, normalised by the thermal expansivity of the low thermal expansivity material. a) 'type 1'-structure *a*; b) 'type 2'-structure *a*; c) 'type 3'-structure *d*; d) 'type 4'-structure *a*; e) 'type 5'-structure *a*; f) 'type 6'-structure a; g) 'type 7'-structure *j*; all in dual-material configuration (DM).

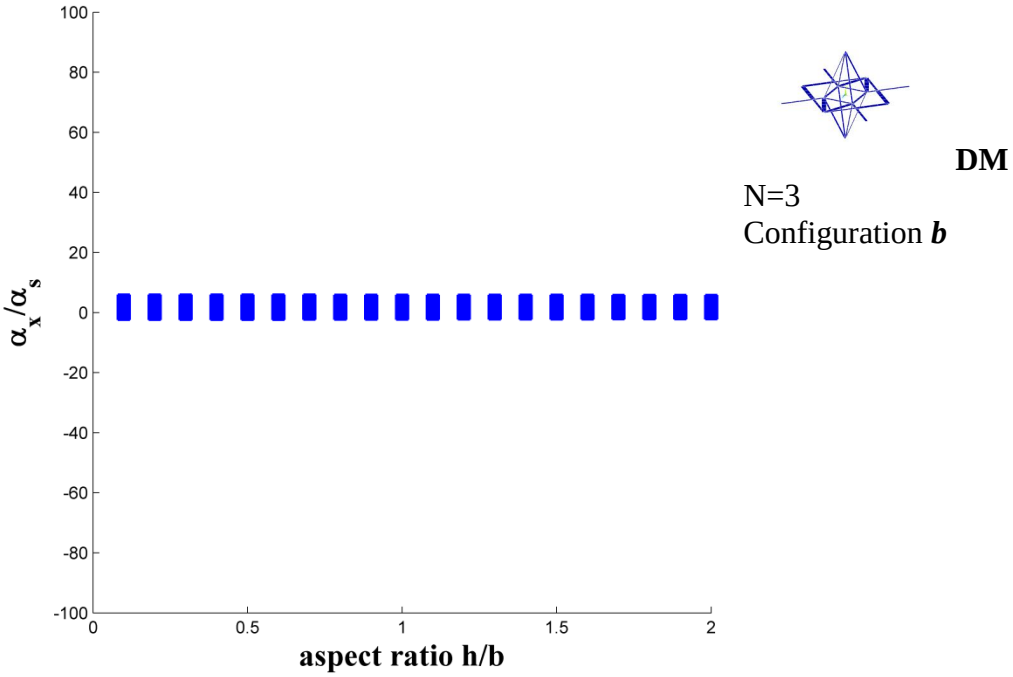

Figure 4.4. The predicted CTE, in the *x* axis of 'type 3'-structure *b* in dual-material configuration (DM), normalised by the thermal expansivity of the low thermal expansivity material.

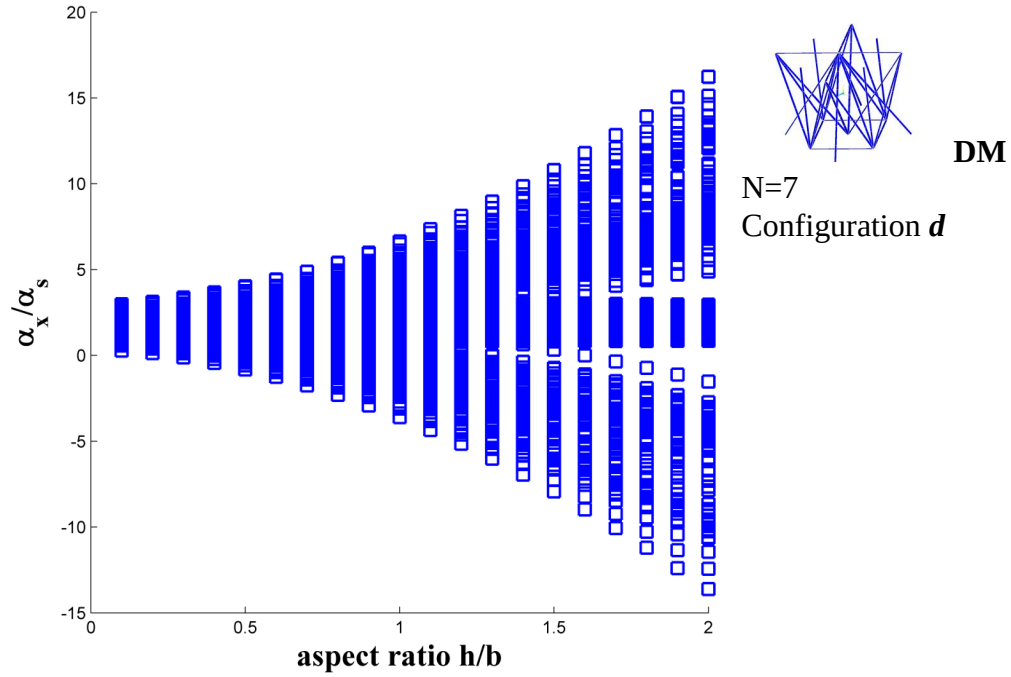

Figure 4.5. The predicted CTE, in the *x* axis of 'type 7'-structure *d* in dual-material configuration (DM), normalised by the thermal expansivity of the low thermal expansivity material.

Elastic Properties

The aspect ratios of the unit cell and phase disposition, within the unit cells, have a marked effect upon the axial stiffness in the *y* axis, E_y, see Figure 4.6 for all data on all the proposed 'type [N]' cases. In respect of all of these proposed 'type [N]' cases, the dual-material configuration always show comparable or reduced moduli compared with their monolithic iso-volume counterpart.

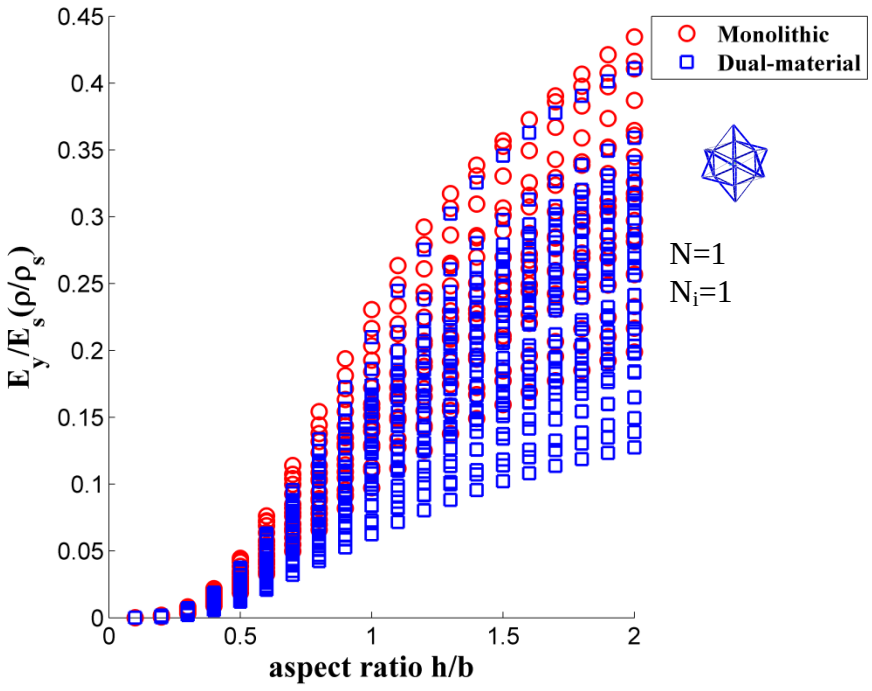

a)

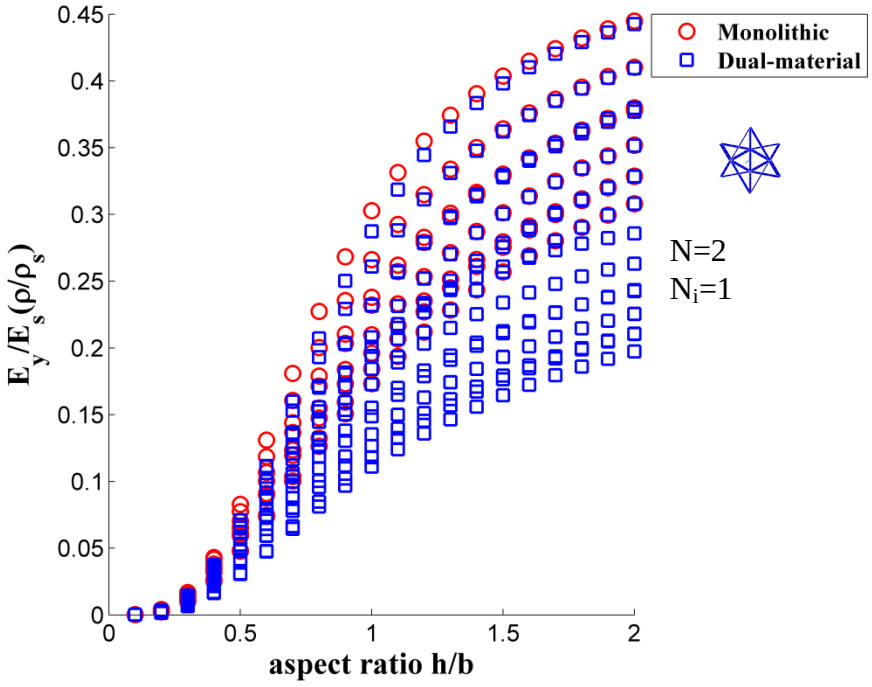
Monolithic
Dual-material
N=2
N_i=1
E_y/E_s(ρ/ρ_s)
aspect ratio h/b
0
0.05
0.1
0.15
0.2
0.25
0.3
0.35
0.4
0.45
0.5
1
1.5
2

b)

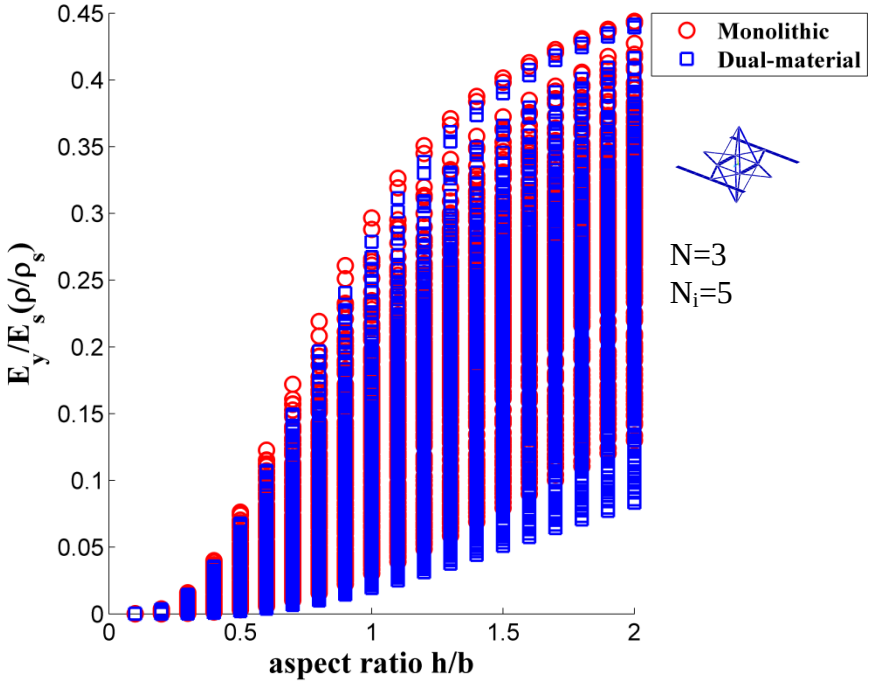
Monolithic
Dual-material
N=3
N_i=5
E_y/E_s(ρ/ρ_s)
aspect ratio h/b
0
0.05
0.1
0.15
0.2
0.25
0.3
0.35
0.4
0.45
0.5
1
1.5
2

c)

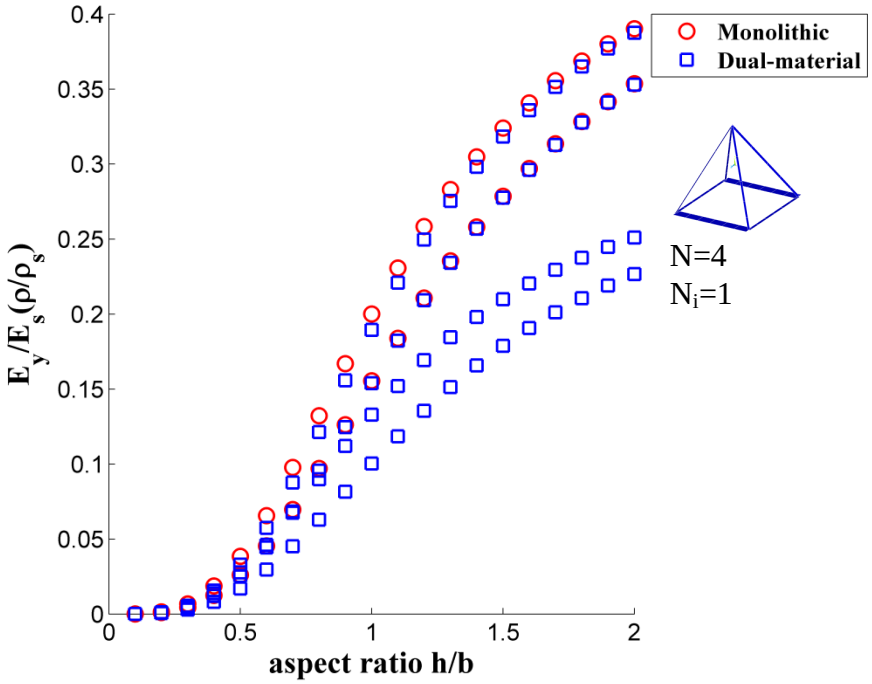
Monolithic
Dual-material
N=4
N_i=1
E_y/E_s(ρ/ρ_s)
aspect ratio h/b
0
0.05
0.1
0.15
0.2
0.25
0.3
0.35
0.4
0.5
1
1.5
2

d)

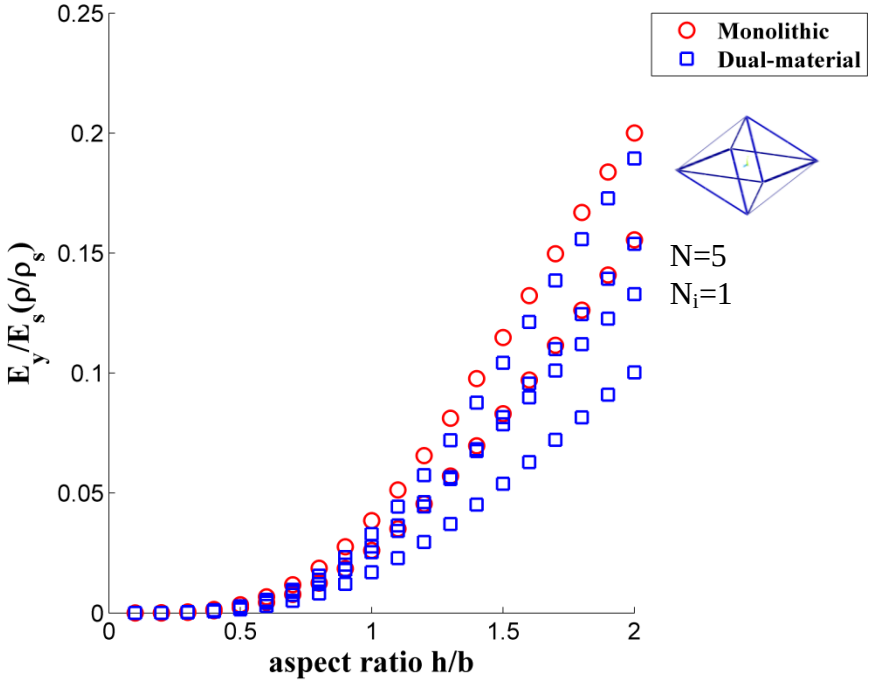
Monolithic
Dual-material
N=5
N_i=1
E_y/E_s(ρ/ρ_s)
aspect ratio h/b
0
0.05
0.1
0.15
0.2
0.25
0.5
1
1.5
2

e)

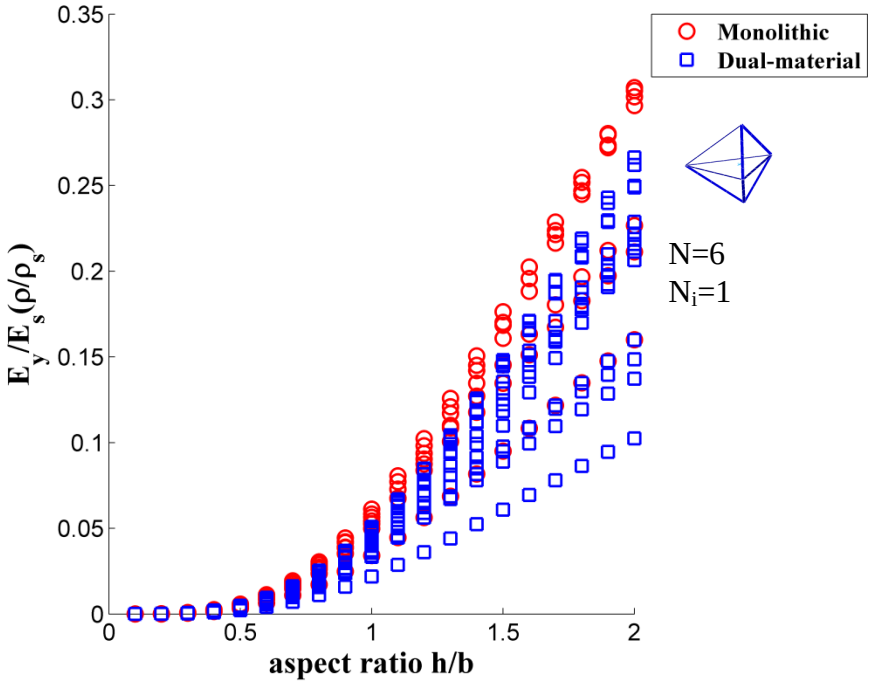

f)

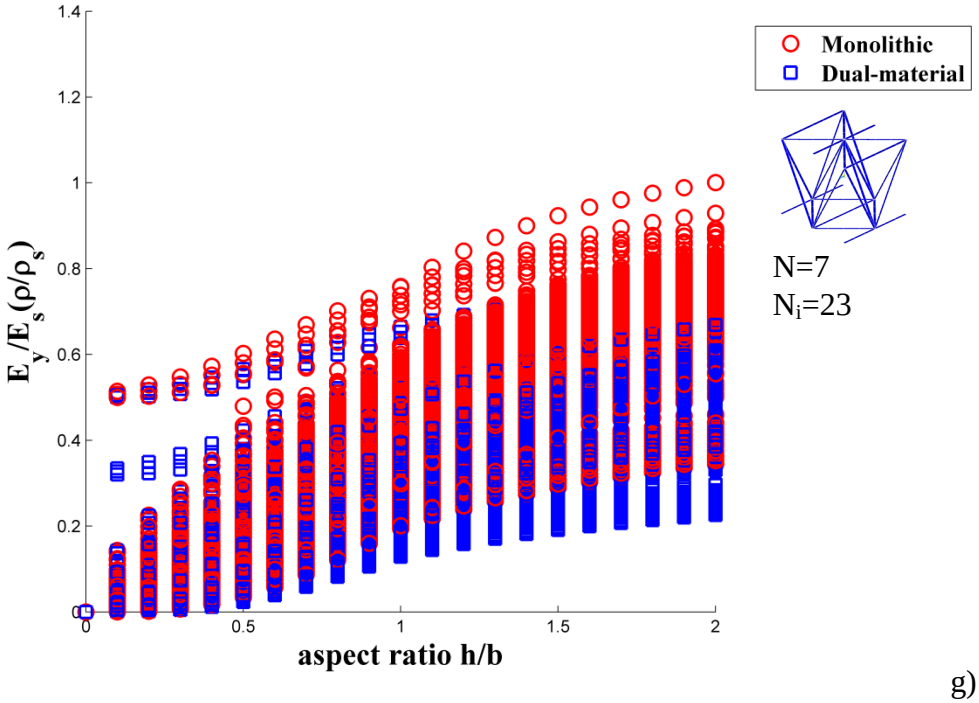

g)

Figure 4.6 (a-g). The predicted Young's modulus, in the y axes of all base geometrical truss structures generated from 'type [N]' cases, in monolithic and dual-material form, normalised by the Young's modulus of the low thermal expansivity solid strut material and the relative density of the truss material. a) 'type 1'; b) 'type 2'; c) 'type 3'; d) 'type 4'; e) 'type 5'; f) 'type 6'; g) 'type 7'. N_i is the number of possible structures for each 'type [N]' case.

Similar trends were found in the *x* and *z* axes for all the 'type [N]' cases proposed. As shown in Figure 4.6 (a-g), the dual-material band (blue circle band corresponding to dual-material structures) has a tendency to be lower than the monolithic material band (red squared band corresponding to monolithic structures). This confirms that dual-material structures generally show lower or, in the best scenario, comparable performance to that of monolithic structures. Also, 'type 4', 'type 5' and 'type 6' cases show comparable performances to monolithic structures on an iso-volume basis, confirming results presented in Chapter 3.

The shear stiffness also has a marked sensitivity to the cell aspect ratio and phase disposition within the unit cells, Figure 4.7 (a-g). Note that G_{zy}, in some cases, was similar to G_{xy} because of symmetry. There is a pronounced maximum in the shear stiffness for all structures with the aspect ratio, h/b $\rightarrow$ 0.7 for structures with single pyramid architectures in the initial structure (e.g. 'type 4'), and h/b $\rightarrow$ 1.4 for structures with double pyramid architectures (e.g. 'type 1'). The monolithic configuration in 'type 4', 'type 5' and 'type' 6 never performs better than the dual-material, Figure 4.7d, 4.7e and 4.7f. These results are in accordance with the design guidelines presented in Chapter 3 (see Equations 3.11 to 3.24).

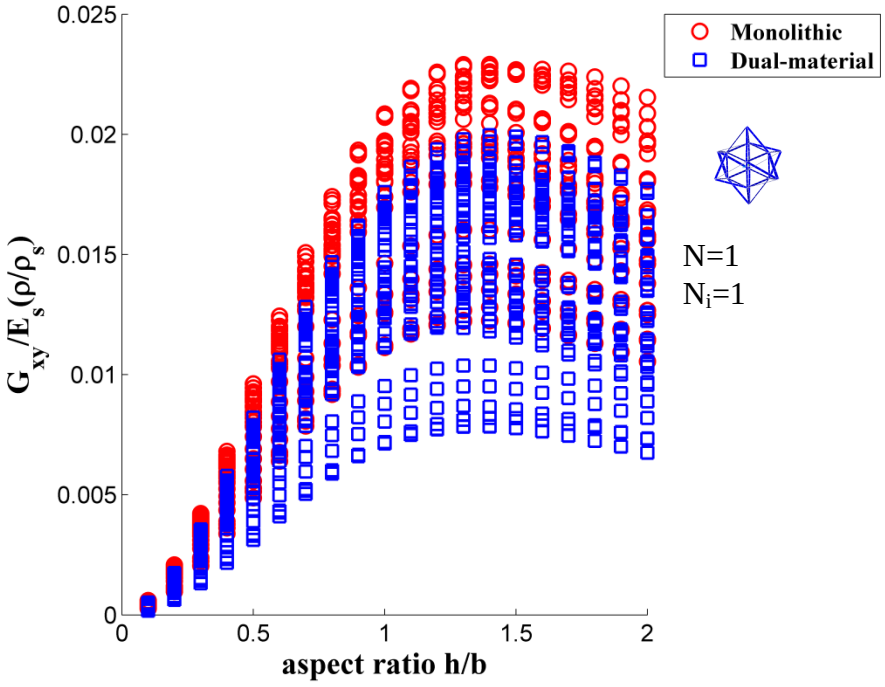
Monolithic
Dual-material
N=1
N_i=1
G_xy/E_s(ρ/ρ_s)
aspect ratio h/b
0.025
0.02
0.015
0.01
0.005
0
0
0.5
1
1.5
2

a)

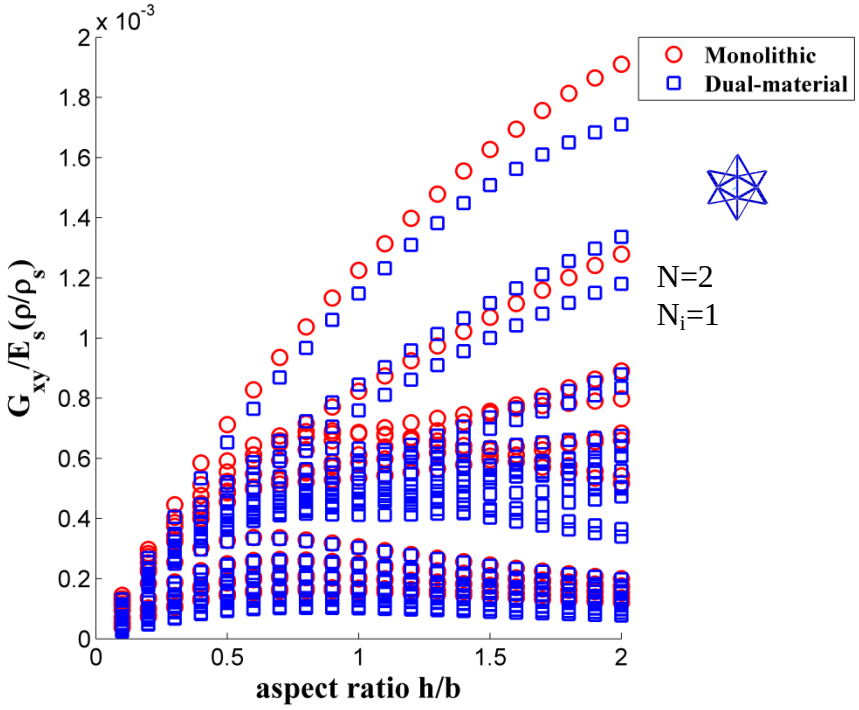
x 10^-3
Monolithic
Dual-material
N=2
N_i=1
G_xy/E_s(ρ/ρ_s)
aspect ratio h/b
2
1.8
1.6
1.4
1.2
1
0.8
0.6
0.4
0.2
0
0
0.5
1
1.5
2

b)

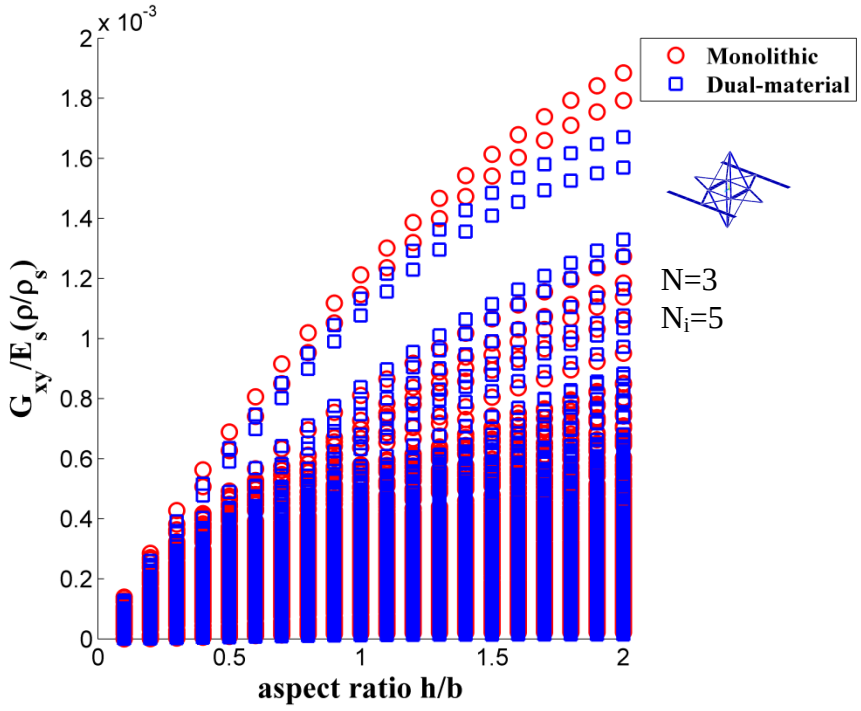
x 10^-3
Monolithic
Dual-material
N=3
N_i=5
G_xy/E_s(ρ/ρ_s)
aspect ratio h/b

c)

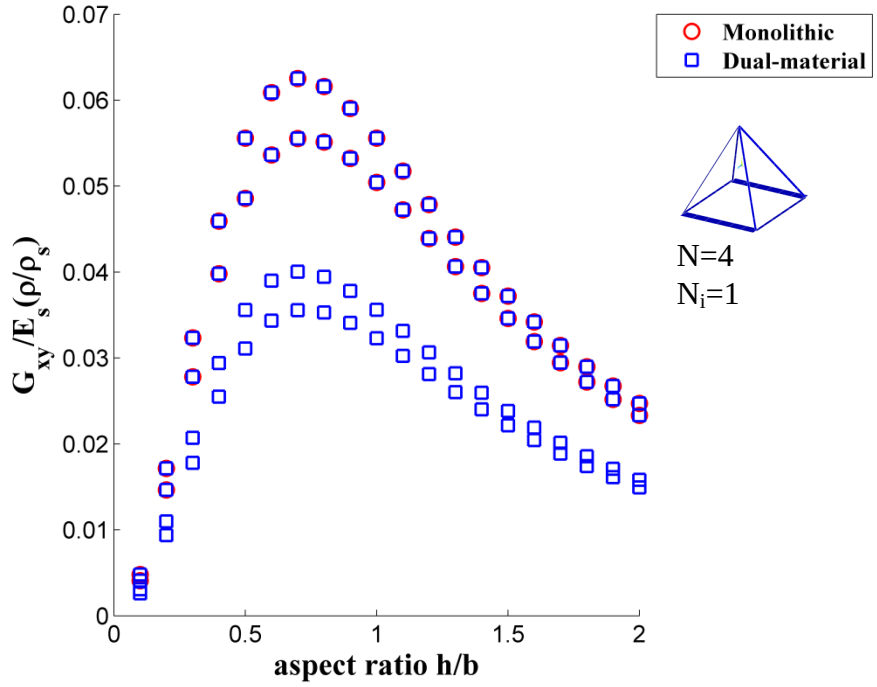
Monolithic
Dual-material
N=4
N_i=1
G_xy/E_s(ρ/ρ_s)
aspect ratio h/b

d)

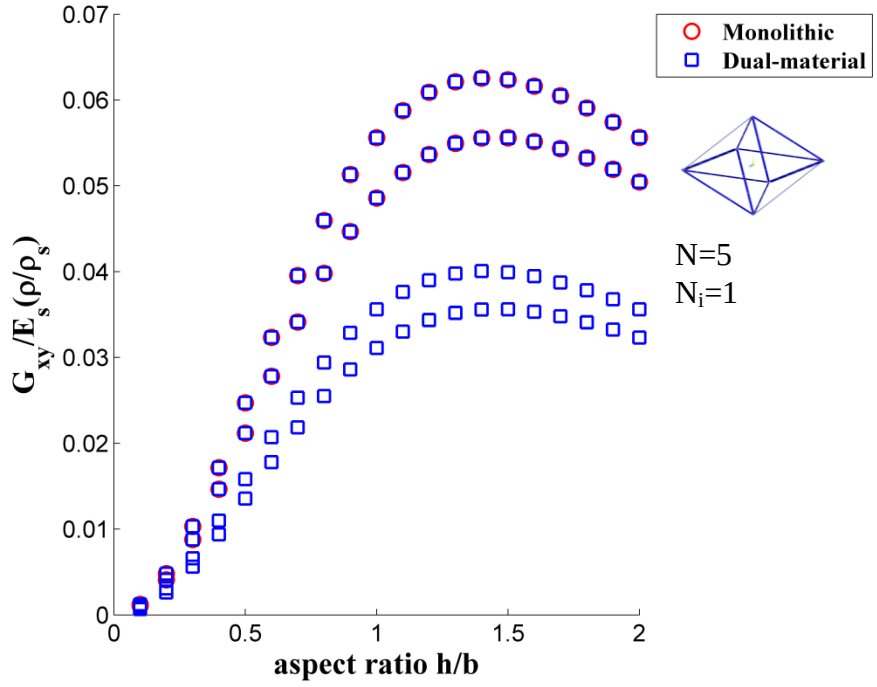
Monolithic
Dual-material
N=5
N_i=1
G_xy/E_s(ρ/ρ_s)
aspect ratio h/b
0
0.01
0.02
0.03
0.04
0.05
0.06
0.07
0.5
1
1.5
2

e)

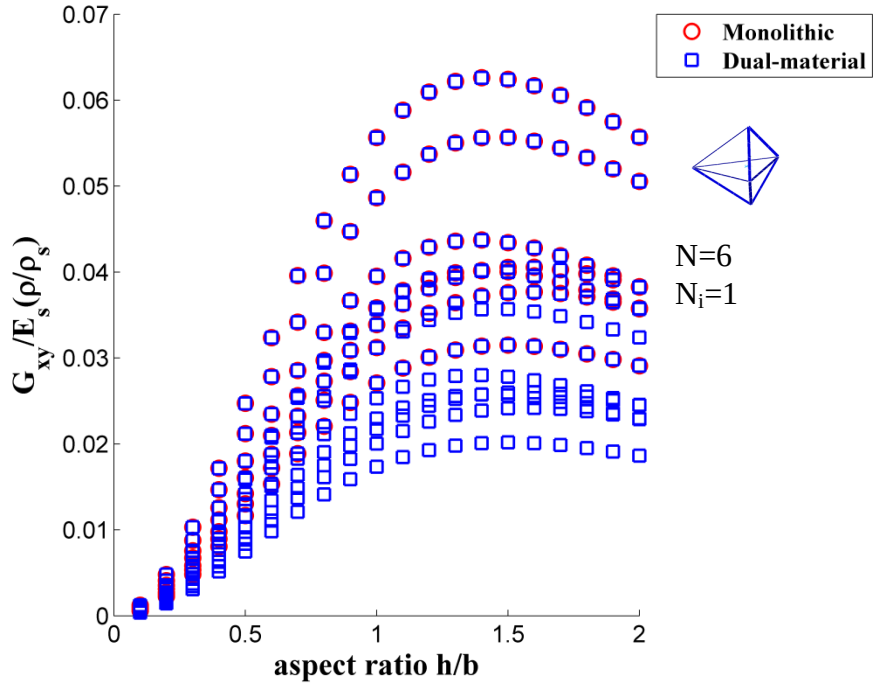
Monolithic
Dual-material
N=6
N_i=1
G_xy/E_s(ρ/ρ_s)
aspect ratio h/b
0
0.01
0.02
0.03
0.04
0.05
0.06
0.07
0.5
1
1.5
2

f)

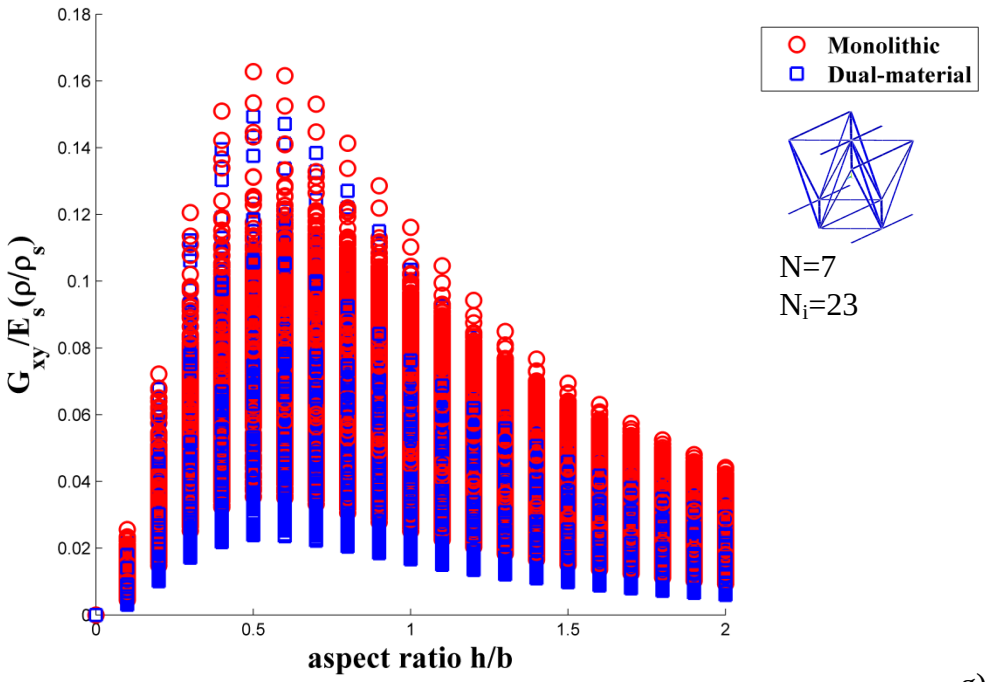

g)

Figure 4.7 (a-g). The predicted shear modulus, in the *x*-*y* direction of all base geometrical truss structures generated from 'type [N]' cases, in monolithic and dual-material form, normalised by the Young's modulus of the low thermal expansivity solid strut material and the relative density of the truss material. a) 'type 1'; b) 'type 2'; c) 'type 3'; d) 'type 4'; e) 'type 5'; f) 'type 6'; g) 'type 7'. N_i is the number of possible structures for each 'type [N]' case.

Poisson's ratio was also sensitive to the aspect ratio of the unit cell and phase disposition within the unit cell. The results show that some types exhibited large, near-zero and negative values of Poisson's ratio along the entire range of aspect ratio, a sometimes desirable property (Evans et al., 1991; Lakes, 1987). Phase dispositions, physical properties of the constituent materials and the aspect ratio of the unit cell seem to impact the value of Poisson's ratio. It sometimes exceeds the upper bound for isotropy, i.e. 0.5, so such structures must be anisotropic, as found in Chapter 3.

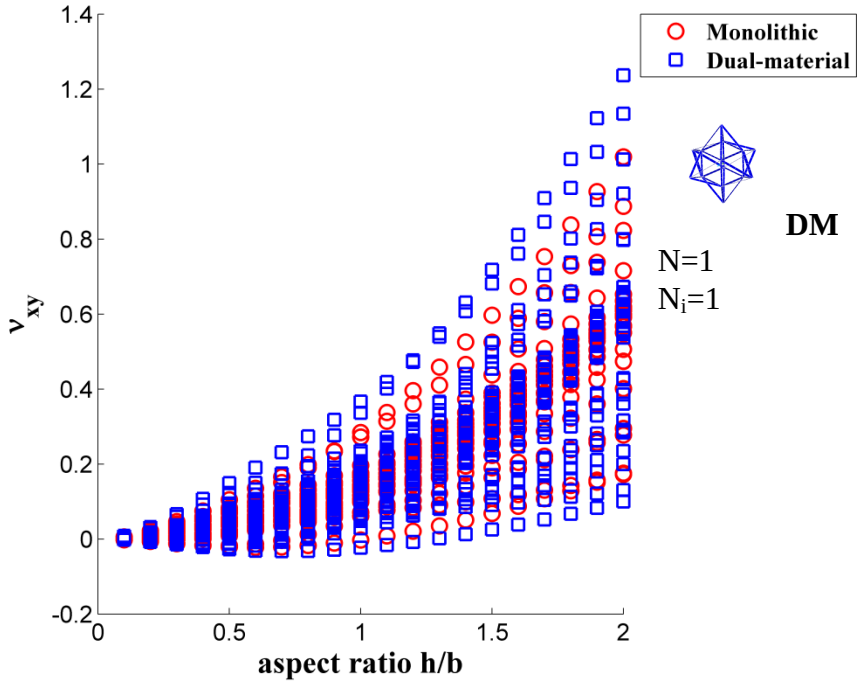
Monolithic
Dual-material
DM
N=1
N_i=1
ν_xy
aspect ratio h/b
1.4
1.2
1
0.8
0.6
0.4
0.2
0
-0.2
0
0.5
1
1.5
2

a)

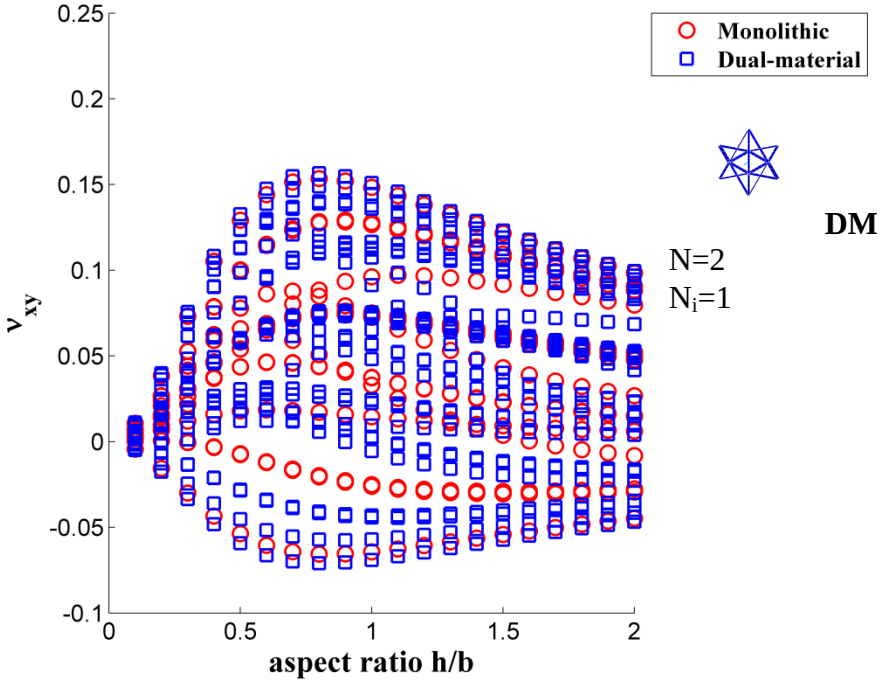
Monolithic
Dual-material
DM
N=2
N_i=1
ν_xy
aspect ratio h/b
0.25
0.2
0.15
0.1
0.05
0
-0.05
-0.1
0
0.5
1
1.5
2

b)

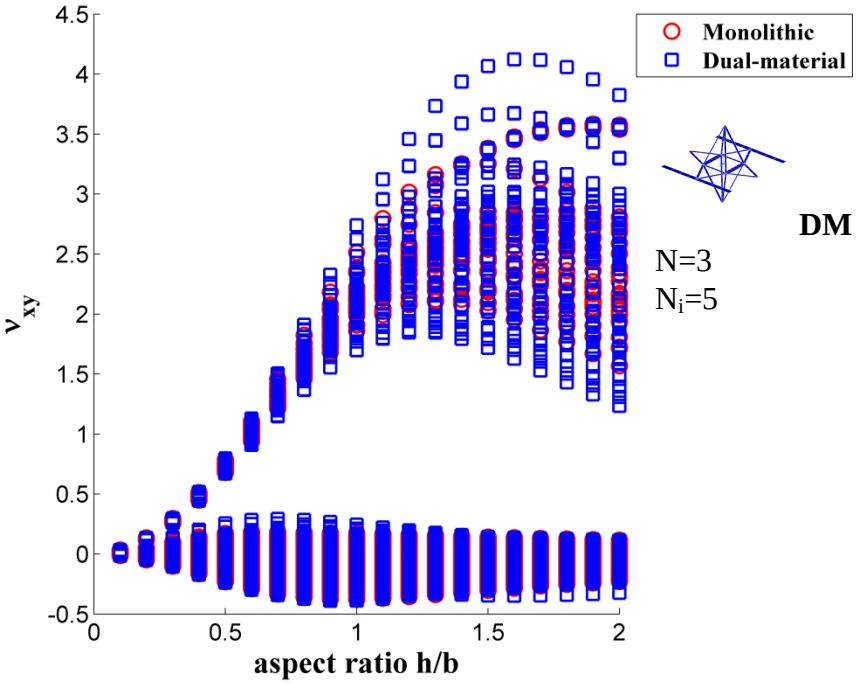
Monolithic
Dual-material
DM
N=3
N_i=5
ν_xy
aspect ratio h/b

c)

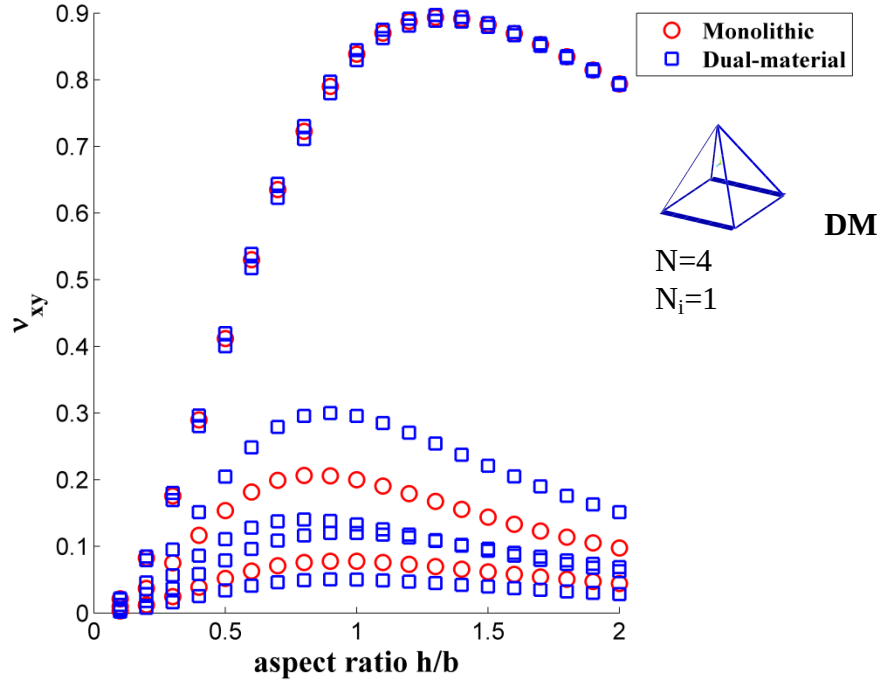
Monolithic
Dual-material
DM
N=4
N_i=1
ν_xy
aspect ratio h/b

d)

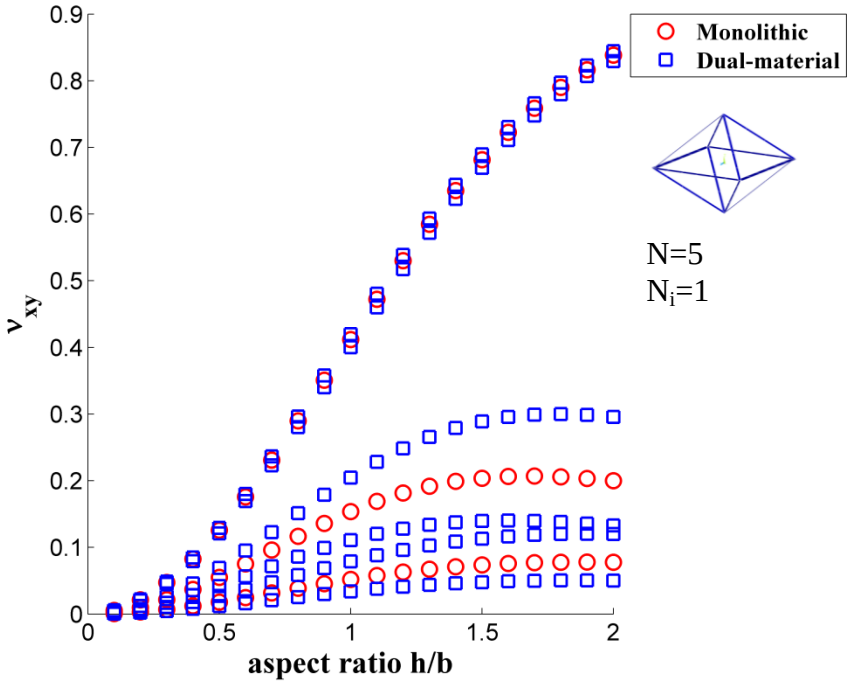
Monolithic
Dual-material
N=5
N_i=1
ν_xy
aspect ratio h/b
0
0.1
0.2
0.3
0.4
0.5
0.6
0.7
0.8
0.9
0.5
1
1.5
2

e)

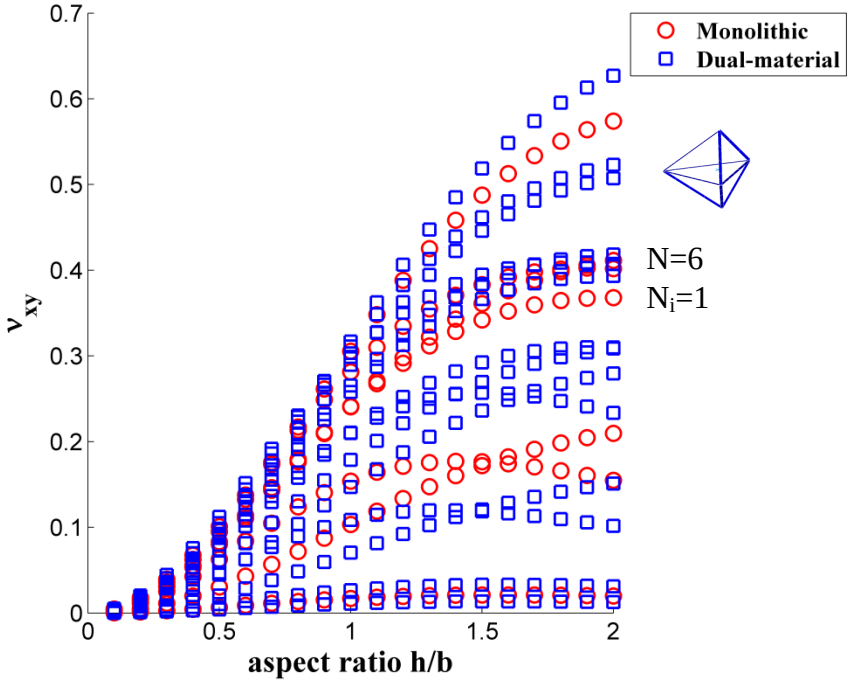
Monolithic
Dual-material
N=6
N_i=1
ν_xy
aspect ratio h/b
0
0.1
0.2
0.3
0.4
0.5
0.6
0.7
0.5
1
1.5
2

f)

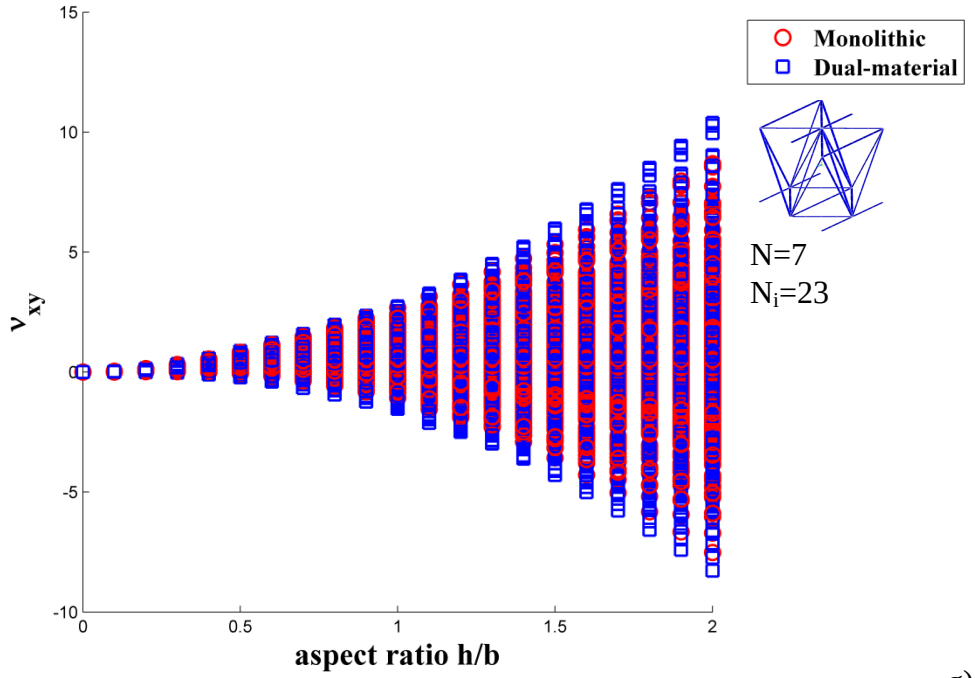

g)

Figure 4.8 (a-g). The predicted Poisson's ratio, in the *x-y* direction of all base geometrical truss structures generated from 'type [N]' cases, in monolithic and dual-material form. a) 'type 1'; b) 'type 2'; c) 'type 3'; d) 'type 4'; e) 'type 5'; f) 'type 6'; g) 'type 7'. N_i is the number of possible structures for each 'type [N]' case.

4.3.3 Comparison with Evans performance indices

Benefits that can be expected upon implementing these dual-material structures are presented and compared with alternative competing structures, as per Evans et al. (2001) and Wadley (2006). In order to be implemented as light-weight sandwich constructions, out-of-plane modulus (E_y) and shear modulus in *x-y* direction (G_{xy}) are the most important properties. The axial and shear moduli of ideal stretch-dominated structures and bending-dominated structures were used as benchmarks to compare the combinatorial structures with known ideal structures, as proposed by many researchers (Evans et al., 2001; Wadley, 2006). The two broken lines, in Figure 4.9a and b, show the envelopes, within which lattice structures lie, according to predictions by Evans (2001). 'Type 7' is the best performing in terms of axial and shear stiffness, Figure 4.9a and 4.9b, for values of the relative thermal

expansivity close to one and near-zero. That is, several of the 'type 7' structures in dual-material configuration largely approach the ideal stretch-dominated behaviour for a monolithic configuration. Increasing the thermal expansivity results in a decrease of moduli for all the 'type [N]' cases proposed. The 'type 5' cases seems to suffer the greater penalties in terms of axial stiffness for high values of CTEs, Figure 4.9a, while 'type 2' and ' type 3' cases substantially underperform in shear. Their performance is well below the bending-dominated structures benchmark for all the CTEs range. The trend, showing that structures approaching near-zero or even negative CTEs have reduced axial performance compared with structures showing CTE equal to the unity, is highlighted in Figure 4.9a. 'Type 1', 'type 3', 'type 6' and 'type 7' cases offer the possibility to obtain near-zero CTEs, retaining satisfactory values of axial stiffness. Shear modulus is unaffected in structures showing near-zero thermal expansivity, in an opposite way, as it decreases in designed structures with higher CTEs. This behaviour is shown by the 'type [N]' cases proposed herein. The 'type 7' case offers the widest range of behaviours compared with the other 'type [N]' cases. It also retains the highest mechanical properties combined with altered CTEs.

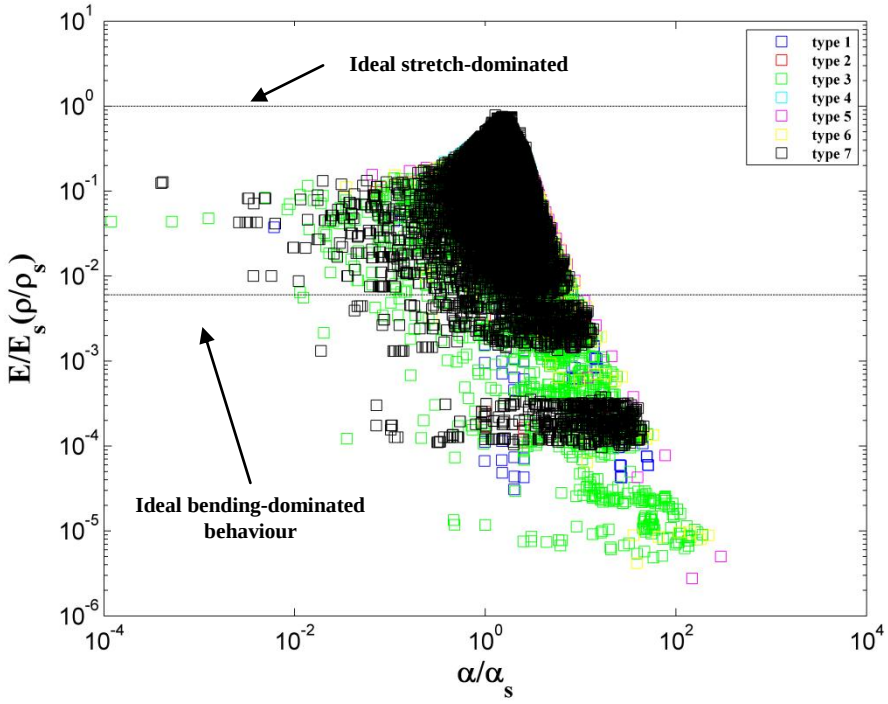

a)

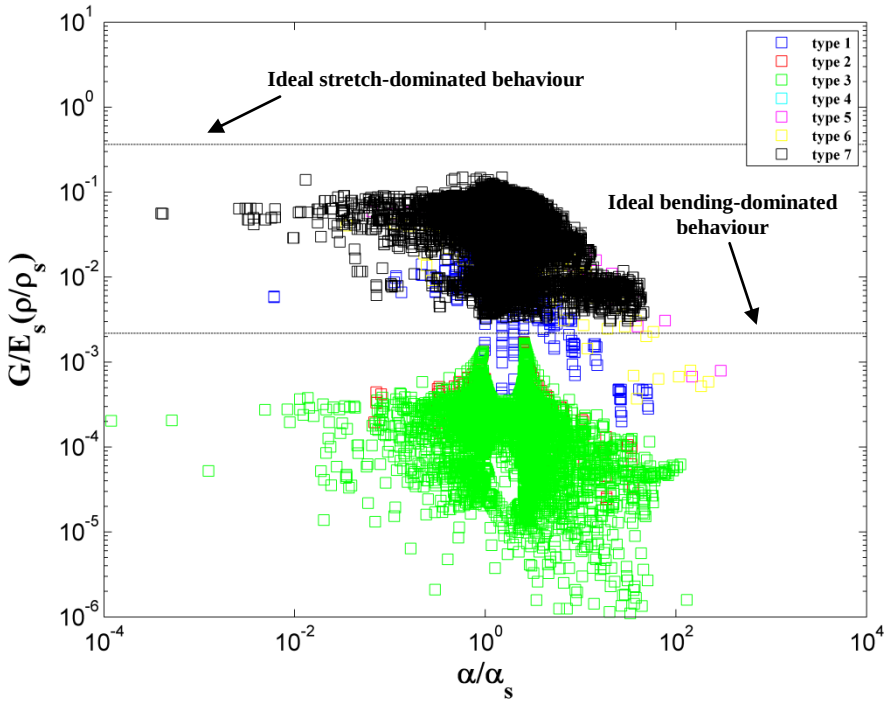

b)

Figure 4.9 (a and b). Young's modulus in y axis and shear modulus in *x-y* direction normalised by the Young's modulus of the low thermal expansivity solid strut material and the relative density of the truss material plotted against CTEs, in the y axes, normalised by the thermal expansivity of the low thermal expansivity material on logarithmic scales for all the 'type [N]' structures in the dual-material form.

4.3.4 Performance maps

Figure 4.10 (a and b) and Figure 4.11 (a and b) highlight the degree of anisotropy of the proposed 'type [N]' structures. All the generated structures show anisotropic behaviour in the range of CTEs and stiffnesses considered. The higher degree of anisotropy is obtained for values of the relative CTE, α/α_s, around unity, see Figure 4.11 (a and b), and for high values of the relative stiffness, E_y/E_s, see Figure 4.10 (a and b).

Figure 4.10a and 4.10b and Figure 4.11a and 4.11b show a symmetry in behaviour in *x* and *z* axes, as expected, in most of the structures generated from 'type 1' to 'type 7'.

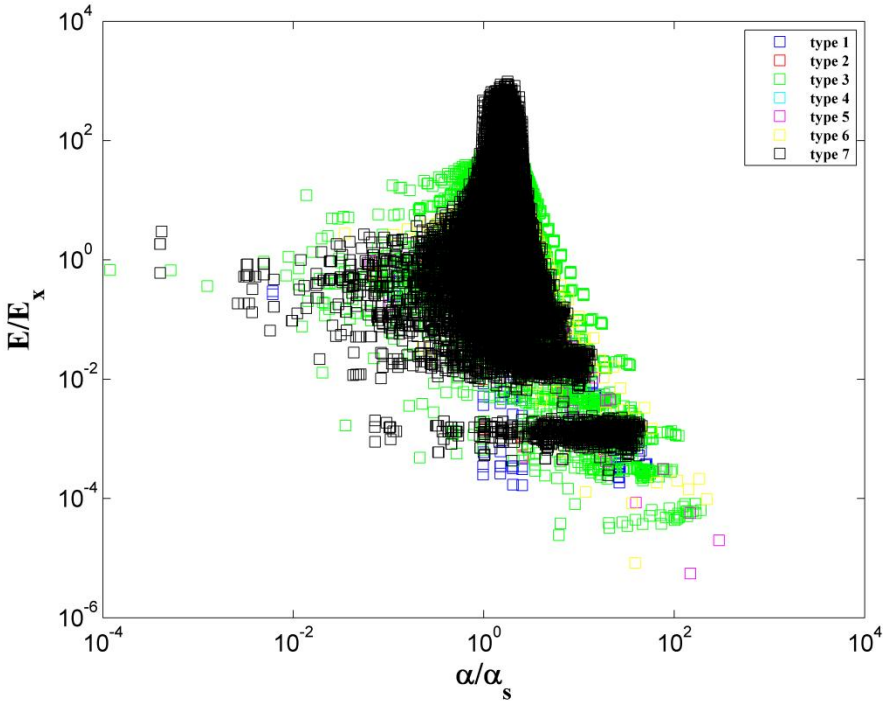

a)

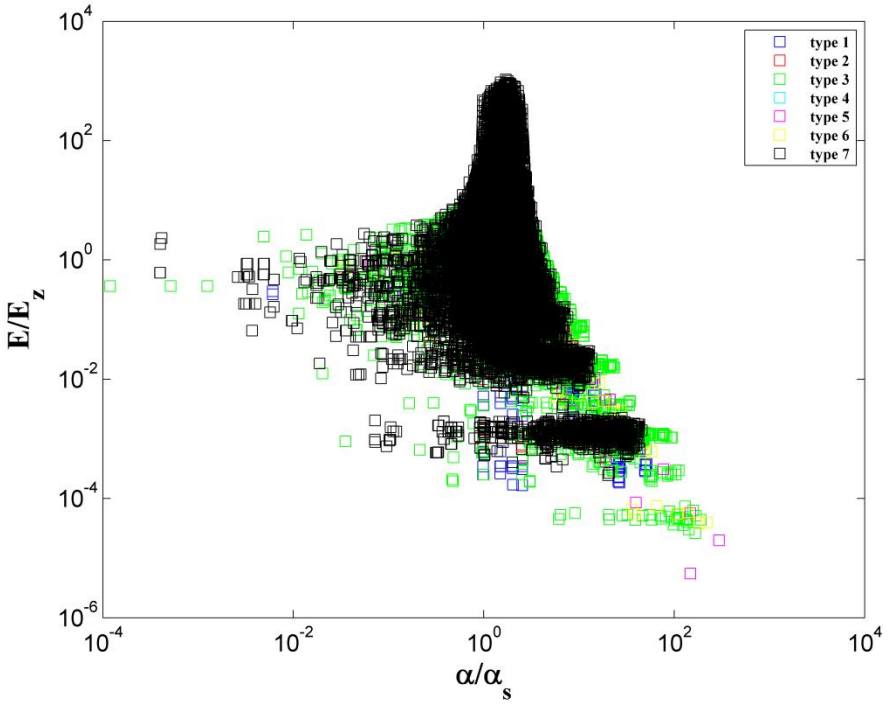

b)

Figure 4.10 (a and b). Young's modulus in *y* axis, E, normalised by the Young's modulus in the other directions plotted against CTEs, in the *y* axes, normalised by the thermal expansivity of the low thermal expansivity material on logarithmic scales for all the 'type [N]' in the dual-material form. a) Young's modulus in *y* axis normalised by the Young's modulus in *x* axis; b) Young's modulus in *y* axis normalised by the Young's modulus in *z* axis.

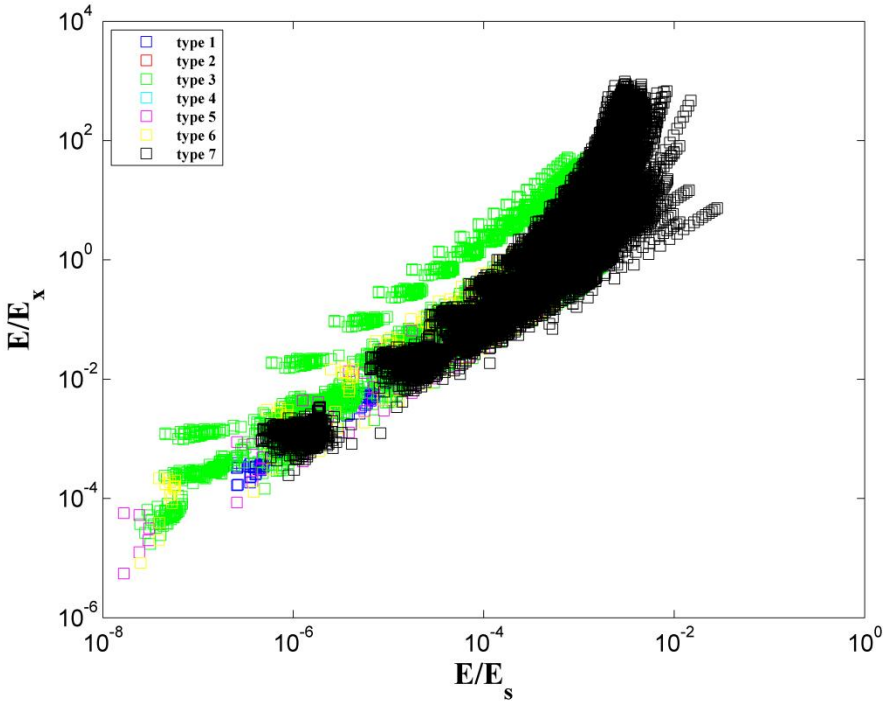

a)

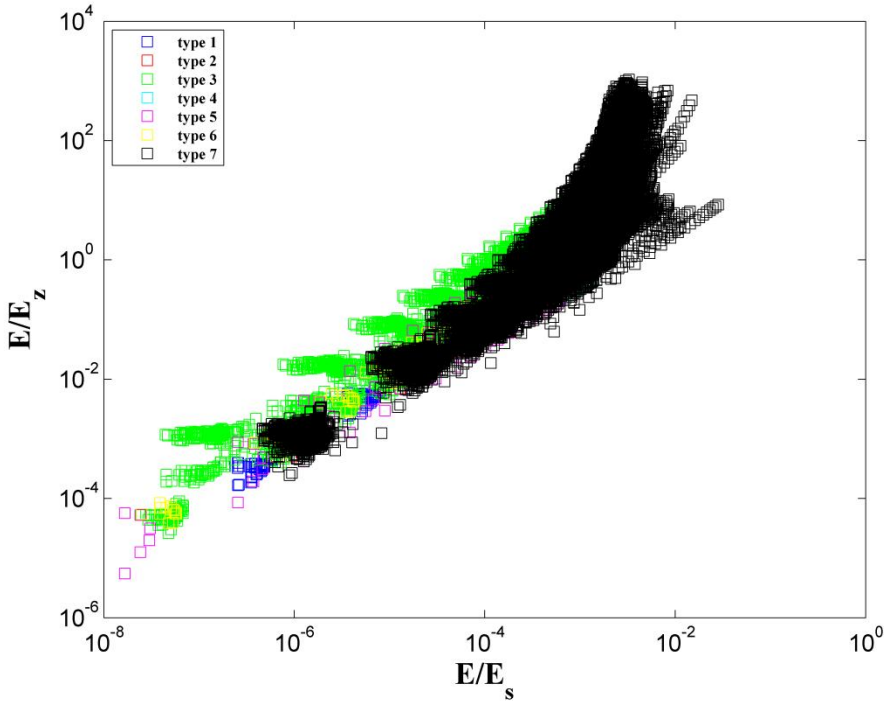

b)

Figure 4.11 (a and b). Young's modulus in *y* axis, E, normalised by the Young's modulus in the other directions plotted against the Young's modulus in *y* axis E_y normalised by the Young's modulus of the low thermal expansivity solid strut material on logarithmic scales for all the 'type [N]' structures in the dual-material form. a) Young's modulus in *y* axis normalised by the Young's modulus in *x* axis; b) Young's modulus in *y* axis normalised by the Young's modulus in *z* axis.

4.3.5 NTE, ZTE and PTE designs

New and typical designs were extracted from the solutions generated. In particular, structures showing negative, near-zero and positive thermal expansivity combined with high axial and shear stiffness, were considered.

NTE designs.

Table 4.4 shows the numerically generated solutions for each considered 'type [N]' structure, showing negative thermal expansivity in the out-of-plane direction combined either with maximised stiffness in *y* direction or maximised shear stiffness in *x*-*y* direction, key properties in sandwich applications. A wide range of solutions, in terms of negative thermal expansivity, can be found for each 'type [N]' because of the fact that different

structures might show a variety of different CTEs for each type, the solutions being: a function of the aspect ratio of the cell, the arrangement of the two phases, the physical properties of the constituent materials, the specific geometries generated, and the particular imposed design objective. In order to keep the solution as general as possible and in order to simplify the problem, specific criteria, considered of practical interest, were imposed. Structures with CTEs less or equal to - 1 were selected, as shown in Figure 4.12. Several solutions were found to lie below the broken line, indicating the ideal bending-dominated behaviour of lattice structures. 'Type 4'-structure, *a*, in the form presented in Table 4.4, had the best compromise between reduced CTE and maximised stiffness, Figure 4.12a. It shows a stiffness 10 times higher than an ideal monolithic bending-dominated structure on an iso-volume basis, combined with a two times lower normalised CTE. 'Type 7'-structure *j* in the form presented in Table 4.4 had the best compromise between reduced CTE and maximised shear, Figure 4.12b. It shows a stiffness 50 times higher than an ideal monolithic bending-dominated structure on an iso-volume basis, combined with a two times lower normalised CTE. 'Type 2' and 'type 3' structures show performance in shear well below the ideal bending-dominated shear behaviour, see Figure 4.12b.

	NTE			
	E_{max}		G_{max}	
type 1	*a*	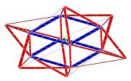	*a*	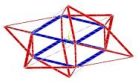
type 2	*a*	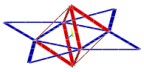	*a*	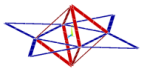
type 3	*c*	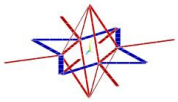	*e*	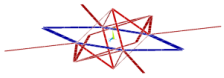
type 4	*a*	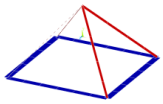	*a*	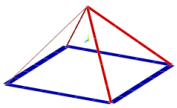
type 5	*a*	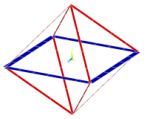	*a*	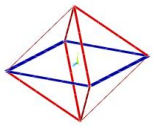
type 6	*a*	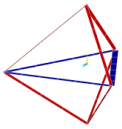	*a*	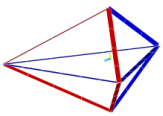
type 7	*k*	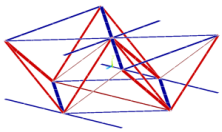	*j*	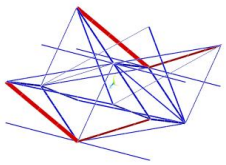

Table 4.4. Designs showing negative CTEs combined with high mechanical performance for all the proposed 'type [N]' cases.

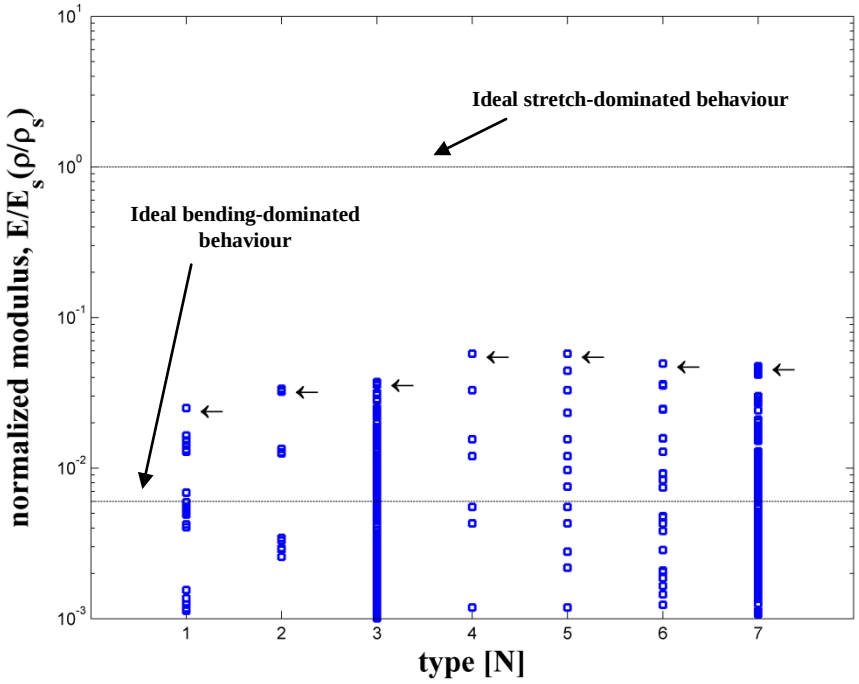

a)

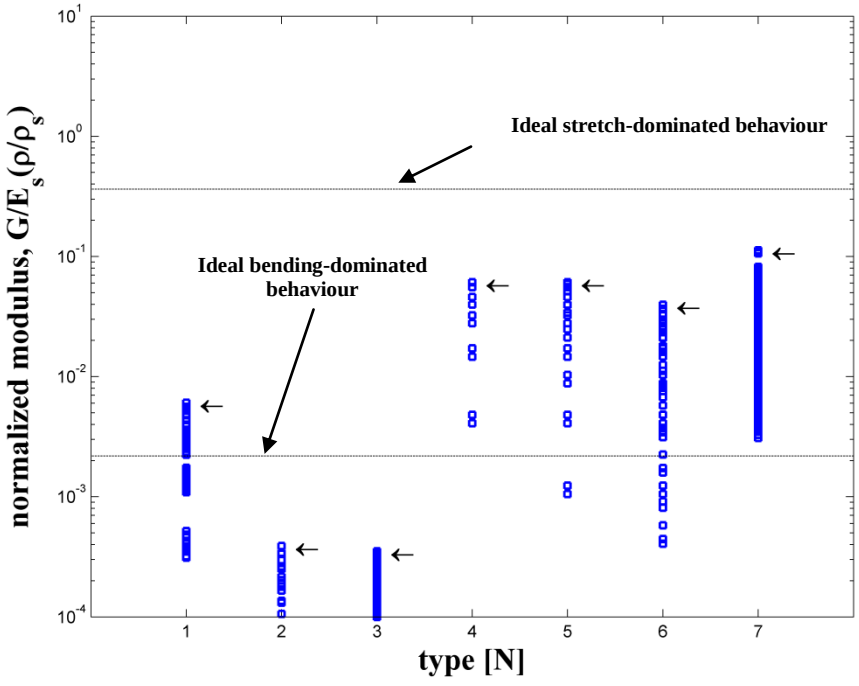

b)

Figure 4.12 (a and b). Solutions showing negative CTEs. The arrows indicate the structures with a) higher stiffness, E_{max}; b) higher shear, G_{max}.

ZTE designs.

Table 4.5 shows the numerically generated solutions for each considered 'type [N]' structure, showing near-zero thermal expansivity in the out-of-plane direction combined either with maximised stiffness in *y* direction or maximised shear stiffness in *x*-*y* direction, key properties in sandwich applications, as mentioned previously. A wide range of solutions, in terms of near-zero thermal expansivity, can be found for each type because of the fact that for each type, the solutions being: a function of the aspect ratio of the cell, the phases' arrangement, the physical properties of the constituent materials, the specific geometries generated, and the particular design objective imposed. Near-zero CTEs were identified in values of normalised CTEs between ± 0.06 and ± 0.1, as shown in Figure 4.13. Several solutions were found to lie below the broken line, indicating the ideal bending-dominated behaviour of lattice structures. 'Type 5'-structure, *a*, 'type 6'-structure, *a*, and type 7-structure, *k,* in the form presented in Table 4.5 had the best compromise between near-zero CTE and maximised stiffness, Figure 4.13a. They show a stiffness 20 times higher than an ideal monolithic bending-dominated structure on an iso-volume basis, combined with normalised CTE around zero. 'Type 7'-structure *k*, in the form presented in Table 4.5, had the best compromise between near-zero CTE and maximised shear, Figure 4.13b. It shows a stiffness 60 times higher than an ideal monolithic bending-dominated structure on an iso-volume basis, combined with a near-zero normalised CTE. Also in this case, 'type 2' and 'type 3' structures show performance well below the ideal bending-dominated shear behaviour, see Figure 4.13b.

	ZTE			
	E_{max}		G_{max}	
type 1	*a*	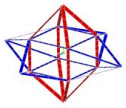	*a*	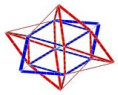
type 2	*a*	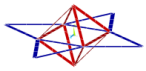	*a*	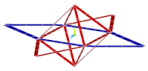
type 3	*c*	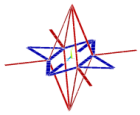	*a*	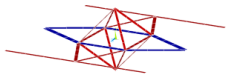
type 4	*1*	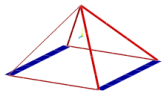	*1*	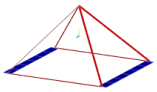
type 5	*a*	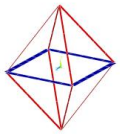	*a*	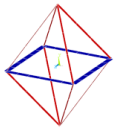
type 6	*a*	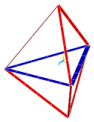	*a*	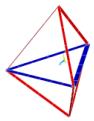
type 7	*k*	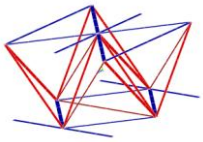	*k*	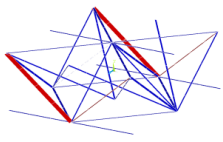

Table 4.5. Designs showing near-zero CTEs combined with high mechanical performance for all the proposed 'type [N]' cases.

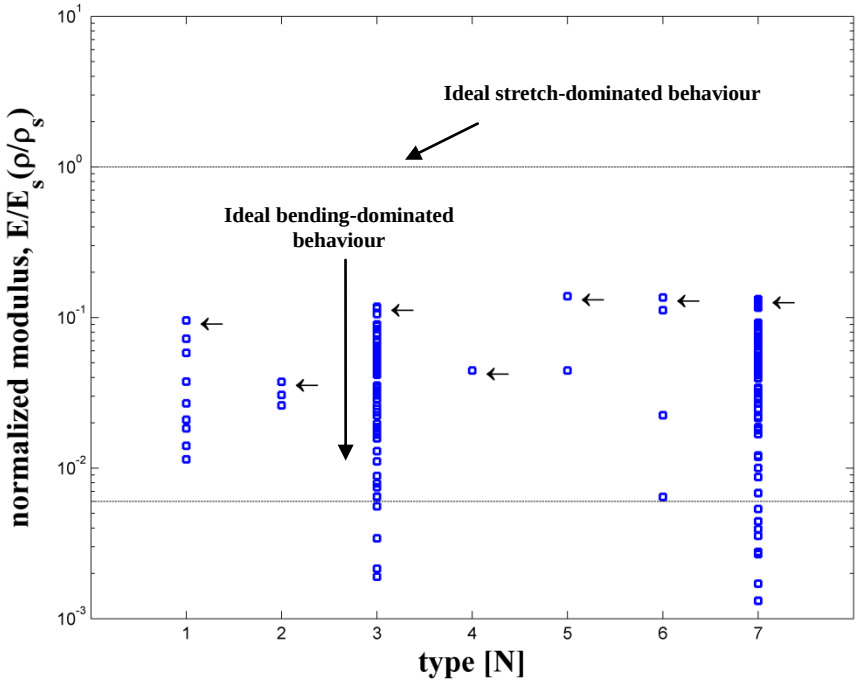

a)

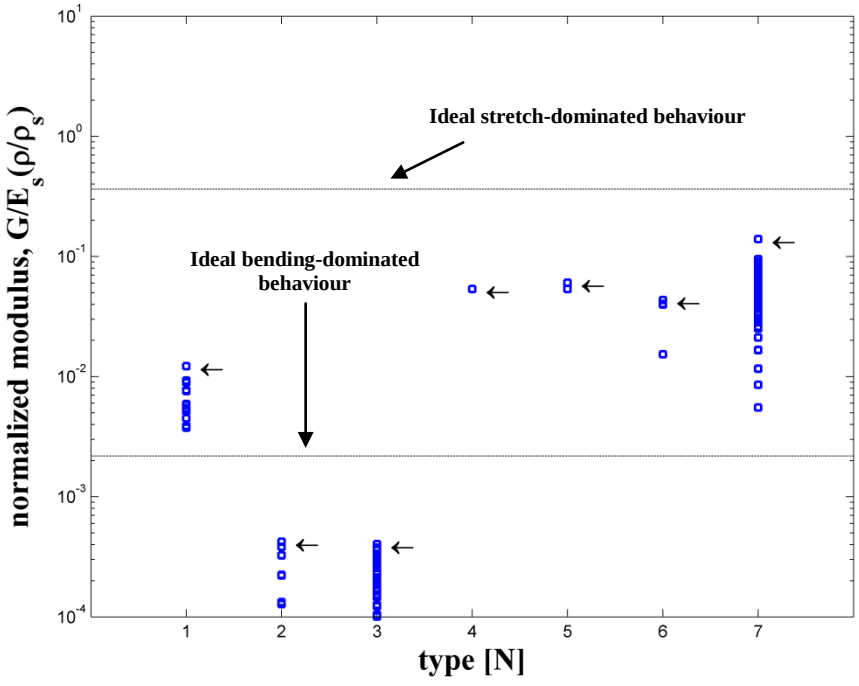

b)

Figure 4.13 (a and b). Solutions showing near-zero CTEs. The arrows indicate the structures with a) higher stiffness, E_{max}; b) higher shear, G_{max}.

PTE designs.

Table 4.6 shows the numerically generated solutions for each type considered, showing positive thermal expansivity in the out-of-plane direction, combined either with maximised stiffness in *y* direction or maximised shear stiffness in *x-y* direction. Positive CTEs were identified in values of normalised CTEs higher or equal to 1.5, as shown in Figure 4.14. Several solutions were found to lie below the broken line, indicating the ideal bending-dominated behaviour of lattice structures. 'Type 7'-structure, *l*, in the form presented in Table 4.6, had the best compromise between positive CTE and maximised stiffness, Figure 4.14a. It shows stiffness 125 times higher than an ideal monolithic bending-dominated structure on an iso-volume basis, combined with a CTE 1.5 times higher. 'Type 7'-structure, *h*, in the form presented in Table 4.6, had the best compromise between positive CTE and maximised shear, Figure 4.14b. It shows a stiffness 55 times higher than an ideal monolithic bending-dominated structure on an iso-volume basis, combined with a near-zero normalised CTE. Also in this case, 'type 2' and 'type 3' structures show performance similar or below the ideal bending-dominated shear behaviour, see Figure 4.14b.

	PTE			
	E_{max}		G_{max}	
type 1	*a*		*a*	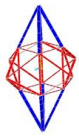
type 2	*a*	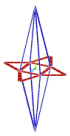	*a*	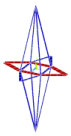
type 3	*a*	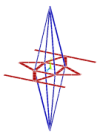	*a*	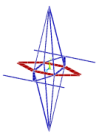
type 4	*a*	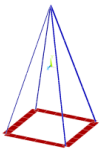	*a*	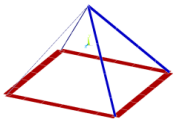
type 5	*a*	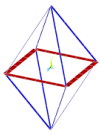	*a*	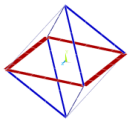
type 6	*a*	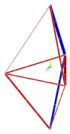	*a*	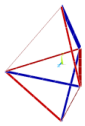
type 7	*l*	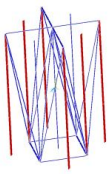	*h*	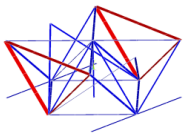

Table 4.6. Designs showing positive CTEs combined with high mechanical performance for all the proposed 'type [N]' cases.

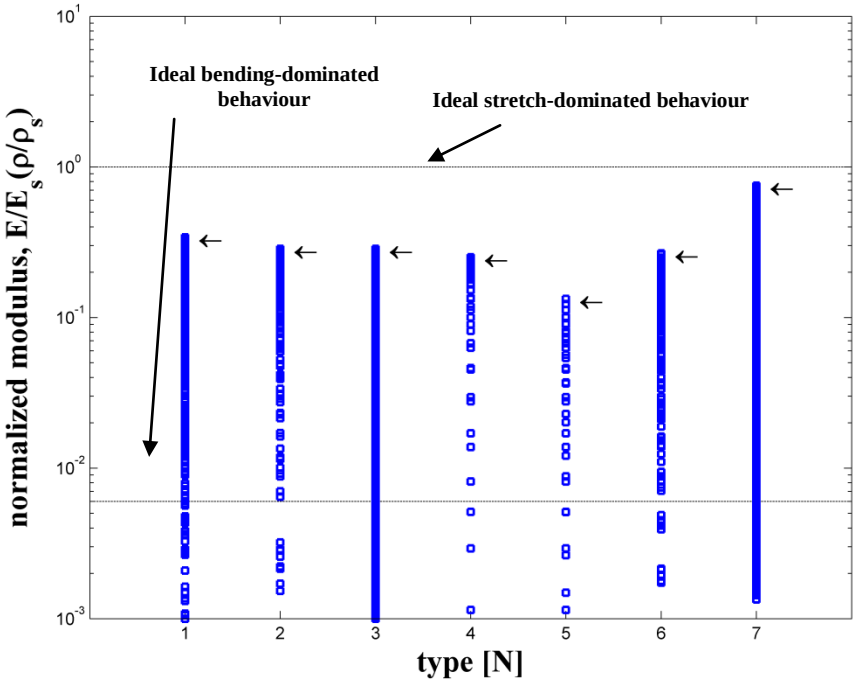

a)

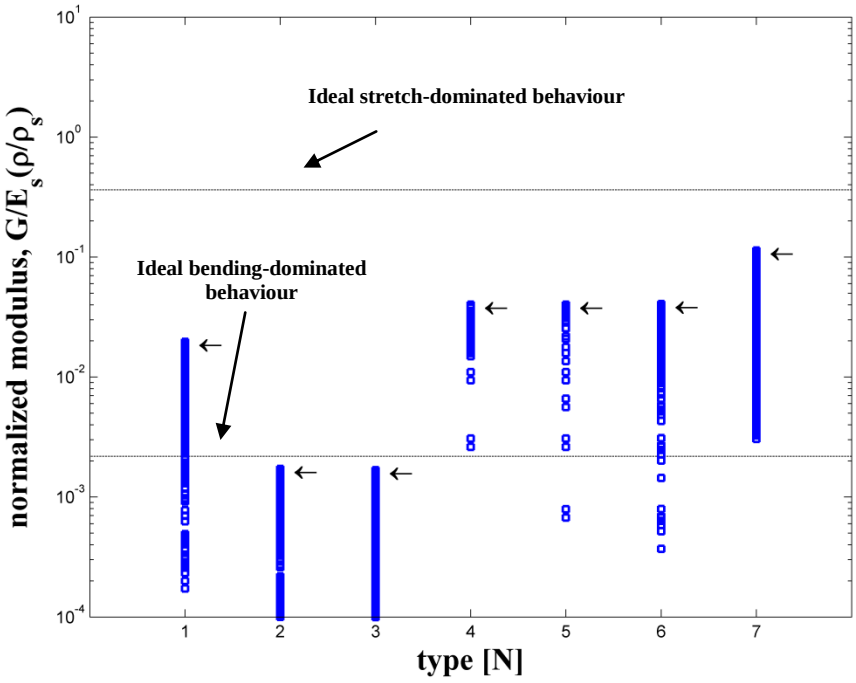

b)

Figure 4.14 (a and b). Solutions showing positive CTEs. The arrows indicate the structures with a) higher stiffness, E_{max}; b) higher shear, G_{max}.

4.4 Discussion

It is clear that the method used is a simple and robust method to produce 3D, and potentially also 2D, truss structures starting from node locations, node connectivity and the number of beams of quarter or eighth models of the final RVE units. Seven initial base geometrical truss structures were proposed but potentially an infinite number of possible geometries could be generated and solved employing this methodology. Since the space of possible structures is infinite, the examples proposed in this chapter were a continuation of what was explored in Chapter 3. However, results produced, employing a higher number of initial base geometrical truss structures, seem not to have added any further solution trends in addition to those already shown with the seven cases already explored. Therefore, the solutions reported in this chapter can be considered exhaustive of the thermomechanical behaviour of such truss structures. Structures proposed in Chapter 3 were used as initial truss structures herein. The aim was to populate the response surface for 3D dual-material trusses, within the limitations and constraints imposed.

A particular advantage of this methodology was the possibility of comparing all the generated structures on an iso-volume basis for dual-materials against monolithic structures, and an iso-volume, combined with iso-mass for all the dual-material structures. This permits the ranking, by performance, of each structure, as shown in Figure 4.9, Figure 4.10 and Figure 4.11. Results, in terms of CTEs and other mechanical properties, confirm the trend shown in Chapter 3, which is mainly due to the marked influence of the aspect ratios on the CTEs of the structures proposed. The results show that it is possible to obtain several values of thermomechanical properties simply by adjusting the location of the dual materials within the truss structure and the aspect ratios of the cell. It is possible to tailor

simultaneously large negative CTE and large positive CTE structures by simply swapping the configurations of dual materials inside the same unit cell.

Young's modulus, shear modulus and Poisson's ratio were largely affected by the aspect ratio of the unit cells. The particular geometry of each generated structure defines the particular trend of the thermomechanical property considered. All the trends found are plotted against the aspect ratio of the unit cells. Results are consistent with Equations 3.11 to 3.24 in Chapter 3. Results show how different arrangement of the phases inside the units affects these properties substantially. For each 'type [N]' structure proposed, it is possible to generate a relatively wide band of behaviours, depending mostly on the possible combinations of phases and physical properties of the constituent materials in each 'type [N]' case, see Figure 4.3 to Figure 4.8. 'Type 3' and 'type 7' had the widest bands of possible solutions.

Extreme values of the Poisson's ratio were found for 'type 2', 'type 3' and 'type 7' structures. This is the result of the particular geometries generated, the aspect ratio of the unit cells, the phase arrangements and the physical properties of the constituent materials. All this was found to influence the Poisson's ratio of the structures.

Relative moduli plotted against CTEs, Figure 4.9, on logarithmic scales for dual-material 'types 1-7' structures, create a map of performance for these 'type [N]' structures and permit their classification in terms of their specific performance. All the types proposed lie in between the ideal behaviour of stretch- and bending-dominated structures in terms of out-of-plane stiffnesses, Figure 4.9a. Some of these structures, generated from 'types 1-7', lie below the ideal bending-dominated behaviour. These structures were mostly the ones with the lower aspect ratio and not fully stretch-dominated.

Figure 4.10 and Figure 4.11 show the anisotropy of the proposed structures. All the 'type [N]' cases are highly anisotropic for values of the CTE higher or equal to the unity. Symmetrical behaviour is shown in *x* and *z* direction. The degree of anisotropy reduces if near-zero CTEs are considered.

The approach used permitted the identification of alternative designs, showing anomalous CTEs, combined with maximised mechanical properties in accordance with set criteria. 'Types 1-7' structures, showing negative thermal expansivity and maximised Young's modulus, are similar to those proposed in Chapter 3, in terms of aspect ratios, and the disposition of the two phases, see Table 4.4. This confirms that truss structures proposed in Chapter 3 represent an optimised solution for applications, where largely reduced CTE, combined with high mechanical performance are required. In general, the proposed new designs match the guidelines set in Chapter 3. Alternative arrangements of phases and materials are shown in Table 4.5 and Table 4.6. It is worth noting that inclined, at around 45 degrees, low thermal expansivity beam members are proposed as the better solution to maximise the shear modulus, combining it with anomalous CTEs, see 'type 7' in Table 4.4, Table 4.5 and Table 4.6. Solutions proposed seemed to be better performing than bending-dominated structures. Some designs were around 60 times better performing than their monolithic bending-dominated structures, and showed a completely unconstrained CTE in at least one direction, Figure 4.12, Figure 4.13 and Figure 4.14.

In some cases ratios of thermal expansion of ± 200 were found, 'type 3', 'type 5' and 'type 6', see Figure 4.3c, e and f. Although these solutions appear to be unlikely, they are the result of an extreme aspect ratio, *h/b*, and arrangements of the phases which modify the internal architectures of the pyramidal or triangular structures in the unit cells, triggering in

these cases an extreme mechanism that drives extreme positive or negative coefficients of thermal expansivity in the structures. However these results are true very locally and actual non-linear states might be achieved by larger changes in temperature. Buckling and collapse of the structure could be expected for these configurations.

The approach and the results presented in this chapter could be used to generate response surfaces for each generated structure to be exploited by advanced optimisation tools. This could be a useful tool to design high-performance trusses combined with altered thermal behaviours.

4.5 Conclusion

A numerical approach to generate high-performance lattice structures has been presented in both dual-material and monolithic configurations. All the possible structures have been generated, employing a combinatorial approach under specified constraints. Seven initial base geometrical truss structures were proposed. The response surface, consisting of all the possible solutions, was populated and solutions compared with well-established benchmarks. This permitted the classification of the 'type [N]' proposed structures, according to their performance. The range of all the possible elastic properties for dual-material and monolithic structures has been simulated and values quantified.

Alternative designs, showing excellent performance compared to stretch- and bending-dominated monolithic structures combined with anomalous thermal expansivity, were presented. Results, in terms of performance, were, in some cases, between 20 to 100 times greater compared with bending-dominated structures in both axial and shear

stiffnesses. All the solutions showed the possibility of tailoring CTEs, in particular negative, near-zero and positive, combined with high mechanical performance.

A rigorous and consistent comparison between new topologies generated and those in the literature must be carried out in order to assess whether the new designs ever generate enhanced solutions in relation to those in the literature. This chapter does not provide full comparison between the new topologies and those presented in the past literature. Therefore, this chapter cannot prove that the new topologies have absolute enhanced properties compared to competitors. However, this research presents preliminary comparisons and further investigations could form part of future research work.

5 EXPERIMENTAL MEASUREMENT OF THERMAL EXPANSIVITY FOR 2D/3D STRUCTURES

5.1 Introduction

Experimental measurement of the CTE of various dual-material lattice structures, notably those proposed in Chapters 2, 3 and 4, is undertaken in this chapter.

Physical samples of dual-material lattices were constructed using common materials, i.e. aluminium and titanium alloys, and fabricated by bonding beam members with an epoxy adhesive. There have been few such prototypes of dual-material lattices despite being the focus of several articles in the research literature. Qi and Halloran (2004) co-extruded a demonstration material and characterised it, demonstrating a negative CTE, as predicted. A recent paper by Steeves et al. (2009) described the testing of a 2D dual-material bonded framework, also fabricated from commonly available materials. The experimental measurements of CTE in this chapter will explore the accuracy of the models developed in previous chapters.

In this chapter, we extend the experimental validation to 2D and 3D dual-material truss structures in both monolithic and dual-material configurations, trying to validate the analytical and numerical models, and addressing any limitation due to the particular manufacturing process employed. Experimental measurements were conducted using an insulated heated chamber, built in-house combined with a dial gauge to measure linear displacements (and direct contact instrument).

5.2 Measurement system selection

Several systems were considered in order to measure the thermal expansivity of the structures proposed. Dynamic mechanical analysis (DMA) and thermomechanical analysis (TMA) were the first to be considered because of their nanometer resolutions, (Qi and Halloran, 2004). Although these technologies are well established to measure linear displacements and are commercially available, they were excluded because of the impossibility of easily manufacturing the dual-material structure samples on a very small scale, up to few millimetres, as required by these types of equipments.

Optical extensometry techniques were also considered (Furness and Clyne, 1991). The most recent models of laser extensometers can offer high accuracy and they are able to accurately measure a wide variety of materials, including high modulus composites, metals, plastics and elastomers. They offer all the advantages of non-contact methods. The use of a high-resolution optical extensometer was also discarded because of the high cost of the equipment.

Attempts to measure the thermal expansivity in lattice structures, with the aid of a high-resolution digital optical camera, was recently reported by Steeves et al. (2009). Results were than elaborated by digital image correlation software. A similar procedure was applied to the 2D structures proposed in Chapter 2. Although this methodology (by video extensometer) gave successful results in the pre-testing of 2D triangulated structures, it was not easily applicable to fully 3D structures. Therefore, other in-house methodologies were explored.

In general, several laser optical lever principles were also considered. The optical lever, a 'contact mode' technique, operates by reflecting a laser beam off the cantilever. The

optical lever greatly magnifies motions of the tip, guaranteeing high accuracy in the measurement. However, because of the high cost of such commercially available equipment and because of the complexity of building such devices in-house, alternative 'contact mode' techniques were developed in-house and used to measure the CTEs of 2D and 3D structures herein investigated.

An in-house insulated heated chamber, combined with the use of a contact measuring method as a dial gauge, was preferred because of the simplicity of construction and use, and for the reasonable accuracy obtainable for relatively large-scale samples.

5.2.1 Insulated heated chamber and dial gauge

A bespoke square based insulated heated chamber was built in-house. The chamber was designed in order to use relatively large-scale truss structure samples up to 130 mm in width and up to 200 mm in height. Several samples of around these dimensions were manufactured. The relatively large-scale samples facilitated the tests and increased the accuracy of the measurements. Thermal Ceramics Superwool® Fibre mat was used to fully insulate the heated chamber. In addition, the overall dimensions of the oven were designed to minimise the thermal dispersion.

Inside the chamber, the environment was heated by cartridge heaters disposed uniformly on the base of the chamber, activated in accordance with thermocouples used to measure the temperature. Power calculations were employed, using the data provided by the cartridge heaters' supplier. The heaters required power to heat up the chamber and the corresponding power of each heater was calculated. K type thermocouples were in contact with the beam members of the structures tested and coupled to controllers outside, in order

to prevent a non-uniform distribution of the temperature inside the chamber and along the structures.

A dial gauge (resolution 0.001 mm, 2119-50, Mitutoyo, Japan), see Figure 5.1, which was found to be at room temperature throughout each experiment, was placed outside the heated chamber and used to measure thermal distortion, as described in detail in Section 5.3.

Figure 5.1. Dial gauge (resolution 0.001 mm, 2119-50, Mitutoyo, Japan).

5.3 Sample preparation and CTE testing

Sample preparation.

Experimental tests and validation of the model predictions was undertaken using physical samples with the Lattice 2 geometry, see Chapter 2, and prototype samples of the double square based pyramid geometry (SqBasedPyr), see Chapter 3.

Lattice 2 geometry was considered since this was the configuration that permitted a remarkable reduction of CTE in at least one direction, the *x* direction. Because of the symmetry within Lattice 2, the experimental samples could be made as half-unit cells, see

Figure 5.2. The half-unit cells were of length l = 105.18 mm and height h = 103.54 mm (relative lengths of the beams b/a equal to 1.40).

Three prototype samples of the double square based pyramid geometry (SqBasedPyr) at different aspect ratios were fabricated, since this was the least complex geometry to manufacture and was predicted to exhibit a large reduction of CTE in the one axis, see Figure 5.3. The aspect ratios of the samples were chosen in order that one sample would exhibit a large positive CTE (aspect ratio h/b equal around 2), the second, a near-zero CTE (aspect ratio h/b equal around 1.8), and the third, a large negative CTE (aspect ratio h/b equal to 0.86).

The low CTE beam members were grade 2 titanium (Durbin Metal Industries Ltd, UK) and the high CTE beam members were aluminium 6082 (Durbin Metal Industries Ltd, UK), all solid and with cross-sectional diameters of 3 mm. As can be seen in Figure 5.2 and Figure 5.3, the full thicknesses of the beams on the vertical edges were retained (for ease of manufacture), but since the thermally driven distortion increases pro rata with the extra thickness, this does not affect the results. The assembly members were pin-jointed and adhered using an epoxy resin (Rapid Epoxy Adhesive 80808, Araldite®) in an attempt to represent a welded framework, as was the case in the model.

Thermal properties of the constituent materials are reported in Table 5.1.

CTE testing.

Samples were positioned inside the chamber, and held with built in-house supports in order to permit the samples to retain the same position during the test. The samples and the dial gauge tip were constrained to stay collinear with the CTE direction in question. A bubble spirit level was used to check the vertical alignment of a quartz bar and of the samples.

A specifically designed thick rubber base was used to reduce vibration in the measurement system due to the external environment.

The quartz bar ($\alpha_l = 0.5 \times 10^{-6}\ K^{-1}$) was placed in contact with a suitable vertex of the sample, so that half the bar was inside the oven, in contact with the sample and the other half was outside the oven, in contact with the dial gauge, see Figure 5.1. As sample dimensions changed with temperature, this displaced the quartz bar and thus the dial gauge tip could be read and recorded manually along with the temperature at that time. Temperatures in the chamber, close to the heated lower chamber surface and to the point close to the highest point of the sample were measured using K type thermocouples and a digital readout. At least three different heating and cooling cycles were made for each sample. Measurements were taken from around 273.15 *K* up to around 338.15 *K*, at approximately 5-10 *K* intervals. Small quantities of liquid nitrogen were poured into the chamber to cool down the system and to bring the initial temperature to below 273.15 *K*, thereby permitting the extension of the temperature range in the experiment. The epoxy resin was found to soften at approximately 348.15 *K*. In order to avoid this, the upper limit of the temperature range was set to around 338.15 *K*. An overview of the measuring system is shown in Figure 5.4.

A linear regression was employed to characterise the relationship between the measured thermal strain, $\Delta L/L$, and temperature, ΔT, of several well-characterised samples of various materials, including metals, polymers and ceramics. These values were used to calculate the 'measured CTE' via the expression in Equation 1.1. Since the CTE of these materials was known, a calibration curve of 'measured CTE' to 'known CTE' could be established, allowing correction of the experimentally measured values.

A typical thermal strain against temperature curve, generated for the samples tested, is reported in Figure 5.5, for instance. The slope of the best fit line is the measured CTE in that particular direction for that structure. The equation of the best fit line of the calibration curve, in Figure 5.6, was subsequently used to convert the measured CTE to the 'actual' thermal expansivity of the samples tested.

Material	E *(GPa)*	ν	ρ *(g/cm^3)*	α *(× 10^{-6} K^{-1})*
Al	73	0.33	2.77	23.30
Ti	114	0.32	4.54	9.26
Al 6082	73.20	0.33	2.77	24
Grade 2 Ti	114	0.32	4.54	9.10

Table 5.1. Mechanical properties of the materials considered in the case studies and in the experimental validation.

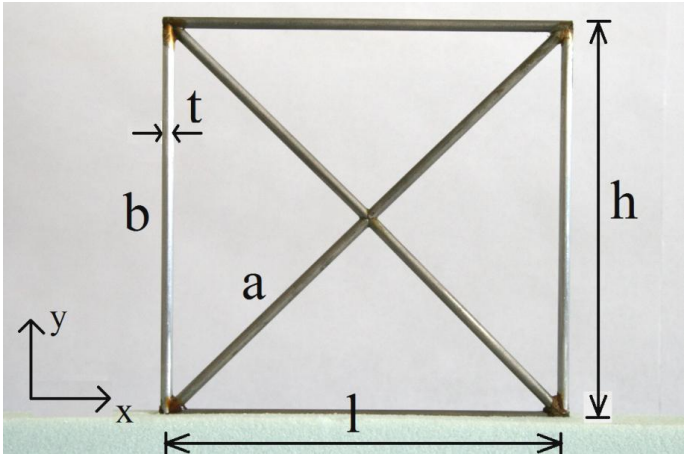

Figure 5.2. Dual-material physical sample with the Lattice 2 geometry; a low CTE beam members, b high CTE beam members (real picture).

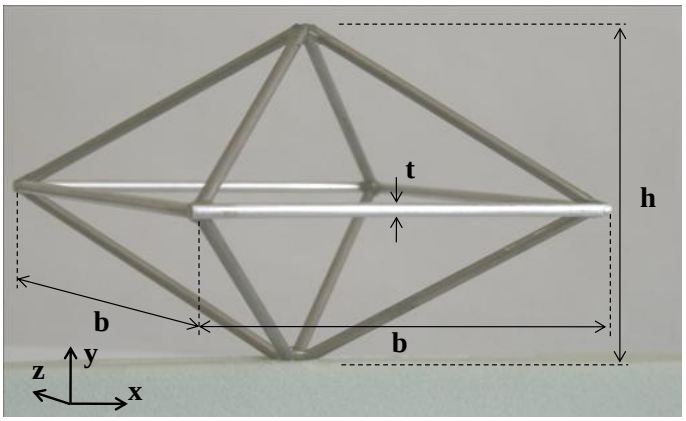

Figure 5.3. Dual-material physical sample: SqBasedPyr with negative thermal expansivity geometry. Low thermal expansivity beam members along h; high themal expansivity beam members along b (real picture).

Figure 5.4. Measuring system designed and controllers (real picture).

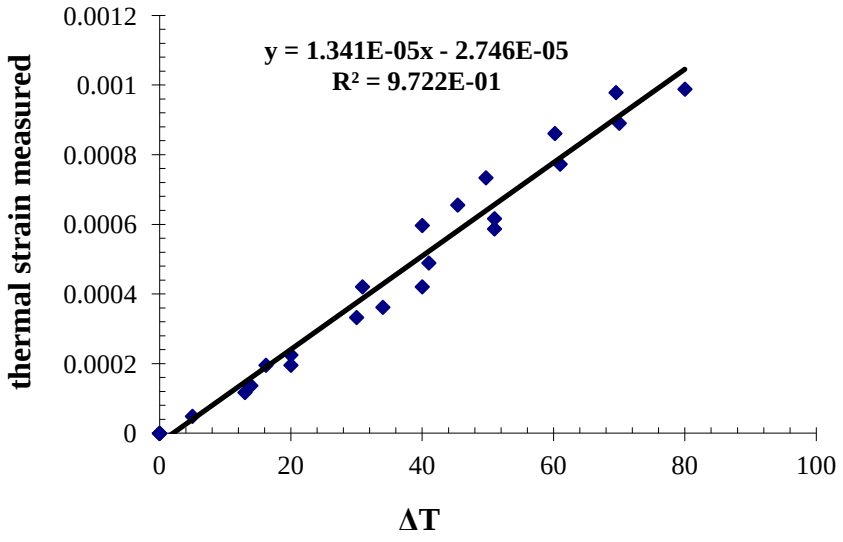

Figure 5.5. Example of thermal strain vs. variation of temperature, ΔT.

5.4 Calibration and Precision.

The experimental system, discussed in Section 5.2.1, was calibrated using samples of well-characterised materials; quartz (Robson Scientific, UK), grade 2 titanium (Durbin Metal Industries Ltd, UK), AL 403™ stainless steel (Durbin Metal Industries Ltd, UK), aluminium 6082 (Durbin Metal Industries Ltd, UK), clear extruded acrylic (Durbin Metal Industries Ltd, UK), Teflon® PTFE (DuPont, USA), and nylon 66 unreinforced (RS, UK). The experimental system precision was checked by repeatedly testing a single sample. This process allowed a reduction of errors associated with the thermal expansion of the equipment itself, e.g. the heating plate and quartz bar, since this was included in the calibration process. A linear regression was employed to characterise the relationship between the measured thermal strain and temperature for these calibration materials.

The line of best fit ($y = mx + b$) was computed from a sample of measurements of x and y, with x, known CTEs and y, measured CTEs. The confidence interval, CI, for the predicted y value for a given value of the independent variable x was computed using:

$$CI = \mp t(\alpha, df) S_{yx} \sqrt{\frac{1}{n} + \frac{(x_i - \bar{x})^2}{\sum_{i-1}^{n}(x_i - \bar{x})^2}}$$

5.1

where t is the critical t statistic, S_{yx} the standard error of the estimate, x_i the given value of x, $\bar{x}$ is the average of the x values and n is the number of observations used in the regression analysis.

The final formula to compute the upper and lower confidence interval was:

$$y \mp CI = (mx + b) \mp t(\alpha, df) S_{yx} \sqrt{\frac{1}{n} + \frac{(x_i - \bar{x})^2}{\sum_{i-1}^{n}(x_i - \bar{x})^2}}$$

5.2

with $\alpha = 0.05$ for a 95% confidence interval and $df = n - 2$

The calibration curve thus computed for the experimental system is shown in Figure 5.6. It is clear that the system was linear over the temperature range considered and scatter was relatively small. A 95% confidence interval is shown in Figure 5.6 which was used to give error values for experimentally measured CTE data, which were specifically between ± 1.6% and ± 30%.

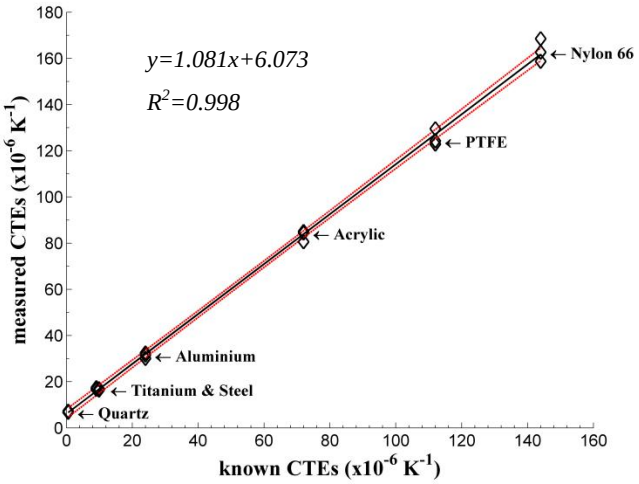

Figure 5.6. Calibration curve of the CTE measuring device. Measured values of CTE are plotted against known values of CTE, with a line of best fit and dashed lines indicating a 95% confidence band.

5.5 Results

To validate the model, it was helpful to compare measured and predicted CTE data for the experimental samples.

The model prediction and experimentally measured CTE values are given in Table 5.2 for Lattice 2, discussed in Chapter 2, and in Table 5.3 for the SqBasedPyr, representing large positive, near-zero and large negative CTE, discussed in Chapter 3. All the samples were tested in dual-material form at least in the direction where a change in CTEs is predicted. The dimension of some 3D prototypes (SqBasedPyr, representing large positive and near-zero CTEs) did not permit measurement of the CTE in *x* direction for such samples because of the restriction, due to the dimension of the chamber. Since no change in CTE was predicted in that direction for these dual-material and, obviously, monolithic structures, the test can be considered fully exhaustive in terms of results, without considering the measurements in *x* direction for them. Two monolithic samples, in the form

of Lattice 2 and SqBasedPyr, representing large negative CTE, were also tested for completeness.

As expected, the predicted and measured CTE values for the monolithic Lattice 2 are very similar, and consistent in both *x* and *y* axes with the CTE of solid aluminium. The difference between the model prediction and experimental measurements for the dual-material sample was slightly higher, approximately 8 %, see Table 5.2.

	Lattice Type		
Monolithic Al 6082		Lattice 2	
	Model prediction	Experimental	Difference %
α_x ($\times 10^{-6}\ K^{-1}$)	24	24.32 ± 1.19	1.3
α_y ($\times 10^{-6}\ K^{-1}$)	24	23.68 ±1.19	-1.3
Dual Al 6082/grade 2 Ti		Lattice 2	
	Model prediction	Experimental	Difference %
α_x ($\times 10^{-6}\ K^{-1}$)	6.35	6.78 ±0.94	6.8
α_y ($\times 10^{-6}\ K^{-1}$)	19.78	21.6 ±1.18	9.0

Table 5.2. The model predicted and experimentally measured CTE values for the monolithic and dual-material Lattice 2 samples.

Predicted and experimentally measured CTE values are given in Table 5.3 for the SqBasedPyr in dual and monolithic forms, representing large positive, near-zero and large negative CTEs. Results are consistent between the predicted and measured data in both *x* and *y* axes for the monolithic structure. There were differences between predictions and experimental measurements for the dual-material samples, ranging between 7% and 40% in the measurement of α_y, particularly for the negative CTE structure, which had large internal stresses (Palumbo et al., 2011). This error arises because of slip in the adhesive joints between beam members. There were no notable differences between prediction and measurements in the data for CTE in the *x* axis.

The FE models predict the properties of the trusses sufficiently well.

	Lattice Type		
Monolithic Al 6082	SqBasedPyr		
	Model prediction	Experimental	Difference %
α_x ($\times 10^{-6}\ K^{-1}$)	24	23.4 ± 1.2	-2.61
α_y ($\times 10^{-6}\ K^{-1}$)	24	22.5 ± 1.2	-6.30
Dual Al 6082/grade 2 Ti	SqBasedPyr (Negative thermal expansivity)		
	Model prediction	Experimental	Difference %
α_x ($\times 10^{-6}\ K^{-1}$)	24	23.9 ± 1.2	-0.3
α_y ($\times 10^{-6}\ K^{-1}$)	-30.8	-18.1 ± 3.1	-41.0
Dual Al 6082/grade 2 Ti	SqBasedPyr (Positive thermal expansivity)		
	Model prediction	Experimental	Difference %
α_y ($\times 10^{-6}\ K^{-1}$)	1.6	1.5 ± 0.4	-7.8
Dual Al 6082/grade 2 Ti	SqBasedPyr (Near-zero thermal expansivity)		
	Model prediction	Experimental	Difference %
α_y ($\times 10^{-6}\ K^{-1}$)	-0.128	-0.106 ± 0.04	-17.2

Table 5.3. The predicted and experimentally measured CTE values for the monolithic and dual-material SqBasedPyr samples.

5.6 Discussion

The models, developed in Chapters 2 and 3, were validated well by the tests on the experimental samples. The small differences in predicted and measured CTEs were likely to be due to i) manufacturing imperfections (non-ideal geometry of the lattice joints), and probably most significantly ii) the finite thickness of the beam members in the experimental samples. Permanent relative displacements of the rods at junctions were visible, indicating that the adhesive had allowed some slipping, most likely at the higher temperatures. The model takes no account of the thickness of the beam members since they are considered to be welded (rigid-jointed) at a point, whereas the samples were welded over finite areas and

their finite thicknesses reduced the effective length of the beam members, see Figure 5.2 and Figure 5.3.

The model predicted sensitivity to relative beam lengths, *b/a*, Lattice 2, and to the aspect ratio of the unit cell, *h/b*, SqBasedPyr, as shown in Table 5.2 and Table 5.3.

Differences between predicted and measured CTEs were also due to creep of the adhesive bonds between beam members, notably in the SqBasedPyr negative CTE structure, which has significant thermally driven internal stresses, see Table 5.3. Although this method of joining such structures has proven unsuitable for application, it nevertheless demonstrates well-tailored CTEs, including negative values. Other methods for joining and/or manufacturing, such as additive layer manufacturing (ALM), appear to be suitable alternatives, albeit they require further development for dual-material structures manufacturing (Mazumder et al., 2000).

Manufacturing of lattices at smaller size scales, using two materials, may present more of a challenge. The leading method for truss cores would seem to be additive layer manufacturing, a rapidly developing area in which multi-material methods are beginning to come to maturity (Stampfl et al., 2004; Willich, 2007). Other alternatives include wire bending operations with secondary brazing processes to join assemblies of dissimilar wires (Wadley et al., 2003).

5.7 Conclusion

Low CTE lattices, comprising grade 2 Ti and Al 6082, were manufactured and tested in a thermal environment. Measurements were conducted using a built in-house heated chamber combined with a high precision dial gauge. Results obtained agree well

with the models' predictions presented in the previous chapters, and demonstrate clearly large negative CTE.

Adhesive-bonding combined with pin-joints was demonstrated to be adequate to join metallic components of a relatively large size. Manufacturing of such lattice structures seems to require nothing new for large-scale constructions and to be possible, via emerging manufacturing technologies, for smaller scale ones.

6 FINITE ELEMENT MODELLING OF TRUSS CORE SANDWICHES

6.1 Introduction

Many applications are based upon sandwich panel concepts, for example the floors, bulkheads, and even the skin and wings of aircraft. Cores forming the centre of sandwich panels usually have prismatic or honeycomb topologies (Wadley, 2006). Although closed-cell honeycomb topology systems can offer superior structural performance, open-cell structures such as truss structures or lattices have recently attracted interest because they provide multifunctional capabilities such as heat exchange, impact protection, actuation and thermal management (Hayes et al., 2004; Rathbun et al., 2006; Wicks and Hutchinson, 2004). Their use in structural applications is still subject to severe constraints related to their low elastic moduli and strength compared to closed-cell topologies.

Numerous truss structures can be configured as the cores of sandwich panels. Chapters 2, 3 and 4 present trusses configured so that their members experience predominantly axial stresses when they are used in sandwich panels that are loaded in bending (i.e. stretch-dominated cores). The strength of such cores is governed by the collapse modes they undergo. These failure modes are well-known and include yielding of the face sheets, wrinkling, shear of the truss core and indentation (Allen and Evans, 2003; Deshpande and Fleck, 2001). The thermomechanical behaviour of such two-dimensional and three-dimensional structures and their optimisation under shear and axial loading have been fully discussed in Chapters 2, 3 and 4.

The stiffness of such truss structures is related to the material properties of the constituent material and the specific geometry considered (Gibson and Ashby, 1999a).

In high-performance aerospace applications, high strength, high modulus and low-density titanium and aluminium alloys are widely used. In the last decade, increasing interest has developed around metal matrix composites (MMC) due to their attractive strength, stiffness, fatigue, and thermal properties (Kunze and Bampton, 2001). In particular, titanium matrix composites (TMC) are the candidate material for a large number of potential aerospace applications (Moongkhamklang et al., 2008). Furthermore, high strength and modulus silicon carbide (SiC) fibres are used to reinforce in a titanium alloy matrix to enhance the mechanical properties in applications where high specific strength is required (Buck, 1987). Such composites usually exhibit reduced values of CTE (Kunze and Bampton, 2001).

Innovative methods have been developed for fabricating small-scale lattice structures, such as additive layer manufacturing (ALM), (Reeves, 2008; Williams et al., 2010). This fabrication permits the manufacture of complex geometries without the limitation of traditional manufacturing processes in terms of geometry complexity and time.

In this chapter, an application proposed by the sponsor EADS, Innovation Works Ltd, UK, was chosen as a case study in which ALM manufacturing technology could be used to fabricate an optimised truss core panel. A truss core sandwich design, optimised for ALM fabrication, was modelled using non-linear finite element code (Ansys, Inc.). The core geometry was chosen from the results set out in previous chapters and according to fabrication constraints. The truss core was fully fabricated in titanium by the project sponsor using an EOS™ M270 ALM process, specifically, a direct metal laser sintering

process (DMLS). A diffusion bonding process was subsequently used to assemble the truss core to face sheets of TMC made of Ti-6Al-4V matrix and SCS-6 fibres by a third company (TISICS Ltd).

Computational modelling of components under specific loading conditions has recently become a relatively fast and reliable method of simulating and predicting the mechanical behaviour of structures before they are experimentally tested, notably in industrial settings.

Finite element analysis was used to predict the behaviour of a truss core sandwich in three-point bending with a Ti-6Al-4V core, manufactured by ALM with bonded TMC face sheets. The main limitation with all modelling and simulation is that predictions are approximations and strongly reliant upon initial assumptions. The main assumptions in the present model included ideally perfect bonding between the truss core and the TMC face sheets, isotropic material behaviour of the TMC face sheets, and approximate boundary conditions to simulate a three-point bending test. Analytical validation of the FE model is presented. Fabrication and experimental testing of samples is to be undertaken by the sponsor company and is currently outstanding.

6.2 Methodology

The Finite Element (FE) method has been employed to simulate the behaviour of a truss core sandwich under three-point bending. The FE method captures the effects of geometric non-linearities along with material non-linearities. Therefore the model is capable of simulating the collapse of a truss core sandwich in three-point bending in both the linear and non-linear regions.

The model was based on the geometry of the manufactured test specimens. The experimental test will be performed by the sponsor, EADS, Innovation Works, Ltd, UK.

A FE analysis program Ansys, Inc., which allowed full non-linear material and geometrical behaviour was used to model both the pyramidal truss core (under compression and shear loading) and the pyramidal truss core sandwiched between TMC solid face sheets under three-point bending. Large displacements typically result in a change in the element orientation, and consequently, affect the element stiffness matrix. To deal with this, the element stiffness matrix was continuously updated using the Newton-Raphson iterative procedure. To determine the ultimate load (limit load for the perfectly plastic solid, for instance) of the structures, load steps were specified. At the end of each step, the program adjusted the stiffness matrix to reflect the non-linear changes in stiffness of the structure.

For the truss core beam members, a two-node 3D elastic beam (BEAM188) element was used, which is a quadratic beam element, with six degrees of freedom at each node. These include translations in the *x*, *y*, and *z* directions and rotations about the *x*, *y*, and *z* directions. This element is well suited for large strain and non-linear applications and it also allows 'transverse shear strain', that is, the cross-section may not necessarily remain normal to the beam axis (see Ansys, Inc., Release 11.0 Documentation). This extension leads to

Timoshenko beam theory and is generally considered useful for thicker beams, whose shear flexibility may be important.

Truss core face sheets were modelled by a four-node quadrilateral layered shell element (SHELL181). These element displacements are compatible with the beam element (BEAM188). This element can be used for layered applications, large rotation, and large strain non-linear applications. The accuracy in modelling shells is governed by the first order shear deformation theory (usually referred to as Mindlin-Reissner shell theory), see Ansys, Inc., Release 11.0 Documentation.

Truss core and face sheet materials' non-linearities are modelled defining non-linear material data (stress-strain curve) by multilinear isotropic hardening (MISO), using von Mises yield criterion. Stress and strain curves for the considered material were defined at the point corresponding to the yield and to the ultimate stress of the materials.

The failure mode for the truss core and the limit load for the sandwich panel were detected, in the areas where the loads were applied, through the comparison of the stresses by the von Mises criterion with the yield of the materials.

TRUSS CORE MODEL

A pyramidal truss core made from cylindrical beam members of radius, r, 0.5 mm, and length, 5.338 mm, was modelled. The repeating unit cell chosen as truss core, has already been optimised, see Chapters 3 and 4, showing excellent mass specific performance. The aspect ratio, $h/b \approx 1.1$ mm was selected in order to maximise the shear stiffness, important for sandwich panel applications. The dimensions of the unit cell were $b \approx 6.5$ mm, and $h \approx 7.2$ mm. The thickness of the bases, t_{ti}, was fixed at 0.7 mm. The overall

dimensions of the unit cell were also chosen to fit within constraints of the ALM manufacturing process.

The model was used to predict the behaviour of the truss core, in particular, to model the effective properties under axial and shear loading, and the collapse strength.

Figure 6.1 shows the considered repeating unit cell, in *x* and *z* directions with a uniform mesh.

The material employed for the truss core was a titanium alloy Ti-6Al-4V with a young modulus Es=114000 MPa and a yield strength σ_Y=880 MPa. It was modelled as an elasto-plastic solid that displays low hardening strain. The stress-strain curve of the material was generated, considering the yield stress and the ultimate tensile stress of the material, at around 1000 *MPa.*

A uniform mesh was used in both truss beam members and the bases of the core employing beams and shell elements, as discussed in the previous section (convergence test has been performed), see Figure 6.1.

Boundary conditions were applied to simulate the unit cell behaviour under axial and shear loading as fully described in Chapters 3 and 4.

The strain dependent compressive and shear stresses, σ_y-ε_y, and σ_{xy}-ε_{xy} were calculated for the unit cell, and the failure identified and located. Stresses were calculated according to Equations 3.1 and 3.3 in a similar way to that discussed in Chapter 3.

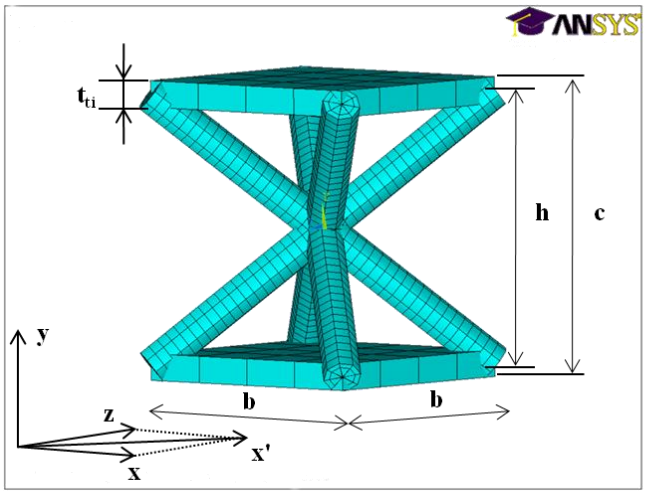

Figure 6.1. Truss core pyramidal unit cell model with uniform mesh. *x'* axis direction along the diagonal of the squared base.

TRUSS CORE SANDWICH MODEL

A truss core sandwich panel was modelled with the geometry as shown in Figure 6.2a, with 21 unit cells repeated in *x* direction, and 3 unit cells in *z* direction.

The model was used to predict the stiffness and collapse strength of the truss core sandwich panel under a three-point bending load.

Materials employed for the truss core were titanium alloy Ti-6Al-4V, as described previously. The face sheets were TMC. The axial Young's modulus can be estimated by the rule of the mixtures:

$$E_s = (1 - f)E_m + fE_f \qquad \textbf{6.1}$$

where f is the volume fraction of the SCS-6 fibre, and E_m and E_f are the Young's moduli of the Ti-6Al-4V matrix and SCS-6 fibre, respectively. For E_f=300000 *MPa*, E_m=114000 *MPA*, and f=0.3, Equation 6.1 gives E_s=169800 *MPa*. TMC was modelled as an isotropic elasto-ideally plastic solid with yield strength σ_Y=1450 *MPa*. Material

properties were fixed according to values relayed by the sponsor and were consistent with literature (Buck, 1987; Moongkhamklang et al., 2008). A more complex model, which may consider transversely isotropic or orthotropic material properties, for instance, would require the determination of specific constants to input in the FE model (see Ansys, Inc., Release 11.0 Documentation). These constants can be evaluated experimentally and input in the model when the experimental test is performed and will improve the accuracy of the model.

In the model, the truss core and face sheets were considered as continua. TMC face sheets of thickness t_{TMC}, 0.95 mm, were perfectly bonded to a truss core of thickness c, with $c=h+t_{ti}$. Figure 6.2a shows uniform mesh (convergence test has been performed), and Figure 6.2b shows boundary condition of the sandwich panel in three-point bending.

Boundary conditions were applied in order to simulate a three-point bend test (Gibson and Ashby, 1999b). The span between the outer supports on the base of the panel was L_p, and the overhang distance between the outer supports was b, the base dimension of a single unit cell. The translation in the y direction of all the nodes located in the extremity of the span L_p and along the width of the panel was restrained to simulate the supports at the base of the sandwich panel, see Figure 6.2b. A uniform displacement was applied in the axial direction (y direction), u_y, to the centre area of the top TMC face sheet on a surface equal to 2 times the element size by the width of panel, see Figure 6.2b, around 3 mm wide and $3b$ deep. In this way, the effect of a rectangular loading support of around 3 mm width was simulated. Since the elements and solutions were fully non-linear, displacements were applied iteratively (akin to discrete load steps) and the solution recorded at the convergence values. To ensure a symmetric response of the sandwich under three-point bending, as

expected, the nodes in the centre of the span on the top face sheet are constrained in the *x* direction.

The peak load versus deflection of the sandwich was predicted. The load limit was found by evaluating the reaction force in correspondence of the centre area, where the uniform displacement u_y was applied.

Collapse modes of the sandwich panel were predicted evaluating the stress in the core and in the face sheet of the sandwich panel for each value of deflection considered. Specifically, the stresses in *x* direction were considered for TMC face sheets (Deshpande and Fleck, 2001) and maximum stresses were considered for the beam elements of the truss core as being failure critical.

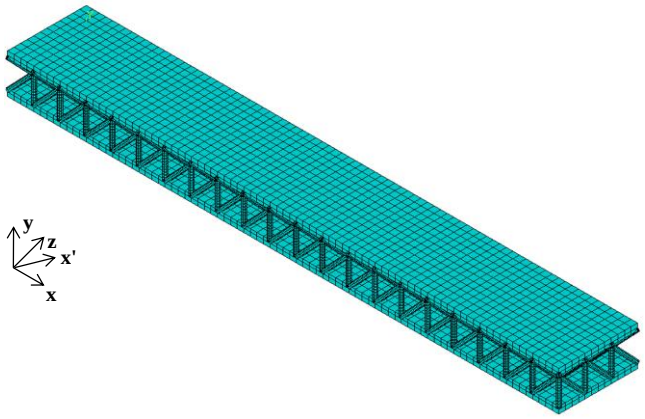

a)

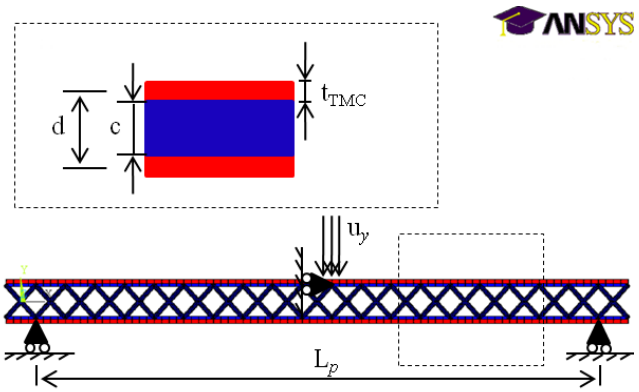

b)

Figure 6.2 (a and b). a) Sandwich panel with uniform mesh; b) sandwich panel under three-point bend loading boundary conditions; titanium alloy truss core (blue); titanium metal matrix composite (red).

6.2.1 Analytical modelling

The computational results were compared with analytical predictions for the effective properties of the truss core and for the stiffness of the sandwich panel under three-point bending.

The beam members of the pyramidal core were assumed to be bonded perfectly to the rigid faces and without friction, and the truss core was assumed to be stretch dominated (only deformed axially), the effective Young's modulus E_y and shear modulus G_{xy} are given by Equations 3.15 and 3.21 respectively, as discussed in Chapter 3. Therefore, the compressive stress and shear stress were calculated by Equations 3.1 and 3.3.

The elastic deflection, δ, is the sum of the flexural and shear deflections, (Allen and Evans, 2003):

$$\delta = \frac{FL_p^3}{48(EI)_{eq}} + \frac{FL_p}{4(AG)_{eq}}$$

6.2

The equivalent flexural rigidity, $(EI)_{eq}$, is

$$(EI)_{eq} \approx \frac{E_{11}^{f} btd^2}{2} \qquad \textbf{6.3}$$

where the Young's modulus of the face sheets in the 1-direction is corresponding to the Young's modulus in *x* direction of the TMC face sheets, E_s, as defined in Equation 6.1, and *t* is equal to t_{TMC}, as shown in Figure 6.2.

The equivalent shear rigidity, $(AG)_{eq}$, is

$$(AG)_{eq} \approx G_{13}^{c} bcd^2 \qquad \textbf{6.4}$$

where the shear modulus of the pyramidal core 13 direction is corresponding to the shear modulus in *xy* direction of the core, G_{xy}, as defined in Equation 3.21.

6.3 Results

TRUSS CORE MODELLING RESULTS

Compression loading in *y* direction and shear loading in *xy* direction simulations were conducted on the pyramidal truss core, considering a repeating unit cell, with the geometry shown in Figure 6.1.

The simulated uniaxial stress versus strain curve, σ_y versus ε_y, for the unit cell considered and the corresponding deformed shape are plotted in Figure 6.3a and Figure 6.4a, respectively. The stress versus strain curve exhibit peak strength of approximately 37 *MPa* set by yield failure at a strain of approximately 2.5%.

Similarly, the simulated shear stress versus strain response, σ_{xy} versus ε_{xy}, of the pyramidal unit cell is plotted in Figure 6.3b. Figure 6.4b shows the corresponding deformed shape. The stress versus strain curve exhibits peak strength of approximately 35 *MPa* set by yield failure at a strain of approximately 2.3%.

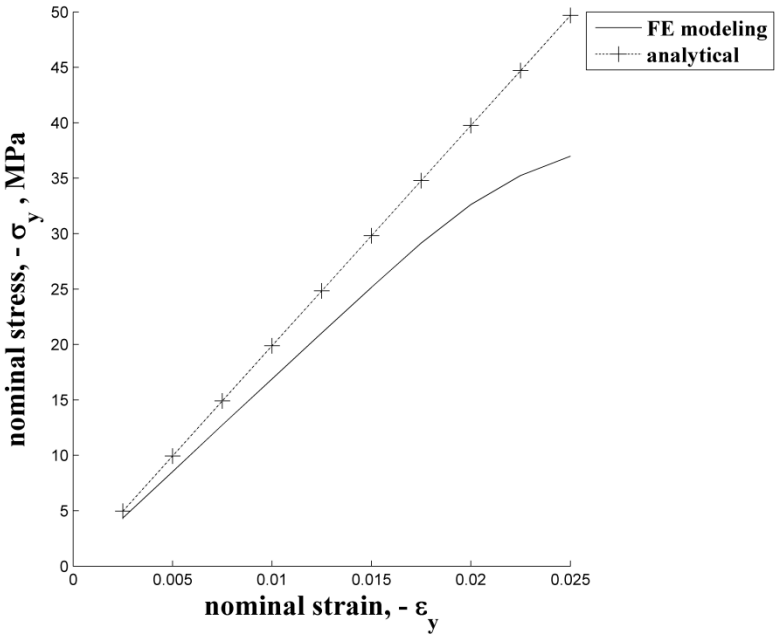

a)

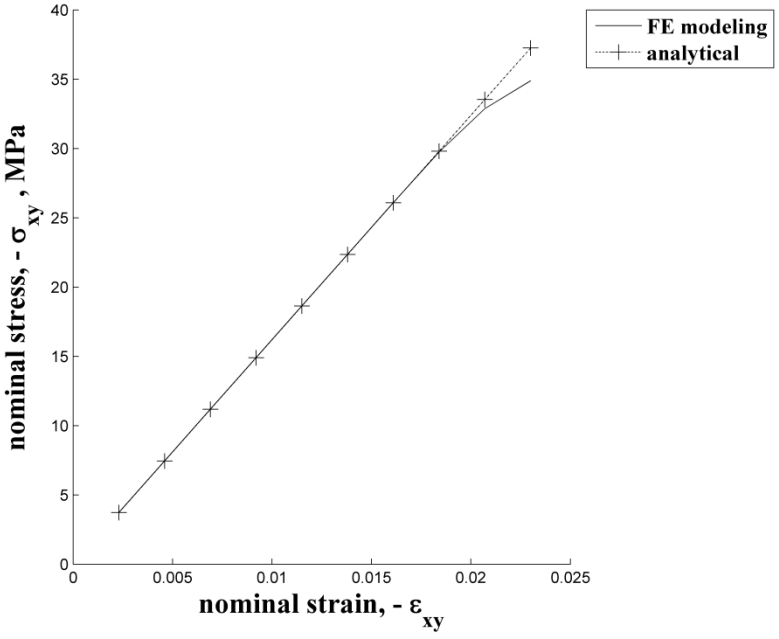

b)

Figure 6.3 (a and b). a) Uniaxial compressive stress versus strain response of the pyramidal core; b) Shear stress versus strain response of the pyramidal core. The dashed lines are analytical predictions.

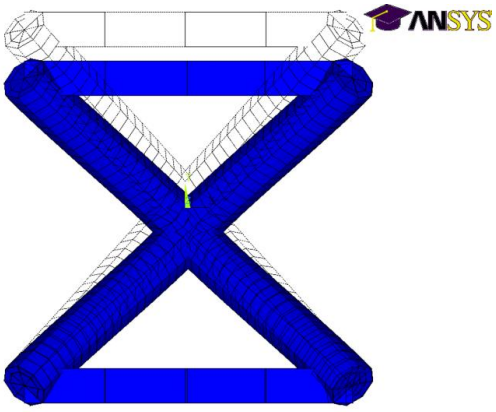

a)

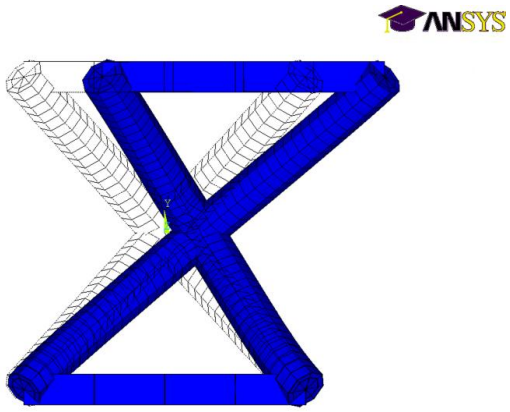

b)

Figure 6.4 (a and b). a) Contour plot of the deformed shape of the truss core unit cell under compressive load; b) Contour plot of the deformed shape of the truss core unit cell under shear load. The deformation is scaled with a factor of 10. In black it is the undeformed shape.

TRUSS CORE SANDWICH MODELLING RESULTS

The simulated collapse responses of the truss core sandwich panel are reported from Figure 6.5 to Figure 6.12. The predicted load versus deflection response is reported in Figure 6.5. The load increases monotonically with deflection until the beam members inclined to the load direction axis start to fail by yield.

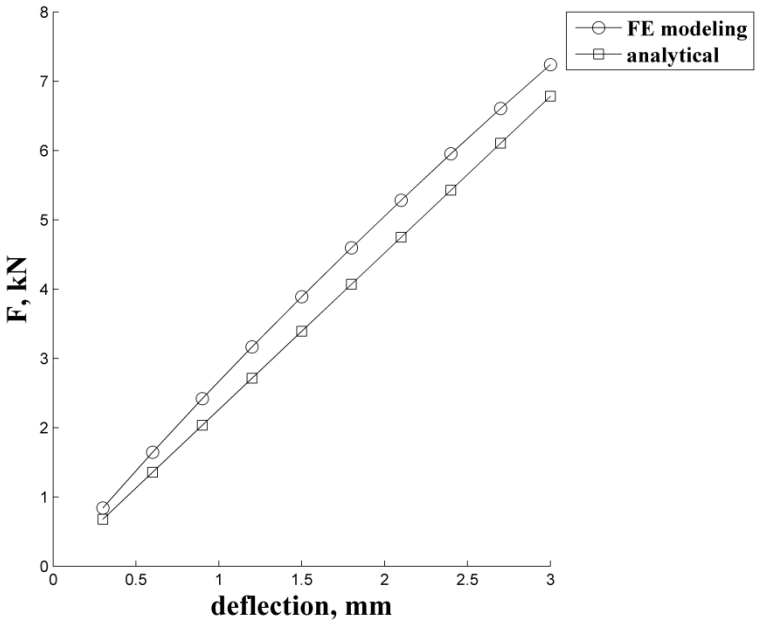

Figure 6.5. Computational and analytical load versus displacement response of the sandwich panel under three-point bending.

The contour plot of von Mises stress is shown in Figure 6.6 for the sandwich panel, with a maximal deflection of around 3 mm. It shows that there is a stress concentration in proximity to the middle span, where the central indenter is simulated. The largest stress levels are experienced on the top and bottom TMC face sheets and in the inclined beam members in the central area of the sandwich. These overall results are confirmed by the stress measured on the TMC face sheets and on the truss core, Figure 6.7 and Figure 6.9, and Figure 6.11, respectively.

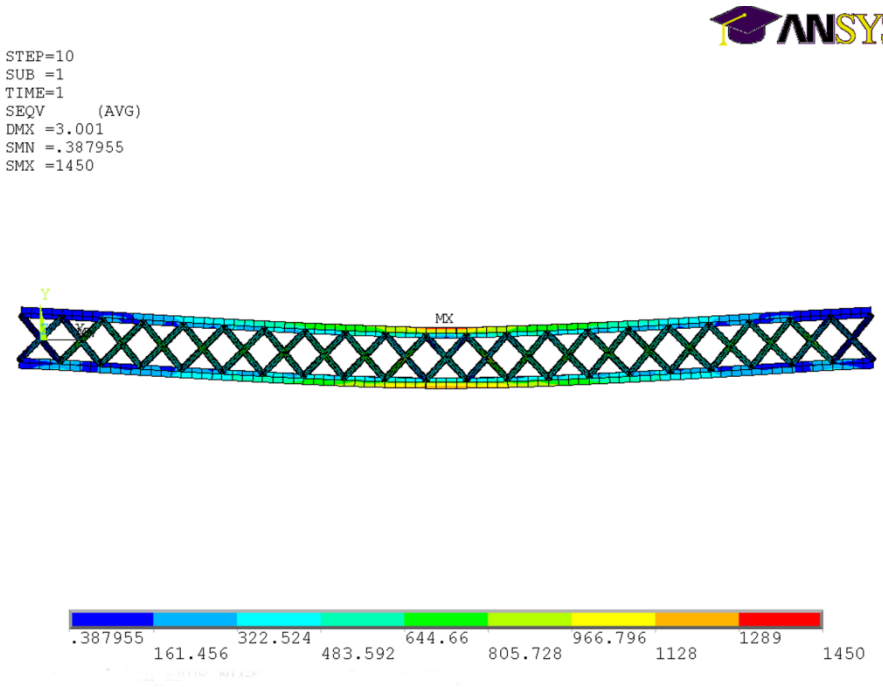

Figure 6.6. Contour plot of von Mises stress results.

Plastic collapse occurs when the top face sheet attains the yield strength in *x* direction, as shown in Figure 6.7, with corresponding yield of the underlying core, as shown in Figure 6.11.

Stress against displacement, σ_{xx} vs. deflection, are reported in Figure 6.8 and Figure 6.10 for the top and bottom face sheets, and σ_{max} against displacement is reported in Figure 6.12 for the beam members of the truss core. Results were taken along the centre span from elements experiencing the maximum stresses in the top and bottom face sheets and truss core. Results confirm that the sandwich collapse is mostly due to yield of the top face sheet and of the beam members of truss core in the middle span, in the region where the displacement simulating the indenter was applied.

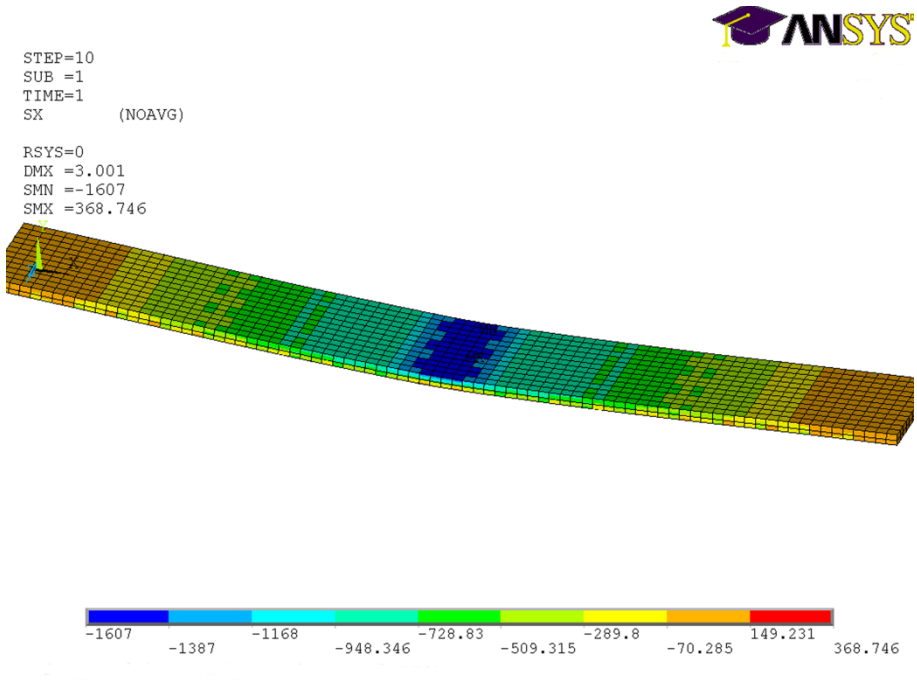

Figure 6.7. Contour plot of stress in *x* direction, σ_{xx}, results from top face sheets, TMC.

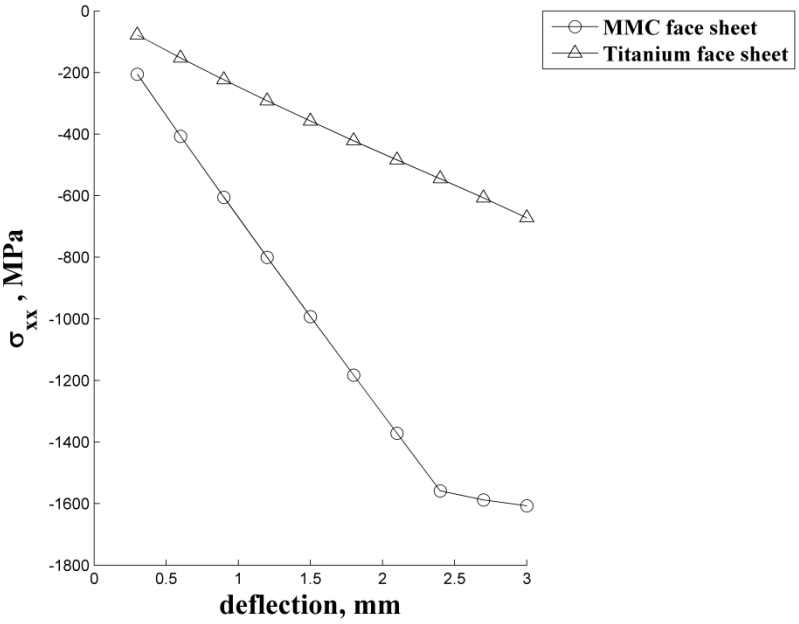

Figure 6.8. σ_{xx} stress against displacement of the top TMC face sheet and titanium face sheet (part of the truss core).

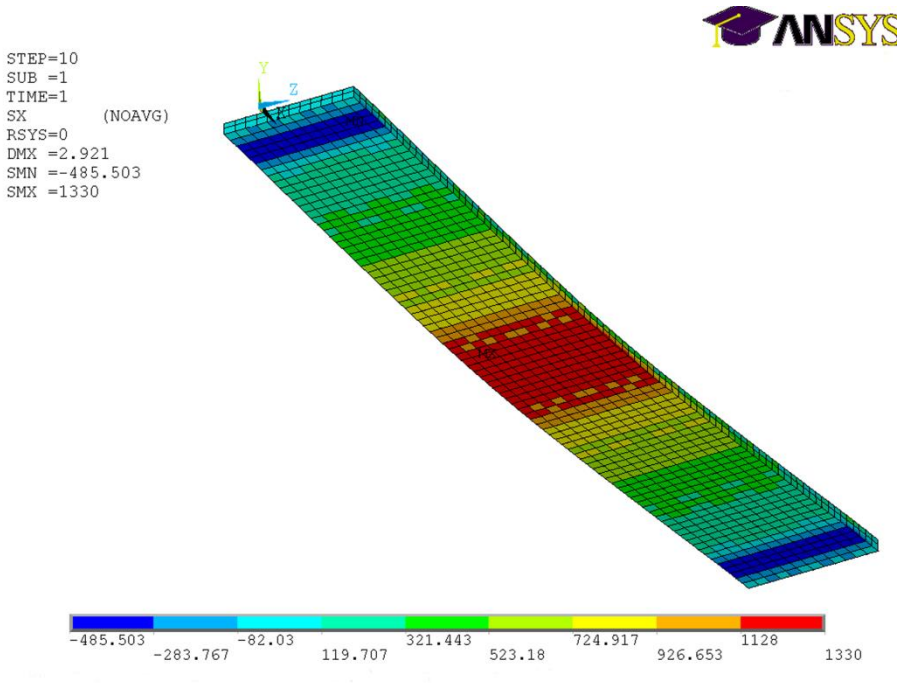

Figure 6.9. Contour plot of stress in *x* direction, σ_{xx}, results from bottom face sheets, TMC.

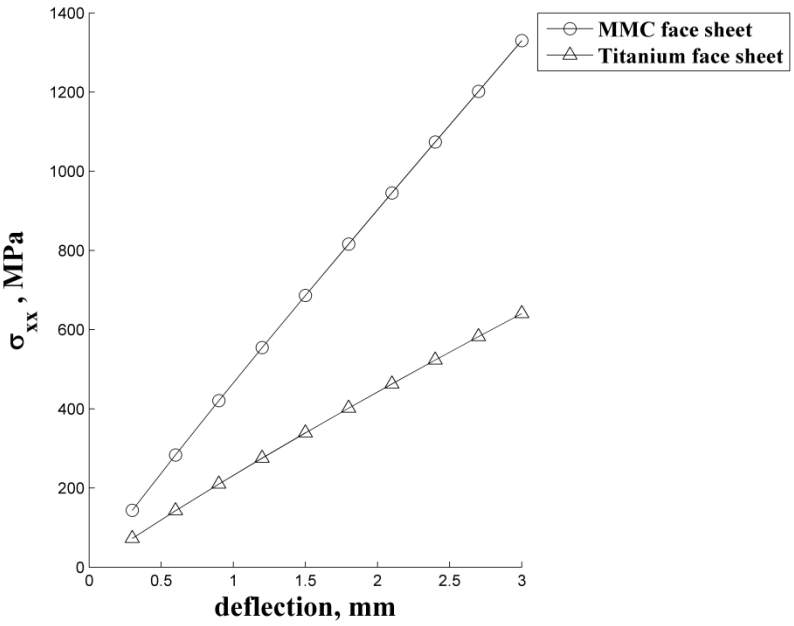

Figure 6.10. σ_{xx} stress against displacement of the bottom TMC face sheet and titanium face sheet (as part of the truss core).

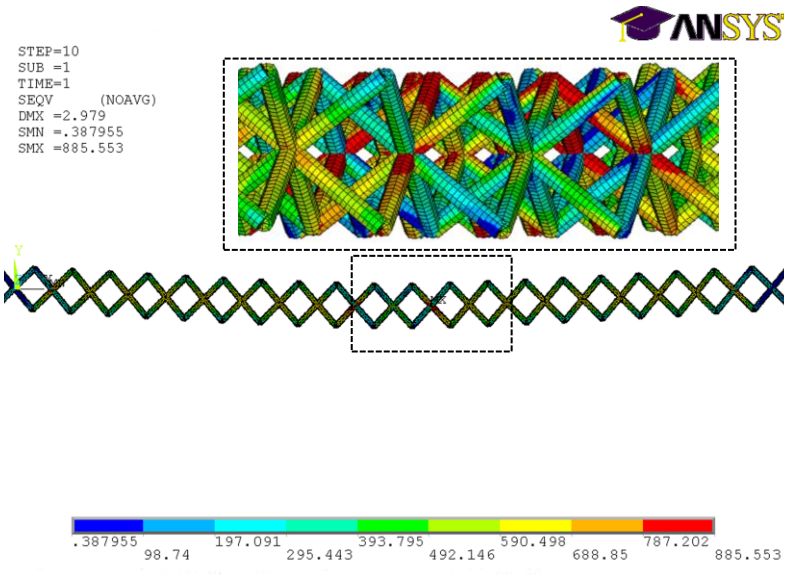

Figure 6.11. Contour plot of maximum stress, σ_{max}, from the beam members of the truss core.

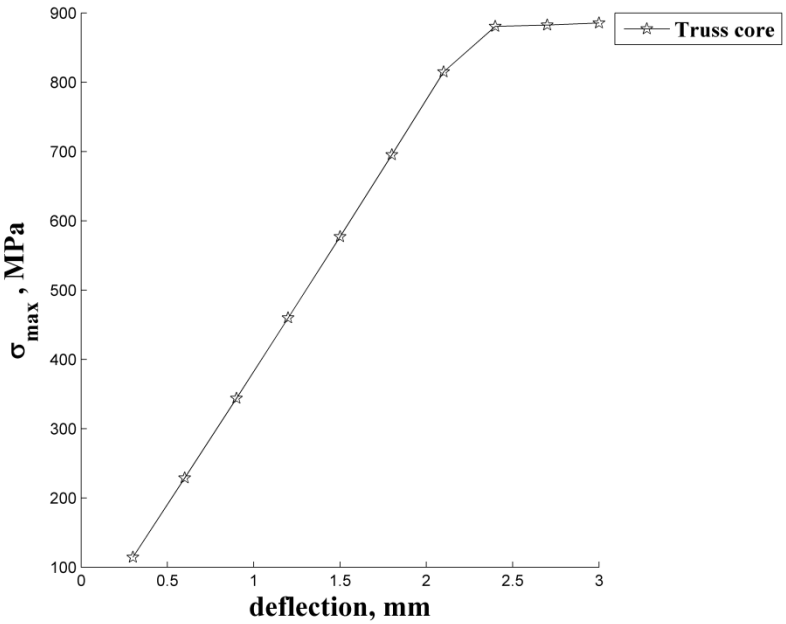

Figure 6.12. σ_{max} stress against displacement of the truss core beam members.

6.3.1 Analytical modelling results

Analytical expressions were given for the effective properties of the pyramidal unit cell. The axial stiffness and the shear stiffness predictions from the FE model agree well with the analytical predictions, see Figure 6.3a and Figure 6.3b.

The analytical strength formula given by Allen (Allen and Evans, 2003) in terms of load and deflection is in good agreement with the FE simulation, Figure 6.5. The FE model of the sandwich panel overestimates the stiffness calculated by the analytical prediction.

6.4 Discussions and conclusions

The sandwich was found to collapse by the dominance of a singular collapse mode mostly, rather than by competing collapse modes.

The measured effective properties of the pyramidal truss core agree well with the findings in Chapter 3 and Chapter 4. Analytical prediction and FE model agree well, Figure 6.3 and Figure 6.4 showing axial and shear loading. The result confirms that the deformation is stretch dominated in both cases. Higher discrepancy is noted between the axial loading analytical prediction and the FE results, than in shear loading. This may be explained by the fact that under axial loading, the bending stiffness can have a bigger contribution than in shear, for the core considered.

The observed collapse mode of the sandwich panel was face yield with the beam members yielding. The load increases monotonically with deflection until the top face sheet fails in compression and the core fails by yield, Figure 6.5. The top TMC face sheet is found to yield in compression, see Figure 6.7 and Figure 6.8. That is mostly due to the loading configuration and combination of face sheets and core materials. In fact, at low

values of t/L_p, the face sheets fail by yield if the core density is high (Gibson and Ashby, 1999b).

The analytical prediction for sandwich stiffness and load limit, shown in Figure 6.5, is in good agreement with the prediction from the FE modelling. Analytical prediction seems to underestimate the FEM prediction. This can be explained by the fact that the model presented in Equation 6.2 considers single layer face sheets. Herein, the face sheets of the sandwich panel can be considered as double layer, considering the titanium layer of the truss core as part of the face sheets. This means in a change in the thickness t of the face sheets and in Young's modulus. However, the good agreement between FE model and the analytical result seems to ensure that the general analytical model describes the mechanism of the problem well enough.

In general, the use of effective properties for the pyramidal core seems to be an acceptable simplification in predicting the overall response of the truss core sandwich under three-point bending. The sandwich proposed for manufacturing by ALM shows collapse by yield of the top face sheet and of the underlying truss core. Collapse due to face wrinkling, core shear mode and/ or indentation does not seem to occur.

Specimen ALMs manufactured by the sponsor will be tested, and results compared with the FE model. An experimental test can offer the possibility to improve the accuracy of the FE model used in this study, and can also offer the possibility of quantifying any limitation due to the manufacturing process employed.

7 DISCUSSION

7.1 Discussion

The main aim of this work was to explore whether a dual-material truss structure can be designed to exhibit enhanced physical properties, in particular, tailored thermal distortion (effectively a Coefficient of Thermal Expansivity, CTE) of near-zero or extreme positive/negative values, without penalties in other important properties such as stiffness and mass. Possible solutions to this problem must be compared with monolithic counterparts or with competing concepts such as carbon fibre composite.

The mechanism underlying tailoring of the CTE of cellular solids and trusses in all of the published literature was described by Miller et al. (2008a), as discussed in Chapters 2 and 3. The important geometric and material parameters which drive CTE and other properties are i) the relative lengths of the high thermal expansivity beams and low thermal expansivity beams, b/a, and the aspect ratio of the unit cells, h/b; ii) the ratio of the constituent materials' CTEs, α_b/α_a. Structures derived can easily be constrained to those easily realisable with current manufacturing processes. It is far harder to implement such restrictions via numerical optimisation methods, e.g. Sigmund and Torquato (1997). For example, the structure of the satellite support truss, described in Chapter 2, can be manufactured via welding or pin-jointing of aluminium and titanium rods, and exhibits near-zero CTE, with similar stiffness and mass as the truss currently implemented.

There is often little, or in some cases no, penalty to be paid in terms of stiffness and mass on an iso-mass or iso-stiffness basis for implementing such dual-material lattices, except in comparison to specialist materials such as Invar®, or low-density materials such

as monolithic carbon fibre composites, see Table 2.3. However, metal alloys such as Invar® are often very dense (8.05 g cm^{-3}) and the price of carbon fibre composite is often an order of magnitude (or more) higher than for aluminium and titanium. These materials have another drawback; their CTE is usually fixed within a small range of values near to but above zero, and this may be undesirable where a match to another component's CTE or exactly zero CTE is required. Certainly, carbon fibre composites have a small range of CTE values available, dependent on the particular stack sequence and volume fraction, but this is limited in scope.

Some more aspects could be taken into consideration in a comparison between carbon fibre composite vs. commonly used aluminium alloys. For instance, i) thermal resistance: carbon fibre composites do degrade quicker as temperature increases, compared with common aluminium alloys; ii) water absorption: carbon fibre composites tend to absorb water, causing degradation in performance; iii) oxidation: carbon fibre composites can suffer contamination by chemicals. Generally, they can oxidise, thereby losing strength. The oxidation rate is low at room temperature but it may increase at higher temperatures; iv) durability: carbon fibre composites will not have durability, in time, as expected for aluminium alloys; v) failure mode: carbon fibre composites failure cannot be fully predicted and controlled as in aluminium alloys. Carbon fibre composite cracks can initiate from minimal defects; vi) costs: carbon fibre composites tend generally to be more expensive than aluminium alloys. These limitations can make dual-material lattices fabricated by metal alloys more attractive than carbon fibre material, especially in applications where high temperatures and management of thermal deformation are involved. The exact tailoring of thermal expansivity by these structures could lead to a wider range of applications and operating temperatures than is currently possible

employing high-performance carbon fibre materials, for instance. Applications could range from high accuracy equipment (such as optics or space antennae) to applications where extreme temperatures or rapidly changing temperatures are encountered (such as engines where tolerance and hence performance are an issue, for instance). In aerospace applications, many space frames are either square or triangular based pyramids. These structures are generally optimal for elastic properties alone. Structures explored in the thesis represent an optimal in terms of elastic properties combined with CTEs. Although in some cases penalties can occur, the solutions obtained can represent a good trade between performance and thermal distortion management.

The lattice structures examined here may reduce CTE by means of swapping overall distortion for internal stress as the slenderness ratio of the rigid-jointed members tends to zero, see Chapter 2. Over the temperature range considered in Chapter 2, i.e. 148.15 - 398.15 *K*, common temperatures in many aerospace applications, stresses do not easily lead to failure. Given wider fluctuations in temperature, these stresses will of course eventually cause failure, most notably fatigue failure in aluminium components. The absolute value of temperature will most likely affect carbon fibre composites which have a degradation temperature typically of 493.15 *K*.

Although missing from the current study, maximum stresses under temperature change in dual-material structures can be evaluated when the rigid-jointed members of the structure are not slender. The max. and min. temperature range for any dual material truss structure could be evaluated. In this way, it is possible to move and distort this temperature range by choice of constitutive materials and geometry of the structures, together with the

limits on mechanical performance and mass, forming a solution space for any particular application.

The evaluation of the stresses under temperature change in dual-material structures permits their comparison with a series of failure criteria, specifically, yield, fatigue, creep, and buckling. These criteria are critical in applications involving high temperatures. Although missing in the current study, failure criteria such as cracking due to material defects, for instance, or failure due to material and geometric non-linearity with large temperature fluctuations could be considered in the design of such dual-material structures.

The critical conditions for near-zero CTE were found for both 2D and 3D structures, see Chapter 2 (Sections 2.3.1 and 2.3.2), Chapter 3 (Section 3.3.1) and Chapter 4 (Section 4.3.2). They were, in general: i) high expansivity beams must be 40-60% longer than lower expansivity beams; ii) there must be at least a four-fold difference between the CTEs of the constituent materials; iii) the aspect ratios, *h/b*, of the unit cells in Chapters 3 and 4 were usually below unity in structures showing reduced CTEs, and above unity in structures showing positive CTE in at least one direction, see Chapter 3 and Chapter 4. These conditions are often found in weight-bearing trusses so there are no real restrictions on design of dual-material near-zero truss structures.

The explicit relations for CTE, mass and elastic properties were developed and since they agree well with both FE modelling and experimental results, they appear to be accurate. They indicate that CTE in such dual-material trusses is driven primarily by the internal geometry of the unit cell (captured here as the second power of the unit cell's aspect ratio h^2/b^2), Table 3.3, so that a pair of materials with only slightly different moduli and CTEs can be formed into a truss with a significantly reduced CTE, albeit at the cost of

an extreme geometry (high or low aspect ratio *h/b*). In those axes where only one material is acting, CTE remains similar to that of that constituent material, see Chapter 3.

The assumption about material and geometrical linearity for the constituent material of the dual-material structures can be considered reasonable for most of the structures considered. However, the range of temperatures over which the structures are stable is related to the range over which the ratio of coefficients of thermal expansivity of the two constituent materials is independent of temperature. Examination of data on the variability of the coefficients of thermal expansivity for several structural materials over a common range of 123.15 *K* to 423.15 *K* indicate titanium and aluminium alloys as the most stable materials to construct dual-material structures. However, materials showing phase transitions over a specific range of temperatures have non-linear CTEs, affecting the stability of the structures. Invar®, for instance, has a phase transition at approximately 523.15 *K*, making CTE non-linear. In this case, a temperature change over 200 *K* would be required to make the proposed designs non-linear.

Composite systems also have strong mismatches in stiffness and CTE, and their geometry is in some ways controllable. It could be possible to make laminated fibre composites with tunable CTEs in which fibres could be arranged in a way to form triangulated geometries. The guidelines proposed in the thesis could be adapted to such composite systems.

Prediction of approximate elastic properties of stretch-dominated triangulated lattice structures (Equations 3.11 to 3.24), forming a guideline of sorts for the design of such structures, were presented, see Chapter 3. These equations do not predict properties for bending-dominated structures (Jefferson et al., 2009; Lakes, 1996, 2007; Sigmund and

Torquato, 1997), which are not triangulated and therefore are much less stiff. These equations could be extended to flexure dominated dual-material structures.

The main limitations in terms of performance (mass and elastic properties) arising from use of dual materials to engender altered CTEs are: i) the reduced stiffnesses of dual-material vs. monolithic configurations arises because of the presence of inherently lower stiffness (higher expansivity material) and on an iso-volume basis is also related to the total number of high and low thermal expansivity beams, see Section 3.4; ii) for most of the proposed structures, the stiffness in the direction in which CTE is altered the most is similar between monolithic and dual-material configurations, because usually only the low expansivity (high stiffness) beams have components acting in this axis, see Section 3.4; iii) for most of the structures proposed, shear stiffness is largely unaffected by dual-material configuration, in both *x*-*y* and *x*-*z* planes, see Section 3.4. Reduction of stiffness in some axes means anisotropy is more marked, and some vibration modes may see reductions in their frequencies and thus become problematical in specific applications, for instance. In general, reduced thermal expansivity is attributable to anisotropic structures.

An attempt to find new truss structures in both monolithic and dual-material form, not yet known in the literature, was discussed in Chapter 4. The numerical combinatorial approach taken permitted exploration of the range of performance and the limitations of such truss structures, which is to define the performance solution. It led towards a better understanding of such structures, showing high mechanical performances combined with anomalous CTEs, exploring all the possible solutions, varying the unit cell geometry and the arrangement of two different phases within the cells. Seven 'parent' truss structures were investigated, from which 33 new truss structures were derived, each having similar

numbers of beams and connectivities. Specifically, structures explored, shown in Table 4.4 to Table 4.6, have the best known combination of altered CTE, high stiffness and low mass. In some cases, the new truss structures performed best and in other cases, the parent trusses, see Table 4.4, for instance. By using this numerical combinatorial approach, performance maps were created, Figure 4.9, which are potentially very useful when considering alternative structures for a specific application. Consideration of further 'parent' structures, of more or less complexity, is unlikely to extend the response surface of the data presented in Chapter 4. Preliminary attempts at introducing further parent structures have yielded no extensions of the current response surface.

All the designs herein are scale-independent and so are as valid for large spacecraft structures as for truss cores. At small sizes, e.g. nano scale, where atomistic forces and thermally induced crystallographic effects come into play, equations for CTE are no longer valid.

The 2D and 3D models were validated well by the tests on the experimental samples. The small differences in predicted and measured CTEs were likely to be due to: i) manufacturing imperfections (non-ideal geometry of the lattice joints); ii) the finite thickness of the beam members in the experimental samples; and probably most significantly, iii) plasticity in the adhesive forming the joints. The FE and analytical models take no account of the thickness of the beam members since they are considered to be welded (rigid-jointed) at a point, whereas the samples were welded over finite areas and their finite thicknesses reduced the effective length of the beam members. There were differences between predictions and experimental measurements for the dual-material samples, ranging between 7% and 40% in the measurement of α_y, particularly for the

negative CTE structure which had large internal stresses, see Chapter 2 and Chapter 3. This error arises because of slip in the adhesive joints between beam members. The FE models predict the properties of the trusses sufficiently well, see Chapter 5.

Manufacture of such lattice structures would seem to present no special problems beyond those already widely known regarding the joining of dissimilar materials together. From the point of view of the calculations herein, the particular method of joining is not very important, so joining beams via pins would be as effective as welding or adhering. Manufacturing of smaller scale lattices, using two materials, presents more of a challenge. The leading method for truss cores would seem to be additive layer manufacturing, a rapidly developing area, in which multi-material methods are beginning to come to maturity (Mazumder et al., 2000; Stampfl et al., 2004; Willich, 2007). Other alternatives include wire bending operations (Wadley et al., 2003).

Fabrication of dual-material structures for real world applications would face similar problems. Pin-jointing would overcome these but would not be possible where complex geometries prevent it. Welding of dissimilar metals also presents problems, especially for aluminium and its alloys.

Fabrication at nano scale of truss structures by synthesis, for instance, could enable diverse applications in nano-electronics and photonic.

Sandwich panel application was proposed by the sponsoring company as a case study which is in current use in a variety of aerospace applications. High-performance truss structures (in terms of elastic properties at least) explored in Chapters 2-4 were considered for use as cores in the sandwich application proposed. The leading method of manufacturing these cores seems to be ALM, especially given the geometrical complexity

and scale of the cores proposed. Proposed designs took consideration of all the actual constraints and advantages related to ALM technology. Since manufacturing with dual materials in ALM is not yet technologically feasible, and because of the small size and geometrical complexity of the trusses, only monolithic lattice structures were considered. Applications as cores in sandwich panels might be the first route by which the ALM manufacturing process is required to develop dual-material capability, see Chapter 6.

8 CONCLUSION AND FURTHER WORK

8.1 Conclusion and further work

It is shown that lattice structures formed from materials with large and positive CTEs can exhibit markedly reduced CTE in at least one axis, page 54. Geometric and material property criteria are given for the reduction of CTE in such lattices to zero or negative values, page 58. Performance against other criteria such as stiffness and mass was not significantly affected by the use of dual-material lattices. This approach can potentially alleviate the need for use of exotic, heavy or expensive materials.

A parametric study was undertaken on seven published 3D truss geometries, with and without dual-material configurations, exploring how the internal geometry of the truss and the resulting thermal expansivity and elastic properties are related. Approximate explicit relations were developed, describing the properties with respect to the internal geometry of the truss structures, see Equations in Table 3.3, (1.1) to (7.3), and 3.11 to 3.24, which are shown to be capable of predicting patterns of behaviour between different geometries, see Figure 3.5, Figure 3.6 and Figure 3.7. It is shown that all of these structures can exhibit very large changes in CTE in dual-material configuration, Figure 3.5 and Figure 3.9a and Figure 3.10a and b. Maximal stiffness is achieved by engendering a larger internal angle, ω_i, and minimising the number of high expansivity beams (which are inherently more compliant than the low expansivity beams), see Figure 3.6, Figure 3.7, Figure 3.9b and c, and Figure 3.10a and b. Reduction in CTE always incurs a penalty in terms of axial stiffness (see Figure 3.6, Figure 3.9b, and Figure 3.10a) but not in shear stiffness (see Figure 3.7, and Figure 3.9c and Figure 3.10b), on an equal volume fraction (or apparent

density) basis. The extent of this penalty is positively linked to the required reduction in CTE, see Figure 3.10a and b. Some structures can exhibit negative Poisson's ratios despite not having re-entrant architectures, see Figure 3.8b.

A combinatorial approach to generate structures and simulate their thermomechanical behaviour was developed. All the possible structures have been generated employing a combinatorial approach under specified constraints. Several geometries were performance ranked on an iso-volume basis and limitation addressed in terms of mechanical properties combined with altered CTEs. Some new truss geometries were identified with performance exceeding that of structures previously published in the literature, page 162. A rigorous and consistent comparison between new topologies generated and those in the literature must be carried out in order to assess whether the new designs ever generate enhanced solutions in relation to those in the literature. However, this research presents preliminary comparisons and further investigations could form part of future research work.

Manufacturing of such lattice structures seems to require nothing new for large-scale constructions and to be possible via emerging manufacturing technologies, for smaller scale ones.

The tool to design dual-material structures with tailored CTE may not yet be fully mature but should lead toward a much better understanding of such structures. An improvement and continuation of the combinatorial generation of 2D/3D trusses and the simulation of their thermomechanical properties for specific applications would be beneficial.

Simulation of coupled thermomechanical properties, such as thermal conductivity, magnetic permeability or electrical conductivity, would extend the understanding and would be beneficial for future exploitation of these structures in real aerospace applications. This could be interesting in order to quantify the real penalties occurring in such dual-material structures under the combined effect of thermal and structural loads, a typical scenario in real-life applications.

Innovative manufacturing processes such as ALM should be further developed for manufacturing dual-material structures. Mechanical properties of such structures should be further investigated by testing physical samples of different sizes.

References

Aboudi, J., Gilat, R., 2005. Micromechanical analysis of lattice blocks. *International Journal of Solids and Structures* 42, 4372-4392.

Aboudi, J., 2008. Thermomechanically coupled micromechanical analysis of multiphase composites. *J. Eng. Math.* 61, 111-132.

Alkhader, M., Vural, M., 2008. Mechanical response of cellular solids: Role of cellular topology and microstructural irregularity. *International Journal of Engineering Science* 46, 1035-1051.

Allen, S., Evans, J.S.O., 2003. Negative thermal expansion and oxygen disorder in cubic $ZrMo_2O_8$. *Physical Review* B 68.

Amos, T.G., Yokochi, A., Sleight, A.W., 1998. Phase Transition and Negative Thermal Expansion in Tetragonal $NbOPO_4$. *Journal of Solid State Chemistry* 141, 303-307.

Ashby, M.F., 2006. The properties of foams and lattices. *Philosophical Transactions of the Royal Society a-Mathematical Physical and Engineering Sciences* 364, 15-30.

Attfield, M.P., Sleight, A.W., 1998. Strong negative thermal expansion in siliceous faujasite. *Chemical Communications*, 601-602.

Avis, D., Katoh, N., Ohsaki, M., Streinu, I., Tanigawa, S.-i., 2008. Enumerating Constrained Non-crossing Minimally Rigid Frameworks. Discrete & amp; *Computational Geometry* 40, 31-46.

Bailey, A.C., Yates, B., 1970. Anisotropic Thermal Expansion of Pyrolytic Graphite at Low Temperatures. *Journal of Applied Physics* 41, 5088.

Barrera, G.D., Bruno, J.A.O., Barron, T.H.K., Allan, N.L., 2005. Negative thermal expansion. *Journal of Physics-Condensed Matter* 17, R217-R252.

Barron, R.M., Barron, T.H.K., Mummery, P.M., Sharkey, M., 1988. Thermal-Expansion and Gruneisen Functions of Polymer Crystal Models .1. Central Forces. *Canadian Journal of Chemistry-Revue Canadienne De Chimie* 66, 718-724.

Barron, T.H.K., Collins, J.G., White, G.K., 1980. Thermal-Expansion of Solids at Low-Temperatures. *Advances in Physics* 29, 609-730.

Baughman, R.H., Galvão, D.S., 1995. Negative volumetric thermal expansion for proposed hinged phases. *Chemical Physics Letters* 240, 180-184.

Bruno, J.A.O., Allan, N.L., Barron, T.H.K., Turner, A.D., 1998. Thermal expansion of polymers: Mechanisms in orthorhombic polyethylene. *Physical Review B* 58, 8416-8427.

Buck, M.E., 1987. High Strength & Modulus Filaments of Boron & Silicon Carbide. *Materials & Design* 8, 272-277.

Cao, D., Bridges, F., Kowach, G.R., Ramirez, A.P., 2002. Frustrated soft modes and negative thermal expansion in ZrW_2O_8. *Physical Review Letters* 89.

Couves, J.W., Jones, R.H., Parker, S.C., Tschaufeser, P., Catlow, C.R.A., 1993. Experimental-Verification of a Predicted Negative Thermal Expansivity of Crystalline Zeolites. *Journal of Physics-Condensed Matter* 5, L329-L332.

David, W.I.F., Evans, J.S.O., Sleight, A.W., 1999. Direct evidence for a low-frequency phonon mode mechanism in the negative thermal expansion compound ZrW2O8. *Europhysics Letters* 46, 661-666.

Deshpande, V.S., Fleck, N.A., 2001. Collapse of truss core sandwich beams in 3-point bending. *International Journal of Solids and Structures* 38, 6275-6305.

Deshpande, V.S., Fleck, N.A., Ashby, M.F., 2001. Effective properties of the octet-truss lattice material. *Journal of the Mechanics and Physics of Solids* 49, 1747-1769.

Ernst, G., Broholm, C., Kowach, G.R., Ramirez, A.P., 1998. Phonon density of states and negative thermal expansion in ZrW_2O_8. *Nature* 396, 147-149.

ESA, Huart, J., 2010. Artisi's impression of Alphasat configured for the Inmarsat 'Geomobile' mission.

Evans, A.G., Hutchinson, J.W., Fleck, N.A., Ashby, M.F., Wadley, H.N.G., 2001. The topological design of multifunctional cellular metals. *Progress in Materials Science* 46, 309-327.

Evans, J.S.O., 1999. Negative thermal expansion materials. *Journal of the Chemical Society-Dalton Transactions*, 3317-3326.

Evans, J.S.O., Mary, T.A., 2000. Structural phase transitions and negative thermal expansion in $Sc_2(MoO_4)_3$. *International Journal of Inorganic Materials* 2, 143-151.

Evans, J.S.O., Mary, T.A., Sleight, A.W., 1998. Negative Thermal Expansion in Sc2(WO4)3. *Journal of Solid State Chemistry* 137, 148-160.

Evans, K.E., 1991. Auxetic polymers: a new range of materials. *Endeavour* 15, 170-174.

Forster, P.M., Sleight, A.W., 1999. Negative thermal expansion in $Y_2W_3O_{12}$. *International Journal of Inorganic Materials* 1, 123-127.

Forster, P.M., Yokochi, A., Sleight, A.W., 1998. Enhanced Negative Thermal Expansion in $Lu_2W_3O_{12}$. *Journal of Solid State Chemistry* 140, 157-158.

Furness, J.A.G., Clyne, T.W., 1991. The application of scanning laser extensometry to explore thermal cycling creep of metal matrix composites. *Materials Science and Engineering: A* 141, 199-207.

Gay, D., Hoa, S.V., 2007. *Composite materials: design and applications.* CRC Press.

Gere, J.M., Goodno, B.J., 2009. *Mechanics of materials.* Cengage Learning.

Gibson, L.J., Ashby, M.F., 1999a. *Cellular solids: Structure and Properties*, 2nd ed. Cambridge University Press, Cambridge.

Gibson, L.J., Ashby, M.F., 1999b. *The design of sandwich panels with foam cores, Cellular solids: Structure and Properties.* Cambridge University Press, Cambridge.

Giddy, A.P., Dove, M.T., Pawley, G.S., Heine, V., 1993. The Determination of Rigid-Unit Modes as Potential Soft Modes for Displacive Phase-Transitions in Framework Crystal-Structures. *Acta Crystallographica Section A* 49, 697-703.

Grima, J.N., Attard, D., Gatt, R., 2008. Truss-type systems exhibiting negative compressibility. *Physica Status Solidi B-Basic Solid State Physics* 245, 2405-2414.

Grima, J.N., Farrugia, P.S., Gatt, R., Zammit, V., 2007. A system with adjustable positive or negative thermal expansion. *Proceedings of the Royal Society a-Mathematical Physical and Engineering Sciences* 463, 1585-1596.

Hall, A.S., Holowenko, A.R., Laughlin, H.G., 1961. *Schaum's outline of theory and problems of machine design.* McGraw-Hill.

Halpin, J.C., Finlayson, K.M., Ashton, J.E., 1992. *Primer on composite materials analysis.* Technomic Pub. Co.

Hayes, A.M., Wang, A., Dempsey, B.M., McDowell, D.L., 2004. Mechanics of linear cellular alloys. *Mechanics of Materials* 36, 691-713.

Hearmon, R.F.S., 1978. *An introduction to applied anisotropic elasticity.* University Microfilms International.

Heine, V., Welche, P.R.L., Dove, M.T., 1999. Geometrical origin and theory of negative thermal expansion in framework structures. *Journal of the American Ceramic Society* 82, 1793-1802.

Hohn, F., Pantenburg, I., Ruschewitz, U., 2002. $Sr[C_2(COO)_2]$: The First Anhydrous Salt of Acetylenedicarboxylic Acid. *Chemistry – A European Journal* 8, 4536-4541.

Hortal, M., Leadbett, A., 1972. Low-Temperature Thermal-Expansion and Gruneisen Functions of Tellurium. *Journal of Physics Part C Solid State Physics* 5, 2129-&.

Hull, D., Clyne, T.W., 1996. *An introduction to composite materials.* Cambridge University Press.

Hyun, S., Karlsson, A.M., Torquato, S., Evans, A.G., 2003. Simulated properties of Kagomé and tetragonal truss core panels. *International Journal of Solids and Structures* 40, 6989-6998.

Ito, T., Suganuma, T., Wakashima, K., 1999. Glass fiber/polypropylene composite laminates with negative coefficients of thermal expansion. *J. Mater. Sci. Lett.* 18, 1363-1365.

Ito, T., Suganuma, T., Wakashima, K., 2000. A micromechanics-based analysis for tailoring glass-fiber-reinforced thermoplastic laminates with near-zero coefficients of thermal expansion. *Composites Science and Technology* 60, 1851-1861.

Jefferson, G., Parthasarathy, T.A., Kerans, R.J., 2009. Tailorable thermal expansion hybrid structures. *International Journal of Solids and Structures* 46, 2372-2387.

Ji, S., 2004. Generalized means as an approach for predicting Young's moduli of multiphase materials. *Materials Science and Engineering A* 366, 195-201.

Jin, S., Mavoori, H., 1998. Low-thermal-expansion copper composites via negative CTE metallic elements. *JOM Journal of the Minerals, Metals and Materials Society* 50, 70-72.

Jorgensen, J.D., Hu, Z., Teslic, S., Argyriou, D.N., Short, S., Evans, J.S.O., Sleight, A.W., 1999. Pressure-induced cubic-to-orthorhombic phase transition in ZrW_2O_8. *Physical Review B* 59, 215.

Kelly, A., McCartney, L.N., Clegg, W.J., Stearn, R.J., 2005. Controlling thermal expansion to obtain negative expansivity using laminated composites. *Composites Science and Technology* 65, 47-59.

Kelly, A., Stearn, R.J., McCartney, L.N., 2006. Composite materials of controlled thermal expansion. *Composites Science and Technology* 66, 154-159.

Khosrovani, N., Sleight, A.W., Vogt, T., 1997. Structure of $ZrV_2O_7$from -263 to 470°C. *Journal of Solid State Chemistry* 132, 355-360.

Kihara, K., 2001. Molecular dynamics interpretation of structural changes in quartz. *Physics and Chemistry of Minerals* 28, 365-376.

Korthuis, V., Khosrovani, N., Sleight, A.W., Roberts, N., Dupree, R., Warren, W.W., 1995. Negative Thermal-Expansion and Phase-Transitions in the ZrV_2-xPxO_7 Series. *Chemistry of Materials* 7, 412-417.

Krenkel, W., 2004. Carbon Fiber Reinforced CMC for High-Performance Structures. *International Journal of Applied Ceramic Technology* 1, 188-200.

Krivovichev, S.V., Filatov, S.K., Burns, P.C., 2002. The cuprite-like framework of OCu_4 tetrahedra in the crystal structure of synthetic melanothallite, Cu_2OCl_2, and its negative thermal expansion. *Canadian Mineralogist* 40, 1185-1190.

Kumar, R.S., McDowell, D.L., 2004. Generalized continuum modeling of 2-D periodic cellular solids. *International Journal of Solids and Structures* 41, 7399-7422.

Kunze, J., Bampton, C., 2001. Challenges to developing and producing MMCs for space applications. *JOM Journal of the Minerals, Metals and Materials Society* 53, 22-25.

Lakes, R., 1987. Foam Structures with a Negative Poisson's Ratio. *Science* 235, 1038-1040.

Lakes, R., 1996. Cellular solid structures with unbounded thermal expansion. *J. Mater. Sci. Lett.* 15, 475-477.

Lakes, R., 2007. Cellular solids with tunable positive or negative thermal expansion of unbounded magnitude. *Applied Physics Letters* 90.

Landert, M., Kelly, A., Stearn, R.J., Hine, P.J., 2004. Negative thermal expansion of laminates. *Journal of Materials Science* 39, 3563-3567.

Lennard-Jones, J.E., 1924. On the Determination of Molecular Fields. *Proc. R. Soc. Lond. A* 106 (738), 463–477.

Li, J., Yokochi, A., Amos, T.G., Sleight, A.W., 2002. Strong negative thermal expansion along the O-Cu-O linkage in $CuScO_2$. *Chemistry of Materials* 14, 2602-2606.

Lightfoot, P., Woodcock, D.A., Maple, M.J., Villaescusa, L.A., Wright, P.A., 2001. The widespread occurrence of negative thermal expansion in zeolites. *Journal of Materials Chemistry* 11, 212-216.

Lim, T.-C., 2005. Anisotropic and negative thermal expansion behavior in a cellular microstructure. *Journal of Materials Science* 40, 3275-3277.

Marinkovic, B.A., Jardim, P.M., Saavedra, A., Lau, L.Y., Baehtz, C., de Avillez, R.R., Rizzo, F., 2004. Negative thermal expansion in hydrated HZSM-5 orthorhombic zeolite. *Microporous and Mesoporous Materials* 71, 117-124.

Mary, T.A., Evans, J.S.O., Vogt, T., Sleight, A.W., 1996. Negative thermal expansion from 0.3 to 1050 Kelvin in ZrW_2O_8. *Science* 272, 90-92.

Mazumder, J., Dutta, D., Kikuchi, N., Ghosh, A., 2000. Closed loop direct metal deposition: art to part. *Optics and Lasers in Engineering* 34, 397-414.

Miller, W., Mackenzie, D.S., Smith, C.W., Evans, K.E., 2008a. A generalised scale-independent mechanism for tailoring of thermal expansivity: Positive and negative. *Mechanics of Materials* 40, 351-361.

Miller, W., Smith, C., Mackenzie, D., Evans, K., 2009. Negative thermal expansion: a review. *Journal of Materials Science* 44, 5441-5451.

Miller, W., Smith, C.W., Dooling, P., Burgess, A.N., Evans, K.E., 2008b. Tailored thermal expansivity in particulate composites for thermal stress management. *Physica Status Solidi (b)* 245, 552-556.

Mirache, D., 2001. Metallic composites in space: A status report. *JOM Journal of the Minerals, Metals and Materials Society* 53, 12-12.

Mittal, R., Chaplot, S.L., 1999. Lattice dynamical calculation of isotropic negative thermal expansion in ZrW_2O_8 over 0-1050 K. *Physical Review B* 60, 7234-7237.

Mittal, R., Chaplot, S.L., Kolesnikov, A.I., Loong, C.K., Jayakumar, O.D., Kulshreshtha, S.K., 2002. Inelastic neutron scattering, lattice dynamics, and synchrotron x-ray diffraction study of $FePO_4$. *Physical Review B* 66.

Mittal, R., Chaplot, S.L., Schober, H., Mary, T.A., 2001. Origin of negative thermal expansion in cubic ZrW_2O_8 revealed by high pressure inelastic neutron scattering. *Physical Review Letters* 86, 4692-4695.

Moongkhamklang, P., Elzey, D.M., Wadley, H.N.G., 2008. Titanium matrix composite lattice structures. *Composites Part A: Applied Science and Manufacturing* 39, 176-187.

Nakajima, N., Yamamura, Y., Tsuji, T., 2003. Synthesis and physical properties of negative thermal expansion materials Zr_1-xMxW_2O_8-y (M = Sc, In, Y) substituted for Zr(IV) sites by M(III) ions. *Solid State Communications* 128, 193-196.

Nye, J.F., 1957. *Physical properties of crystals: their representation by tensors and matrices.* Clarendon Press, Oxford.

Oruganti, R.K., Ghosh, A.K., Mazumder, J., 2004. Thermal expansion behavior in fabricated cellular structures. *Materials Science and Engineering A* 371, 24-34.

Palumbo, N.M.A., Smith, C.W., Miller, W., Evans, K.E., 2011. Near-zero thermal expansivity 2-D lattice structures: Performance in terms of mass and mechanical properties. *Acta Materialia* 59, 2392-2403.

Pryde, A.K.A., Dove, M.T., Heine, V., 1998. Simulation studies of ZrW_2O_8 at high pressure. *Journal of Physics-Condensed Matter* 10, 8417-8428.

Pryde, A.K.A., Hammonds, K.D., Dove, M.T., Heine, V., Gale, J.D., Warren, M.C., 1996. Origin of the negative thermal expansion in ZrW_2O_8 and ZrV_2O_7. *Journal of Physics-Condensed Matter* 8, 10973-10982.

Qi, J., Halloran, J.W., 2004. Negative thermal expansion artificial material from iron-nickel alloys by oxide co-extrusion with reductive sintering. *Journal of Materials Science* 39, 4113-4118.

Queheillalt, D.T., Murty, Y., Wadley, H.N.G., 2008. Mechanical properties of an extruded pyramidal lattice truss sandwich structure. *Scripta Materialia* 58, 76-79.

Queheillalt, D.T., Wadley, H.N.G., 2005. Pyramidal lattice truss structures with hollow trusses. *Materials Science and Engineering A* 397, 132-137.

Ramirez, A.P., Kowach, G.R., 1998. Large low temperature specific heat in the negative thermal expansion compound ZrW_2O_8. *Physical Review Letters* 80, 4903-4906.

Rathbun, H.J., Zok, F.W., Waltner, S.A., Mercer, C., Evans, A.G., Queheillalt, D.T., Wadley, H.N.G., 2006. Structural performance of metallic sandwich beams with hollow truss cores. *Acta Materialia* 54, 5509-5518.

Reeves, P., 2008. Direct Rapid Manufacturing of Metallic Parts - A UK Industry overview, *Econolyst*.

Riley, D.P., 1945. The Thermal Expansion of Graphite: Part II. Theoretical. *Proceedings of the Physical Society of London* 57, 486-495.

Roy, R., Agrawal, D., 1997. Thermal-expansion materials not so new. *Nature* 388, 433-433.

Sigmund, O., Torquato, S., 1996. Composites with extremal thermal expansion coefficients. *Applied Physics Letters* 69, 3203-3205.

Sigmund, O., Torquato, S., 1997. Design of materials with extreme thermal expansion using a three-phase topology optimization method. *Journal of the Mechanics and Physics of Solids* 45, 1037-1067.

Sleight, A.W., 1995. Thermal Contraction. *Endeavour* 19, 64-68.

Sleight, A.W., 1998a. Compounds that contract on heating. *Inorganic Chemistry* 37, 2854-2860.

Sleight, A.W., 1998b. Negative thermal expansion materials. *Current Opinion in Solid State & Materials Science* 3, 128-131.

Sonmez, M., 2011. Discrete optimum design of truss structures using artificial bee colony algorithm. *Structural and Multidisciplinary Optimization* 43, 85-97.

Soriano, M.R., Barrera, G.D., Allan, N.L., 2001. Vibrational energies and thermal expansion of layered compounds: $MgCl_2$. *Chemical Physics Letters* 350, 543-550.

Stampfl, J., Seyr, M.M., Luxner, M.H., Pettermann, H.E., Woesz, A., Fratzl, P., 2004. REGULAR, LOW DENSITY CELLULAR STRUCTURES - RAPID PROTOTYPING, NUMERICAL SIMULATION, MECHANICAL TESTING, in: Joanna Aizenberg, W.J.L., Christine Orme, and Rizhi Wang, (Ed.), *Mater. Res. Soc. Symp*.

Steeves, C., Mercer, C., Antinucci, E., He, M., Evans, A., 2009. Experimental investigation of the thermal properties of tailored expansion lattices. *International Journal of Mechanics and Materials in Design* 5, 195-202.

Steeves, C.A., Evans, A.G., 2011. Optimization of Thermal Protection Systems Utilizing Sandwich Structures with Low Coefficient of Thermal Expansion Lattice Hot Faces. *Journal of the American Ceramic Society*, 1-7.

Steeves, C.A., Lucato, S.L., He, M., Antinucci, E., Hutchinson, J.W., Evans, A.G., 2007. Concepts for structurally robust materials that combine low thermal expansion with high stiffness. *Journal of the Mechanics and Physics of Solids* 55, 1803-1822.

Stevens, R., Woodfield, B.F., Boerio-Goates, J., Crawford, M.K., 2004. Heat capacities, third-law entropies and thermodynamic functions of the negative thermal expansion material Zn_2GeO_4 from T = (0 to 400) K. *Journal of Chemical Thermodynamics* 36, 349-357.

Sypeck, D.J., 2005. Cellular Truss Core Sandwich Structures. *Applied Composite Materials* 12, 229-246.

Tao, J.Z., Sleight, A.W., 2003a. The role of rigid unit modes in negative thermal expansion. *Journal of Solid State Chemistry* 173, 442-448.

Tao, J.Z., Sleight, A.W., 2003b. Free energy minimization calculations of negative thermal expansion in $AlPO_4$-17. *Journal of Physics and Chemistry of Solids* 64, 1473-1479

Tran, H., Lee, J., 2010. Determination of a unique configuration of free-form tensegrity structures. *Acta Mechanica* 220, 331-348.

Uozumi, T., Kito, A., 2007. Carbon fibre-reinforced plastic truss structures for satellite using braiding/resin transfer moulding process. *Proceedings of the Institution of Mechanical Engineers, Part L: Journal of Materials: Design and Applications* 221, 93-101.

Wadley, H.N.G., 2006. Multifunctional periodic cellular metals. *Philosophical Transactions of the Royal Society a-Mathematical Physical and Engineering Sciences* 364, 31-68.

Wadley, H.N.G., Fleck, N.A., Evans, A.G., 2003. Fabrication and structural performance of periodic cellular metal sandwich structures. *Composites Science and Technology* 63, 2331-2343.

Wallach, J.C., Gibson, L.J., 2001. Mechanical behavior of a three-dimensional truss material. *International Journal of Solids and Structures* 38, 7181-7196.

Wang, J., Evans, A.G., Dharmasena, K., Wadley, H.N.G., 2003. On the performance of truss panels with Kagome cores. *International Journal of Solids and Structures* 40, 6981-6988.

White, G.K., 1972. Thermal-Expansion of Trigonal Elements at Low-Temperatures - as, Sb and Bi. *Journal of Physics Part C Solid State Physics* 5, 2731.

White, G.K., Roberts, R.B., 1988. Thermal-Expansion of Willemite, Zn2sio4. *Australian Journal of Physics* 41, 791-795.

White, G.K., Collocott, S.J., Collins, J.G., 1990. Thermal-Properties of Paratellurite (Teo2) at Low-Temperatures. *Journal of Physics-Condensed Matter* 2, 7715-7718.

Wicks, N., Hutchinson, J.W., 2001. Optimal truss plates. *International Journal of Solids and Structures* 38, 5165-5183.

Wicks, N., Hutchinson, J.W., 2004. Sandwich Plates Actuated by a Kagome Planar Truss. *Journal of Applied Mechanics* 71, 652-662.

Williams, C., Cochran, J., Rosen, D., 2010. Additive manufacturing of metallic cellular materials via three-dimensional printing. *The International Journal of Advanced Manufacturing Technology*, 1-9.

Williams, C.B., Mistree, F.M., Rosen, D.W., 2005. Investigation of Solid Freeform Fabrication Processes for the Manufacture of Parts with Designed Mesostructure, ASME, Long Beach, California.

Willich, G., 2007. Demands of space industry on rapid technologies 2007, Eurorapid 2007. Astrium GmbH, Frankfurt/Main.

Woodcock, D.A., Lightfoot, P., 1999. Comparison of the structural behaviour of the low thermal expansion NZP phases $MTi_2(PO_4)_3$ (M = Li, Na, K). *Journal of materials chemistry* 9, 2907-2911.

Xue, M.-D., Duan, J., Xiang, Z.-H., 2007. Thermally-induced bending-torsion coupling vibration of large scale space structures. *Computational Mechanics* 40, 707-723.

Xue, M., Ding, Y., 2004. Two kinds of tube elements for transient thermal–structural analysis of large space structures. *International Journal for Numerical Methods in Engineering* 59, 1335-1353.

Yamahara, K., Okazaki, K., Kawamura, K., 2001. Molecular dynamics study of the thermal behaviour of silica glass/melt and cristobalite. *Journal of Non-Crystalline Solids* 291, 32-42.

Yan, C., Lifeng, W., Jianyue, R., 2008. Multi-functional SiC/Al Composites for Aerospace Applications. *Chinese Journal of Aeronautics* 21, 578-584.

Yates, B., Cooper, R.F., Kreitman, M.M., 1971. Low-Temperature Thermal Expansion of Zinc Oxide - Vibrations in Zinc Oxide and Sphalerite Zinc Sulfide. *Physical Review B* 4, 1314.

Zhou, J., Shrotriya, P., Soboyejo, W.O., 2004. On the deformation of aluminum lattice block structures: from struts to structures. *Mechanics of Materials* 36, 723-737.